Third-Order Nonlinear Optical Study on Sublimated/Langmuir-Blodgett Thin Films of Lanthanide Porphyrin Phthalocyanine Dimer/Heterodimer and Symmetric Trimer Systems by Time-Resolved Non-Degenerate Four-Wave Mixing

by

Mr. PAN, Ligang

Thesis Submitted in Partial Fullfillment of the Requirements
for
the Degree of Doctor of Science (Ph.D.)

Département de physique, Faculté des sciences,
Université de Sherbrooke,
Sherbrooke, Québec, Canada.

October 1996

Members of Jury:
— Professor Serge Jandl
— Professor Denis Moris
— Professor Daniel Houde (Directer of the Thesis)
— Professor Laurent G. Caron (Directer of the Thesis)

Invited Member:
— Professor
Marguerite-Marie Denariez-Roberge

谨以此献给
我的妻子孙朝霞，
我们的孩子瀛洲与雄飞
及　我们的父母们，祖父母们！

To My Wife SUN Zhaoxia,
Our Sons Yingzhou & Xiongfei,
and Our Parents and Grand-Parents!

À ma femme SUN Zhaoxia,
nos enfants Yingzhou & Xiongfei,
et nos parents et grand-parents!

Zu meiner Frau SUN Zhaoxia,
unseren Kindern Yingzhou & Xionfei,
und unseren Eltern und Großeltern!

この論文を
わたしの夫人孫朝霞さんと，
わたしたちの息子，瀛洲と雄飛さんと，
わたしたちの父母さんと，
わたしたちのわじいさんわばあさんに
さしあげます！

К Моей Госпоже Сун Цаошйа,
Нашим Детям Инзцоу и Щионфы,
Нашим Родилям,
и Нашим Дедам и Бабушкам!

Résumé

Ce travail porte sur l'étude par la technique de mélange à quatre ondes résolu dans le temps ("time-resolved four-wave mixing" ou "TRFWM") de couches minces de différents matériaux organiques d'intérêt pour l'optique non-linéaire. Il s'agit de couches sublimées du dimère neodymium porphyrine phthalocyanine $Pc^{2-}Nd^{III}Pc^{\bullet}$, de l'hétérodimère cérium porphyrine phthalocyanine $Pc^{2-}Ce^{IV}TPP^{2-}$, des trimères cérium porphyrine phthalocyanine $TPP^{2-}Ce^{III}Pc^{2-}Ce^{III}TPP^{2-}$ et neodymium porphyrine phthalocyanine $Pc^{2-}Nd^{III}TPP^{2-}Nd^{III}Pc^{2-}$, ainsi que de couches Langmuir-Blodgett du dimère mixte cobalt porphyrine phthalocyanine $CoPC_{22}{}^{+4}$ / H_2PcTS^{4-}.

Cette thèse fait état de plusieurs premières: ***première étude par TRFWM de couches organiques sublimées, première observation et investigation de la contribution des mécanismes de diffusion à l'atténuation du réseau de diffraction transitoire généré par TRFWM, première observation et investigation d'un effet photoréfractif dans les couches minces de multimères organiques***, et ***première étude et dépistage d'un nouveau phénomène de mutation de mode de vibration.***

Les valeurs absolues de la susceptibilité optique non-linéaire de troisième-ordre $\chi^{(3)}$ des couches ont pu être déterminées grâce à une étude comparée avec une lame de verre de quartz servant de référence.

Ce travail montre que la technique de TRFWM est non seulement utile mais surtout très sensible et fort puissante pour l'étude des procédés optiques non-linéaires dynamiques de troisième ordre dans les matériaux organiques. Elle permet entre autre de mesurer des mécanismes inobservables par absorption transitoire ou par d'autres méthodes d'optique non-linéaire.

Les études des systèmes dimère/hétérodimère et trimère/hétérodimère de terres rares porphyrine phthalocyanine montrent enfin que ces matériaux sont très intéressants pour leurs propriétés optiques non-linéaires. Ce sont ***de nouvelles familles de matériaux organiques très prometteurs pour les études et les applications de l'effet photoréfractif.*** Ils sont polyvalents et ont un grand potentiel comme matériaux optiques non-linéaires.

Abstract

Time-resolved four-wave mixing (TRFWM) studies have been carried out on sublimated films of the neodymium phthalocyanine dimer $Pc^{2-}Nd^{III}Pc^{\bullet}$, the cerium porphyrin phthalocyanine sandwich mixed heterodimer $Pc^{2-}Ce^{IV}TPP^{2-}$, the cerium porphyrin phthalocyanine symmetric trimer $TPP^{2-}Ce^{III}Pc^{2-}Ce^{III}TPP^{2-}$, the neodymium porphyrin phthalocyanine trimer $Pc^{2-}Nd^{III}TPP^{2-}Nd^{III}Pc^{2-}$, and Langmuir-Blodgett films of the cobalt porphyrin phthalocyanine mixed dimer $CoPC_{22}{}^{4+}$ / H_2PcTS^{4-}.

In this work, we have presented a number of novel results: ***the first non-degenerate time-resolved four-wave mixing (NDTRFWM) experiment on a sublimated film***, ***the first observation and identification of the diffusion contribution to the degrating process***, ***the first observation and identification of photorefractive effect in an organic multimer thin film***, and ***the first observation and identification of a correlated phonon mode shifting phenomenon***.

The absolute values of the third-order nonlinear optical susceptibility $\chi^{(3)}$ of the samples have been determined by comparing the third-order nonlinear optical responses of the samples with those of a slide of reference fused quartz under the same experimental conditions.

It is shown that TRFWM is a very useful, very sensitive and very powerful tool to investigate the dynamics of the third-order nonlinear optical processes in a medium, especially those that can not be detected by transient absorption and other means of probing nonlinear optical properties.

Through this work, it can be seen that lanthanide porphyrin phthalocyanine dimer/ heterodimer trimer/heterotrimer systems could be ***a new family of organic materials most promising for the investigation and the applications of photorefractive effect.*** They are very versatile and have a great potential as nonlinear optical materials.

摘 要

本文介绍对以升华法制备的钕呔菁二聚体$Pc^{2-}Nd^{III}Pc^{\bullet}$，钕卟啉呔菁异二聚体$Pc^{2-}Ce^{IV}TPP^{2-}$，铈卟啉呔菁三聚体$TPP^{2-}Ce^{III}Pc^{2-}Ce^{III}TPP^{2-}$,钕卟啉呔菁三聚体$Pc^{2-}Nd^{III}TPP^{2-}Nd^{III}Pc^{2-}$的薄膜，及对钴卟啉呔菁混合二聚体$CoPC_{22}^{4-}/H_2PcTS^{4-}$的 Langmuir-Blodgett薄膜所做的时间可分辨四波混频(TRFWM)的研究。

本文展示了**第一个在升华薄膜上所做的时间可分辨四波混频的实验**。通过比较同种样品的时间可分辨四波混频(TRFWM)实验的结果与暂态吸收实验的结果，**第一次决定了扩散对退光栅过程的贡献**。同时，我们还观察并研究了有机薄膜中的**第一个光致折射率改变的效应**及**第一个相关声子模频移的现象**。

通过比较在同样实验条件下实验样品与参考硅玻璃片的三阶非线性光学响应，定出了实验样品的三阶非线性光学极化率 $\chi^{(3)}$ 的绝对值。

本文证实了时间可分辨四波混频(TRFWM)是研究介质中三阶非线性光学动态效应的一种非常有用、非常灵敏、及极为强有力工具，尤其是对那些为暂态吸收光谱及其他非线性光学实验手段所不能探测到的某些过程来说，更是这样。

由本文可以看出，镧系卟啉呔菁二聚体/异二聚体、三聚体/异三聚体系统可能是**应用与研究光致折射率改变效应的一种新的极有希望有机材料家族**。同时，这些系统具有很强的多向适用性，是一种具有很大潜在应用价值的非线性光学材料。

Acknowledgement

First of all, I would like to thank my two directors, Professor Laurent G. Caron, former Chairman of *Canadian Association of Physics*, and Professor Daniel Houde. It is Professor Laurent G. Caron who gave me the opportunity to study and work in *l'Universé de Sherbrooke*. Without his kindness and discerning eyes, I would have had no chance and no scope to exercise my abilities. It is Professor Daniel Houde who set up the femtosecond laser laboratory and proposed a research project which, although very difficult, proved to be very interesting, meaningful, and worth investigating in time and efforts. In his lab, I spent five unforgettable and fruitful years learning a great deal from him and accumulating the experiences that allowed me to mature as a scientific researcher. I would like to add that he is one of the best teachers I have ever seen. Without his attentive and enlightening guidance, this work would have been impossible.

Second I would like to thank Dr. Thu-Hua Tran-Thi, her group in *CEA, Centre d`Études Atomiques de Saclay, France*, and her collaborators Professor André De Cian, Professor Driss Chabach, Professor Raymond Weiss. She and her group made an important contribution to this work. During my visiting in *CEA*, I benefited a lot from her kind arrangements and enthusiastic help.

I would like to thank Professor Marcel Aubin, who gave me my first French professional course in physics. With his warm and gentle help, I passed a difficult turning point in my life.

I want to thank Professor Serge Jandl, Chairman of Department of Physics, and his wife Carla Jandl. The former gave me a course in physics, the latter gave me a course in French. From their teachings, I gained a lot.

I would like to thank Dr. Paul Grenier, who worked with Professor. Daniel Houde to establish the femtosecond laser lab and helped me to quickly get access to all the facilities.

I wish to thank Dr. Rashmilkant Sudiwala, a specialist in Langmuir-Blodgett techniques. By means of his kind help, I got into the LB world and was able to complete an important part of this work.

I would like to thank Professor André-Marie Tremblay, Professor Alain Caillé, and Professor André Lemieux, for their kind help to me, and thank the Department of Physics and *C.R.P.S.* (*Centre de Recherche en Physique du Solide*) of the Department of Physics for the financial support.

Many thanks to Professor Lê Dao and his group for their collaboration in making the sublimated films.

Furthermore, I would like to thank Professor Jean Beerens and Mr. Jacques Corbin of the Department of Physics of Sherbrooke University, for their help in measuring the thickness of the samples, and thank Professor Jacques Beauvais, *le directeur de Salle Blanche* and Mr. Michel Paquette, *du Département de Génie Electrique de l'Université de Sherbrooke*, for their help in measuring the refractive index of the samples.

I also thank Dr. Jean François Lipskier, Dr. Thierry Fournier and Dr. Isabelle Salabert. Their photo-chemical study on the lanthanide porphyrin phthalocyanine dimer/heterodimer trimer/heterotrimer by transient absorption was of great importance to this work.

Thanks also are given to the Medical Research Council of Canada and the Centre of Excellence in Molecular and Interfacial Dynamics, CIDA and France-Québec, for their support of this work.

Finally, I would like to thank Dr. Claude Pépin, Ms. Stephanie Marengo and all the members of the *groupe CRM (Conseil de Recherche Médicale) de recherches en sciences des radiations du Département de Médecine Nucléaire et de Radiobiologie, Faculté de Médecine, Université de Sherbrooke*. Thanks to all the known or unknown persons who have contributed to this research work.

Table of Contents

List of Figures

List of Tables

List of Abbreviations

2WM	Two-Wave Mixing
4WM	Four-Wave Mixing
A	Acceptor
AS	Antena System
ATP	Adenosine Tri-Phosphate
BPH	bacteriochlorophyll
BPS	Bacteria Photosystem
Ce	Cerium
$CoPC_{22}^{4+}$ / H_2PcTS^{4-}	cobalt porphyrin phthalocyanine mixed dimer
CPM	Colliding Pulse Mode-locked (dye laser)
CT	Charge Transfer
CTSC	Charge Transfer State Coupling
D	Donor
DC	Direct Current
DM	Dimer
EC	Excitonic Coupling
EEM	Excitonic Excitation Migration
ET	Electron Transfer
FDFWM	Fully-Degenerated Four-Wave Mixing
FWDFG	four-wave difference-frequency generation
FWI	Four-Wave Interaction
FWSFG	four-wave sum-frequency generation
FWUC	four-wave up-conversion
HDM	Heterodimer
HBP	1,2,3,4,8,9,10,11,15,16,17,18,22,23,24,25,-hexadecahyrotetrabenzo[*b,g,l,q*]porphyrin

HTM	Heterotrimer
HOMO	Highest Occupied Molecular Orbit
ICT	Intramolecular Charge Transfer
KDP	potassium (K) Dihydrogen Phosphate
KTP	potassium (K) Titanyl Phosphate
LBF	Langmuir-Blodgett Film
LMCT	Ligand to Metal Charge Transfer
Ln	Lanthanium
Lu	Lutetium
LUMO	Lowest Unoccupied Molecular Orbit
MD	Mixed Dimer
MDM	Molecular Dipole Migration
MLCT	Metal to Ligand Charge Transfers
NADP	Nicotinamide Adenine Dinucleotide Phosphate
Nd	Neodium
NDFWM	Non-Degenerated Four-Wave Mixing
NDTRFWM	Non-Degenerate Time-Resolve Four-Wave Mixing
NLO	Nonlinear Optics
NRE	Non-Resonant Excitation
OEP	2,3,7,8,12,13,17,18-octaethylporphyrin
OMP	2,3,7,8,12,13,17,18-octamethylporphyrin
OPRM	Organic Phortorefractive Material
P	Porphyrin
Pc	Phthalocyanine
$Pc^{2-}Ce^{IV}TPP^{2-}$	cerium porphyrin phthalocyanine sandwich mixed heterodimer
$Pc^{2-}Nd^{III}Pc^{\bullet}$	neodymium porphyrin phthalocyanine dimer
$Pc^{2-}Nd^{III}TPP^{2-}Nd^{III}Pc^{2-}$	neodymium porphyrin phthalocyanine trimer

PDFWM	Partially-Degenerated Four-Wave Mixing
PR	Photo Refractivity, Photo Refractive
PRE	Photo Refractive Effect
PS	Photosystem
PSU	Photo Synthetic Unit
RC	Reaction Center, Resistance-Capacity
SHG	Second Harmonic Generation
SOC	Spin-Orbit Coupling
TA	Transien Absorption
TAP	5,10,15,20-tetra(p-anisyl)porphyrin
TClP	5,10,15,20-tetra(*p*-chlorophenyl)porphyrin
THG	Third Harmonic Generation
TM	Trimer
TPP	5,10,15,20-tetraphenylporphyrin
$TPP^{2-}Ce^{III}Pc^{2-}Ce^{III}TPP^{2-}$	cerium porphyrin phthalocyanine symmetric trimer
TRTG	time-resolved transient grating
TRFWM	Time-Resolved Four-Wave Mixing
TTP	5,10,15,20-tetra(*p*-tolyl)porphyrin
TRNDFWM	Time-Resolved Non-Degenerate Four-Wave Mixing
TRTG	Time-Resolved Transient Grating

Introduction

The importance of nonlinear optical phenomena has been known for a long time. Since the 1980s, materials research and development for nonlinear optical applications have rapidly progressed so that several systems are available commercially. To date, the systems have been utilized in *information processing*, *optical switching*, *optical frequency conversion*, and *telecommunications*. The advancing development of optotechnology has encouraged research on suitable nonlinear optical materials. A wide variety of materials, including inorganic and organic crystals, polymers, semiconductors, composites and metal-based systems, possess noticeable nonlinear optical properties. In recent years, organometallic compounds, by their unique characteristics, such as diversity of metals, oxidation states, ligands, and geometries, have achieved success in and brought a new dimension to the area of nonlinear optics.

In last six years, investigations of organometallic systems have been greatly intensified, because[1, 3]:

1. Organometallic system can possess metal → ligand or ligand → metal charge transfer (MLCT, LMCT) bands in the visible region of the spectrum, which are usually associated with large second-order activity.

2. The compounds have great possibilities for redox changes, a property largely associated with the metal center, which can be electron poor or rich depending on the oxidation state and ligand environment. Facile redox ability can lead to large hyperpolarizability, with the metal center being an extremely strong donor/acceptor in comparison to conventional organic systems.

3. Chromophores, such as phthalocyanines, containing metal ions, are among the most intensely coloured materials known. The strength of the optical absorption band is also associated with large optical nonlinearities [4].

4. Many organometallic compounds have low-lying excited states with their dipole moments significantly different from their respective ground state dipole moments. Most of the excited states involve charge transfer between the central metal and

one or more of the associated ligands and have a large oscillator strength. This will provide a substantial contribution to the hyperpolarizability.

5. Organometallic compounds also have important advantages in the range and mix of non-aromatic ligands that can be attached to the metals. These ligands can shift the occupied and unoccupied metal d orbitals that interact with the π-electron orbitals of the conjugated systems. This provides a mechanism for fine-tuning and optimizing the bulk susceptibility.

6. Furthermore, the metal centers in these molecules can constitute a chiral species [5]. When dissolved, they will form materials that crystallize in non-centrosymmetric space groups, essential for a non-zero $\chi^{(2)}$ value.

7. Incorporation of transition metal ions, such as lanthanide ions, can also be expected in some cases to increase the solubility of a material in common organic solvents, therefore enhancing its processability.

The crucial aspect in the progression of nonlinear optical studies has been the development of experimental techniques for investigating and measuring a material's non-linear optical properties. Over the years, several methods have been widely used to make nonlinear optical studies, such as, *Kurtz powder technique* [6, 9], *electric field induced second harmonic generation* (EFISH) [10 - 13], *hyper-Rayleigh scattering* (HRS) [14, 15], *third harmonic generation* (THG) [16, 17], and *degenerate four-wave mixing* (DFWM) [18 - 22]. More surprisingly, though ***non-degenerate four-wave mixing*** (NDFWM), both in resonant and non-resonant situations, is a powerful technique to study dynamical properties of physical systems, very few reported experimental investigations of organometallics have used this important technique. Commonly, a combination of techniques is necessary for a complete investigation of a material's nonlinear optical behaviour.

The third-order nonlinear optical studies on organometallic materials can be divided into six major classes[23]: *metallocenes, metallopolyyne polymers, polysilanes and-germanes, metal dithiolene complexes, thiophenes, and phthalocyaninato metal complexes.*

The phthalocyanines and porphyrins are two extremely interesting and useful classes of compounds. Their extensively delocalized two-dimensional π-electron systems have broken through some limitations of most other third-order non-linear optical compounds featuring pseudo-one-dimensional π-electron conjugation systems. This has led to considerable interest in the two dimensional π-conjugated phthalocyanine systems and, in particular, the complexes containing a wide variety of metals.

Phthalocyanine has a similar macrocycle to porphyrin and its absorption spectrum is complementary to that of porphyrin. Therefore, the dimer formed by linking porphyrin and phthalocyanine will absorb more efficiently the solar energy than the monomer of porphyrin or phthalocyanine [24]. Nevertheless, until now, only Tran-Thi [25-27], Gaspard [28, 29], and Xu [30, 32] have synthesized porphyrin phthalocyanine dimer/heterodimer and made observations on energy transfer and charge separation processes. Gaspard and Xu found that these are related to the molecular configurations. Tran-Thi, through the research on Langmuir-Blodgett films of porphyrin phthalocyanines, found that the dimer/heterodimer have a face-to-face geometry, in which there is a strong excitonic coupling between the porphyrin and the phthalocyanine. Compared with the studies on the other polymers of metallo organics and on the metallo monomers of porphyrin and phthalocyanine, the research on metallo multimers (dimer / heterodimer and trimer / heterotrimer) of the porphyrin phthalocyanine, is just at its beginning.

Though research on the optical nonlinearity of organometallic complex is very active, the relationship between the structure and the nonlinear optical properties are still unclear. Unlike the design of second-order nonlinear optical materials, which follows some well defined guidelines, models for the synthesis of third-order species are much less developed. Presently, research on the third-order nonlinearities of porphyrin phthalocyanine is focused mainly on the monomers and on the effects of replacing the central metal ion on the optical nonlinearities. A systematic research on the third-order nonlinearities of porphyrin phthalocyanine dimer/heterodimer and trimer/heterotrimer systems has not yet been undertaken.

In this work, we present a third-order nonlinear optical study of sublimated and Langmuir-Blodgett thin films of lanthanide porphyrin phthalocyanine

dimer/heterodimer and trimer/heterotrimer systems using a non-degenerate time-resolved four-wave mixing technique.

Chapter 1 introduces some important general consideration in the experiment: (1.1.) *ultrafast time-resolved spectroscopy,* (1.2.) *prototype model system used in the experiment,* (1.3.) *two important experimental phenomena encountered,* and (1.4.) *the outline of our research work.* Chapter 2 presents the theoretical and experimental basics for this work, especially of *four-wave interactions.* Chapter 3 describes the experimental system. Chapter 4 presents and discusses the experimental results. Finally, Chapter 5 makes a conclusion on this research work.

Chapter 1

General Consideration

This is an experimental research work on nonlinear optical dynamic behaviours of the sublimated and Langmuir-Blodgett thin films of lanthanide porphyrin phthalocyanine multimers. Time-Resolved Non-Degenerated Four-Wave Mixing (TRNDFWM) has been used as a major experimental technique in this work. Nonlinear optical responses of the lanthanide porphyrin phthalocyanine dimers, herodimers and trimers have been investigated by TRNDFWM.

This chapter will give some detailed aspects of the experiment techniques, description of the materials used, and motivation of this research work.

1.1. Ultrafast Time-Resolved Spectroscopy

TRNDFWM is one of the most useful ultrafast coherent spectroscopy techniques. Coherent spectroscopy implies investigations both in the time and frequency domains, yielding information on dynamic processes as well as line widths and line positions of the molecular systems under investigation.

Initially started in the mid-sixties, coherent spectroscopy is intimately connected with the development of intense coherent light sources which, as already mentioned, are prerequisite to the study of nonlinear optical effects.

Until about the mid-sixties, the performance of the time-resolved techniques was limited to the microsecond region in the case of absorption spectroscopy and to the nanosecond region in the case of fluorescence. During the late sixties, the appearance of giant pulse lasers brought the time resolution into the nanosecond range. A major advance in the generation of ultrashort optical pulses happened after

the invention of mode-locking techniques [33, 34]. Passive mode-locking of the ruby laser by Mocker [35] opened a new era for ultrashort optical pulse generation. Shortly thereafter, the generation of the first optical pulse in the picosecond range with a Nd:glass laser was reported by De Maria [36]. Since that time, there followed a number of dramatic advances in ultrashort laser pulse generation as shown in Fig. 1.1.0.1. . The shortest optical pulse width available at a given year fells at an exponential rate. Each reduction in pulse width has always been accompanied by an advance in technology [37].

Until now, using colliding pulse mode-locking (CPM) [38 - 40], pulse compression [41 - 49], and other techniques, one has been able to reduce the optical pulse width to six femtoseconds [50, 51]. This approaches the ultimate limit in the visible region set by the uncertainty principle.

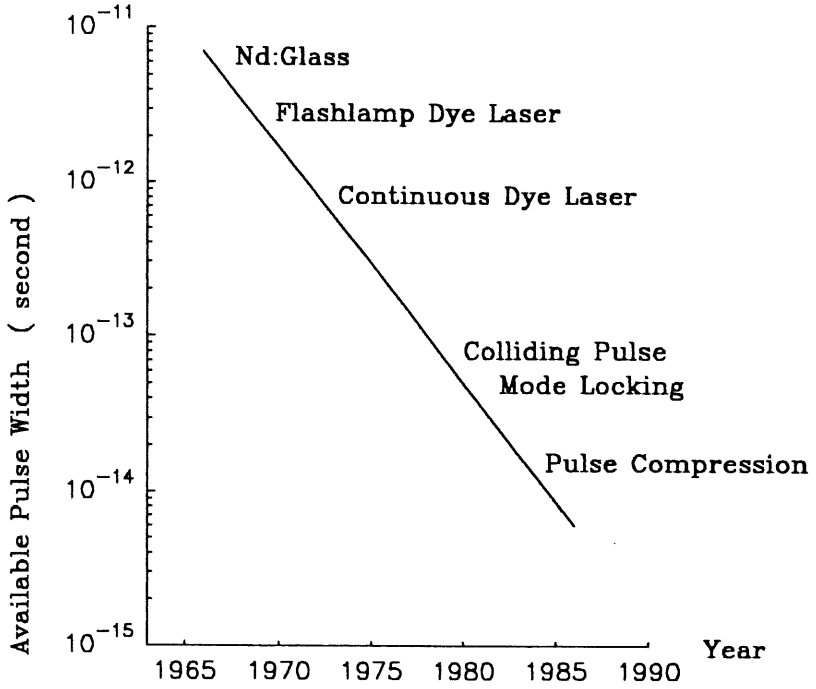

Figure 1.1.0.1. Plot of the Logarithm of the Shortest Available Optical Pulse Width versus Years.

The ability to generate ultrashort light pulses has extended coherent spectroscopy to real-time measurements of rapid dynamic processes on picosecond and femtosecond time scales. Most of the time-resolved spectroscopy investigations are concerned with such processes in condensed phases. The progress in the

experimental capabilities has stimulated theoretical investigations and improved our understanding of the interactions in liquids and solids.

1.1.1. Time-Resolved Spectroscopy

While different sub-Doppler techniques aim at higher spectral resolutions, time-resolved spectroscopic techniques target on higher time resolutions.

The generation of extremely short and intense laser pulses has opened the door to the study of fast transient phenomena. Picosecond and femtosecond light pulses make it possible to investigate ultrafast processes occurring during the excitation and the deactivation of molecular states in solvents and solids.

Optoelectronic detection systems, such as fast photodiodes and sampling oscilloscopes, have reached a time resolution of 10^{-10} s, or 100 ps. This is still too long to resolve many fast transient events on a picosecond and subpicosecond time scale. Thus, in picosecond and sub-picosecond spectroscopy, one had to develop a series of new techniques to measure the durations and the profiles of the light pulses, and to probe the ultrafast relaxation processes.

Except for the streak camera which can reach time resolutions of a few picoseconds, most of the methods used to measure pico- and subpico-second phenomena are based on optical delay lines and on some nonlinear optical effects, such as SHG. In optical delay line systems, as shown in Fig. 1.1.1.1., an ultrashort laser pulse is divided by a beam splitter into two, or more if necessary, replica pulses which travel different path lengths before they are recombined. Hence, the measurement of a time interval Δt has been converted into that of a path difference $\Delta x = c\Delta t$, where c is the light velocity. For example, in our experiment, the minimum spatial interval available for the delay line system made by KLINGER of $\Delta x_{min} = 0.2$ micrometer, is equivalent to the time interval $\Delta t = \Delta x / c = 0.2$ mic $\times$ 3.3564095 fs/mic ≈ 0.7 fs, which is still shorter than the pulse width of the shortest light pulse presently available in the visible region, i.e. 6 fs. Therefore, the resolution

of most detecting systems is now only limited by the pulse duration of the laser source that is used, rather than by the delay line.

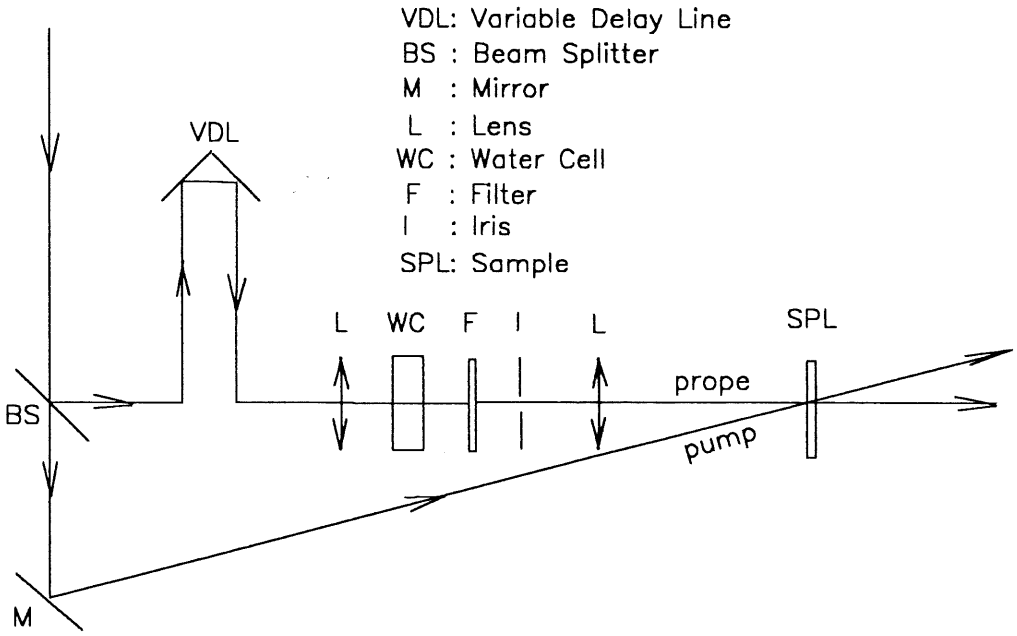

Figure 1.1.1.1. Optical Delay Line, White Continuum Generation and Time-Resolved Spectroscopic Measurement with Probe-Pump Technique in Transient Absorption.

1.1.2. Pump - Probe Technique

Most of molecular fast relaxation processes are between the nanosecond to picosecond ranges, as shown in Fig. 1.1.2.1. [52]. Thus with ultrashort laser pulses, the limiting factor for time resolution is no longer the pulse duration but the response of the detection systems.

The limitation of the detection system can be overcome by a pump and probe technique. A single ultrashort laser pulse is divided into a group of strong pump beams and a weak probe beam, which can be monochromatic or white continuum. The delay Δt between pump and probe can be controlled by varying the length of the optical path difference between the probe and the pump beams. Strong pump beams

create an excitation in a molecular system and the probe beam probes the relaxation of the excitation as a function of the delay time Δt. Now, the time resolution is limited only by the pump and the probe pulse duration. One of the applications of pump-probe technique is the measurement of the decay times of short-lived excited states, as shown in Fig. 1.1.2.2. (a). When the probe pulse has a path difference x_1 (< 0) with respect to pump pulse (Fig. 1.1.2.2. (a)), the probe pulse will spend less time $|t_1 = x_1/c|$ to arrive at the sample than the pump pulse does (Fig. 1.1.2.2. (b)), and this corresponds to a negative delay time τ_1 (probe-to-pump) (Fig. 1.1.2.2. (c)). At this moment, since when the probe pulse arrives there is no excitation in the sample, the system will give no response at all. If the probe pulse arrives at the sample with a longer light path x_2 (> 0) with respect to the pump pulse, the probe pulse will spend more time $t_2 = x_2/c$ to reach the sample than the pump pulse does and this corresponds to a positive delay time τ_2 (probe-to-pump). At this moment, the probe pulse arrives at the sample in a time τ_2 after the excitation has been created (Fig. 1.1.2.2. (b)), the energy level 1 has been populated with a non-zero population N_1, so that the probe pulse will feel the decay of this population. Therefore, if delay time scans from the negative delay (negative light path difference between probe and pump) to the positive delay (positive light path difference between probe and pump) in steps, then the detecting system will directly measure the response curve point by point, shown as in Fig. 1.1.2.2. (c).

Although numerous techniques refer to pump-probe methods, the most powerful one is based on white continuum generation.

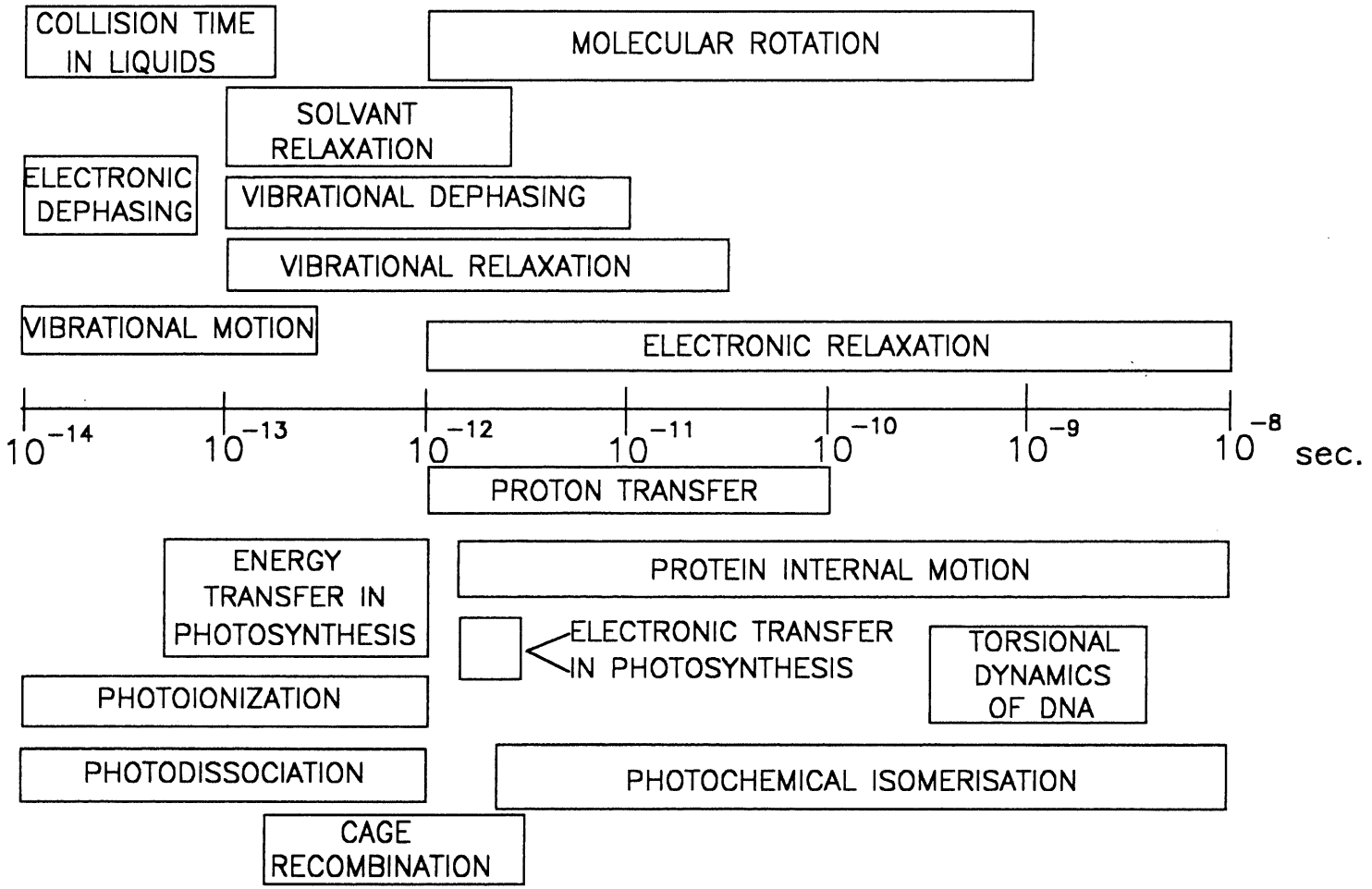

Figure 1.1.2.1. Approximate Time Scales of Elementary Molecular Relaxation Phenomena and Some Chemical and Biological Manifestations of these Phenomena.

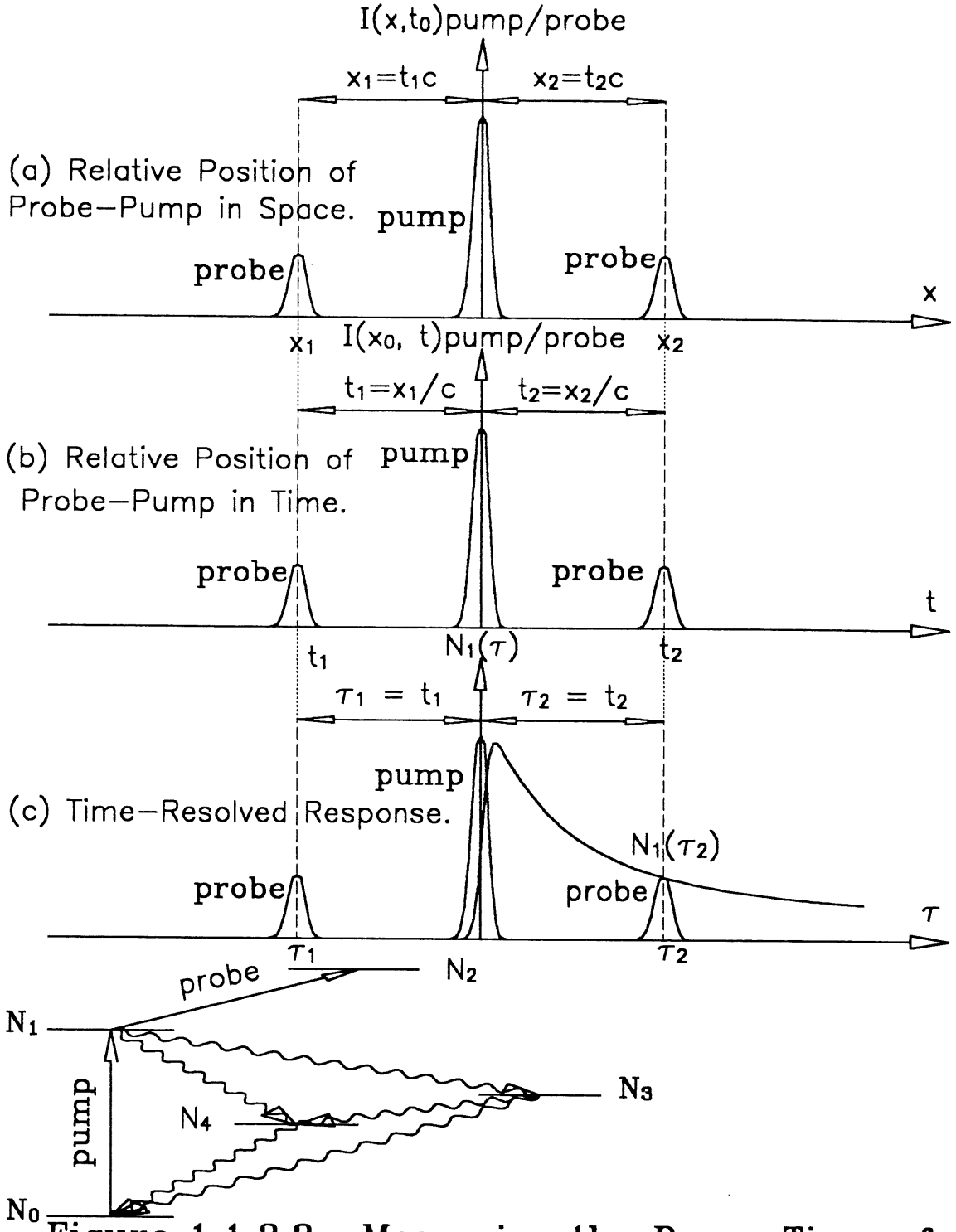

Figure 1.1.2.2. Measuring the Decay Time of Short–lived Excited States by Time–Resolved Pump–Probe Techniques.

1.1.3. White Continuum Generation

White continuum generation is a particularly spectacular application of nonlinear frequency mixing. When a strong laser beam is focused within a glass or within a liquid such as CCl_4, water or phosphoric acid, there is an emission of a pulse of white light whose duration is comparable to that of the pump pulse.

People now generally agree that this continuum originates from two superposed phenomena. First, high intensity optical pulses propagating through a medium will distort the atomic or electronic configurations and change the refractive index appreciably. The refractive index becomes time-dependent so the phase of the optical wave is altered. This generally leads to a broadening of the spectrum. This process is called *self-phase modulation* [52, 53]. Second, in isotropic liquids, there is a supplementary spectral broadening due to *four photon parametric interactions* [54 - 57].

In fact, white-continuum generation is one of the crucial techniques in ultrafast spectroscopy. The spectrum of the continuum extends from the near ultraviolet to the infrared and thus provides a versatile coherent light source for a huge range of spectroscopic studies. Without it, many ultrafast spectroscopic applications would not be available.

1.1.4. Basic research Opportunities for Ultrashort Time-Resolved Spectroscopy

From various time-resolved coherent techniques, we can obtain the following information [58]:

1. whether a transition is homogeneously broadened or not;
2. the decaying times of homogeneously or inhomogeneously broadened spectral features;
3. the dominant line broadening mechanisms;

4. the pure dephasing times;
5. the energy relaxation times;
6. the mechanisms and paths of energy relaxation;
7. the collision times;
8. the nonresonant susceptibilities;
9. transition frequencies within conjugated spectra regions;
10. precise frequency differences of vibrational modes separated by up to 10×10^{12} Hz = 10 THz (10 tera Hertz, $\Delta t \cdot \Delta \upsilon \sim 1 \rightarrow \Delta \upsilon \sim 1/\Delta t$, $\Delta t \geq 100$ fs = 10^{-13} s $\rightarrow \Delta \upsilon \leq 10^{13}$ Hz).

A particular technique gives only one or few of the above. A combination of different techniques is usually necessary for obtaining more information.

1.1.5. Transient Grating Method

Among the time-resolved spectroscopic methods which pump-probe techniques, we chose the transient grating method [59] to detect transient responses of our model systems.

1.1.5.1. Formation of the Transient Grating

In this technique, two pump (excitation) pulses arrive simultaneously at the sample. The two sychronized pump beams interfere with each other and produce a spatially modulated field which is called an *interference grating*. When a material is placed into the interference region of the pump waves, some light-matter interaction, such as absorption, creates a corresponding spatial modulation (*grating*) of some material properties, such as.:

1. the population of excited electronic states,
2. the conduction electron density (in semiconductors),

3. the space charge and the accompanying field (photorefractive materials),
4. the temperature,
5. the molecular orientation (fluids), and
6. the concentration (mixtures).

Thus a *transient grating* (because it will disappear in a finite time after the excitation) is formed due to population or phase redistribution which occurs under strong light fields. Most of these changes can be described by the population of one, several, or a whole continuum of excited (e.g. electronic, phonon) states of the sample material. Therefore, the corresponding gratings are also termed as *population gratings* in a general sense.

1.1.5.2. Detection of the Decay of the Transient Grating

In order to make time-resolved measurements of the dynamics of the transient grating, a third beam called *probe* needs to be used. When arriving at the sample, the probe beam is deflected by the light induced grating, producing a signal beam. The intensity of the signal beam is measured as a function of the time delay between the pump beams and the probe beam which contains information on the dynamics of the system. This Bragg scattering from the light induced transient grating, in terms of nonlinear optics, is viewed as a *four-wave interaction* (FWI) or *four-wave mixing* (FWM) process. This will be discussed in details in the following chapters.

The decay of the grating is commonly detected by diffraction of the probe light beam. The diffracted light can either be recorded directly or heterodynedly with a split-off beam from the probe light. The former is simple but requires higher pump and probe power to get sufficiently strong signals. The latter is more sensitive but the setup more complicated. In our experimental setup, we use only direct detection scheme.

For ideal plane waves, the diffraction efficiency η for the first order diffracted beam can be expressed [60]:

$$\eta = \frac{I_{diffracted}}{I_{probe}} = \left| \frac{\pi \Delta \tilde{n} d}{\lambda_{probe}} \right|^2 = \left[\left(\frac{\pi \Delta n d}{\lambda_{probe}} \right)^2 + \left(\frac{\pi \Delta \kappa d}{\lambda_{probe}} \right)^2 \right] \qquad (1.1.5.2.1.)$$

where $\Delta\tilde{n}$, Δn, $\Delta\kappa$ are changes in the complex refractive index and its real and imaginary parts in the sample due to transient grating, d is the thickness of the sample, and $I_{diffracted}$, I_{probe} are the intensities of the diffracted beam and the probe beam. This formula is valid for a grating with a sufficiently small $|\Delta\tilde{n}|^2 = |\Delta n + i\Delta\kappa|^2$ and a low absorption material, i.e., $\kappa d << 1$.

Very small refractive index changes Δn and optical path changes Δnd can be measured, typically, with a diffraction efficiency $\eta \approx 10^{-15}$, corresponding to an optical path change $\approx \lambda/1000$. The phase shift in that extreme case has to be measured with interferometric sensitivity.

Amplitude ($\Delta n = 0$) and *phase* ($\Delta\kappa = 0$) *gratings* can be differentiated by illuminating the sample with a parallel beam and observing the self-image appearing at different distances behind the grating [61], or alternatively by *heterodyne detection.*

1.1.5.3. Comparison of the Transient Grating Method with the Transient Absorption Technique

In this work, the post-excitation-dynamic processes of the porphyrin phthalocyanine dimer/heterodimer trimer/heterotrimer have been measured by time-resolved four-wave mixing (TRFWM), or equivalently called time-resolved transient grating (TRTG) method. The transient absorption (TA) results obtained on the same samples provide reference data since they give us information about the energy levels (bands) and their related lifetimes. It is therefore useful at this point to compare some crucial aspects of these techniques.

Table 1.1.5.3.1. lists the major differences between the transient absorption and the transient grating methods.

Table 1.1.5.3.1. The Major Differences Between the Transient Grating Method and the Transient Absorption Technique

	Terms	Transient Absorption	Transient Grating
1.	Pump Beams	1	2
2.	Probe Beams	1	1
3.	Nonlinear Optical Process	2nd-order	3rd-order
4.	Spatial Modulation	Homogenous	Grating-Like Sinusoidal
5.	Coherence	No	Yes
6.	Phase-Matching	No	Yes
7.	Detection	Transmission	Diffraction
8.	Sensitivity	$\propto \Delta\alpha = 2k_0\Delta\kappa$	$\propto \lvert\Delta n + i\Delta\kappa\rvert^2$
9.	Transport Phenomena	Non-Detectable	Detectable
10.	Information Extracted	Bands, Life Time τ	Life Time τ, *Diffusion* Time τ_Φ ....., etc.
11.	Response to Non-Resonant Excitation	No.	Yes.
12.	Response to Resonant Excitation	Yes.	Yes.

From the table it can be seen that there are only three beams involved in transient absorption, while there are four in the transient grating. The former is a second-order nonlinear optical (NLO) process and the latter is a third-order NLO process. Technically speaking, the latter is more difficult to implement because it involves more beams and needs higher pumping and probing powers. Furthermore, transient absorption measures the change in absorption coefficient, while transient grating detects diffraction efficiency which is in proportion to the square of the change of the complex refractive index. Therefore TRTG is more sensitive than TA in probing dynamic processes occurring after the excitation is produced.

Due to the difference between the modes of excitation, any transport process with charge transfer or and energy transfer occurring during the de-excitation can only be picked up by the grating-like modulation of TRTG, and not by TA which has homogeneous excitations. Hence, the diffusion processes are detectable only for TRTG and not for TA.

When the frequency of the pump light is not in an absorbing region of the material (non-resonant excitation, NRE), TA systems will get no signal at all, but TRTG systems will still give a response through the phase grating caused by virtual electron excitations. The signal of the NRE contains information about the pulse duration of the pump pules and the probe pulse.

In the resonant excitation case, TRTG systems can also feel the relaxation processes that TA systems will feel for the same material. But the TRTG systems may not yield exactly the same response as the TA systems do, because the response of the TRTG system is sensitive to any de-activation process in contrary to the TA system.

In short, TRTG is a more sensitive and more useful technique to probe the dynamic processes of de-excitation than TA, although the former needs the important information from the latter about the bands and the life times of the materials under investigation.

Of course, suitable materials have to be available for research in nonlinear optics and various kinds of applications.

1.2. Prototype Model Systems Used in the Experiment

1.2.1. Nonlinear Optical Materials

All materials, including all forms of matter, gases, liquids, and solids, have nonlinear optical properties. But, the intensity of the optical field needed to make these effects observable, varies over many orders of magnitude. This depends on the detailed nature of the electronic structure, the dynamic behaviour, as well as the symmetry and details of the geometric arrangement of the atomic and molecular components of the medium. From the device point of view, the most important nonlinear optical materials are in solid form and should meet a wide variety of auxiliary material requirements, including extraordinary stability with respect to ambient conditions and to high intensity light source, processability for pattern and shape definition, and integratibility with additional different materials.

There are a lot of materials possessing nonlinear optical properties: inorganic and organic crystals, polymers, semiconductors, composites and metal-based systems. However, none of these has proven to be the "silicon" of nonlinear optics because each material not only has properties that are advantageous for certain applications, but it also has properties that are disadvantageous for others. Therefore, there is still a need for the development of materials satisfying the critical requirements of devices for information processing, optical frequency conversion, integrated optics, and telecommunications.

We can roughly divide nonlinear optical materials into two major types: *molecular materials* and *bulk materials*.

For the first type, the materials consist of chemically bonded units which interact in bulk through weak Van der Waals forces. Many organic crystals and polymers belong to this class of materials. Nonlinearities in this kind of materials originate primarily from the molecular structure. The micro-nonlinearities in form of the hyperpolarizabilities of constituent molecules can be related to macro-nonlinearities in form of bulk nonlinear optical susceptibilities. The first step to optimize optical

nonlinearity in this class of materials is at the molecular structure level. For this, one needs to understand the relationship between the molecular electronic structure and the induced molecular nonlinear polarization.

In the second class of materials, nonlinearities are regarded as arising from quasi-free electrons like those in metals and semiconductors. The electronic characteristics of the bulk medium determines the optical nonlinearities. The origin of the nonlinearities for this type of materials needs a different theoretical framework. Examples of this kind of materials are: quantum well structures derived from GaAs and II-VI semiconductors, e.g. CdSe, inorganic crystals in which no single molecular unit in the ionic lattice can be identified, like KDP (potassium dihydrogen phosphate) and KTP (potassium titanyl phosphate).

Compared to inorganic nonlinear optical materials, the development of organic, or, more generally, molecular nonlinear optical materials is quite recent. Organic and other molecular materials are being more and more recognized as the promising materials for the future. These materials are interesting because their various molecular characteristics and their synthetic versatilities can be used to vary and optimize molecular structures in order to maximize nonlinear response, or to optimize the auxiliary properties like mechanical and thermal stability, and laser damage threshold. Organic materials can be cast into thin crystalline films, layer by layer, using the Langmuir-Blodgett technique and other deposition techniques, e.g. sublimation. These films show highly oriented structures and optimized nonlinearities. Some of the prominent advantages of many organic materials and high-performance polymers are high mechanical strength as well as excellent environmental and thermal stability, which can be many orders higher that those of inorganic materials. The unique π-bonding chemical structure of organic molecular materials leads to extremely large nonresonant (non-absorptive) optical nonlinearities, in many cases much higher than those of their inorganic counterparts. Devices with nonresonant electronic optical non-linearities will have the fastest response times limited only by the width of the driving laser pulse while also eliminating heat dissipation, beam depletion, thermally induced nonlinearities and other disadvantages of inorganic nonlinear optical materials. The considerably lower dielectric constant of organic materials yields a low RC time constant. Thus, the

electrooptic modulating devices made from these materials can operate with band-widths greater than 10 GHz (G = 10^9).

Aside from its potential technological interest, research on nonlinear optical materials also offers challenging opportunities for a fundamental understanding of the physics of nonlinear optical interactions. Before one can firmly control the molecular structure in order to enhance optical nonlinearities, there are still many things that must be done to understand completely the relationship between molecular structures and microscopic optical nonlinearities.

One of the most important type of organic nonlinear optical materials is porphyrin phthalocyanine metal complex systems.

1.2.2. Porphyrin and Phthalocyanine

The prototype model systems used in our experiment is based on porphyrin and phthalocyanine metal complexes. Porphyrins and the corresponding metal complexes function as electron transfer agents in many biological systems and play a very important role in many biochemical processes. Porphyrins contain a tetrapyrrolic macrocycle which can be chelated with most metallic ions, even some non-metallic ions, to form corresponding complexes.

The simplest porphyrin, called *porphine*, is shown in Fig. 1.2.2.1. .

The natural part of porphyrins can be obtained when the positions β and β′ = 2, 3, 7, 8, 12, 13, 17, 18 of the pyrrole cycles in Fig. 1.2.2.1. are replaced by substitutive groups [62, 63]. There also exist a number of synthetic porphyrins which depend on the nature of the substitutive groups and on the exact replaced positions in the porphine frame. One of the complete artificially synthetic examples of porphyrins is *phthalocyanine* (Pc), shown in Fig. 1.2.2.2. .

Phthalocyanines have a similar structure to porphine, which consists in replacing four carbon atoms at position α, β, γ, δ in Fig. 1.2.2.1. by four nitrogen atoms, and substituting β′ position (β′ = 2, 3, 7, 8, 12, 13, 17, 18 in Fig. 1.2.2.1.) on pyrrole

cycles by benzene cycles. This compound was discovered in 1907 by Braun et al. [64], but was not identified until 1933 by Linstead et al [65, 66].

Other artificial synthetic examples of porphyrins are tetrapyrrole complexes of mono-, bis-, tris- lanthanide porphyrins which were used in our work. These will be discussed in detail in following sections.

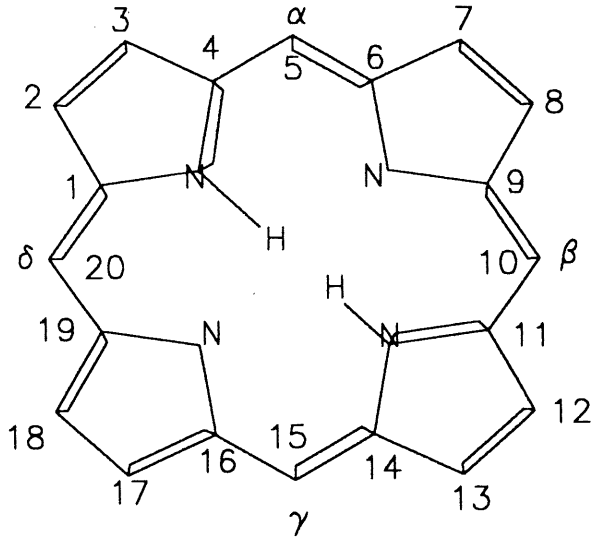

Figure 1.2.2.1. Molecular Structure of Porphin.

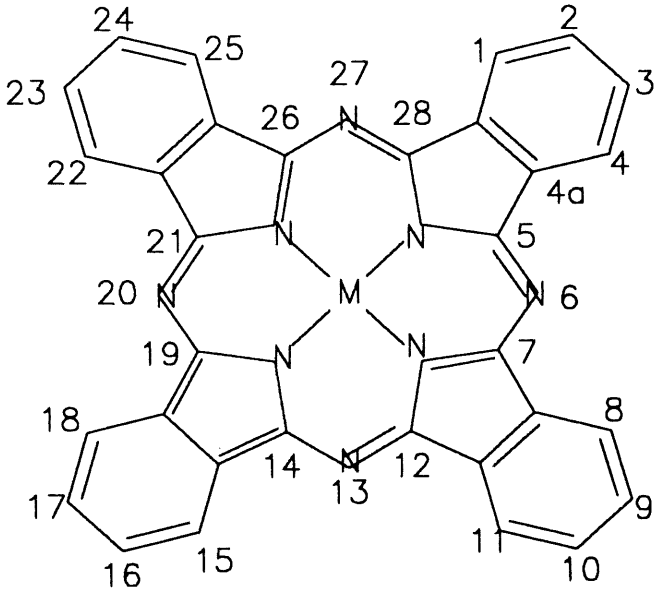

Figure 1.2.2.2. Molecular Structure of Phtalocyanines.

1.2.3. Lanthanide Porphyrin Phthalocyanine Dimeric/Heterodimeric Trimeric/Heterotrimeric Prototype Model Systems

In recent years, the research on optical nonlinearities of organic materials has attracted much attention both in the fundamental aspects to clarify their origins and mechanisms, and in their applications to develop optical devices being capable of processing optical information [67 - 71], etc., using the different frequency-mixing schemes offered by various orders of nonlinearity. Organic materials offer a number of advantages over mineral compounds. First, they are of superior flexibility in processing and manipulation, which enables us to improve particular optical characteristics by engineering the molecular properties. Moreover, they have large nonlinear optical susceptibility, ultrafast response, thermal and chemical stability. In order to increase the magnitude of the third-order susceptibility $\chi^{(3)}$, several methods have been proposed: multilock conjugated polymerization based on organic superlattices, donor-acceptor substitution on π-conjugated linear chains and use of π-conjugated molecules having symmetric structure [72 - 79]. In particular, conjugated π -electron systems have been known to have large optical nonlinearities and ultrafast optical responses [80 - 86]. Their nonlinear optical properties can be studied using various techniques such as, second harmonic generation (SHG), third harmonic generation (THG), four-wave mixing (FWM) and transient absorption, etc. [86 - 100].

Many organic materials containing delocalized π-electrons have been observed to have large optical nonlinearities and ultrafast responses [101, 102]. Most other third-order nonlinear optical compounds feature π-electron conjugation along a backbone and are pseudo-one dimensional systems. Those materials show limitations in their optical nonlinearities. This had led to considerable interest in the two-dimensional π-conjugated porphyrin [103] and phthalocyanine [104] systems, especially the complexes with a wide variety of metals. Among these systems, stacked and highly conjugated ones, such as lanthanide bis-/tris-porphyrins and bis-/tris-phthalocyanines, are interesting in many respects. These share the common properties for most porphyrins and phthalocyanines, i.e., chemical and thermal stability, versatile and flexible to make modification in properties by changing the central metal ion or the side groups at the edge of the macrocycle. They are of technological importance for the

manufacture of pigments, exhibiting unique characteristics such as catalyst, electrocatalysis, xerography and medical properties [105]. The delocalized π-electron in these systems can serve as source of charge carriers and is the origin of photoelectric properties directly related to primitive charge separation processes in photosynthesis and optical nonlinearities. In this aspect, they provide a series of model systems to study photoinduced electron transfer reactions occurring on ultrafast time scales in photosynthetic reaction centers both in theory and in experiment [86 - 91, 106 - 117]. Their sharp absorption bands in the visible and in the near infrared can be used for resonance enhancement of third-order susceptibility $\chi^{(3)}$. This makes them promising materials for third-order optical nonlinearities. The compounds are receiving increased attention. However, very few studies have been done on electrostatic mixed dimers obtained by covalently bonding porphyrin and phthalocyanine moieties bearing oppositely charged substituents [118 - 121].

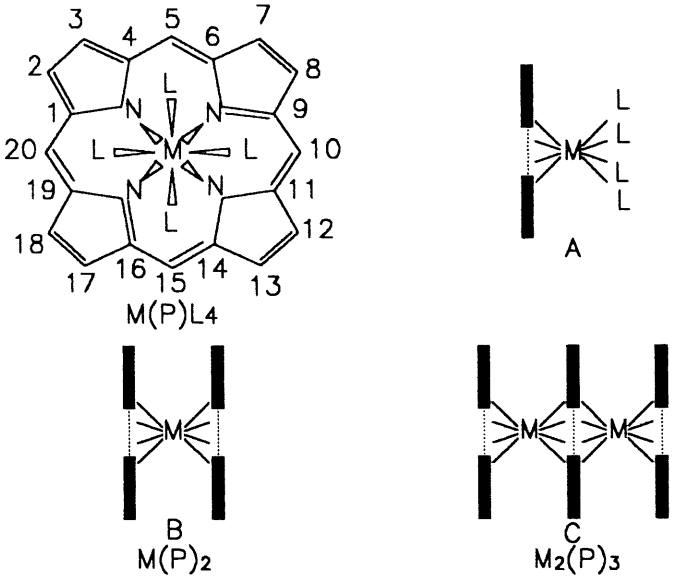

Figure 1.2.3.1. Constitution of Octacoordinated Metal Monotetrapyrroles M(P)L_4 and Configurations with A: Monotetrapyrro B: Bistetrapyrroles $M(P)_2$ and C: Tristetrapyrroles $M_2(P)_3$, M = Lanthanide Metal Ion

We chose the lanthanide porphyrin dimer/heterodimer and trimer/heterotrimer as prototype model systems in which to study dynamic processes such as electron transfer, energy transfer, related nonlinear optical properties, and their relationship to the molecular structure.

Table 1.2.3.1. Specifications of Porphyrins

No.	P in M(P)L_4	Name of the P in M (P) L_4	R in position 2~20 in Fig. 1.2.3.1.
0	P	a general porphyrin, phthalocyanine	
1	Pc	phthalocyanine	N in 5, 10, 15, 20; C_6H_6 in 2/3, 7/8, 12/13, 17/18
2	TTP	5,10,15,20-tetra(*p*-tolyl)porphyrin	p CH_3 C_6H_4 in 5, 10, 15, 20
3	OEP	2,3,7,8,12,13,17,18-octaethylporphyrin	C_2H_5 in 2, 3, 7, 8, 12, 13, 17, 18
4	TPP	5,10,15,20-tetraphenylporphyrin	C_6H_5 in 5, 10, 15, 20
5	TClP	5,10,15,20-tetra(*p*-chlorophenyl)porphyrin	pClC_6H_4 in 5, 10, 15, 20
6	HBP	1,2,3,4,8,9,10,11,15,16,17,18,22,23, 24,25,-hexadecahyrotetrabenzo [*b,g,l,q*]porphyrin	(CH_2)$_4$ in 2/3, 7/8, 12/13, 17/18
7	OMP	2,3,7,8,12,13,17,18-octamethylporphyrin	CH_3 in 2, 3, 7, 8, 12, 13, 17, 18
8	TAP	5,10,15,20-tetra(p-anisyl)porphyrin	p $CH_3OC_6H_4$ in 5, 10, 15, 20

A complete understanding of the photophysical behaviour of porphyrins and related chromophores within the Van der Waals distance will provide us with a deep insight into how the electron donor in photosynthetic reaction centers influences the initial stages of charge separation processes [122, 123]. Moreover this knowledge will enable us to modify molecular systems in a controllable manner so as to maximize their nonlinearities. This is needed by photonics and various kinds of other applications.

Lanthanide porphyrin dimers/heterodimers and trimers/heterotrimers represent a series of ideal molecular systems which can be used to study the electronic structure and dynamics of strongly interacting porphyrins. These metalloporphyrin complexes,

consisting of a lanthanide ion sandwiched between two porphyrin macrocycles, are distinguished by their rigid structure, ~ 3 Å inter-ring separation, unusual electronic absorption spectrum, and a prominent near-infrared band for the oxidized species [124 - 131].

The detailed synthetic processes for some of the lanthanide porphyrin monomers, dimers, heterodimers, trimers and heterotrimers, are explained in ref. [129]. The molecular structures, the specifications of porphyrins, and related abbreviations of these mono-, bis- and tris-porphyrinate and their unsymmetric counterparts, are shown in Table 1.2.3.1. and Fig. 1.2.3.1. .

The electronic structure of porphyrins and phthalocyanines is basically an aromatic one with a system of eighteen conjugated π electrons. Therefore, the macrocycles of pyrroles are very often planar, though there might be some distortion if the size of the central metal ion can not be adapted to the central cavity determined by the four nitrogen atoms [132, 133].

When porphyrins and phthalocyanines are stacked and bridged by a covalent link via lanthanide ions, a face to face geometry is favoured in these dimeric /heterodimeric trimeric/heterotrimeric systems due to the coulombic attraction and the strong π-π interaction of the two highly conjugated tetrapyrrole macrocycles. As a consequence, dramatic changes occur in the spectral and photophysical behaviour of the dimers/heterodimers trimers/heterotrimers as opposed to the mixtures of the corresponding unsubstituted monomers. In these former systems, there is a spatial face-to-face arrangement of the monomers which gives rise to the following interesting features:

1. The extraction of an electron from the porphyrin π orbit is easier than from the corresponding monomer, which means the devices with these systems will need less driving power than those with corresponding monomers.
2. The fluorescence of bis-tetrapyrroles is quenched contrary to the monotetrapyrroles and thus there are smaller light losses.
3. The oxidized bis-tetrapyrroles show a strong near-infrared absorption band at about 1300 nm.

4. These double-deckers show analogies to the electron donor dimer in photo synthetic systems in green plants and photosynthetic bacteria, in regard to structure and electron configuration [126, 129, 134 - 136]. Thus, they provide a series of structural and spectroscopic model systems [126, 128, 134, 136, 137] for the original charge separation processes in the reaction center of photosynthetic systems [138 - 140].

5. When one of the rings is oxidized into a radical [141], these sandwich systems may serve as molecular metals [142] or intrinsic semiconductors [143].

6. Porphyrins and phthalocyanines are two classes of very chemically versatile compounds. By varying the central metal ion or peripheral substituents and incorporating two different kinds of tetrapyrrole ligands, one can obtain a great deal of different molecular systems having a wide range of different redox properties, photophysical characteristics, and optical nonlinearities. This feature gives us more freedom to select a suitable model system that will provide more detailed information about how electrons and energy are transferred, about how the processes are related to molecular and electronic structures. This will ultimately enable us to control/govern and alter/modify the properties of a molecular system precisely and arbitrarily.

7. The association of different tetrapyrrole macrocycles results in a wide range of donor-acceptor complex systems. In these cofacial dimers or heterodimers, charge transfer can efficiently compete with the excitation transfer process [144]. Accordingly, by a discreet and prudent choice of the donor and acceptor, one can direct the transfer process to be of energy or electron type.

8. They can serve as organic semiconductors. For example, one of these complexes, lanthanide bis-phthalocyanines $LnPc_2$, shows electrochromatic properties: in solution or deposited as thin films, they exhibit different colours according to the applied potential [145 - 148]. This makes them promising materials for visual displays.

9. Pc_2Lu is reported as the first molecular semiconductor [149 - 151] and the first stable free radical phthalocyanine [152].

When two phthalocyanine rings are linked by a single metal ion with valence of +3 [153], a bis-phthalocyanine is formed, as in the case of neodymium here, $NdPc_2$, and the three electrons are shared between the two phthalocyanine rings to make charge neutrality. These metallobis-phthalocyanines belong to a class of mixed-valance compounds with low-lying intervalence charge transfer transition [154 - 156]. D. Markovitsi and T. H. Tran-Thi et al. [157] interpreted the structure of the compounds as $Pc^{-2}Nd^{+3}Pc^{-1}$, such that the charge is localized on one ring and the intervalence transition corresponds to electron hopping from one ring to the other. Later analysis showed that the unpaired electron is substantially delocalized over the two phthalocyanine rings. This is supported by a theoretical calculation [158] on a completely delocalized structure model of bis-phthalocyanine $(Pc_2)^{-3}$. Therefore, these molecules may be considered as a three-dimensional delocalized π-electron system involving an intervalence charge transfer transition. The electron structure of the trimer is $Pc^{2-}Nd^{3+}TPP^{2-}Nd^{3+}Pc^{2-}$, where the six electrons are shared between the phthalocyanine rings at the two sides and porphyrin at the center.

All in all, these molecular cofacial complex systems are highly desirable for both fundamental and applied studies of various kinds of electrical, optical, and optoelectrical materials.

From the device point of view, the most important kind of nonlinear optical material is solid. There are two sorts of techniques available to make highly ordered solid molecular assemblies: the Langmuir-Blodgett technique and the sublimation technique, which were both used in our research work. Theoretically speaking, the former should be better than the latter as far as the uniformity of the system is concerned. But in our experiment, we have observed that it was not always so. Sometimes the Langmuir-Blodgett samples gave us too intense diffused light to make it impossible for us to extract the signal from the noise background.

Previous NLO studies of third-order susceptibilities on bis-phthalocyanine [106 - 117] involve the effects of substitution of metal atoms, most of them in solutions, few on solid film, using third-harmonic generation and degenerate four-wave mixing in the near-infrared or in a region near strong absorbing Q band in the visible. Recently, efforts have been put on the effect of peripheral substituents [159], additional

conjugation such as naphthalocyanine [159, 160], central metal atom chelater [161] and spin coated multilayer film by DFWM on $\chi^{(3)}$ [162]. There have been a number of reports on the third-order nonlinear optical properties of porphyrin derivatives [163, 164] and phthalocyanines [165]. However, most of these reports involve third-harmonic generation and degenerate four-wave mixing measurements in solutions. There are few experiments using materials in solid state, which is viable for optical devices.

None of the above reported studies were performed by time-resolved non-degenerate four-wave mixing, even though TRNDFWM is a more useful and more sensitive technique to probe the dynamics of third-order nonlinearities. Coherent four-wave mixing excludes many different types of nonlinear optical phenomena depending on the phase-matching condition and on any encountered resonance . Its time-resolved form provides one of the most versatile means of studying the microscopic and macroscopic dynamics of a system. Depending on the time ordering, polarization, frequencies and pulse duration of the incident fields, one might detect the rotational /librational vibrational, or electronic structure/dynamics of a chromophore/bath system in the condensed phase. One of the most commonly seen forms of the time-resolved four-mixing uses two (or one) pump pulses to excite a system by the action of the two fields on a relevant state. Following the excitation, the third delayed probe pulse interrogates the evolved system and generates the fourth wave exiting as a function of the delay time. The forth diffracted signal contains abundant information about the system.

Because we are interested in investigating the dynamics of electron transfer processes in lanthanide dimer/heterodimer and trimer/heterotrimer systems, which are accompanied by many ultrafast relaxation processes in the picosecond or femtosecond range and many related nonlinear optical effects, the ultrafast time-resolved spectroscopy technique seems one of the best tools. Some of the important experimental phenomena we have encountered are *Electron transfer* and *photorefractivity.*

1.3. Two Important Experimental Phenomena Encountered

1.3.1. Electron Transfer

There is a lot of studies [166, 167] showing that the electronic contribution to optical nonlinearities dominates the frequency range from DC to optical ones. This also appears to be a property common to optical nonlinear organic solids. In lanthanide porphyrin phthalocyanine hetero-multimer systems, molecular relaxation processes always accompany electron transfer process, which is also an important sources of electronic contributions to optical nonlinearities.

Electron transfer (ET) is a term common to physics, chemistry and biochemistry, which describes electron migration between electron donors and electron acceptors. The electron transfer concept takes its origin in *redox* processes involving the transfer of electrons: the removal of one or several electrons from a species is called *oxidation*, whereas any gain of electrons is called *reduction*. The electron transfer process can be intermolecular or intramolecular. If the electron transfer is from one primary bond to another, one calls it *out-sphere electron transfer* or *non-bonded ET*. If it is within a single primary bond, one calls it *inner-sphere electron transfer* or *bonded ET* [168 - 170]. A generalized ET step between donor (D) and acceptor (A) can be expressed in the following schemes:

$$D + A \Leftrightarrow \underset{\text{precursor complex}}{(DA)} \rightarrow \left[DA \leftrightarrow D^{+\bullet}A^{-\bullet} \right]^{\neq} \rightarrow \underset{\text{successor complex}}{(D^{+\bullet}A^{-\bullet})} \Leftrightarrow D^{+\bullet} + A^{-\bullet}, \qquad (1.3.1.1.)$$

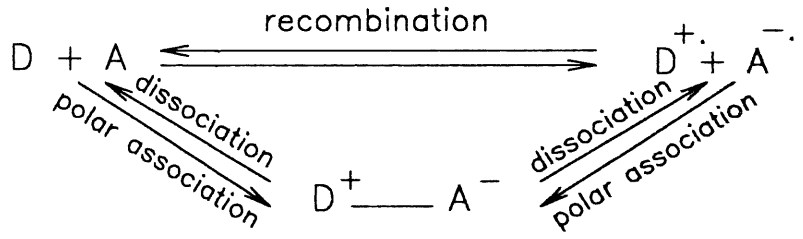

. (1.3.1..2.)

where the symbols "+•" and "-•" denote positive and negative radicals, and "≠" indicates that the process is an indifferent equilibrium one.

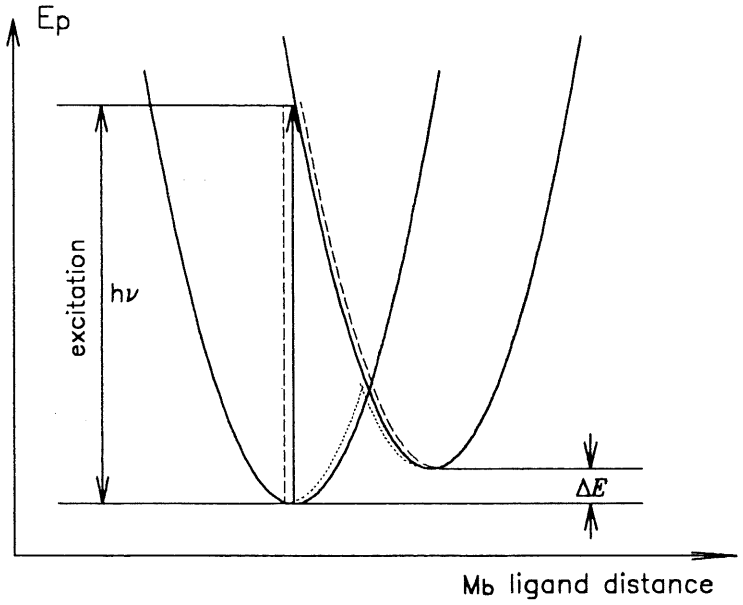

Figure 1.3.1.1. Potential Energy versus Metal–ligand Bond Length for Binuclear Complexes Containing a Reducing Metal Ion and an Oxidizing Metal Ion:

$$M_{\alpha}^{red} \text{ --- } L \text{ --- } M_{\beta}^{ox} \xrightarrow{h\nu} M_{\alpha}^{ox} \text{ --- } L \text{ --- } M_{\beta}^{red}$$

red: reductant

ox: oxidant

L: bridging ligand between Mα and Mβ

In our case, we are interested in both *intermolecular and intramolecular electron transfers*, especially in *photoinduced charge* processes.

Conventionally, one often assimilates photon induced electronic transitions and intramolecular transfers [171 - 173], as shown in Fig. 1.3.1.1. and Fig. 1.3.1.2. .

In Fig. 1.3.1.1., the dashed line shows the path taken by the electronic excitation of the molecule, representing an electron that is transferred from one part of the molecule to another. The dotted curve corresponds to a thermal intramolecular electron transfer.

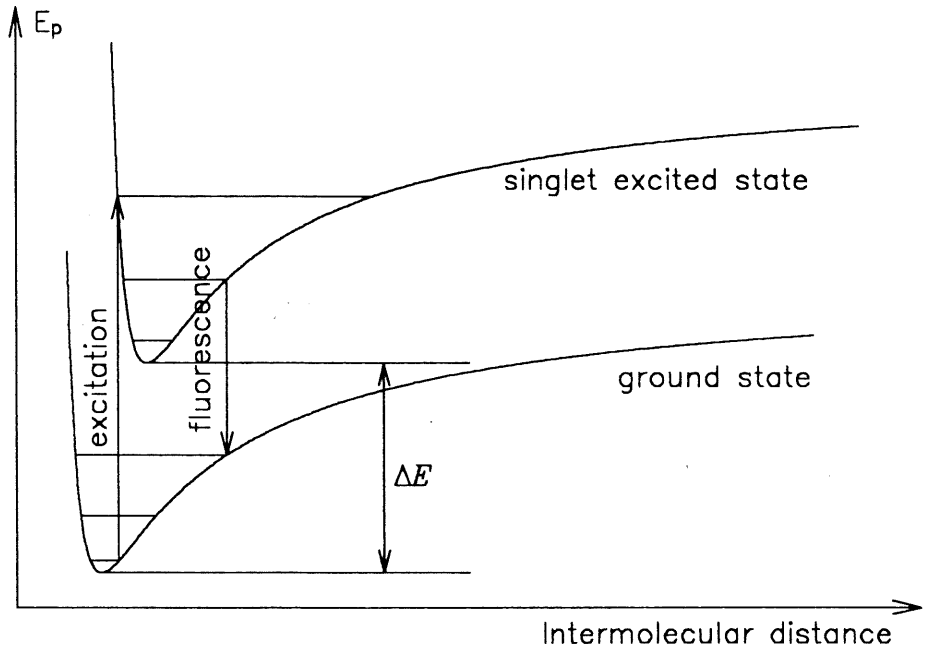

Figure 1.3.1.2. Electronic Transitions in a Diatomic Molecule.

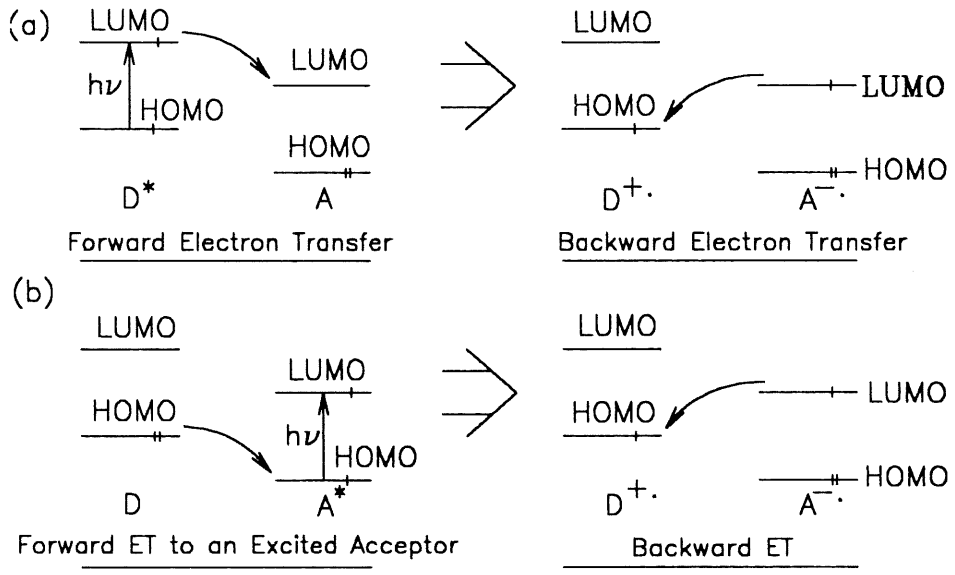

Figure 1.3.1.3. Simplified View of Forward and Backward Electron Transfers Involving (a): an Excited Donor, and (b): an Excited Acceptor.

The major difference between these two cases is the value of ΔE. The magnitude of the value ΔE in Fig. 1.3.1.2. precludes a thermal pathway except in those very special cases where the fundamental state is very close to the electronically excited one. One often refers to *ligand-to-metal and metal-to-ligand charge transfers* (LMCT, MLCT) [174, 175], in Fig. 1.3.1.1. and to *metal-to-ligand charge transfer* (MLCT) [176, 177], in Fig. 1.3.1.2. .

Generally, the term photoinduced intramolecular electron transfer is used to describe the transfer of an electron or a hole from an excited chromophore to the lowest unoccupied molecular orbit (LUMO) or the highest occupied molecular orbit (HOMO) of another chromophore in its fundamental state. If the donor and acceptor chromophores are part of a structure that constantly holds them in strong interaction, which may be a stable one (cyclophane) or a transitory one (electron donor-acceptor complex), one can view the excitation as first inducing an electron transition in one of the partners and then transferring the electron to the other partner. That is specifically what is in the lanthanide porphyrin dimeric or heterodimeric prototype model systems we are interested in, in photosynthetic systems in green plants and in photosynthetic bacteria.

A simplified electron transfer scheme is shown in Fig. 1.3.1.3. [178].

1.3.2. Photorefractivity

A photorefractive (PR) material is a medium in which an external light beam induces a change in the refractive index. It is perhaps the least well understood mechanism in nonlinear optics. It represents one of the areas of greatest current activity for physicists and chemists. There are very few materials known to be photorefractive [179] as listed in Table 1.3.2.1.1. . ***There are only two families of organic materials known***: doped organic crystals [180] and doped organic polymers [181 - 183]. ***There is no organic multimer (dimers etc.) photorefractive material ever having been found and reported.***

Photorefractivity was first discovered [184] as an optical damage effect in $LiNbO_3$. The effect is similar to optical phase conjugation (in fact, it is sometimes called self-pumped phase conjugation.). During the process, which occurs in crystalline materials, patterns are developed in the index of refraction by interference of the light as it is reflected internally throughout the crystal. A phenomenological description of the photorefractive effect can be found in reference [185] and a theoretical one in reference [179].

For the last thirty years since photorefractivity was discovered, it has been associated with changes of the refractive index caused by the following sequence of phenomena: the photo-excitation, the transport and trapping of electric charge carriers, the establishment of an internal electric field originating from the trapped charge distribution, and the existence of an electro-optic Pockels effect.

A general review of photorefractive materials was given in ref. [186]. The detailed theory, physical characterization and practice of the use of known photorefractivities can be seen in ref. [187], and most recently in ref. [179].

Three classes of inorganic PR materials dominate, as shown in Table 1.3.2.1.1.:

1. ferroelectric oxides, such as $LiNbO_3$, $BaTiO_3$;
2. sillenite family of oxides, exemplified by $Bi_{12}\ SiO_{20}$ (BSO), $Bi_{12}\ TiO_{20}$ (BTO) and $Bi_{12}\ GeO_{20}$ (BGO); and
3. compound semiconductor, for instance, GaAs, InP.

The semiconductors are sensitive only in the infrared, while the other materials work in the visible.

Functional organic photorefractive crystals are not actually known. The only example of an organic PR material (OPRM) previously known is pyridinium ylide [180] which experiences reversible photorefraction attributed to local polarization caused by trapping of photoinduced charges at structural defects in the crystal. The most recently discovered OPRMs are bisA-NPDA (bisphenol-*A*-diglycidylether 4-nitro-1,2-phenylenediamine) [181], PVK-TNF (poly *N*-vinylcarbazole 2,4,7,-trinitro-9-fluorennone) [182], and PMMA:DTNBI:C_{60} (poly-methylmethacrylate:1,2,-dimethyl-2,2-tetrame-thylene-5-nitrobenzimidazoline:fullerene) [183], listed in Table 1.3.2.1.1. .

Table 1.3.2.1.1. Photorefractive Materials

Materials	Birefringence	Optical Activity
Ferroelectrics [179]	Intrinsic	No
$BaTiO_3$		
$KNbO_3$		
$LiNbO_3$, $LiTaO_3$		
$Sr_{1-x}Ba_xNb_2O_6$ (SBN)		
KBN		
Sillenites [179]	Induced	Yes
BSO ($Bi_{12}SiO_{20}$)		
BGO ($Bi_{12}GeO_{20}$)		
BTO ($Bi_{12}TiO_{20}$)		
Semiconductors [179]	Induced	No
GaAs		
InP		
CdTe		
Organics	Induced	No
Pyridinium ylide [180]		
bisA-NPDA [181]		
PVK-TNF [182]		
PMMA:DTNBI:C_{60} [183]		

where, bisA-NPDA = bisphenol-*A*-diglycidylether 4-nitro-1,2-phenylenediamine;
PVK-TNF = poly *N*-vinylcarbazole 2,4,7,-trinitro-9-fluorennone;
PMMA:DTNBI:C_{60} = poly-methylmethacrylate:1,2,-dimethyl-2,2-tetramethylene-5-nitrobenzimidazoline:fullerene.

Though almost every PR experiment has been explained either by the band model or by the hopping model, a general comprehensive model of photorefractivity has not been published in any literature.

1.4. The Outline of Our Research Work

We have combined the ultrashort time-resolved spectroscopy method with the four-wave mixing process to study the dynamic behaviour of the lanthanide porphyrin dimeric/heterodimeric trimeric/heterotrimeric prototype model systems.

From the nonlinear optics point of view, our research is a fundamental experimental one. We are specifically interested in the four-wave mixing process in order to get important parameters and data, such as relaxation times for different processes and third order nonlinear susceptibility $\chi^{(3)}$, so as to characterize the nonlinearity of the model systems.

From the nonlinear optical material point of view, we hope that the results of our nonlinear optical research on the organic molecular model systems will be used to find suitable organic molecular materials with which to build various kinds of nonlinear optical devices for photonics.

Our choice of the materials is based on the facts that these dimer/heterodimer and trimer/heterotrimer systems can be:

1. materials requiring low driving power,
2. materials with low power consumption,
3. potentially useful materials in the near infrared,
4. ideal structural and spectroscopic prototype systems of photosynthesis,
5. potentially useful materials of molecular metals or intrinsic semiconductors,
6. potentially useful materials for photonics,
7. suitable model systems for electron or energy transfer processes, and
8. potentially useful materials for visual display.

Our research work is just a first step to the systematic investigation of the nonlinear optical properties of these multimer system.

Chapter 2

Theoretical and Experimental Background

2.1. Basis for Macroscopic Electromagnetic Field Theory of Nonlinear Optics

Generally speaking, all media are nonlinear. Each nonlinear optical process in the media consists of two parts: first, the intense light (power density > 2.5 kW/cm^2 , or field strength > 1 kV/cm) induces a nonlinear response in the medium, which is described by the constitutive equations (2.1.1.), and then the reacting medium nonlinearly modifies the optical fields, causing a different output with a change in frequency, phase, polarization or path, which is described by Maxwell's equations (2.1.2.) [188 -190]:

$$\begin{aligned} &\mathbf{D} = \varepsilon_0 \mathbf{E} + \mathbf{P}, \quad \mathbf{P} = \mathbf{P}(\mathbf{E}), \\ &\mathbf{H} = \frac{\mathbf{B}}{\mu_0} - \mathbf{M}, \quad \mathbf{M} = \mathbf{M}(\mathbf{B}); \end{aligned} \tag{2.1.1.}$$

$$\begin{aligned} &\nabla \times \mathbf{E} = -\frac{\partial \mathbf{B}}{\partial t}, \\ &\nabla \times \mathbf{B} = \mu_0 \left(\frac{\partial \mathbf{D}}{\partial t} + \nabla \times \mathbf{M} + \mathrm{J}_f\right), \\ &\nabla \cdot \mathbf{D} = \rho_f, \\ &\nabla \cdot \mathbf{B} = 0. \end{aligned} \tag{2.1.2.}$$

Equation (2.1.1.) and Equation (2.1.2.) constitute the foundations of macroscopic electromagnetic field theory of nonlinear optics.

The optical response of a medium can be described by the interaction of the electric dipole with the light field. At the microscopic level, this interaction results in *the induced dipole moment* **p** and *the Stark energy* ε_{Stark} given as

$$\mathbf{p} = \mathbf{p}_0 + \alpha \cdot \mathbf{E} + \beta : \mathbf{EE} + \gamma : \mathbf{EEE} + \cdots\cdots , \qquad (2.1.3.)$$

$$\varepsilon_{Stark} = -\mathbf{p}_0 \cdot \mathrm{E} - \frac{1}{2}\mathbf{E} \cdot \alpha \cdot \mathbf{E} - \frac{1}{3}\mathbf{E} \cdot \beta : \mathbf{EE} - \frac{1}{4}\mathbf{E} \cdot \gamma : \mathbf{EEE} - \cdots\cdots , \qquad (2.1.4.)$$

where

$$\mathbf{p}_0 = \mathbf{p}|_{\mathbf{E}=0} = -\left.\frac{\partial \varepsilon_{Stark}}{\partial \mathbf{E}}\right|_{\mathbf{E}=0} \qquad (2.1.5.)$$

is the *static dipole* (*permanent dipole*) *moment* in the absence of an electric field, and

$$\alpha = \left.\frac{\partial \mathbf{p}}{\partial \mathbf{E}}\right|_{\mathbf{E}=0} = -\left.\frac{\partial^2 \varepsilon_{Stark}}{\partial \mathbf{E}\, \partial \mathbf{E}}\right|_{\mathbf{E}=0} \qquad (2.1.6.)$$

is *the linear polarizability*, a second order tensor.

The terms

$$\beta = \left.\frac{\partial^2 \mathbf{p}}{\partial \mathbf{E}\, \partial \mathbf{E}}\right|_{\mathbf{E}=0} = -\left.\frac{\partial^3 \varepsilon_{Stark}}{\partial \mathbf{E}\, \partial \mathbf{E}\, \partial \mathbf{E}}\right|_{\mathbf{E}=0} \qquad (2.1.7.)$$

and

$$\gamma = \left.\frac{\partial^3 \mathbf{p}}{\partial \mathbf{E}\, \partial \mathbf{E}\, \partial \mathbf{E}}\right|_{\mathbf{E}=0} = -\left.\frac{\partial^4 \varepsilon_{Stark}}{\partial \mathbf{E}\, \partial \mathbf{E}\, \partial \mathbf{E}\, \partial \mathbf{E}}\right|_{\mathbf{E}=0} \qquad (2.1.8.)$$

are called *first and second hyperpolarizabilities.* They are third and fourth order tensors respectively, describing nonlinear optical interactions in the media.

At the macroscopic level, *the bulk polarization* and *the Stark energy*, similar to (2.1.3.) and (2.1.4.), can be expressed as:

$$\mathbf{P} = \mathbf{P}_0 + \chi^{(1)} \cdot \mathbf{E} + \chi^{(2)} : \mathbf{EE} + \chi^{(3)} : \mathbf{EEE} + \cdots\cdots \qquad (2.1.9.)$$

and

$$\mathcal{E}_{\text{Stark}} = -\mathbf{P}_0 \cdot \mathrm{E} - \frac{1}{2}\mathbf{E}\cdot\chi^{(1)}\cdot\mathbf{E} - \frac{1}{3}\mathbf{E}\cdot\chi^{(2)}:\mathbf{EE} - \frac{1}{4}\mathbf{E}\cdot\chi^{(3)}:\mathbf{EEE} - \cdots\cdots \quad (2.1.10.)$$

where

$$\mathbf{P}_0 = \mathbf{P}\big|_{\mathbf{E}=0} = -\left.\frac{\partial\,\mathcal{E}_{\text{Stark}}}{\partial\,\mathbf{E}}\right|_{\mathbf{E}=0}, \quad (2.1.11.)$$

$$\chi^{(1)} = \left.\frac{\partial\,\mathbf{P}}{\partial\,\mathbf{E}}\right|_{\mathbf{E}=0} = -\left.\frac{\partial^2\,\mathcal{E}_{\text{Stark}}}{\partial\mathbf{E}\,\partial\mathbf{E}}\right|_{\mathbf{E}=0}, \quad (2.1.12.)$$

$$\chi^{(2)} = \left.\frac{\partial^2\,\mathbf{P}}{\partial\mathbf{E}\,\partial\mathbf{E}}\right|_{\mathbf{E}=0} = -\left.\frac{\partial^3\,\mathcal{E}_{\text{Stark}}}{\partial\mathbf{E}\,\partial\mathbf{E}\,\partial\mathbf{E}}\right|_{\mathbf{E}=0}, \quad (2.1.13.)$$

and

$$\chi^{(3)} = \left.\frac{\partial^3\,\mathbf{P}}{\partial\mathbf{E}\,\partial\mathbf{E}\,\partial\mathbf{E}}\right|_{\mathbf{E}=0} = -\left.\frac{\partial^4\,\mathcal{E}_{\text{Stark}}}{\partial\mathbf{E}\,\partial\mathbf{E}\,\partial\mathbf{E}\,\partial\mathbf{E}}\right|_{\mathbf{E}=0} \quad (2.1.14.)$$

are the macroscopic analogues of $\mathbf{p}_0$, α, β, γ. $\mathbf{P}_0$ is *the built-in static dipole* of the sample. $\chi^{(1)}$, a second order tensor, is *the linear susceptibility* which describes the linear optical response. Third and fourth order tensors $\chi^{(2)}$, $\chi^{(3)}$, are *the second* and *the third order nonlinear optical susceptibilities*, which are referred to as *the first and the second nonlinear susceptibilities*.

The expansions (2.1.3.), (2.1.4.), (2.1.9.) and (2.1.10.) are valid in the dipolar approximation where the wavelength of the optical field is large compared to the dimensions of the polarizable unit. The series expansions can break down for increased field strengths. One proves that the description is no longer valid when the electric field strength approaches the strength of atomic fields that bind electric charges ($\mathrm{E} \sim \mathrm{E_a} = e^2/(4\pi\varepsilon_0 a) \approx 10^8 \sim 10^9$ V/cm) [188]. Fortunately, most nonlinear effects are observed at fields of $10^3 \sim 10^4$ V/cm (laser intensities in kW/cm^2 ~ MW/cm^2 range) when the series expansion expressions (2.1.3.), (2.1.4.), (2.1.9.)

and (2.1.10.) are generally still applicable. These expressions are not appropriate at or near a resonance frequency, which should be treated with care.

2.2. Macroscopic Expressions for Optical Nonlinearities

For the macroscopic nonlinearities, one starts from Maxwell's equations (2.1.2.) and constitutive equations (2.1.1.).

In the general case, the induced polarization $\mathbf{P} = \mathbf{P}(\mathbf{E})$, can be expressed as [186 -188]:

$$
\begin{aligned}
&\mathbf{P}(\mathbf{r},t) = \\
&= \varepsilon_0 \sum_{j=1} \int_{-\infty}^{+\infty} \vec{\chi}^{(j)}(\mathbf{r}-\mathbf{r}_1, t-t_1; \cdots\cdots; \mathbf{r}-\mathbf{r}_j, t-t_j) : \prod_{m=1}^{j} \mathbf{E}(\mathbf{r}_m, t_m)\, d\mathbf{r}_m\, dt_m = \\
&= \varepsilon_0 \int_{-\infty}^{+\infty} \vec{\chi}^{(1)}(\mathbf{r}-\mathbf{r}_1, t-t_1) \cdot \mathbf{E}(\mathbf{r}_1, t_1)\, d\mathbf{r}_1\, dt_1 + \\
&+ \varepsilon_0 \int_{-\infty}^{+\infty} \vec{\chi}^{(2)}(\mathbf{r}-\mathbf{r}_1, t-t_1; \mathbf{r}-\mathbf{r}_2, t-t_2) : \mathbf{E}(\mathbf{r}_1, t_1)\mathbf{E}(\mathbf{r}_2, t_2)\, d\mathbf{r}_1\, dt_1 d\mathbf{r}_2\, dt_2 + \\
&+ \varepsilon_0 \int_{-\infty}^{+\infty} \vec{\chi}^{(3)}(\mathbf{r}-\mathbf{r}_1, t-t_1; \mathbf{r}-\mathbf{r}_2, t-t_2; \mathbf{r}-\mathbf{r}_3, t-t_3) : \mathbf{E}(\mathbf{r}_1, t_1) \times \\
&\times \mathbf{E}(\mathbf{r}_2, t_2)\mathbf{E}(\mathbf{r}_3, t_3)\, d\mathbf{r}_1\, dt_1 d\mathbf{r}_2\, dt_2 d\mathbf{r}_3\, dt_3 + \cdots\cdots = \\
&= \mathbf{P}^{(1)}(\mathbf{r},t) + \mathbf{P}^{(2)}(\mathbf{r},t) + \mathbf{P}^{(3)}(\mathbf{r},t) + \cdots\cdots .
\end{aligned}
\qquad (2.2.1.)
$$

Let us define the following Fourier transforms:

$$
\begin{aligned}
\mathbf{P}(\mathbf{k},\omega) &= \mathcal{F}(\mathbf{P}(\mathbf{r},t)) = \int e^{-i(\mathbf{k}\cdot\mathbf{r}-\omega t)} \mathbf{P}(\mathbf{r},t)\, d\mathbf{r}\, dt = \\
&= \sum_{j=1} \int e^{-i(\mathbf{k}\cdot\mathbf{r}-\omega t)} \mathbf{P}^{(j)}(\mathbf{r},t)\, d\mathbf{r}\, dt = \sum_{j=1} \mathbf{P}^{(j)}(\mathbf{k},\omega),
\end{aligned}
\qquad (2.2.2.)
$$

$$\chi^{(j)}(\mathbf{k},\omega) = \mathcal{F}(\chi^{(j)}(\mathbf{r},t)) = \int_{-\infty}^{+\infty} e^{-i(\mathbf{k}\cdot\mathbf{r}-\omega t)}\,\chi^{(j)}(\mathbf{r},t)\,d\mathbf{r}\,dt =$$
$$= \chi^{(j)}(\mathbf{k}_1,\omega_1;\cdots\cdots;\mathbf{k}_j,\omega_j) = \qquad (2.2.3.)$$
$$= \prod_{m=1}^{j}\int_{-\infty}^{+\infty} e^{-i(\mathbf{k}_m\cdot\xi_m-\omega_m\tau_m)}d\xi_m\,d\tau_m\,\chi^{(j)}(\xi_1,\tau_1;\cdots\cdots;\xi_j,\tau_j).$$

If $\mathbf{E}(\mathbf{r}, t)$ can be expressed as a superposition of a finite number of monochromatic plane waves,

$$\mathrm{E}(\mathbf{r},t) = \sum_{\alpha} E(\mathrm{k}_\alpha,\omega_\alpha)\exp[i(\mathrm{k}_\alpha\cdot\mathrm{r}-\omega_\alpha t)], \qquad (2.2.4.)$$

then the different powers of electric field $\mathbf{E}(\mathbf{r},t)$ appearing in (2.2.1) can also be Fourier transformed:

$$\mathcal{F}(\mathbf{E}(\mathbf{r},t)) = \int \mathbf{E}(\mathbf{r},t)\exp[-i(\mathbf{k}\cdot\mathbf{r}-\omega t)]\,d\mathbf{r}\,dt =$$
$$= \int\sum_{\alpha 1} \boldsymbol{E}(\mathbf{k}_{\alpha 1},\omega_{\alpha 1})\exp[-i((\mathbf{k}-\mathbf{k}_{\alpha 1})\cdot\mathbf{r}-(\omega-\omega_{\alpha 1})t)]\,d\mathbf{r}\,dt = \qquad (2.2.5.)$$
$$= \sum_{\alpha 1} \boldsymbol{E}(\mathbf{k}_{\alpha 1},\omega_{\alpha 1})\,\delta(\mathbf{k}-\mathbf{k}_{\alpha 1})\,\delta(\omega-\omega_{\alpha 1}),$$

$$\mathcal{F}(\mathbf{E}(\mathbf{r},t)\,\mathbf{E}(\mathbf{r},t)) = \int \mathbf{E}(\mathbf{r},t)\,\mathbf{E}(\mathbf{r},t)\exp[-i(\mathbf{k}\cdot\mathbf{r}-\omega t)]\,d\mathbf{r}\,dt =$$
$$= \int\sum_{\alpha 1,\alpha 2} \boldsymbol{E}(\mathbf{k}_{\alpha 1},\omega_{\alpha 1})\,\boldsymbol{E}(\mathbf{k}_{\alpha 2},\omega_{\alpha 2})\times$$
$$\times\exp[-i((\mathbf{k}-\mathbf{k}_{\alpha 1}-\mathbf{k}_{\alpha 2})\cdot\mathbf{r}-(\omega-\omega_{\alpha 1}-\omega_{\alpha 2})t)]\,d\mathbf{r}\,dt = \qquad (2.2.6.)$$
$$= \sum_{\alpha 1,\alpha 2} \boldsymbol{E}(\mathbf{k}_{\alpha 1},\omega_{\alpha 1})\,\boldsymbol{E}(\mathbf{k}_{\alpha 2},\omega_{\alpha 2})\,\delta(\mathbf{k}-\mathbf{k}_{\alpha 1}-\mathbf{k}_{\alpha 2})\,\delta(\omega-\omega_{\alpha 1}-\omega_{\alpha 2}),$$

$$\mathcal{J}(\mathbf{E}(\mathbf{r},t)\,\mathbf{E}(\mathbf{r},t)\,\mathbf{E}(\mathbf{r},t)) = \int \mathbf{E}(\mathbf{r},t)\,\mathbf{E}(\mathbf{r},t)\,\mathbf{E}(\mathbf{r},t)\exp[-i(\mathbf{k}\cdot\mathbf{r}-\omega t)]\,d\mathbf{r}\,dt =$$
$$= \int \sum_{\alpha 1,\alpha 2,\alpha 3} E(\mathbf{k}_{\alpha 1},\omega_{\alpha 1})\,E(\mathbf{k}_{\alpha 2},\omega_{\alpha 2})\,E(\mathbf{k}_{\alpha 2},\omega_{\alpha 2}) \times$$
$$\times \exp[-i((\mathbf{k}-\mathbf{k}_{\alpha 1}-\mathbf{k}_{\alpha 2}-\mathbf{k}_{\alpha 3})\cdot\mathbf{r}-(\omega-\omega_{\alpha 1}-\omega_{\alpha 2}-\omega_{\alpha 3})t)]\,d\mathbf{r}\,dt =$$
$$= \sum_{\alpha 1,\alpha 2,\alpha 3} E(\mathbf{k}_{\alpha 1},\omega_{\alpha 1})\,E(\mathbf{k}_{\alpha 2},\omega_{\alpha 2})\,E(\mathbf{k}_{\alpha 2},\omega_{\alpha 2}) \times$$
$$\times \delta(\mathbf{k}-\mathbf{k}_{\alpha 1}-\mathbf{k}_{\alpha 2})\,\delta(\omega-\omega_{\alpha 1}-\omega_{\alpha 2}-\omega_{\alpha 3}),\cdots\cdots. \qquad (2.2.7.)$$

Because the j-order polarization $\mathbf{P}^{(j)}$ in t-**r** space is just a t-**r** convolution of the corresponding fields and susceptibilities shown in (2.2.1.), the convolution of the Fourier transform in ω-**k** space of the j-order polarization $\mathbf{P}^{(j)}$ should be the product of the Fourier transforms of the corresponding fields and susceptibilities, i.e.,

$$\begin{aligned}
&\mathbf{P}^{(1)}(k,\omega) = \mathcal{J}(\mathbf{P}^{(1)}(\mathbf{r},t)) = \mathcal{J}(\chi^{(1)}(\mathbf{r},t)\otimes\mathbf{E}(\mathbf{r},t)) = \\
&= \mathcal{J}(\chi^{(1)}(\mathbf{r},t))\,\mathcal{J}(\mathbf{E}(\mathbf{r},t)) = \\
&= \chi^{(1)}(k,\omega)\sum_{\alpha 1} E(\mathbf{k}_{\alpha 1},\omega_{\alpha 1})\,\delta(\mathbf{k}-\mathbf{k}_{\alpha 1})\,\delta(\omega-\omega_{\alpha 1}) = \\
&= \sum_{\alpha 1}\chi^{(1)}(k,\omega)E(\mathbf{k}_{\alpha 1},\omega_{\alpha 1})\,\delta(\mathbf{k}-\mathbf{k}_{\alpha 1})\,\delta(\omega-\omega_{\alpha 1}) = \\
&= \chi^{(1)}(k=\mathbf{k}_{\alpha 1},\omega=\omega_{\alpha 1})E(\mathbf{k}_{\alpha 1},\omega_{\alpha 1}),
\end{aligned} \qquad (2.2.8.)$$

$$\begin{aligned}
&\mathbf{P}^{(2)}(k,\omega) = \mathcal{J}(\mathbf{P}^{(2)}(\mathbf{r},t)) = \mathcal{J}(\chi^{(2)}(\mathbf{r},t)\otimes\mathbf{E}(\mathbf{r},t)\mathbf{E}(\mathbf{r},t)) = \\
&= \mathcal{J}(\chi^{(2)}(\mathbf{r},t))\,\mathcal{J}(\mathbf{E}(\mathbf{r},t)\mathbf{E}(\mathbf{r},t)) = \\
&= \chi^{(2)}(k,\omega)\sum_{\alpha 1,\alpha 2} E(\mathbf{k}_{\alpha 1},\omega_{\alpha 1})\,E(\mathbf{k}_{\alpha 2},\omega_{\alpha 2}) \times \\
&\qquad \times \delta(\mathbf{k}-\mathbf{k}_{\alpha 1})\,\delta(\mathbf{k}-\mathbf{k}_{\alpha 2})\,\delta(\omega-\omega_{\alpha 1})\,\delta(\omega-\omega_{\alpha 2}) = \\
&= \sum_{\alpha 1,\alpha 2}\chi^{(2)}(k,\omega)E(\mathbf{k}_{\alpha 1},\omega_{\alpha 1})\,E(\mathbf{k}_{\alpha 2},\omega_{\alpha 2}) \times \\
&\qquad \times \delta(\mathbf{k}-\mathbf{k}_{\alpha 1})\,\delta(\mathbf{k}-\mathbf{k}_{\alpha 2})\,\delta(\omega-\omega_{\alpha 1})\,\delta(\omega-\omega_{\alpha 2}) = \\
&= \chi^{(2)}(k=\sum_{j=1}^{2}\mathbf{k}_{\alpha j},\omega=\sum_{j=1}^{2}\omega_{\alpha j})E(\mathbf{k}_{\alpha 1},\omega_{\alpha 1})\,E(\mathbf{k}_{\alpha 2},\omega_{\alpha 2}),
\end{aligned} \qquad (2.2.9.)$$

$$\mathbf{P}^{(3)}(\boldsymbol{k},\omega)=\mathcal{J}\left(\mathbf{P}^{(3)}(\mathbf{r},t)\right)=\mathcal{J}\left(\chi^{(3)}(\mathbf{r},t)\otimes(\mathbf{E}(\mathbf{r},t)\mathbf{E}(\mathbf{r},t)\mathbf{E}(\mathbf{r},t))\right)=$$
$$=\mathcal{J}\left(\chi^{(3)}(\mathbf{r},t)\right)\mathcal{J}(\mathbf{E}(\mathbf{r},t)\,\mathbf{E}(\mathbf{r},t)\,\mathbf{E}(\mathbf{r},t))=$$
$$=\chi^{(3)}(\boldsymbol{k},\omega)\sum_{\alpha1,\alpha2,\alpha3}E(\mathbf{k}_{\alpha1},\omega_{\alpha1})\,E(\mathbf{k}_{\alpha2},\omega_{\alpha2})\,E(\mathbf{k}_{\alpha3},\omega_{\alpha3})\times$$
$$\times\delta(\mathbf{k}-\mathbf{k}_{\alpha1}-\mathbf{k}_{\alpha2}-\mathbf{k}_{\alpha3})\,\delta(\omega-\omega_{\alpha1}-\omega_{\alpha2}-\omega_{\alpha3})=$$
$$=\sum_{\alpha1,\alpha2,\alpha3}\chi^{(3)}(\boldsymbol{k},\omega)E(\mathbf{k}_{\alpha1},\omega_{\alpha1})\,E(\mathbf{k}_{\alpha2},\omega_{\alpha2})\,E(\mathbf{k}_{\alpha3},\omega_{\alpha3})\times$$
$$\times\delta(\mathbf{k}-\mathbf{k}_{\alpha1}-\mathbf{k}_{\alpha2}-\mathbf{k}_{\alpha3})\,\delta(\omega-\omega_{\alpha1}-\omega_{\alpha2}-\omega_{\alpha3})=$$
$$=\chi^{(3)}(\boldsymbol{k}=\sum_{j=1}^{3}\mathbf{k}_{\alpha j},\omega=\sum_{j=1}^{3}\omega_{\alpha j})E(\mathbf{k}_{\alpha1},\omega_{\alpha1})E(\mathbf{k}_{\alpha2},\omega_{\alpha2})E(\mathbf{k}_{\alpha3},\omega_{\alpha3}),\cdots\cdots.$$

(2.2.10.)

Therefore, for the *j*-order nonlinear process, we have:

$$\mathbf{P}^{(j)}(\mathbf{k},\omega)=\varepsilon_0\,\chi^{(j)}(\mathbf{k}=\sum_{m=1}^{j}\mathbf{k}_m,\omega=\sum_{m=1}^{j}\omega_m):\prod_{m=1}^{j}E(\mathbf{k}_m,\omega_m) \qquad (2.2.11.)$$

where the $\chi^{(j)}$

$$\chi^{(j)}(\mathbf{k}=\sum_{m=1}^{j}\mathbf{k}_{m\ 1},\omega=\sum_{m=1}^{j}\omega_m)=$$
$$=\prod_{m=1}^{j}\int_{-\infty}^{+\infty}e^{-i(\mathbf{k}_m\cdot\xi_m-\omega_m\tau_m)}d\xi_m\,d\tau_m\,\chi^{(j)}\left(\xi_1,\tau_1;\cdots\cdots;\xi_j,\tau_j\right) \qquad (2.2.12.)$$

are *the linear* ($j=1$) and *nonlinear* ($j>1$) *susceptibilities*, which characterize the optical properties of the medium. Proper evaluation of $\chi^{(j)}$ can be done only in a full quantum-mechanical calculation which will give the microscopic expressions for the nonlinear polarisation $\mathbf{P}^{(j)}$ and nonlinear susceptibilities $\chi^{(j)}$. These give the steady-state nonlinear optical response of a medium and govern the nonlinear wave propagation in the medium.

From Maxwell's equations (2.1.2.) we have

$$\left[\nabla\times(\nabla\times)+\frac{1}{c^2}\frac{\partial^2}{\partial t^2}\right]\mathrm{E}(\mathrm{r},t)=-\frac{1}{\varepsilon_0 c^2}\frac{\partial^2}{\partial t^2}\mathrm{P}(\mathrm{r},t), \qquad (2.2.13.)$$

using *infinite plane wave* (IPW) approximation:

$$\begin{cases} \mathbf{E}(\mathbf{r},t) = \sum_l E(\mathbf{k}_l,\omega_l)\ \exp[i(\mathbf{k}_l\cdot\mathbf{r}-\omega_l t)], \\ \mathbf{P}(\mathbf{r},t) = \mathbf{P}^{(1)}(\mathbf{r},t)+\mathbf{P}^{NL}(\mathbf{r},t), \\ \mathbf{P}^{(1)}(\mathbf{r},t) = \sum_l \mathbf{P}_l^{(1)}(\mathbf{k}_l,\omega_l) = \varepsilon_0 \sum_l \overleftrightarrow{\chi}^{(1)}(\mathbf{r}_l,\omega_l):E(\mathbf{k}_l,\omega_l), \\ \mathbf{P}^{NL}(\mathbf{r},t) = \sum_{j\geq 2}\mathbf{P}^{(j)}(\mathbf{r},t) = \sum_l \mathbf{P}_l^{NL}(\mathbf{k}_l,\omega_l) = \sum_l P^{NL}(\mathbf{k}_l,\omega_l)\exp[i(\mathbf{k}_l\cdot\mathbf{r}-\omega_l t)], \end{cases}$$

(2.2.14.)

we get:

$$\left[\ \nabla\times(\ \nabla\times\ ) - \frac{\omega^2}{c^2}\vec{\varepsilon}\cdot\ \right]\mathbf{E}(\mathbf{k},\omega) = \frac{\omega^2}{\varepsilon_0 c^2}\mathbf{P}^{NL}(\ \mathbf{k},\omega\ ), \qquad (2.2.15.)$$

where

$$\vec{\varepsilon} = \varepsilon_0\left(\ 1+\vec{\chi}^{(1)}(\omega)\ \right),\ \ \vec{\varepsilon}_j = \varepsilon_0\left(\ 1+\vec{\chi}^{(1)}(\omega_j)\ \right), \qquad (2.2.16.)$$

$$\mathbf{E}(\mathbf{k},\omega) = \mathbf{E}_0\, e^{\,i(\mathbf{k}\cdot\mathbf{r}-\omega t)},\ \ \mathbf{E}(\mathbf{k}_j,\omega_j) = \mathbf{E}_{0j}\, e^{\,i(\mathbf{k}_j\cdot\mathbf{r}-\omega_j t)}, \qquad (2.2.17.)$$

$$\mathbf{P}^{NL}(\mathbf{k},\omega) = \mathbf{P}_0^{NL} e^{i(\mathbf{k}\cdot\mathbf{r}-\omega t)} = \sum_{j\geq 2}\mathbf{P}^{NL(j)}(\mathbf{k},\omega),$$

$$\mathbf{P}^{NL(j)}(\mathbf{k},\omega) = \varepsilon_0\,\vec{\chi}^{(j)}_{j\geq 2}\left(\mathbf{k}=\sum_{m=1}^{j}\mathbf{k}_m,\ \omega=\sum_{m=1}^{j}\omega_m\right):\prod_{m=1}^{j}\mathbf{E}(\mathbf{k}_m,\omega_m). \qquad (2.2.18.)$$

Equation (2.2.15) is known as ***the coupled wave equation*** which is ***the starting point for solving the problem of nonlinear wave propagation in a medium***.

2.3. *J*th-Order Nonlinear Optical Interaction Processes in a Medium

Theoretically speaking, the solution for a *j*th-order nonlinear optical interaction in a medium can be obtained using the coupled wave approach. In practice only second- and third-order nonlinear optical interactions are of interest. In the following discussion, we will omit the superscript "NL" in $\mathbf{P}^{NL(j)}$ directly use the notations $\mathbf{P}^{(2)}$, $\mathbf{P}^{(3)}$, etc. .

Let us now look at the details. Let us define the following abbreviations:

$$\begin{aligned}
&\hat{\mathbf{D}} = \hat{\mathbf{D}}(\omega) = [\,\nabla\times(\nabla\times) - \frac{\omega^2}{c^2}\vec{\varepsilon}(\omega)\cdot\,],\ \hat{\mathbf{D}}_j = \hat{\mathbf{D}}(\omega_j);\\
&\mathrm{d} = \mathrm{d}(\omega) = \frac{\omega^2}{\varepsilon_0\,\mathbf{c}^2}, \qquad \mathrm{d}_j = \mathrm{d}(\omega_j) = \frac{\omega_j^2}{\varepsilon_0\,\mathbf{c}^2};\\
&\mathbf{E} = \mathbf{E}(\boldsymbol{k},\omega), \qquad \mathbf{E}_j = \mathbf{E}(\boldsymbol{k}_j,\omega_j);\\
&\mathbf{P}^{(\mathrm{m})} = \mathbf{P}^{(\mathrm{m})}(\boldsymbol{k},\omega), \quad \mathbf{P}_j^{(\mathrm{m})} = \mathbf{P}^{(\mathrm{m})}(\boldsymbol{k}_j,\omega_j).
\end{aligned} \qquad (2.3.1.)$$

For a ***three wave interaction*** process, the coupled wave equation (2.2.15.) can be expressed, for a ***four-wave interaction*** process, as

$$\begin{aligned}
&\hat{\mathbf{D}}_1\,\mathbf{E}_1 = \mathrm{d}_1\mathbf{P}_1^{(3)} = \mathrm{d}_1\varepsilon_0\vec{\chi}^{(3)}\left(\mathbf{k}_1 = -\mathbf{k}_2 - \mathbf{k}_3 + \mathbf{k}_4,\ \omega_1 = -\omega_2 - \omega_3 + \omega_4\right):\mathbf{E}_2^*\mathbf{E}_3^*\mathbf{E}_4,\\
&\hat{\mathbf{D}}_2\,\mathbf{E}_2 = \mathrm{d}_2\mathbf{P}_2^{(3)} = \mathrm{d}_2\varepsilon_0\vec{\chi}^{(3)}\left(\mathbf{k}_2 = -\mathbf{k}_3 + \mathbf{k}_4 - \mathbf{k}_1,\ \omega_2 = -\omega_3 + \omega_4 - \omega_1\right):\mathbf{E}_3^*\mathbf{E}_4\mathbf{E}_1^*,\\
&\hat{\mathbf{D}}_3\,\mathbf{E}_3 = \mathrm{d}_3\mathbf{P}_3^{(3)} = \mathrm{d}_3\varepsilon_0\vec{\chi}^{(3)}\left(\mathbf{k}_3 = \mathbf{k}_4 - \mathbf{k}_1 - \mathbf{k}_2,\ \omega_3 = \omega_4 - \omega_2 - \omega_1\right):\mathbf{E}_4\,\mathbf{E}_1^*\mathbf{E}_2^*,\\
&\hat{\mathbf{D}}_4\,\mathbf{E}_4 = \mathrm{d}_4\mathbf{P}_4^{(3)} = \mathrm{d}_4\varepsilon_0\vec{\chi}^{(3)}\left(\mathbf{k}_4 = \mathbf{k}_1 + \mathbf{k}_2 + \mathbf{k}_3,\ \omega_4 = \omega_1 + \omega_2 + \omega_3\right):\mathbf{E}_1\,\mathbf{E}_2\,\mathbf{E}_3.
\end{aligned} \qquad (2.3.2.)$$

where the nonlinear susceptibilities $\mathbf{P}_j^{(2)}$, $j = 1, 2, 3$; $\mathbf{P}_j^{(3)}$, $j = 1, 2, 3, 4$; play the roles of the coupling agents which determine the energy transfer rate between the waves.

For the *j*th order nonlinear optical interaction process in a medium, the energy conservation condition

$$\omega_{j+1} = \sum_{i=1}^{j} \omega_i \qquad (2.3.3.)$$

is needed. Nevertheless, in a finite medium, the momentum conservation condition

$$\boldsymbol{k}_{j+1} = \sum_{i=1}^{j} \boldsymbol{k}_i \qquad (2.3.4.)$$

is not strictly required. But, it is preferred for maximization of the wave coupling. This leads to one of the most important considerations in many NLO processes known as ***the phase matching condition***

$$\Delta \boldsymbol{k} = \left| \boldsymbol{k}_{j+1} - \sum_{i=1}^{j} \boldsymbol{k}_i \right| = 0, \qquad (2.3.5.)$$

where $\Delta \boldsymbol{k}$ is often called ***the*** (***phase***) ***mismatch***.

Since the accurate solution of the coupled wave equations (2.2.15.) is too difficult to obtain, we have to resort to several simplified approximations among which are *the slowly varying amplitude approximation* (**SVA**), *the infinite plane wave approximation* (**IPW**), and *the constant pump intensity approximation* (**CPI**) [189 - 191] .

For a plane wave propagating along the ± z axis, we can write (see (2.2.14.))

$$\mathbf{E}(z,t) = \mathbf{E}_0(z)\ e^{i(\boldsymbol{k}\cdot\mathbf{z} \mp \omega t)}. \qquad (2.3.6.)$$

Using coupled wave equations (2.2.15.) and the SVA approximation, that is

$$\left|\frac{\partial^2 E(z)}{\partial z^2}\right| << \left| k \frac{\partial E(z)}{\partial z} \right|, \qquad (2.3.7.)$$

in the steady state case, we get

$$\frac{\partial}{\partial z} \mathbf{E}_0 (z) = \pm \frac{i \omega^2}{2 k \varepsilon_0 c^2} \mathbf{P}^{NL}(z)\, e^{-i(\boldsymbol{k}\cdot\mathbf{z} \mp \omega t)}, \qquad (2.3.8.)$$

for the slowly varying part. If the slowly varying part is time-dependent, we have

$$\left(\frac{\partial}{\partial z} \pm \frac{\partial}{v_g \partial t} \right) \mathbf{E}_0 (z,t) = \pm i \frac{\omega^2}{2k\varepsilon_0 c^2} \mathbf{P}^{NL} (z,t)\, e^{i(\boldsymbol{k}\cdot\mathbf{z} \mp \omega t)}. \qquad (2.3.9.)$$

$\mathbf{P}^{NL}(z,t)$ was defined in (2.2.14.).

We can see that equation (2.3.9) will reduce to equation (2.3.8.), if the variation of the amplitude **E** (z, t) is negligible compared with the time T that the light takes to travel through the interaction distance *l* (for thin sample, *l* equal to the thickness of the sample).

$$T = \frac{l}{v_g(\omega)} = \frac{l \cdot \sqrt{\varepsilon_r(\omega)}}{c} \qquad (2.3.10.)$$

where $v_g(\omega)$, $\varepsilon_r(\omega)$ and $\sqrt{\varepsilon_r(\omega)}$ are group velocity, relative dielectric constant and refractive index of the wave.

Equation (2.3.8.) and Equation (2.3.9) will be used in section 4.5. to get the expression to determine third-order nonlinear susceptibilities of the experimental samples.

2.4. Third-Order Nonlinear Optical Effects: Four-Wave Interactions

Wave interaction in a nonlinear medium causes wave mixing which, in the second-order case, leads to *sum-frequency generation* (SFG), *second harmonic generation* (SHG), and *difference-frequency generation* (DFG) [190 - 192]. The first and the second processes are used to extend the laser tuneable range to shorter wavelengths, the third one to longer wavelengths. The third-order process is generally called *four-wave interaction* (FWI)[193].

The physical picture of wave interactions is like this: the input laser beams at ω_1, ω_2, ·····, ω_j , interact in the medium and generate a *nonlinear polarization* $\mathbf{P}^{NL(j)} = = \mathbf{P}^{(j)} = \chi^{(j)} : \mathbf{E}_1 \mathbf{E}_2 \cdots \mathbf{E}_j$, $(j \geq 2)$, which, as a subsource in a collection of oscillating dipoles, produces a new radiation output at $\omega_{j+1} = \Sigma_{i=1,j} \omega_i$.

Although, in general, the output radiation can appear in all directions, the requirement of effective energy transformation in the *j*th order nonlinear optical process implies that both *momentum conservation* (in form of *phase matching condition*)

$$\mathbf{p}_{j+1} = \pm\mathbf{p}_1 \pm \mathbf{p}_2 \pm \cdots\cdots \pm \mathbf{p}_j, \qquad (2.4.1.)$$

or

$$\boldsymbol{k}_{j+1} = \pm\boldsymbol{k}_1 \pm \boldsymbol{k}_2 \pm \cdots\cdots \pm \boldsymbol{k}_j, \qquad (2.4.2.)$$

and *energy conservation*

$$\omega_{j+1} = \pm\omega_1 \pm \omega_2 \pm \cdots\cdots \pm \omega_j, \qquad (2.4.3.)$$

must be satisfied.

Using SVA, IPW, CPI approximations, and with the boundary condition on the light intensity $I^{(j)}_{\omega_s}(z)|_{z=0,\, j=2,3} = 0$, one can get the intensity of the output signal at frequency $\omega_{j+1} = \omega_1 \pm \omega_2 \cdots \pm \omega_j$, in third order processes, as [33, 37]

$$I_{\omega_s}^{(3)} = constant \left|\mathbf{e}_s \cdot \vec{\chi}^{(3)}(\omega_s = \omega_1 \pm \omega_2 \pm \omega_3) : \mathbf{e}_1\mathbf{e}_2\mathbf{e}_3\right|^2 \times$$
$$\times \frac{\left(\sin\frac{\Delta_3 k\, z}{2}\right)^2}{\left(\frac{\Delta_3 k\, z}{2}\right)^2} \cdot z^2 \cdot I_{\omega_1} I_{\omega_2} I_{\omega_3} \qquad (2.4.4.)$$

where

$$\Delta_3 k = \left|\boldsymbol{k}_s - (\pm\boldsymbol{k}_1 \pm \boldsymbol{k}_2 \pm \boldsymbol{k}_3)\right|, \qquad (2.4.5.)$$

are *phase mismatches* for the third-order nonlinear optical interaction.

From (2.4.4.), (2.4.5.), we can see that the output power will be at its maximum if phase matching ($\Delta_3 k = 0$) is reached. This condition has been used in our experiment to decide the propagation directions of three input beams and one output beam.

2.5. Nonlinear Optical Experiment Requirements

From the experimental point of view, in order to get high conversion efficiency, the following conditions should preferably be satisfied:

(1) the coupled waves are collinearly or near-collinearly phase matched (in this way all the waves will add up instead of partially cancelling each other);

(2) the medium is nearly lossless or has low absorption at the wavelength of the pump and probe pulses (in some extreme cases, high absorption will leave too little light powers to drive the nonlinear optical application or the nonlinear effects);

(3) the SVA is valid (because the energy transfer among the waves is usually significant only after the waves travel over a distance much longer than their wavelengths);

(4) walk-off effect is minimized (otherwise, the beams will lose their phase-matching because birefringence will affect the different polarization of the light);

(5) the laser beam quality should be good (best in TM_{00} mode for the optimal coupling between the waves);

(6) high quality nonlinear optical samples or crystals should be used in order to get perfect phase matching throughout;

(7) temperature should be as uniform as possible through the sample or crystal; gradient will cause some extra unexpected effects, such as damage to the sample.

These are the major consideration in our experiment, though in four-wave mixing process, additional conditions, for example, phase matching and keeping intensities of three input beams under the damage threshold of the samples, etc., need to be satisfied.

2.6. Four-Wave Interaction and Four-Wave Mixing

Four-wave interactions (FWI) include *four-wave up-conversion* (FWUC) or *four-wave sum-frequency generation* (FWSFG), in which $\omega_s = \omega_1+\omega_2+\omega_3$. A special case, $\omega_1 = \omega_2 = \omega_3 = \omega_{input}$ ($\omega_s = 3\omega_{input}$) is called *third harmonic generation* (THG). We can also have a *four-wave difference-frequency generation* (FWDFG), in which $\omega_s = \omega_1 + \omega_2 - \omega_3$. The second case is often referred as ***four-wave mixing*** (FWM).

The wave vector diagrams for the three different situations of FWM are depicted in Fig. 2.6.1. . If $\omega_1 \neq \omega_2 \neq \omega_3 \neq \omega_s$, FWM is called ***non-degenerate four-wave mixing*** (NDFWM), otherwise, it is called ***degenerate four-wave mixing*** (DFWM). In the fully degenerated case, $\omega_s = \omega_1 = \omega_2 = \omega_3$ (FDFWM). Obviously, there exists a third possible case in which only two different frequencies are involved: $\omega_1 = \omega_3$, $\omega_s = \omega_2$. This situation, referred to as ***partially degenerate four-wave mixing*** (PDFWM) or often as ***non-degenerate four-wave mixing,*** is just the situation covered by our TRFWM experiment and is sometimes termed ***scattering from light-induced gratings***.

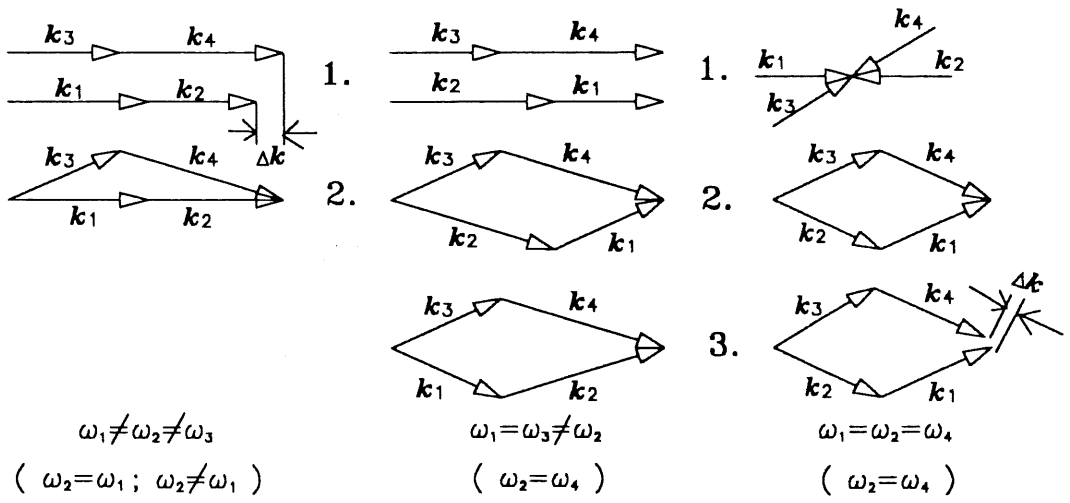

(a). NDFWM:
1. Co-Axis Geometry
2. Off-Axis Geometry

(b). PDFWM:
1. One-Beam Geometry
2. Two-Beam Geometry
3. Four-Beam Geometry

(c). FDFWM:
1. Pairwise Counterpropagation
2. Co-Propagating Beams
3. Four Beams with Phase-Mismatching

Figure 2.6.1. Wavevector Diagrams of the Four-Wave Interaction Processes.

In our spectroscopic investigation of dimeric/heterodimeric, trimeric/hetero-trimeric model systems we chose:

$$\omega_1 = \omega_3 = \omega_{pp},\ \omega_s = \omega_2 = \omega_{pb} \qquad (2.6.1.)$$

where, pp = pump, pb = probe. For this case, equations (2.4.4.) and (2.4.5.) now become

$$I_s^{(3)} = constant \left| \mathbf{e}_s \tilde{\chi}^{(3)} \cdot (\boldsymbol{k}_s, \omega_s) : \mathbf{e}_{pp_1} \mathbf{e}_{pp_2} \mathbf{e}_{pb} \right|^2 \times \times \frac{\left(\sin \frac{\Delta_3 k z}{2} \right)^2}{\left(\frac{\Delta_3 k z}{2} \right)^2} \cdot z^2 \cdot I_{pp_1} I_{pp_2} I_{pb}, \qquad (2.6.2.)$$

$$\Delta_3 \boldsymbol{k} = \left| \boldsymbol{k}_s - (\boldsymbol{k}_{pp1} - \boldsymbol{k}_{pp2} + \boldsymbol{k}_{pb}) \right|, \qquad (2.6.3.)$$

$$\omega_s = \omega_1 - \omega_2 + \omega_3. \qquad (2.6.4.)$$

In our experiment, we used two pump beams with the same frequency, therefore, the output signal beam is of the frequency

$$\omega_s = (\omega_{pump1} - \omega_{pump2} + \omega_{probe})|_{\omega_{pump1} = \omega_{pump2}} = \omega_{probe}. \qquad (2.6.5.)$$

So far, we have discussed only steady-state FWM. Nevertheless, transient effects may become important when using pulsed resonant excitation.

2.7. Transient Response of a Medium in Four-Wave Mixing

As in the steady-state case, the source term in transient FWM is still the third-order polarization $\mathbf{P}^{(3)}$. The only difference is that $\mathbf{P}^{(3)}$ is now a time-dependent function of the excitation and the relaxation of the medium. Though the response I_S will be a transient one, the major conclusions are similar to those obtained from equation (2.6.2.). A quantum mechanical calculation of the transient response of four-wave mixing in a medium, has been given in Appendix 2. Here we only discuss transient response of four-wave mixing in a medium in a classical field theory view. The results from the discussion have been directly used in our experimental data fitting.

2.7.1. A Classical Field Theory View

Through a quantum mechanical calculation of the optical nonlinearity in a medium, one obtained the relation between the microscopic molecular structure and the macroscopic $\chi^{(i)}$, e.g. for four-wave mixing processes, the third-order nonlinear optical polarizability $\chi^{(3)}$. In order to verify the correctness of a theoretical model, one has to

compare the results or predictions made by the model with those of the experiment. To do this, one needs to establish a link between the theoretical expressions and the experimental observables. As discussed in the previous section, one can start from the constitutive equation (2.3.1.).

We shall restrict our discussion to the situation of interest, that is four-wave mixing.

The polarization at the time t, which is induced by the pumping and probing fields $\mathbf{E}^{pp1}$, $\mathbf{E}^{pp2}$, $\mathbf{E}^{pb}$, at the previous time τ_1, τ_2, and τ_3, is given by the constitutive equation:

$$\mathbf{P}^{ind}(t) = \int_{-\infty}^{+\infty} d\tau_1 d\tau_2 d\tau_3 \vec{R}(t-\tau_1, t-\tau_2, t-\tau_3)\ \mathbf{E}^{pp1}(\tau_1)\mathbf{E}^{pp2\,*}(\tau_2)\mathbf{E}^{pb}(\tau_3), \qquad (2.7.1.1.)$$

where $\vec{R}(t-\tau_1,\ t-\tau_2, t-\tau_3)$ is the material's response to the external fields.

In our four-wave mixing system, the two pumping beams are synchronized so as to generate a transient grating which diffracts the probing beam and yields the FWM signal. Thus, one get:

$$\mathbf{P}^{ind}(t) = \int_{-\infty}^{+\infty} d\tau_1\, d\tau_3 \vec{R}(t-\tau_1,\ t-\tau_3) \left|\mathbf{E}^{pp}(\tau_1)\right|^2 \mathbf{E}^{pb}(\tau_3). \qquad (2.7.1.2.)$$

Because the probing beam feels only the change in the refractive index caused by the excitation of the two pumping beams, one can write

$$\vec{R}(t-\tau_1, t-\tau_3) = \vec{R}(t-\tau_1)\,\delta(t-\tau_3), \qquad (2.7.1.3.)$$

and thus

$$\mathbf{P}^{ind}(t) = \mathbf{E}^{pb}(t) \int_{-\infty}^{+\infty} d\tau_1 \, \tilde{R}(t-\tau_1) \left| \mathbf{E}^{pp}(\tau_1) \right|^2 . \qquad (2.7.1.4.)$$

By changing the integration variable from $t - \tau_1$ to τ:

$$\tau = t - \tau_1 \qquad (2.7.1.5.)$$

one gets

$$\mathbf{P}^{ind}(t) = \mathbf{E}^{pb}(t) \int_{-\infty}^{+\infty} d\tau \tilde{R}(\tau) \left| \mathbf{E}^{pp}(t-\tau) \right|^2 . \qquad (2.7.1.6.)$$

If the probing beam is delayed by τ_d with respect to $\tau = 0$, the instant when the pumping beams arrived, then, changing $(t-\tau)$ to $(t-\tau_d-\tau)$, formula (2.7.1.6.) becomes:

$$\mathbf{P}^{ind}_{\tau_d}(t) = \mathbf{P}^{ind}(t-\tau_d) = \mathbf{E}^{pb}(t-\tau_d) \int_{-\infty}^{+\infty} d\tau \tilde{R}(\tau) \left| \mathbf{E}^{pp}(t-\tau_d-\tau) \right|^2 \qquad (2.7.1.7.)$$

Defining the z axis along symmetric axis of the propagation direction of the beams, and φ_{pb} as the angle between the polarization of the probe beam and the x axis, then the two components of the induced polarization can be expressed as

$$P^{ind}_{\tau_d\, x}(t) = E^{pb}(t-\tau_d) \int_{-\infty}^{+\infty} d\tau R_{xxxx}(\tau) \, I^{pp}(t-\tau_d-\tau) \cos\varphi_{pb}, \qquad (2.7.1.8.)$$

$$P^{ind}_{\tau_d\, y}(t) = E^{pb}(t-\tau_d) \int_{-\infty}^{+\infty} d\tau R_{yyxx}(\tau) \, I^{pp}(t-\tau_d-\tau) \sin\varphi_{pb}. \qquad (2.7.1.9.)$$

In the general case, the response of the material to the induced external fields has the form

$$R(\tau) = \chi^{(3)}_{electron} \delta(\tau) + \sum_i \chi^{(3)}_i R_i(\tau), \qquad (2.7.1.10.)$$

where $\chi^{(3)}_{electron}$ and $\chi^{(3)}_i$ are third-order nonlinear susceptibilities corresponding to the virtual electron transitions and to the *i*th relaxation component, respectively.

Therefore, one has

$$P^{ind}_{x\,\tau_d}(t)=\left[\chi^{electron}I^{pp}(t)+\int_{-\infty}^{+\infty}d\tau\sum_i\chi^i_{1111}R_i(\tau)I^{pp}(t-\tau)\right]E^{pb}(t-\tau_d)\cos\varphi_{pb}\,, \tag{2.7.1.11.}$$

$$P^{ind}_{y\,\tau_d}(t)=\left[\chi^{electron}I^{pp}(t)+\int_{-\infty}^{+\infty}d\tau\sum_i\chi^i_{2211}R_i(\tau)I^{pp}(t-\tau)\right]E^{pb}(t-\tau_d)\sin\varphi_{pb}\,. \tag{2.7.1.12.}$$

Let us define

$$\begin{aligned}RP_x(t)&=\chi^{electron}I^{pp}(t)+\int_{-\infty}^{+\infty}d\tau\sum_i\chi^i_{1111}R_i(\tau)I^{pp}(t-\tau)=\\&=\chi^{electron}I^{pp}(t)+\int_{-\infty}^{+\infty}d\tau\,R_x(\tau)I^{pp}(t-\tau),\end{aligned} \tag{2.7.1.13.}$$

$$\begin{aligned}RP_y(t)&=\chi^{electron}I^{pp}(t)+\int_{-\infty}^{+\infty}d\tau\sum_i\chi^i_{2211}R_i(\tau)I^{pp}(t-\tau)=\\&=\chi^{electron}I^{pp}(t)+\int_{-\infty}^{+\infty}d\tau\,R_y(\tau)I^{pp}(t-\tau).\end{aligned} \tag{2.7.1.14.}$$

When detecting the FWM signal, a Wollaston prism can be used to separate different polarization components. If the polarization axis of the Wollaston prism makes an angle φ_w in respect to the x axis, then the four-wave mixing signal parallel or perpendicular to the polarization axis of the prism, $S_{\parallel}$ and $S_{\perp}$, can be expressed as (because the probe pulse has a limited duration around τ_d):

$$S_{\parallel}(\tau_d) \propto \int_{-\infty}^{+\infty} dt \left| P^{ind}_{\tau_d \parallel}(t) \right|^2 = \int_{-\infty}^{+\infty} dt \left| P^{ind}_{x\,\tau_d}(t) \cos\varphi_w + P^{ind}_{y\,\tau_d}(t) \sin\varphi_w \right|^2,$$

(2.7.1.15.)

$$S_{\perp}(\tau_d) \propto \int_{-\infty}^{+\infty} dt \left| P^{ind}_{\tau_d \perp}(t) \right|^2 = \int_{-\infty}^{+\infty} dt \left| -P^{ind}_{x\,\tau_d}(t) \sin\varphi_w + P^{ind}_{y\,\tau_d}(t) \cos\varphi_w \right|^2.$$

(2.7.1.16.)

These can be written as

$$S_{\parallel}(\tau_d) \propto \int_{-\infty}^{+\infty} dt \left\{ |RP_x(t)|^2 \cos^2\varphi_{pb} \cos^2\varphi_w + |RP_x(t)|^2 \sin^2\varphi_{pb} \sin^2\varphi_w + \right.$$
$$\left. + \left[RP_x(t) RP^*_y(t) + RP^*_x(t) RP_y(t) \right] \cos\varphi_{pb} \sin\varphi_{pb} \cos\varphi_w \sin\varphi_w \right\} I^{pb}(t-\tau_d),$$

(2.7.1.17.)

and

$$S_{\perp}(\tau_d) \propto \int_{-\infty}^{+\infty} dt \left\{ |RP_x(t)|^2 \cos^2\varphi_{pb} \sin^2\varphi_w + |RP_x(t)|^2 \sin^2\varphi_{pb} \cos^2\varphi_w + \right.$$
$$\left. - \left[RP_x(t) RP^*_y(t) + RP^*_x(t) RP_y(t) \right] \cos\varphi_{pb} \sin\varphi_{pb} \cos\varphi_w \sin\varphi_w \right\} I^{pb}(t-\tau_d).$$

(2.7.1.18.)

2.7.2. Coupling Phonons

In frequency space, the third-order nonlinear response has the following form [194]:

$$R(\omega,\mathbf{q}) = \frac{\chi_{ijkl}}{\omega^2 - \upsilon^2(\mathbf{q}) - 2i\gamma\,\upsilon(\mathbf{q})} = \frac{\chi_{ijkl}}{\omega^2 - \upsilon^2(\mathbf{q}) - 2i\,\upsilon(\mathbf{q})/\tau}, \qquad (2.7.2.1.)$$

where ω is the system response frequency and $\nu(\mathbf{q})$ is the phonon frequency.

The corresponding form in time is either

$$R_{ijkl}(t) = \chi^{(3)}_{ijkl}\, e^{-t/\tau}, \qquad (2.7.2.2.)$$

for population relaxation, or

$$R_{ijkl}(t) = \chi^{(3)}_{ijkl}\, e^{-t/\tau}\, \frac{\sin(\omega t + \varphi)}{\omega}, \qquad (2.7.2.3.)$$

for the coupling to the phonons without dispersion, or

$$R_{ijkl}(t) = \int d\mathbf{q}\; \chi^{(3)}_{ijkl}\, e^{-t/\tau(\mathbf{q})}\, \frac{\sin[\omega(\mathbf{q})t + \varphi]}{\omega(\mathbf{q})}\, e^{-m(\mathbf{q}-\mathbf{q}_0)^2}, \qquad (2.7.2.4.)$$

for the coupling to the phonons with dispersion, where m is a constant and the gaussian form is introduced because of the existence of gaussian pump and probe pulse shapes [193].

In our experiment, we are interested in investigating the transient response of a system whose population is excited to a higher level and then goes through a cascade of relaxations to intermediate levels.

2.7.3. Population Relaxation

According to Appendix I, the analytical expression of the transient response caused by the population relaxation of the four-level system is:

$$R(t) = \left[\chi_1^{(3)} + \chi_2^{(3)} \frac{g_{12}}{T_1} \frac{T_1 T_2}{T_1 - T_2} + \chi_3^{(3)} \left(\frac{g_{13}}{T_1} - \frac{g_{12}}{T_1} \frac{g_{23}}{T_2} \frac{T_1 T_2}{T_1 - T_2}\right) \frac{T_1 T_3}{T_1 - T_3}\right] e^{-t/T_1} +$$
$$+ \left[-\chi_2^{(3)} \frac{g_{12}}{T_1} \frac{T_1 T_2}{T_1 - T_2} - \chi_3^{(3)} \frac{g_{12}}{T_1} \frac{g_{23}}{T_2} \frac{T_1 T_2}{T_1 - T_2} \frac{T_2 T_3}{T_2 - T_3}\right] e^{-t/T_2} +$$
$$+ \chi_3^{(3)} \left[-\left(\frac{g_{13}}{T_1} - \frac{g_{12}}{T_1} \frac{g_{23}}{T_2} \frac{T_1 T_2}{T_1 - T_2}\right) \frac{T_1 T_3}{T_1 - T_3} + \frac{g_{12}}{T_1} \frac{g_{23}}{T_2} \frac{T_1 T_2}{T_1 - T_2} \frac{T_2 T_3}{T_2 - T_3}\right] e^{-t/T_3} . \quad (2.7.3.1.)$$

where, $\chi_i^{(3)}$ is relative strength of different relaxation components, T_i is the relaxation time of i-th level, T_{ij} is the relaxation time of the system from i-th level to j-th level, and $g_{ij} = T_{ij} / T_i$ is a statistical weight factor. All these parameter are adjustable in the fitting of the experimental results.

Chapter 3

Experiment

3.1. Experimental Set-up

Our experimental system is shown in the block diagram of Fig. 3.1.1. It can be divided into six subsystems:

(1) femtosecond laser generator;

(2) femtosecond laser amplifier;

(3) four-wave mixing system;

(4) detection system;

(5) data acquisition system;

(6) synchronism control system.

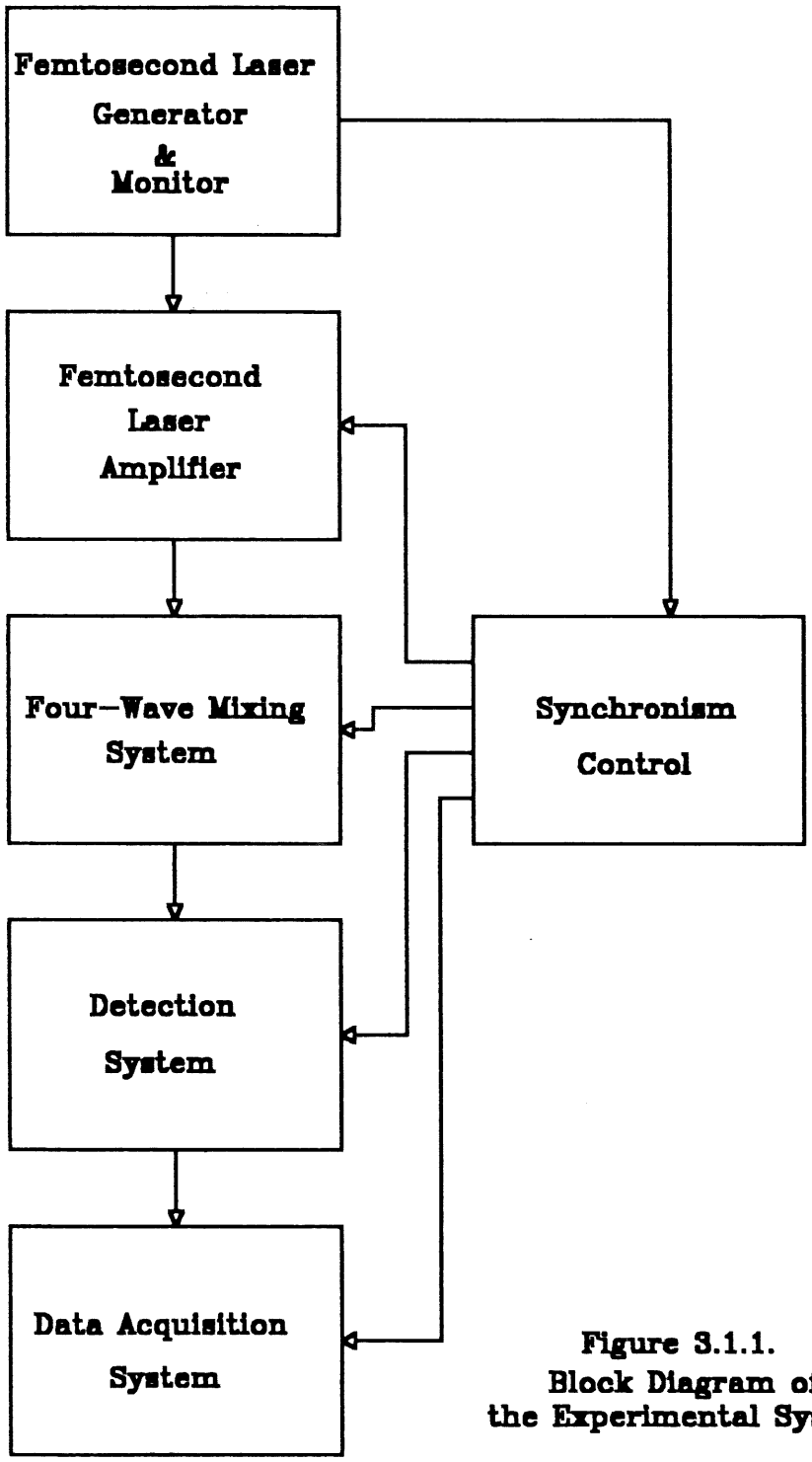

Figure 3.1.1.
Block Diagram of the Experimental System

A schematic representation of each of these subsystems is shown in Fig.3.1.2 .

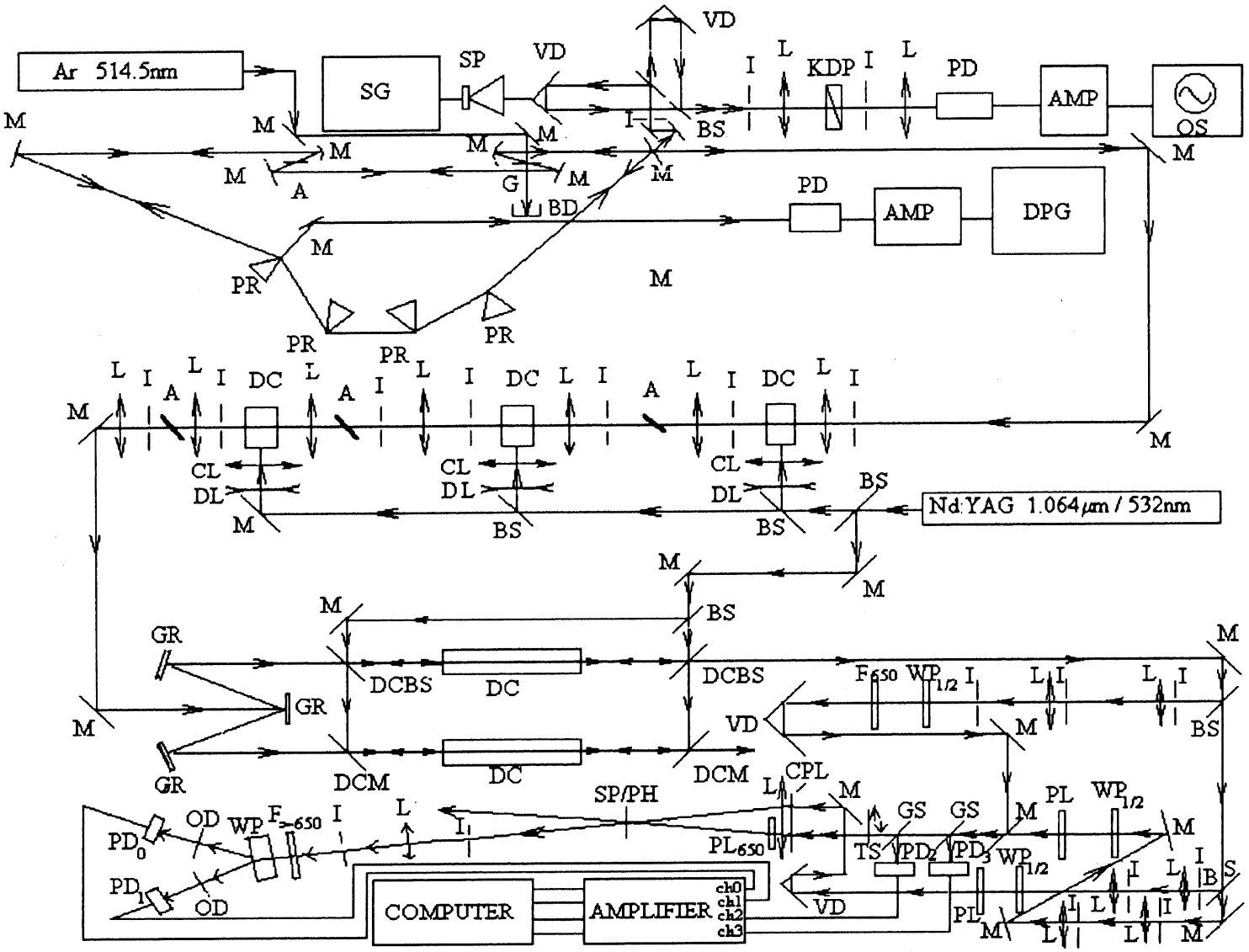

Figure 3.1.2. Details of Experimental System.

We have used the following abbreviations:

A: Absorber
AMP: Amplifier
AT: Attenuator
BD: Beam Dump
BS: Beam Splitter
CL: Cylindrical Lens
CP: Computer
CPL: Calibrating Plate
DC: Dye Cell
DCBS: Dichroic Beam Splitter
DCM: Dichroic Mirror
DL: Divergent Lens
DPG: Delay / Pulse Generator
F: Filter
GR: Grating
GS: Glass
I: Iris
JT: Jet
L: Lens
M: Mirror
OS: Oscilloscope
OD: Optical Density
PD: Photodiode
PL: Polarizer
PM: Photomultiplier
PR: Prism
PRM: Pyramid
SG: Signal Generator
SP: Speaker
SP / PH: Sample / Pinhole
TS: Transparent Shuttle
TP: Thompson Polarizer
TLP: Taylor Polarizer
VD: Variable Delay
WC: Water Cell
WP: Wollaston Polarizer
$WP_{1/2}$: Wave Piece (half wavelength)

3.2. Femtosecond Laser Generator and Monitor

As shown in Fig. 3.2.1, the femtosecond laser generator principally consists of a colliding pulse mode-locked dye laser (CPM), pumped by an Argon laser at 514.5 nm to give an output at 620 nm with $\tau \approx 60$ fs, P = 1 nJ/pulse, f = 85 MHz [195 - 201]. In the center of the CPM cavity, there are a gain jet G with rhodamine 6G pumped by an Argon laser and a saturating absorbing jet (A) with DODCI (diethyloxadicarbocyanine iodide).

The crucial idea behind the CPM is to utilize the interaction or "collision" of two pulses in the laser cavity, propagating in opposite directions, to enhance the effectiveness of the saturable absorber.

The absorber and the gain jet are placed at a relative distance of approximately one quarter of the round trip around the ring. Thus, starting from the saturable absorber, the two oppositely propagating pulses will profit from the gain jet and meet again at the absorber with the same time delay corresponding to a round trip time. In this manner, both pulses acquire the same gain, the effective saturation parameter is increased by a factor of three over that for a conventional passive mode-locked dye laser, and the formation of extra pulses in the cavity has been effectively reduced.

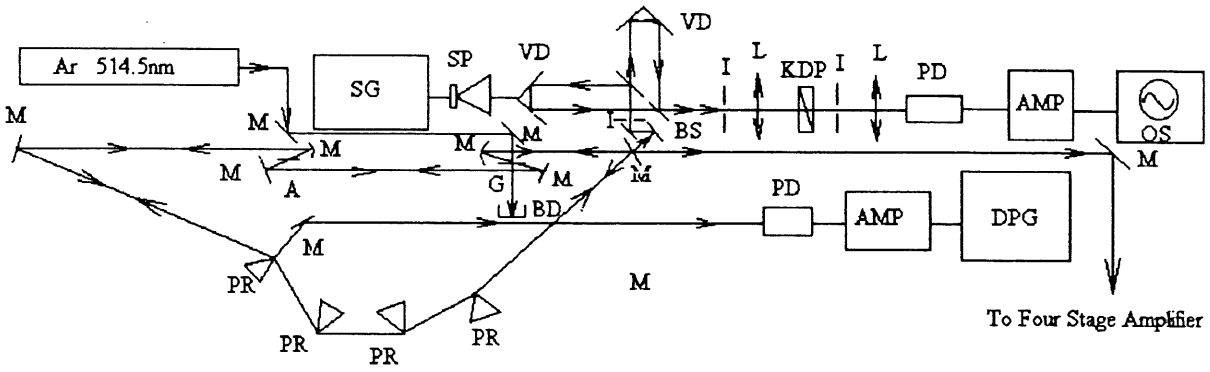

Figure 3.2.1. Femtosecond Laser Generator & Monitor.

Since the optimum performance of a femtosecond dye laser is critically dependent on the group velocity dispersion in the optical cavity, four prisms have been inserted into the CPM cavity to compensate the group velocity dispersion. These negative group velocity dispersion pieces make the dispersion adjustable by moving one of the prisms along a normal to the prism base [201, 203]. This results in a shorter output pulse from the CPM.

There are two beams that exit the CPM from a semi-reflective mirror with R = 98 %. One beam is directed to the four stage femtosecond laser amplification system while the other is fed into a femtosecond laser monitor system so as to get real time information about the pulse duration of the laser pulses.

Most of the ultrashort pulse duration measurements require measuring the second or higher order autocorrelation function [204]:

$$G^{(j)}(\tau_1, \tau_2, \cdots, \tau_{j-1}) = \frac{\langle I(t)I(t+\tau_1)\cdots I(t+\tau_{j-1})\rangle}{\langle I^j(t)\rangle}. \qquad (3.2.1.)$$

In the $j = 2$ case, one has

$$G^{(2)}(\tau) = \frac{\langle I(t)I(t+\tau)\rangle}{\langle I(t)\rangle} \qquad (3.2.2.)$$

Experimentally, these functions can be obtained by the SHG effects. In our monitor system, the beam coming from the CPM is divided into two by a beam splitter. In the balance position of the microscopic displacement piece that is driven by a speaker (SP), the two beams are adjusted to have the same time delay. Then, the two beams are focused into a KDP crystal. By monitoring the SHG signal from the KDP on an oscilloscope, when the speaker is on, one can observe the shape and pulse duration, whose value can be pre-calibrated and seen directly on the screen.

3.3. Femtosecond Laser Amplifier

The output laser pulse from the CPM, although being relatively short and having typically the power of 1 nJ/pulse, is still too low for most ultrashort laser spectroscopy investigations. It needs to be further amplified. This is accomplished by a four-stage femtosecond dye laser amplifier, shown in Fig. 3.3.1. .

The amplifier is pumped by a KDP frequency doubled, Q-switched Nd^{+3}:YAG laser at 532 nm with repetition rate of 10 Hz. It yields an output pulse at 620 nm with 100 fs pulse duration and 0.30 mJ/pulse in energy. The first three amplifying dye-cells (DC) are pumped transversely. Every cell is followed by a saturable dye absorber jet A, to eliminate the spontaneous radiation which would be otherwise added to the 620 nm beam to be amplified. After passing the previous three stages of amplification, two grating pair systems have been introduced in order to compress the laser entering the last stage amplifier. This amplifier has been perfected by

Dr. Daniel Houde, who ingeniously designed it to generate **two** equivalent outputs instead of just **one** as usually the case.

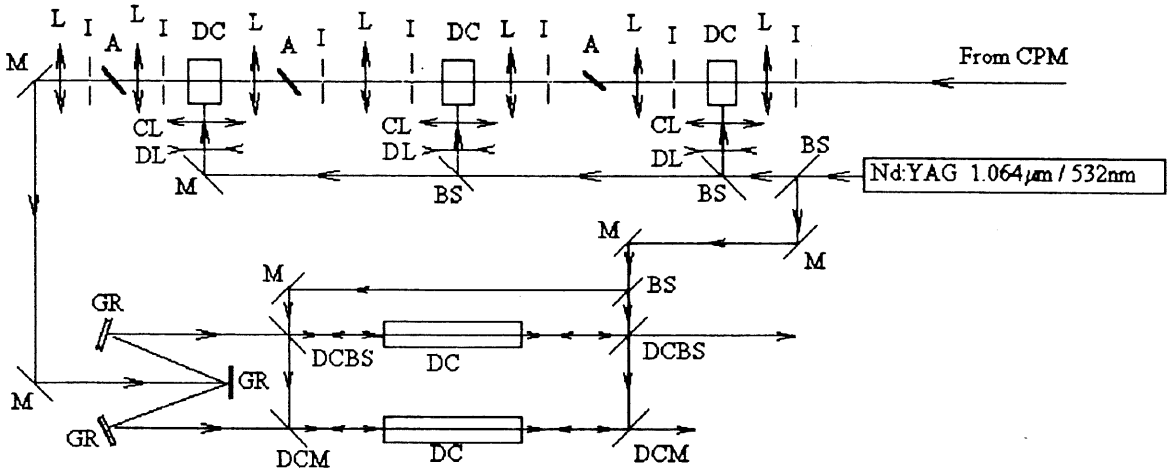

Figure 3.3.1. Four-Stage Femtosecond Laser Amplifier.

As shown in Fig. 3.3.1., the crucial part of the last stage amplification consists of a pair of dichroic beam splitters (DCBS) and a pair of dichroic mirrors (DCM). The DCBSs divide the 532 nm pumping laser beams from the Nd^{+3}:YAG into two equal parts while letting the 620 nm laser from the previous three stage amplifier to pass unchanged. The DCMs totally reflect the 532 nm pumping beams but let the 620 nm laser to pass. In the last stage amplification, two 620 nm laser beams, that come out as +1 and −1 order diffraction from the second compressing gratings, are pumped longitudinally in the two Sulforhodamine 640 dye cells (DC). This ingenious design allows one to make full use of the resources of the system. It outputs two equal 620 nm laser beams having a pulse duration 100 fs, a repetition rate of 10 Hz and a typical energy of 0.3 mJ/pulse.

3.4. Four-Wave Mixing System

The time-resolved non-degenerated four-wave mixing (TRNDFWM) system used in our experiment is shown in Fig. 3.4.0.1. .

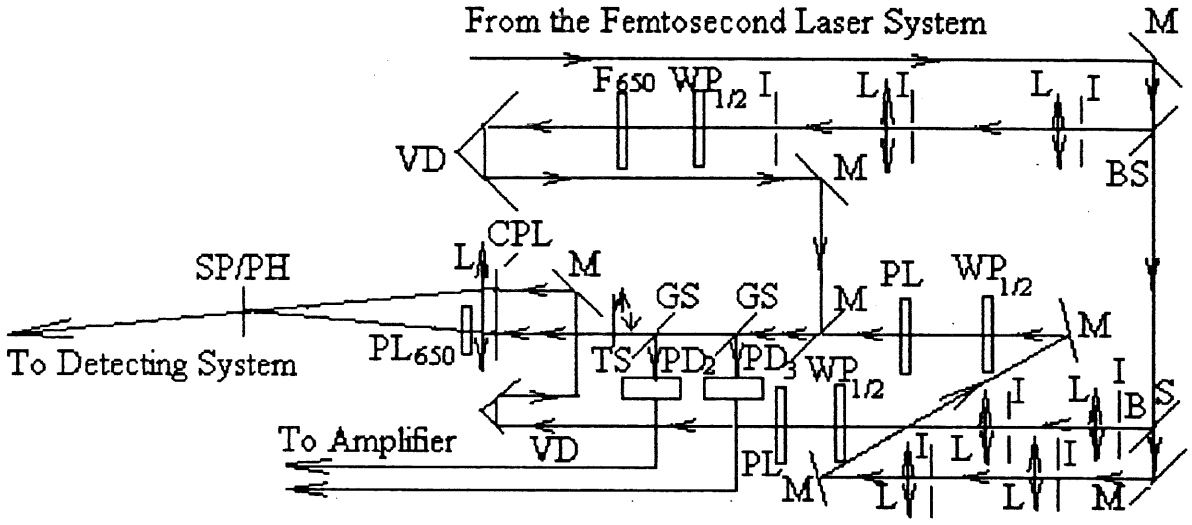

Figure 3.4.0.1. Four-Wave Mixing System.

The amplified laser beam, exiting from one of the arms of the femtosecond laser amplifier, is divided into three by beam splitters (BS). Two of them serve as pump pulses, whose polarisation directions are controlled by the half wave pieces ($WP_{1/2}$) and Thompson polarizer (TP or PL). The third 620 nm pulse is focused into a 60 μm ethaleneglucol jet (JT) to generate a wide-band subpicosecond white continuum, from which a λ = 650 nm, $\delta\lambda$ = 10 nm pulse is selected by an interference filter (F_{650}). This 650 nm pulse serves as probe. Its polarization direction is also controlled by a half-wave piece and a Thompson polarizer. The three beams are focused by a group of lenses onto the sample with a spot size approximately 600 μm in diameter. Pump pulse and probe pulse are sampled by two glass pieces (GS). The sampled lights are fed into two photodiodes (PD_2, PD_3) where they are converted into electric signals, which are served as the reference for data acquisition system.

3.4.1. Spatial Arrangement of Four-Wave Mixing Beams.

The spatial arrangement of the beams involved in four-wave mixing is given in Fig.3.4.1.1.

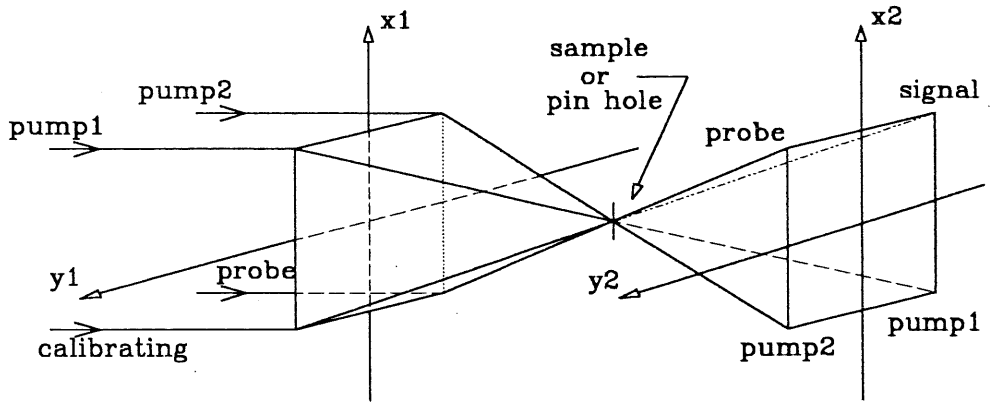

Figure 3.4.1.1. Spatial Arrangement of Four-Wave Mixing Beams

The propagation directions of the pumps, probe and signal pulses are pre-set and controlled by the relative position between a calibrating plate (CPL, in Fig. 3.4.0.1.) and a pinhole (PH, in Fig.3.4.0.1.). The CPL has four holes, two used by two pump beams and one by the probe beam. The fourth is used to calibrate the signal beam propagation direction. The spatial arrangement leads to angles of 1.21° and 2.4° between the probe beam and the two pump beams. Once the calibration has been done, the sample (SP, in Fig. 3.4.0.1.) or reference crystal/glass/quartz will be put into exactly the same position that the pinhole held before. With this specific spatial arrangement, the diffracted FWM signal will exit in the phase-matching direction $\boldsymbol{k}_s = \boldsymbol{k}_1 - \boldsymbol{k}_2 + \boldsymbol{k}_3$, as shown in Fig. 3.4.1.2. .

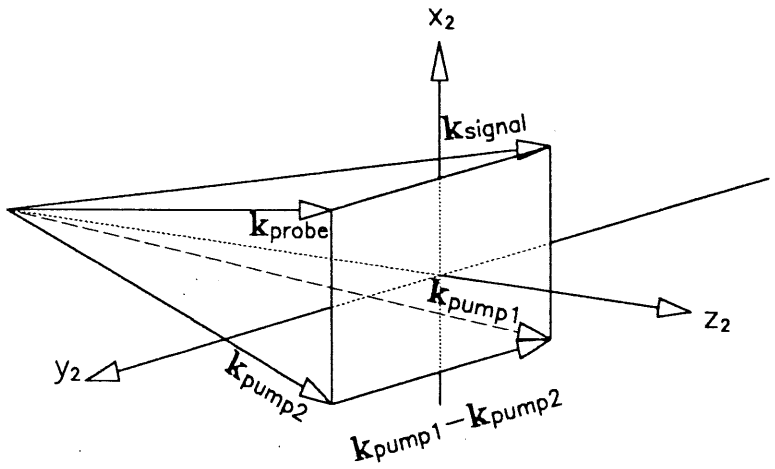

$$\mathbf{k}_{signal}=\mathbf{k}_{probe}-(\ \mathbf{k}_{pump2}-\mathbf{k}_{pump1})=$$
$$=\mathbf{k}_{probe}+(\ \mathbf{k}_{pump1}-\mathbf{k}_{pump2}\ )$$
$$\omega_{signal}=\omega_{probe}+(\ \omega_{pump1}-\omega_{pump2}\ )=$$
$$=\omega_{probe}$$

Figure 3.4.1.2. Wave Vector Diagram of Four-Wave Mixing Process.

3.4.2. Synchronization of the Two Pump Pulses

Before starting any TRFWM measurement, the two pump pulses must be synchronized. This is done by observing the autograting effect in the reference crystal, $SrTiO_3$. After carefully calibrating the wave propagation directions and putting the reference crystal in place, one then adjusts the relative delay between the two pump pulses by moving the variable delay line (VD, in Fig. 3.4.0.1.). Putting a screen in the x_2Oy_2 plane, shown in Fig. 3.4.1.1., when synchronism is achieved, an autograting pattern, shown in Fig. 3.4.2.1., will appear. This pattern can be seen easily if the pump power is sufficiently intense.

By scanning the probe variable delay line (VD, in Fig. 3.4.0.1.) which is controlled by a step motor and computer software, one can find a position where the three pulses are properly synchronized. This occurs when the largest response is observed on the screen of a monitoring oscilloscope that is connected to the channel

0 or channel 1 output from the amplifier. Once the three beam synchronization position has been found, one can start to scan the reference quartz or glass, and then the sample to be measured.

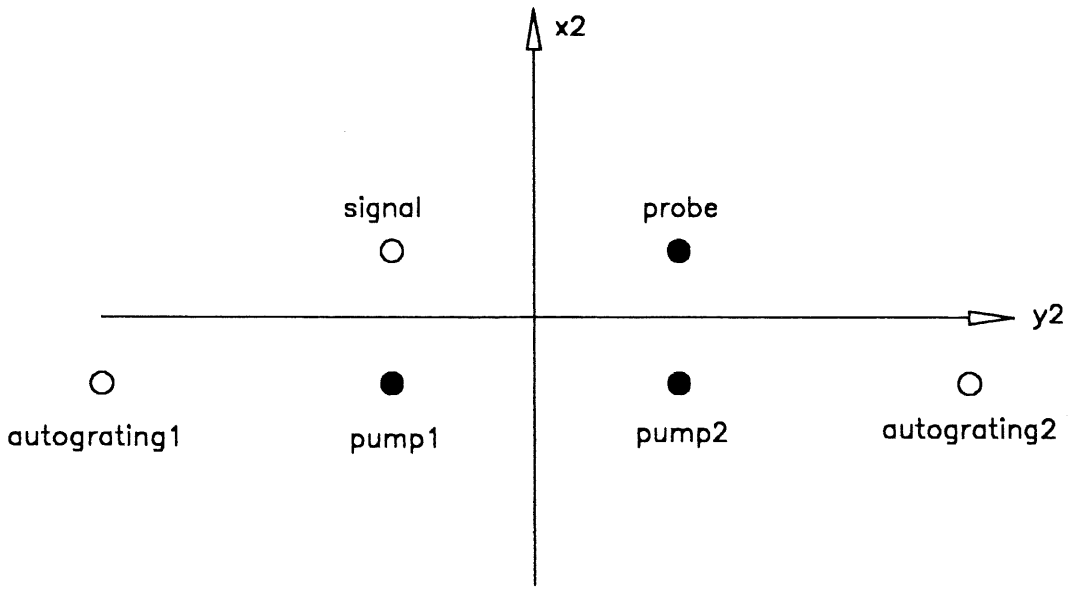

Figure 3.4.2.1. Relative Positions of Pump1, Pump2, Probe, Diffracted Signal, and Autograting Beams.

The maximum length of the probe delay line is 50 cm, which corresponds to a delay time of 1.7×10^6 fs = 1.7 ns, and the minimum step is 0.2 μm, which corresponds to a time interval of 0.66 fs. Because the scanning generally needs to start from a negative delay position, for which the probe pulse will arrive at the sample or reference earlier than the two pump pulses and thus no FWM signal will be available (recording of the system base line), the longest delay time we can reach in the experiment is about 1.3 ns.

3.5. Four-Wave Mixing Signal Detection System

The four-wave mixing signal detection system is described in Fig.3.5.1. . The diffracted FWM signal is first spatially selected by a group of iris (I) and lens (L), then filtered in frequency by a low passing band filter starting at 650 nm ($F_{>650}$), and finally fed into a Wollaston prism (WP) which separates the two orthonormal polarizations of the beam. The intensity in each path is detected via two photodiodes.

The above two step selection of FWM signals and the use of a 650 nm probe beam have greatly increased the signal to noise ratio. The 620 nm pump beam diffusion background from the samples is suppressed. The diffused light would otherwise in some cases, e.g. for Langmuir-Blodgett thin films, give us a serious problem and make it impossible to extract the signal from the noise background. We have introduced special technique called ***transparent shuttle***,which is made of a piece of glass (Shown in Figure 3.4.0.1., symbolized by **TS**), to overcome this obstacle. After the whole system is optimized and the two pump beams are synchronized, when starting data acquisition, first put this shuttle into the light path of one of the pump beams. At this moment, **the pump beams has not been cut off but been de-synchronized** since the transparent glass piece introduced an extra light path for one of the pump beams, what is collected by the data acquisition system is just the strong diffusion background ***B***. Then, in second step, open the shuttle, let the two pump beams pass through and arrive at the sample simultaneously, recording the intensity ***A***, under this condition. Finally, the data acquisition system can get the real signal ***S*** embedded in the strong diffusion noise background:

$$S = A - B. \qquad (3.5.1.)$$

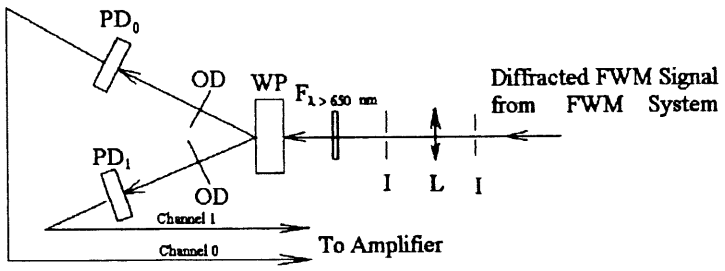

Figure 3.5.1. Four-Wave Mixing Signal Detection System.

3.6. Four-Wave Mixing Data Acquisition System

The four-wave mixing data acquisition system is depicted in Fig. 3.6.1. There are four channel signals: channel 0, perpendicular diffracted FWM signal; channel 1, horizontal diffracted FWM signal; channel 2, pump pulse reference; and channel 3, probe pulse reference. These are first sent into an amplifier and then collected by a software controlled A/D card. Before starting the acquisition, a programme called "histogram", makes a measurement of the statistical distribution of the number of pulses versus the intensity of the pump pulse (channel 0) and the probe pulse (channel 1). This procedure gives the ranges in intensity of the pump and the probe and allows proper validation of the data: when the intensities of pump and probe are inside the premeasured ranges, then the data collected is valid, otherwise the data should be abandoned. Every experimental data point is statistically averaged, typically 50 ~ 150 valid pulses per data point, depending on the stability of the total system. When finishing acquisition of a data point, the computer gives an instruction to the step motor of the delay line to advance a certain value. According to our experience, a step-changing scheme has to be used during the data acquisition in order to best compromise between the shortest response time (~ 100 fs) and the longest detectable response time (~ 1.3 ns).

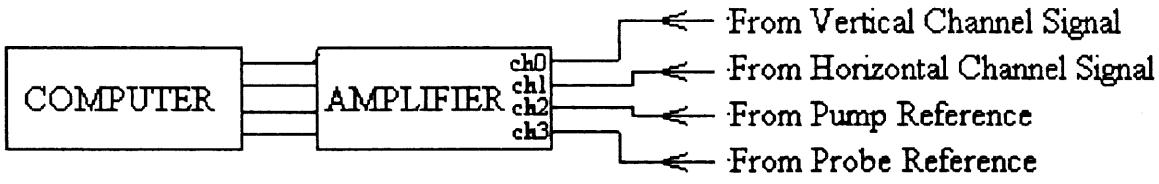

Figure 3.6.1. Four-Wave Mixing Data Acquisition System.

3.7. Synchronism Control System

The synchronism control system is presented in Fig. 3.7.1. . In the CPM cavity, a weak 620 nm femtosecond laser signal sample is reflected from the surface of one of the prisms and collected by a photodiode (PD). The converted signal is preamplified (AMP) and then sent into a delay pulse generator (DPG) which will in return send a

series of trig pulses to all the subsystems that need to be synchronized, e.g. Nd^{3+}: YAG, A/D card, etc. . A proper adjustment of the delays allows the total system to work in a more efficient way.

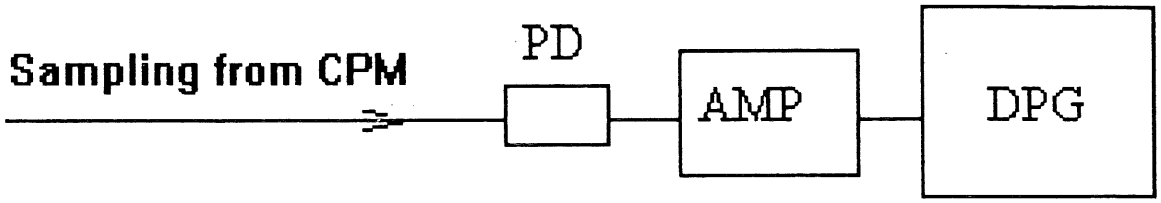

Figure 3.7.1. Synchronism Control System.

3.8. Experiment Approaches

For a successful TRNDFWM experiment, the following parameters or factors should be adjusted or decided on, being careful to keep a proper balance between some of them:

(1) the spot sizes and shapes of the two pump beams and the probe beam,

(2) the relative intensity of the pump and the probe beams,

(3) the polarization of the three input beams,

(4) the propagation directions of the FWM beams (three inputs and one output),

(5) the type of detectors,

(6) the dynamic ranges for the intensity of the two pump pulses and the probe pulse,

(7) the wavelength of the probe and of the diffracted light,

(8) the position of the sample, the reference crystal, the reference glass, or the reference quartz,

(9) synchronization of the two pump pulses,

(10) overlapping distance of the three input beams,

(11) the system's time resolution limit, pulse duration of the pump and the probe pulses,

(12) the number of pulses per data point,

(13) the steps (in microns) and the number of steps of the delay line, in different time scale regions,

(14) phase-matching type of the beams in the sample or the reference,

(15) phase matching angles for every possible cases,

(17) stability of the total system, and

(18) synchronism between all the subsystems.

Most of these parameters and factors have been described in previous sections.

The general procedure of a TRFWM experiment is summarized as follows:

(1) pre-adjusting the whole system,

(2) setting each of the above parameters or factors,

(3) making an acquisition for a reference sample, e.g. crystal, glass, or quartz, to get some information about the experimental system which will be used for data fitting and making calculations of the third-order nonlinear optical susceptibility $\chi^{(3)}$, etc.,

(4) doing a pre-scan for the sample to be measured to get the parameters necessary for making the data acquisition,

(5) making sample data acquisition,

(6) fitting the temporal spectra of the reference,

(7) fitting the temporal spectral of sample,

(8) repeating the above procedures, if necessary.

If the results from the experiment are satisfactory one must then make a theoretical calculation and analysis to extract the information contained in the data and attribute them to suitable physical mechanisms.

Chapter 4

Results and Discussion

In this chapter, we present the results of time-resolved four wave mixing (TRFWM) studies on

1. sublimated films of cerium porphyrin phthalocyanine sandwich mixed heterodimer, $Pc^{2-}Ce^{IV}TPP^{2-}$,
2. sublimated films of cerium porphyrin phthalocyanine symmetric trimer, $TPP^{2-}Ce^{III}Pc^{2-}Ce^{III}TPP^{2-}$,
3. Langmuir-Blodgett films of cobalt porphyrin phthalocyanine mixed dimer $CoPC_{22}^{4+}$ / H_2PcTS^{4-},
4. sublimated films of neodymium porphyrin phthalocyanine dimer $Pc^{2-}Nd^{III}Pc^{\bullet}$, and
5. sublimated films of neodymium porphyrin phthalocyanine trimer $Pc^{2-}Nd^{III}TPP^{2-}Nd^{III}Pc^{2-}$.

The results have been compared with those from transient absorption experiments on these samples so as to attribute the different relaxation components to the different relaxation paths. It is found that, due to the existence of intramolecular charge transfer and intermolecular excitonic excitation migration, degrating times of these sample in FWM experiments are shorter than those having only population relaxation from one excited state to the other. Third-order nonlinear optical responses of the samples have been measured by TRFWM. The absolute values of the third-order nonlinear optical susceptibility $\chi^{(3)}$ of these samples are determined by comparing the third-order nonlinear optical responses of the samples with those of a slide of fused quartz under exactly the same experimental conditions, taking quartz $\chi^{(3)}$ value as a standard reference.

We have performed ***the first TRFWM experiment on sublimated films***, observed and investigated ***the first two correlated phonon mode shifting phenomenon*** and ***the first photorefractive effect in an organic multimer thin film***, and made ***the first identification of diffusion contribution to the degrating process***.

4.1. Time-Resolved Four-Wave Mixing Study on the Sublimated Film of Cerium Porphyrin Phthalocyanine Heterodimer $Pc^{2-}Ce^{IV}TPP^{2-}$

4.1.1. Experimental Aspects

Details of the preparation of $Pc^{2-}Ce^{IV}TPP^{2-}$ are given in [205, 206]. Sublimated films of the compound were made in the laboratory of Prof. Lê Dao, in INRS-Energie/ Matériaux de Varennes, Montréal, Québec, Canada, as described in reference [207]. The ground state absorption spectra of $Pc^{2-}Ce^{IV}TPP^{2-}$ have been recorded by a HITACHI U-2000 spectrometer. The time resolved transient response has been detected by a four-wave mixing system, explained in Chapter 3, section 3.4., which is similar to that used by Etchepare et al. in their transient grating experiment [207]. A colliding pulse mode-locked (CPM) dye laser pumped by an Argon laser at 514.5 nm and amplified by a four-stage amplifier gave rise to a 100 fs pulse centred at 620 nm having a repetition rate of 10 Hz. The spatial arrangement of the four-wave mixing beams is shown in Fig. 3.4.1.1. . Two pump pulses with the same wavelength λ_p = 620 nm and at an angle of 2.11^0 in respect to each other, and a third probe pulse, with a wavelength at 650 nm and at the angles of 1.21^0 and 2.4^0 with respect to the two pump pulses, impinge on the sublimated sample of $Pc^{2-}Ce^{IV}TPP^{2-}$ lying on quartz substrate with a spot size being approximately 600 μm. The fourth diffracted four-wave mixing signal was detected as a function of the probe pulse delay time with respect to the two synchronized pump pulses. The two pump pulses and the probe pulse are polarized in the same direction. The given FWM geometry gives a coherent signal that is seen in the $\boldsymbol{k}_s = \boldsymbol{k}_1 - \boldsymbol{k}_2 + \boldsymbol{k}_3$ direction as shown in Fig. 3.4.1.2. . The signal is spatially selected by the given geometry, filtered at wavelength 650 nm by a low-pass band filter and

then fed into a Wollaston prism linked with two photodiodes which convert the signals into electronic ones. This arrangement allows us to get rid of the strong diffusion background coming from the 620 nm pump beams falling on the sample, which would otherwise in some cases give us a serious problem. The temporal shapes of the pump and probe pulses were determined by measuring TRFWM signal in a reference glass or fused quartz slide, then fitting the experimental data according to an appropriate theoretical model.

4.1.2. Results and Discussion

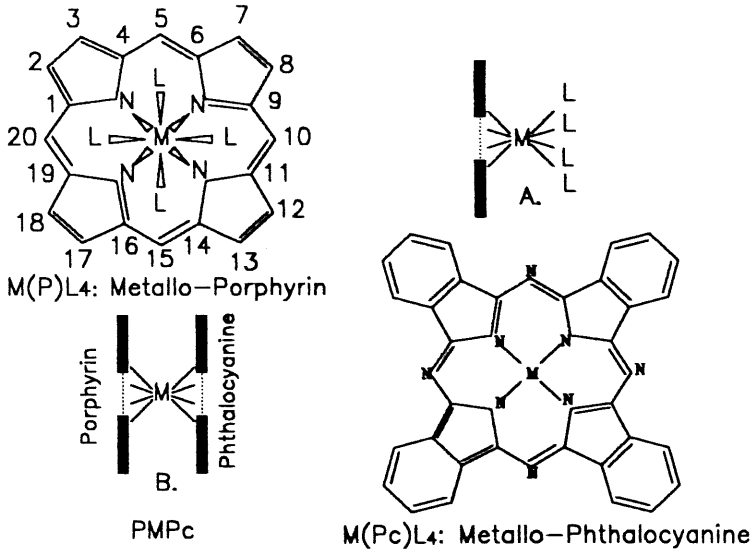

Figure 4.1.2.0.1. Constitution of Octacoordinated Metal Mono–tetrapyrroles M(P)L4 and Configurations with A: Monotetrapyrroles, B: Bistetrapyrroles PMPc, e.g., PcCeTPP, M = Lanthanide Metal Ion.

The structure of the heterodimer is depicted in Fig. 4.1.2.0.1. . When R in position 5, 10, 15, 20 of porphyrin are replaced by group $CH_3C_6H_4$, it gives rise to 5, 10, 15, 20-tetra (*p*-tolyl) porphyrin, i.e., TPP.

The absorption spectra of the ground state of the film of $Pc^{2-}Ce^{IV}TPP^{2-}$ sublimated on a quartz substrate is displayed in Fig. 4.1.2.0.2., which shows the Soret band of the phthalocyanine and porphyrin moieties centered at 342 nm and 423 nm [205, 206, 209]. The two visible and near-infrared absorption bands in the regions 540 - 650 nm

and 700 - 900 nm were attributed to the phthalocyanine Q bands in the dimer, thought the first visible band probably contains a contribution of the porphyrin Q bands. These last bands generally appear around 540 - 630 nm in the spectra of Ce(IV) bis-porphyrins.

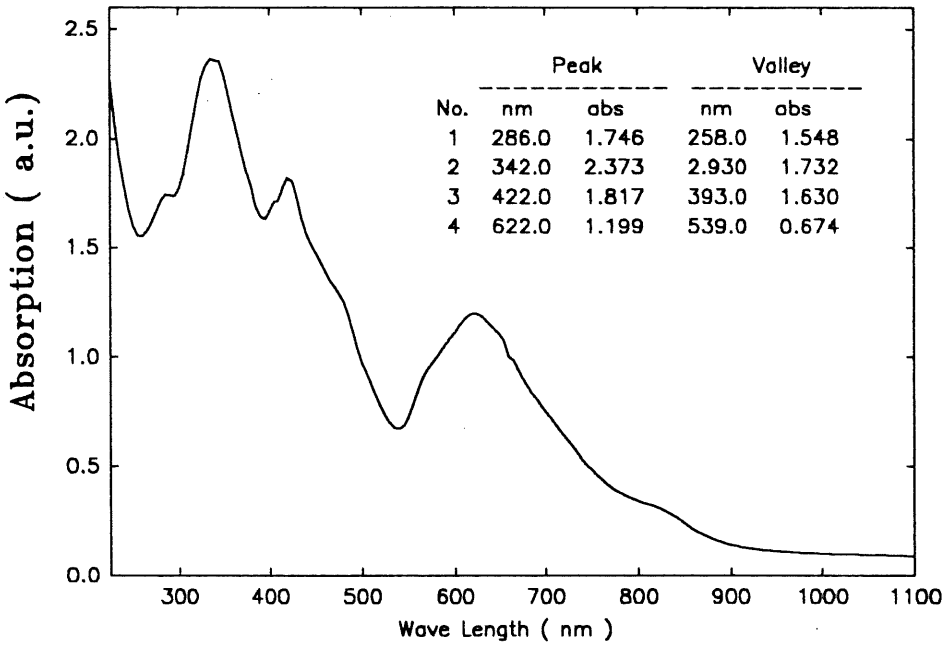

Figure 4.1.2.0.2. Ground State Absorption Spectrum of the Sublimated Film of the Heterodimer PcCeTPP on a Quartz Substrate.

4.1.2.1. Time-Resolved Four-Wave Mixing Experimental Results

TRFWM signals at the $k_s = k_1 - k_2 + k_3$ phase matching direction are shown in Fig. 4.1.2.1.1. ~ Fig. 4.1.2.1.4. by downward triangles as a function of delay time τ_d between the two synchronized pump pulses and the probe pulse. Different time scales of 10 ps, 100 ps, 500 ps, up to 1.3 ns are plotted. From the diagram having the smallest time scale one can see that the shortest relaxation component is still several times bigger than the system's resolution, i.e., the pump/probe pulse duration ($\approx$ 100 fs), which is determined by fitting the TRFWM data of a reference glass. The diagram with the longest time scale shows that the sublimated heterodimer system possesses

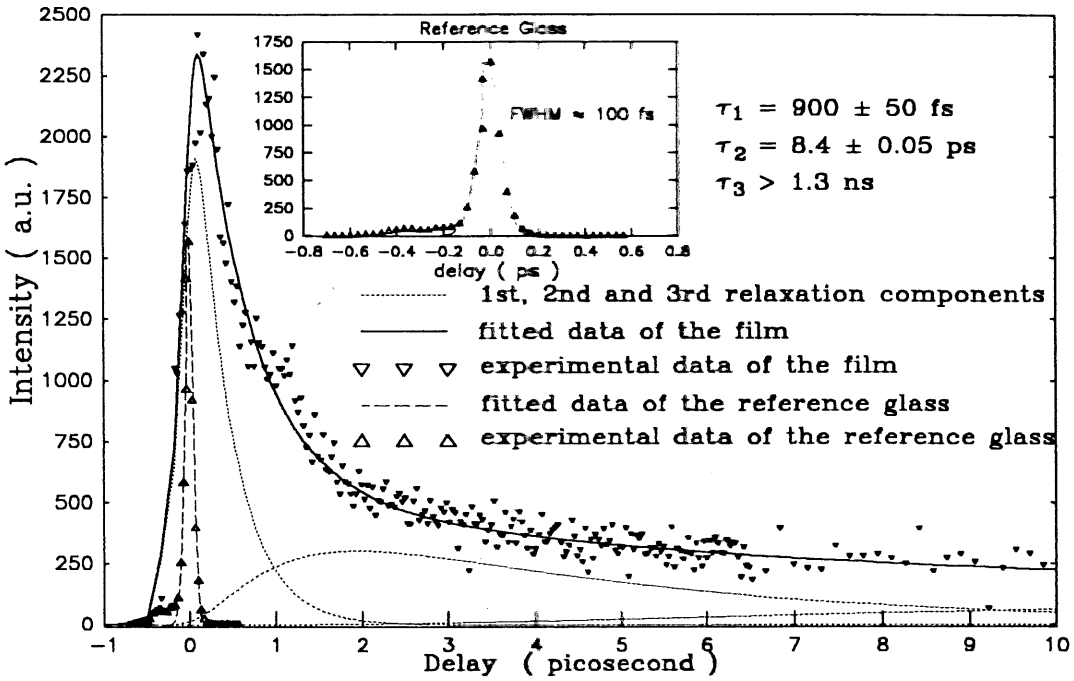

Figure 4.1.2.1.1. TRFWM Signal at Phase-Matching Direction as a Function of Probe-to-Pump Delay Time for the Sublimated Film of the Heterdimer PcCeTPP on a Quartz Substrate in a Time Scale up to 10 ps.

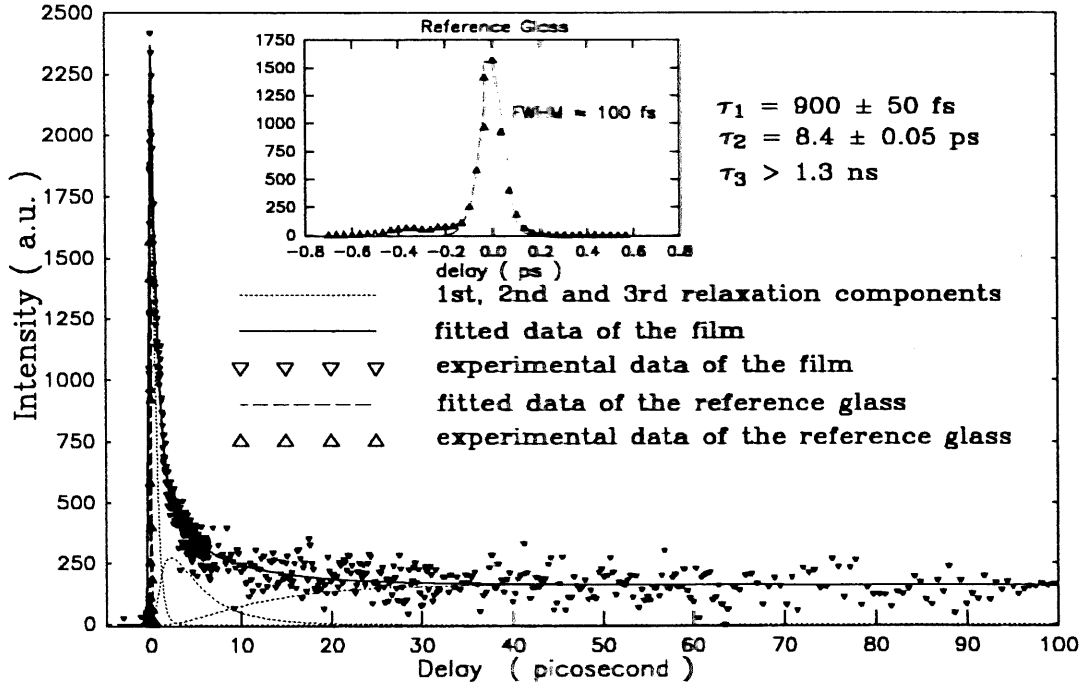

Figure 4.1.2.1.2. TRFWM Signal at Phase-Matching Direction as a Function of Probe-to-Pump Delay Time for the Sublimated Film of the Heterodimer PcCeTPP on a Quartz Substrate in a Time Scale up to 100 ps.

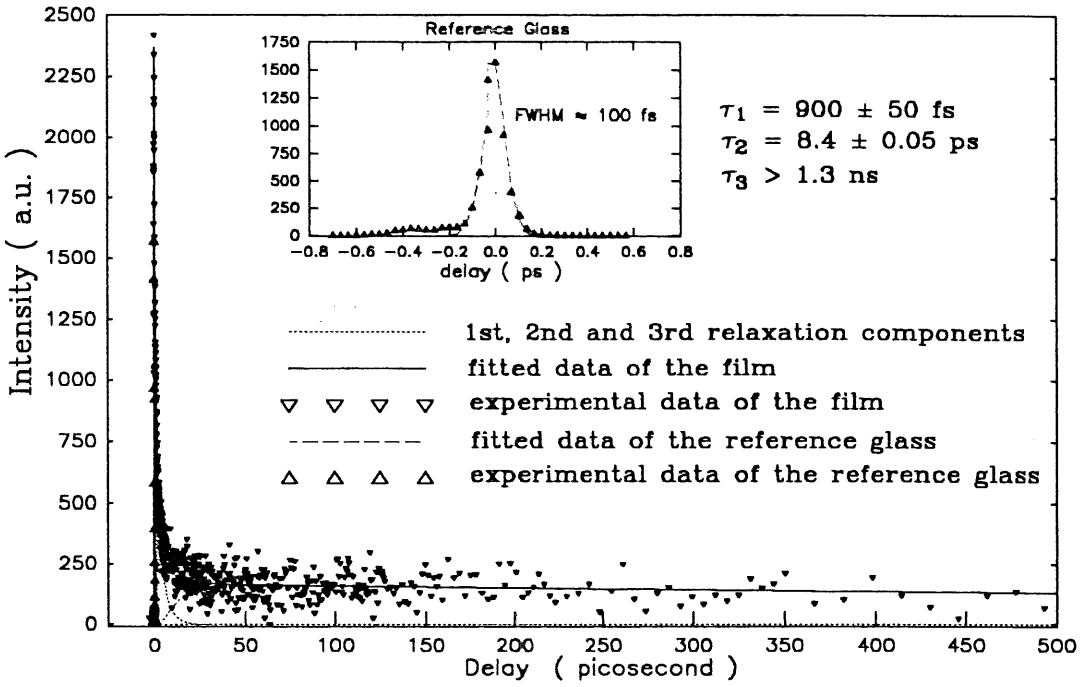

Figure 4.1.2.1.3. TRFWM Signal at Phase-Matching Direction as a function of Probe-to-Pump Delay Time for the Sublimated Film of the Heterodimer PcCeTPP on a Quartz Substrate in a Time Scale up to 500 ps.

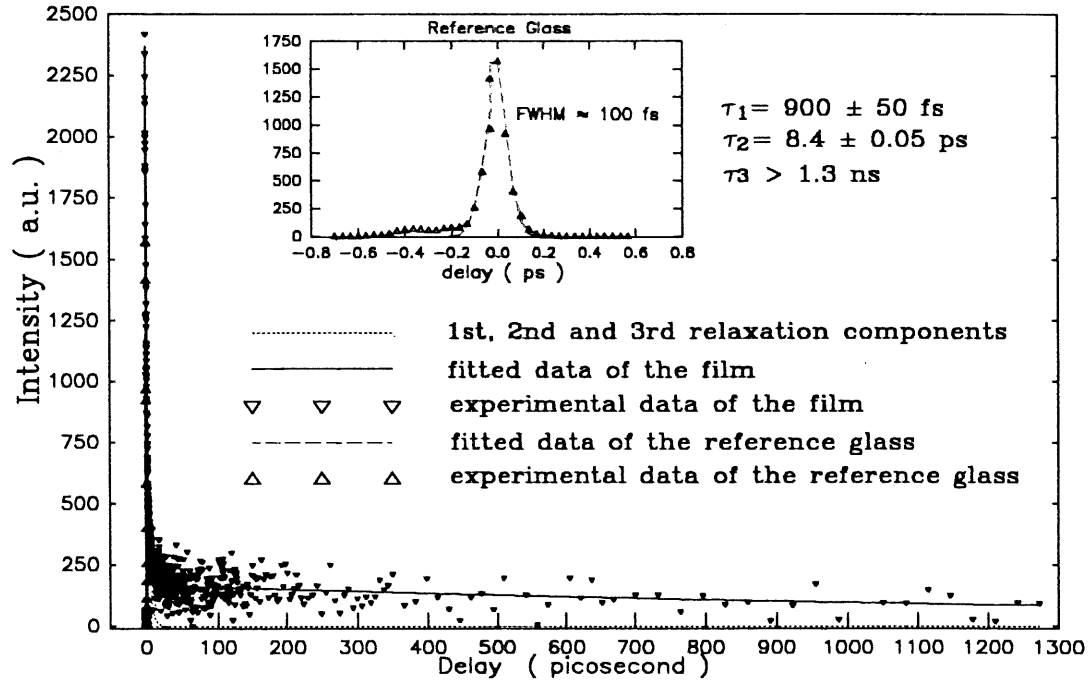

Figure 4.1.2.1.4. TRFWM Signal at Phase-Matching Direction as a Function of Probe-to-Pump Delay Time for the Sublimated Film of the Heterodimer PcCeTPP on a Quartz Substrate in a Time Scale up to 1.3 ns.

a very long response time much above the detection limit of our TRFWM system, i.e., 1.3 ns. In section 4.5., this will be proposed to be a photorefractive effect. The measured signals are free from coherent artifacts, which, coming from virtual electron excitation, would have appeared as a sharp spike at zero delay. The most interesting and the most conspicuous phenomenon that, to our best knowledge, has never been seen and reported on a thin film sample, is the appearance of the two oscillating components shown in Fig. 4.1.2.7.1. . Quite surprisingly, one can identify two correlated phonon modes that shift from one to the other in a relatively short period of time. This phenomenon will be studied in section 4.1.2.7. .

4.1.2.2. Transient Absorption Experimental Results

In order to attribute the different relaxation components of the data from the TRFWM experiment to the appropriate physical mechanisms, it is essential to compare the experimental results with those from transient absorption experiment. The lanthanide bisphthalocyanine with a metal ion M^{IV}, e.g., Ce^{IV}, having an electron configuration $4f^1 5d^1 6s^2$, is paramagnetic. In the transient absorption experiment [210], 620 nm pump pulse generates a first excited state S_1 with a population $P_1(t)$. This population has a longitudinal relaxation time $\tau_1 = T_1^{(TA1)} = ((T_1^{CT})^{-1} + (T_1^{ISC})^{-1})^{-1}$ = 1.2 ps. It relaxes with a time T_1^{CT} towards a charge transfer state CT having a population $P_2(t)$ and with a time T_1^{ISC} towards an excited triplet state T_1 having a population $P_3'(t)$. Finally the charge transfer state relaxes towards the ground state S_0 with a time $\tau_2 = T_1^{(TA2)}$ = 22 ps while the triplet excited state T_1 does so with a time $\tau_3 = T_1^{(TA3)}$ = 130 ps. These three values give rise to the second line in Table 4.1.2.9.1. . The related processes are depicted schematically in Fig. 4.1.2.2.1. (a) and summarized in the following schematic mechanisms:

$$^{S_0}\left[TPP^{2-}Ce^{IV}Pc^{2-}\right] \xrightarrow{h\upsilon} {}^{S_1}\left[TPP^{2-}Ce^{IV}Pc^{2-}\right]^*,$$

$$^{S_1}\left[TPP^{2-}Ce^{IV}Pc^{2-}\right]^* \xrightarrow{\tau_1=T_1^{(TA1)}} \begin{cases} \xrightarrow{T_1^{(CT)}} {}^{CT}\left[TPP^{2-}Ce^{III}Pc^{\bullet}\right]^* \\ \xrightarrow{T_1^{(ISC)}} {}^{T_1}\left[TPP^{2-}Ce^{IV}Pc^{2-}\right]^* \end{cases},$$

$$^{CT}\left[TPP^{2-}Ce^{III}Pc^{\bullet}\right]^* \xrightarrow{\tau_2=T_1^{(TA2)}} {}^{S_0}\left[TPP^{2-}Ce^{IV}Pc^{2-}\right],$$

$$^{T_1}\left[TPP^{2-}Ce^{IV}Pc^{2-}\right]^* \xrightarrow{\tau_3=T_1^{(TA3)}} {}^{S_0}\left[TPP^{2-}Ce^{IV}Pc^{2-}\right].$$

(4.1.2.2.1.)

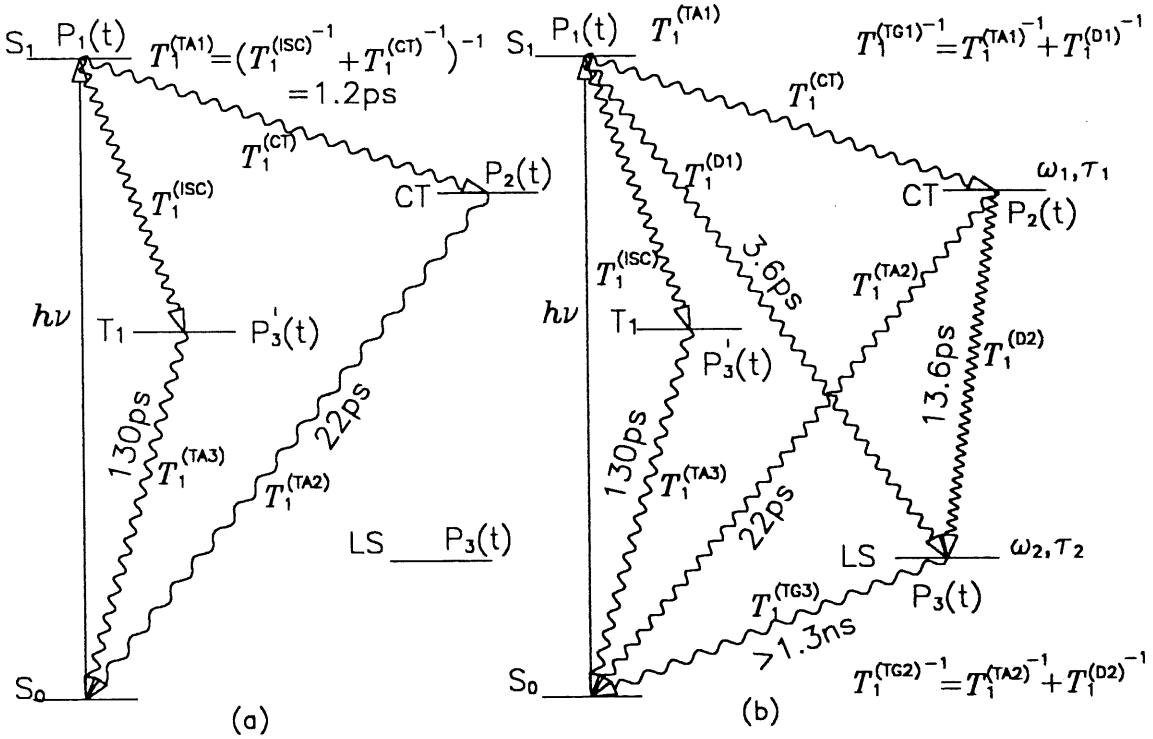

Figure 4.1.2.2.1. Schematic Presentation of the Relaxation Path of the Sublimated Heterodimer Film of PcCeTPP in the Experiment of (a): Transient Absorption (TA), and (b): Time-Resolved Four-Wave Mixing (TRFWM) and Two Correlated Vibration Modes ω_1,τ_1 and ω_2,τ_2.

4.1.2.3. Fitting of Time-Resolved Four-Wave Mixing Experimental Data

The information of the given molecular systems can be extracted from the TRNDFWM experimental data using the theoretical calculation carried out in Chapter 2., section 2.7. . This gives the following expression which we used to fit the experimental data:

$$S_v(\tau_d) = \int dt \left[\int d\tau \left(R_{\text{coupled phonon}}(\tau) + R_{3\text{population relaxation}}(\tau) \right) I_{\text{pump}}(t-\tau) \right]^2 \times$$
$$\times I_{\text{probe}}(t-\tau_d) =$$
$$= \int dt \left[\int d\tau \left(R_{\text{coupled phonon}}(\tau) + \sum_{i=1}^{3} \chi^{(3)}_{\text{pop.rel.,i}} P_i(\tau) \right) I_{\text{pump}}(t-\tau) \right]^2 I_{\text{probe}}(t-\tau_d) \qquad (4.1.2.3.1.)$$

where $\chi^{(3)}_{\text{phonon}}$ and $\chi^{(3)}_{\text{pop.rel.,i}}$ are the third-order nonlinear susceptibilities for the correlated phonon and for the *i*th component of population relaxation, I_{pump} and I_{probe} are the intensities of the pump light and probe light.

When treating the data without oscillation, only the response from a four-level system which relaxes from one to the other, is needed:

$$R_{3pop.rel.}(t) = \left[\chi_1^{(3)} + \chi_2^{(3)} \frac{1}{T_{12}} \frac{T_1 T_2}{T_1 - T_2} + \chi_3^{(3)} \left(\frac{1}{T_{13}} - \frac{1}{T_{12}} \frac{1}{T_{23}} \frac{T_1 T_2}{T_1 - T_2} \right) \frac{T_1 T_3}{T_1 - T_3} \right] e^{-t/\tau_1} + \left[-\chi_2^{(3)} \frac{1}{T_{12}} \frac{T_1 T_2}{T_1 - T_2} - \right.$$
$$\left. - \chi_3^{(3)} \frac{1}{T_{12}} \frac{1}{T_{23}} \frac{T_1 T_2}{T_1 - T_2} \frac{T_2 T_3}{T_2 - T_3} \right] e^{-t/\tau_2} + \chi_3^{(3)} \left[-\left(\frac{1}{T_{13}} - \frac{1}{T_{12}} \frac{1}{T_{23}} \frac{T_1 T_2}{T_1 - T_2} \right) \frac{T_1 T_3}{T_1 - T_3} + \frac{1}{T_{12}} \frac{1}{T_{23}} \frac{T_1 T_2}{T_1 - T_2} \frac{T_2 T_3}{T_2 - T_3} \right] e^{-t/\tau_3} . \qquad (4.1.2.3.2.)$$

where, in our specific case here, 1, 2, 3 denote singlet excited state S_1, charge transfer state CT and low-lying state LS respectively; $\tau_i = T_i$ is the relaxation time of the level

i, and T_{ij} is the relaxation time of the system from level i to j (i, j = 1, 2, 3). In complicated cases, more relaxation terms and more response functions can be added into (4.1.2.3.1). Nevertheless, this minimal four-level model is sufficient for our aim.

The routine procedure for data processing are: first fitting the experimental data of the reference (usually, using glass or fused quartz slide) to get the parameters about pump and probe pulses (FWHM, temporal shape, either gaussian, biexponential, or sech), then using these parameters to fit the experimental data of the sample by appropriate models.

The TRFWM signal was measured as a function of probe delay time with respect to the pump pulses. The experimental results are shown in Fig. 4.1.2.1.1. ~ Fig. 4.1.2.1.4., symbolized by the downwards triangles, with the different time scales of 10 ps, 100 ps, 500 ps and 1.3 ns. The full lines in Fig. 4.1.2.1.1. ~ Fig. 4.1.2.1.4. and a long dash line in Fig. 4.1.2.7.1. ~ Fig.4.1.2.7.8. refer to the contribution of the three excited state populations. The dotted lines in Fig. 4.1.2.1.1. ~ Fig. 4.1.2.1.4. represent the three population relaxation components respectively. The temporal shape of the pump-probe pulses, determined by measuring TRFWM signal on reference glass (quartz), is also shown in Fig. 4.1.2.1.1. ~ Fig. 4.1.2.1.4. . This shows that the time resolution of the TRFWM system is better than 100 fs.

The fit of the oscillating part of the experimental data will be treated in the next section. For the non-oscillating part, three relaxation components with time constants of 0.9 ps, 8.4 ps and 1.3 ns (beyond the limitation of our delay line) have been determined (the solid lines shown in Fig. 4.1.2.1.1. ~ Fig. 4.1.2.1.4., and long dash lines in Fig. 4.1.2.7.1. ~ Fig.4.1.2.7.8.). The three components, $T_1^{(TG1)}$ = 0.9 ps, $T_1^{(TG2)}$ = 8.4 ps and $T_1^{(TG3)}$ 1.3 ns, observed by fitting TRFWM experimental data, have been listed in the third line of the Table 4.1.2.9.1. .

From the table, we can see that the first two de-excitation components from time-resolved four-wave experiment are shorter than those from transient absorption experiment. The last one, however, is much longer. These findings reflect two important effects: ***diffusion contribution to the degrating process*** and ***the photorefractive effect in the sublimated film***.

In order to interpret the fitted experimental results and attribute them to suitable physical processes, in sections 4.1.2.4. - 4.1.2.6., we will propose and discuss three possible physical models, which will be used in sections 4.1.2.7. - 4.1.2.8. to explain the experimental phenomena.

4.1.2.4. Singlet Migration by Coupling of the Charge Transfer State between Neighbouring Molecules

We shall now discuss the various mechanisms by which these excitations can move in the solid state. This motion is of the Davydov type [211].

One possible mechanism, for the migration of the excited singlet state involves the charge transfer state. The strong electric dipole associated with the latter favours a strong intermolecular transfer coupling between the two species. In the TRFWM experiment, ultrashort pump pulse creates a transient charge transfer state in the cerium porphyrin phthalocyanine heterodimer $Pc^{2-}Ce^{IV}TPP^{2-}$, as indicated by transient absorption experiment. Because there exist microscopic crystalline domains in the sublimated film, as shown in Fig. 4.1.2.8.1., the molecules are expected to be arranged more regularly in these domains. This favours intersystem coupling among the neighbouring molecules. Due to the similarity between the neighbouring molecules, the excitation can be transferred quickly and effectively from one place to the other.

As depicted in Fig. 4.1.2.4.1. (A), at the beginning, molecule a_1^0 is in the ground state S_0. When excited by the pump $h\upsilon = hc/\lambda\,|_{\lambda = 620\ nm}$, it goes into the singlet excited state S_1, and its molecular configuration changed from a_1^0: $(Pc^{2-}Ce^{IV}TPP^{2-})^{S_0}$ to a_1: $(Pc^{2-}Ce^{IV}TPP^{2-})^{*S_1}$. During the de-excitation, if the system makes a transition to a charge transfer state (CT), the phthalocyanine moiety is oxidized from Pc^{2-} into a radical $Pc^{\cdot-}$, while the cerium ion is reduced from Ce^{IV} to Ce^{III}. This corresponding to transfer an electron from phthalocyaninePc^{2-} to Ce^{IV} through ring-to-metal charge transfer (RMCT). The molecule a_1: $(Pc^{2-}Ce^{IV}TPP^{2-})^{*S_1}$ has been transferred to a_1': $(Pc^{\cdot-}Ce^{III}TPP^{2-})^{*CT}$. The molecule looses an energy $E_{SCT} = E_{S_1} - E_{CT}$ in this process. If during the transition, a neighbouring molecule is already in a charge

transfer state a_2': $(Pc^{\cdot-}Ce^{III}TPP^{2-})^{*CT}$, as a result of the ring to metal charge transfer state coupling (RMCTSC) between the neighbouring molecules a_1 and a_2', the molecule a_2': $(Pc^{\cdot-}Ce^{III}TPP^{2-})^{*CT}$ can effectively re-absorb this energy $E_{SCT} = E_{S_1} - E_{CT}$, and transfer an electron back from cerium Ce^{III} to phthalocyanine $Pc^{\cdot-}$. After that, the molecule a_2': $(Pc^{\cdot-}Ce^{III}TPP^{2-})^{*CT}$ will get back to its excited singlet state a_2: $(Pc^{2-}Ce^{IV}TPP^{2-})^{*S_1}$. The above process can be summarized in the following scheme:

$$a_0:(Pc^{2-}Ce^{IV}TPP^{2-})^{S_0} \xrightarrow{h\nu} a_1:(Pc^{2-}Ce^{IV}TPP^{2-})^{*S_1}$$

$$\Downarrow \xrightarrow{\text{RMCTSC}} a_2':(Pc^{\cdot-}Ce^{III}TPP^{2-})^{*CT}$$

$$a_1':(Pc^{\cdot-}Ce^{III}TPP^{2-})^{*CT} \qquad \Downarrow$$

$$a_2:(Pc^{2-}Ce^{IV}TPP^{2-})^{*S_1}$$

$$\Downarrow \xrightarrow{\text{RMCTSC}}$$

(4.1.2.4.1.)

When the process is finished, the singlet excited state has been transferred from molecule a_1 to its neighbouring molecule a_2, and the molecule a_2: $(Pc^{2-}Ce^{IV}TPP^{2-})^{*S_1}$ is ready to start another similar cycle. In this way, the singlet excited state will migrate from molecule a_1 to molecule a_2, from a_2 to $\cdots$, $\cdots$ to a_j, from a_j to a_{j+1} etc., i.e.:

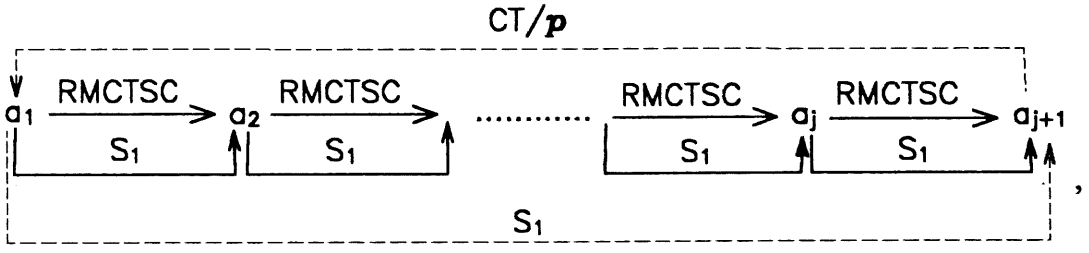

(4.1.2.4.2.)

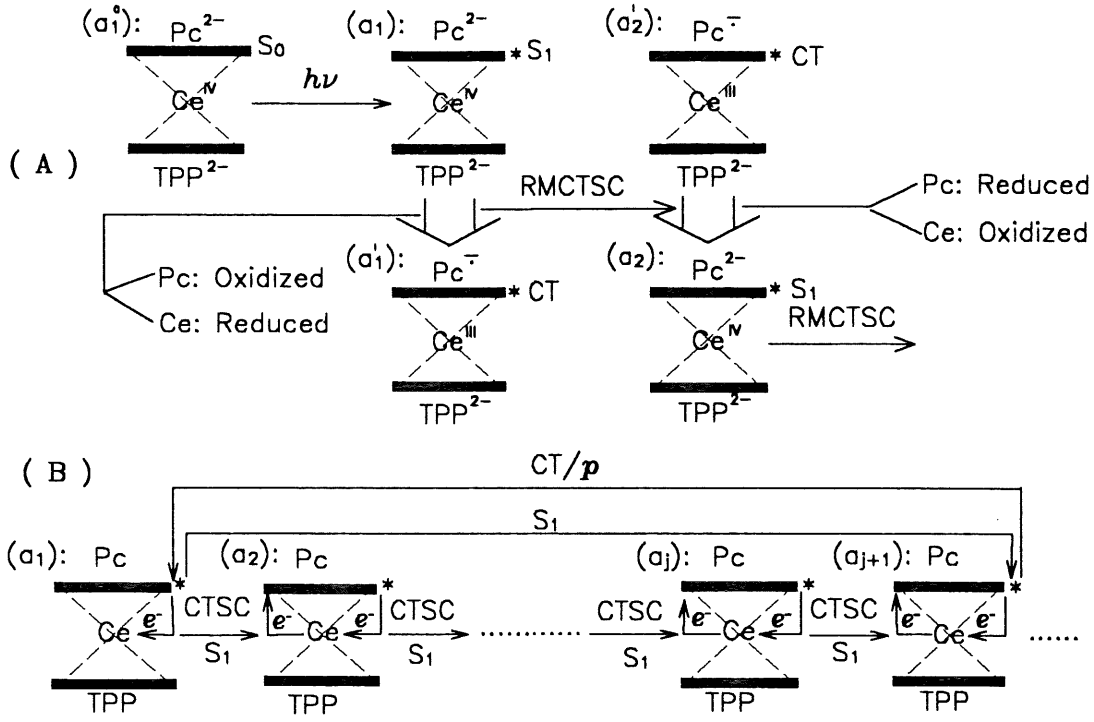

Figure 4.1.2.4.1. Singlet Excited State Migration by the Ring to Metal Charge Transfer State Coupling (RMCTSC) between the Neighbouring Molecules in the Sublimated Film of the Heterodimer $Pc^{2-}Ce^{IV}TPP^{2-}$.

or equivalently, a distant charge state/molecular dipole has been exchanged with a singlet excited state. We will see in the following sections, how this will contribute to the degrating process and eventually to a photorefractive effect in the sublimed film of the heterodimer $Pc^{2-}Ce^{IV}TPP^{2-}$.

Furthermore, the localized electron transfer during which electron moves between phthalocyanine moiety Pc^{2-} and the central cerium ion Ce^{IV}, will cause the system configuration changing between a_1: $(Pc^{2-}Ce^{IV}TPP^{2-})^{*S_1}$ and a_1': $(Pc^{-}Ce^{III}TPP^{2-})^{*CT}$. This is just the very origin of the two correlated phone mode shifting phenomenon, which will be discussed thoroughly in section 4.1.2.7. .

4.1.2.5. Charge Transfer State Migration by Spin-Orbit Coupling between the Neighbouring Molecules

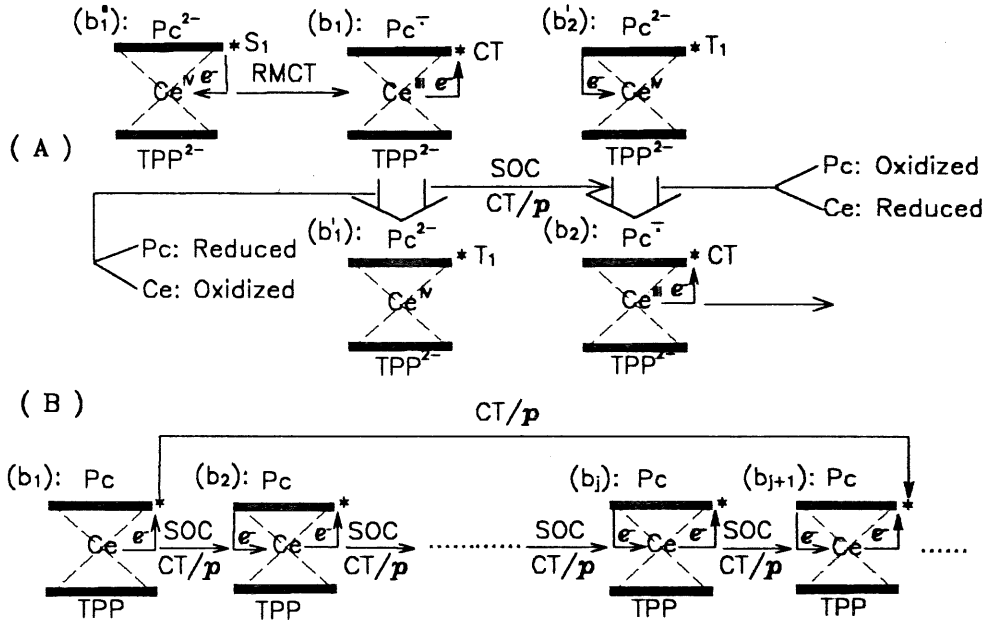

Figure 4.1.2.5.1. Charge Transfer State Migration by Spin-Orbit Coupling between the Neighbouring Molecules in the Sublimated Film of the Heterodimer $Pc^{2-}Ce^{IV}TPP^{2-}$.

The charge transfer state of the heterodimer $Pc^{2-}Ce^{IV}TPP^{2-}$ has a molecular configuration a_1': $(Pc^{-}Ce^{III}TPP^{2-})^{*CT}$ compared with all other molecular excited state configurations $(Pc^{2-}Ce^{IV}TPP^{2-})^{*}$. The phthalocyanine molecule in the CT state is a radical and the whole molecule is just equivalent to a dipole $\boldsymbol{p}$. Crystalline arrangement of the molecules makes it possible that the wave function overlap can occur between its neighbouring molecules. This mixing with the neighbour's excited state results in a strong coupling between them. As depicted in Fig. 4.1.2.5.1. (A), if a molecule b_1 in its charge transfer state b_1: $(Pc^{\bullet}Ce^{III}TPP^{2-})^{*CT}$ has a neighbouring molecule b_2 in its triplet state b_2': $(Pc^{2-}Ce^{VI}TPP^{2-})^{*T_1}$, then b_1 can make a transition from its charge transfer state CT to its triplet state T_1, by spin-orbit coupling (SOC) between the neighbouring molecules, and molecule b_2 can absorb the energy emitted by b_1, change its spin and molecular configuration to b_2: $(Pc^{\bullet}Ce^{III}TPP^{2-})^{*CT}$. Now the molecule b_2 is ready to start another similar cycle. In this way, the charge transfer state or

equivalently the molecular dipole p, will be transferred from its origin to a place far away, as summarized in (4.1.2.5.1.).

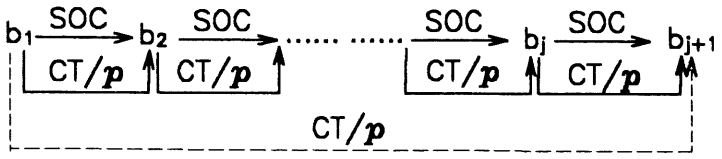

(4.1.2.5.1.)

It is believed that this molecular dipole migration contributes to the photorefractive effect observed in the sublimated film of the heterodimer.

4.1.2.6. Excitation Migration by Excitonic Coupling between the Neighbouring Molecules

Even without charge-transfer-state coupling and spin-orbit coupling between neighbouring molecules, the excitation can still be transferred by excitonic coupling between the molecules.

Analogous to singlet and triplet excitation migration, the excitonic excitation migration process is shown in Fig. 4.1.2.6.1., the excitation $h\upsilon = hc/\lambda\,|_{\lambda = 620\ nm}$ turns the molecule c_1^0: $(Pc^{2-}Ce^{IV}TPP^{2-})^{S_0}$ in the ground state S_0 into an excited one c_1: $(Pc^{2-}Ce^{IV}TPP^{2-})^{*S_1}$. Owing to the ordered arrangement of the molecules in the microscopic crystalline domains, which favours intermolecular interactions and the excitonic coupling between the neighbouring molecules, this excitation can be transferred to the neighbouring molecule, as shown in the following scheme:

$$c_0{:}(Pc^{2-}Ce^{IV}TPP^{2-}) \xrightarrow{h\nu} c_1{:}(Pc^{2-}Ce^{IV}TPP^{2-})^* \xrightarrow{EC} c_2{:}(Pc^{2-}Ce^{IV}TPP^{2-})^*$$

(4.1.2.6.1.)

When the process is completed, a portion of the energy E_{EC} has been transferred from the molecule c_1 to the neighbouring molecule c_2. Now c_2 is ready to start the next similar process, if it is feasible. In this fashion, the excitation will be transferred

rapidly and efficiently from one molecule to the other and finally far away from its original place, as summarized in Fig. 4.1.2.6.1. .

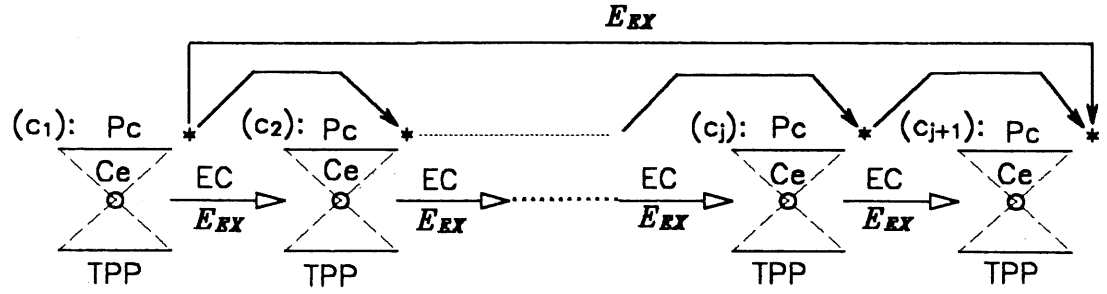

Figure 4.1.2.6.1. Excitation Migration by the Excitonic Coupling between the Adjacent Molecules in the Sublimated Film of the Heterodimer $Pc^{2-}Ce^{IV}TPP^{2-}$.

This excitonic excitation migration will also contribute to the degrating process and cause a shorter response in TRFWM, as we will see in the following sections. It is also important to the photorefractive effect in the sublimed film of the heterodimer $Pc^{2-}Ce^{IV}TPP^{2-}$.

4.1.2.7. Identification of Two-Correlated-Phonon Mode-Shifting Phenomenon

As mentioned in section 4.1.2.1., one of the most interesting phenomena observed in our TRFWM results on the sublimated film of the heterodimer $Pc^{2-}Ce^{IV}TPP^{2-}$ is that there is an oscillatory modulation superposed on the decaying curves. This modulation can not be fitted by any simple superposition of independent phonon modes, which would be the natural way to treat the phonon modes in most situations.

The oscillatory behaviour we have recorded in the TRFWM experiment, is shown in Fig. 4.1.2.7.1. . It is similar to what we have reported earlier in a crystal of conducting polymer α-$[BEDT\text{-}TTF]_2I_3$ [212] and in a crystal of ferroelectric $KTa_{0.93}Nb_{0.07}O_3$ [213, 214]. In the both cases, we observed very strong oscillations which were attributed to

librational mode for the former and to soft-polariton mode for the latter. In this case, we observed clearly two modulation periods, one with a lower frequency of about 30 cm^{-1} on left side of the curve (or a period of roughly 1.1 ps) and another with a higher frequency around 40 cm^{-1} (or a period of approximately 0.8 ps) which are shorter than a crossover time of 3 ps. The crossover time is in line with the decay time of the S_1 population or the rise time of the CT population. The amplitude of the modulation is also consistent with the 8.4 ps decay rate of the CT state. The oscillation signal is extremely difficult to be obtained in a sublimated thin heterodimer film compared with those of the big crystals of the organic conductor and the ferroelectric. Since a special noise reduction technique, called **Transparent Shuttle** (Figure 3.4.0.1., and section 3.5.), has been used, and, to get the signal ***S***, the background noise ***B*** has been substracted from the collected light *A* (equation (3.5.1.), what we got is definitely a real signal. Though oscillation signal of the heterodimer is not as perfect as those of the previous two samples, it is good and strong enough to be distinguished from the background. We confirmed this oscillation behaviour by having observed the same phenomena ***reproduceably*** in the sublimated samples made in different time for the same heterodimer compound.

In order to fit the results with a physically meaningful model, we first use independent phonon mode or any combination of them as we did before in references 212 - 214. According to (2.7.2.2.), for a coupling phonon mode with a frequency ω and a damping time τ, the corresponding response of a molecular system is:

$$R(t) = \chi_{ijkl}\, e^{-t/\tau}\, \frac{\sin(\omega t + \varphi)}{\omega} \qquad (4.1.2.7.1.)$$

where φ is a phase factor.

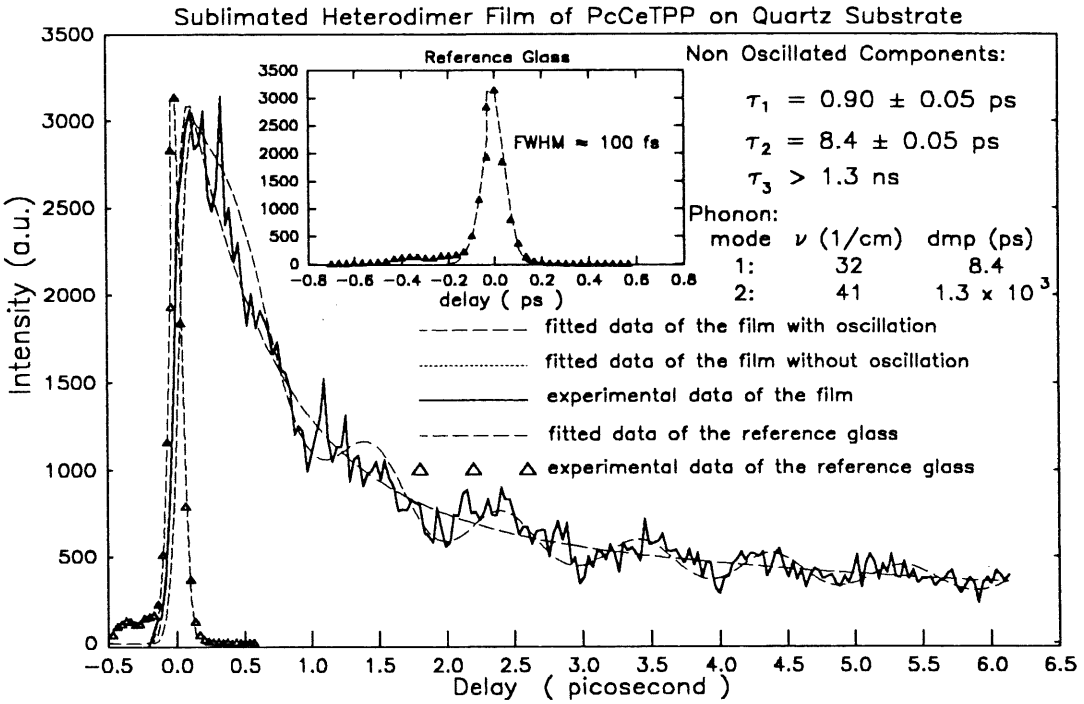

Figure 4.1.2.7.1. Oscillating Part of TRFWM Signal at Phase-Matching Direction as a Function of Pump-to-Probe Delay Time Fitted with Two Correlated Phonon Modes Shifting from One to the Other.

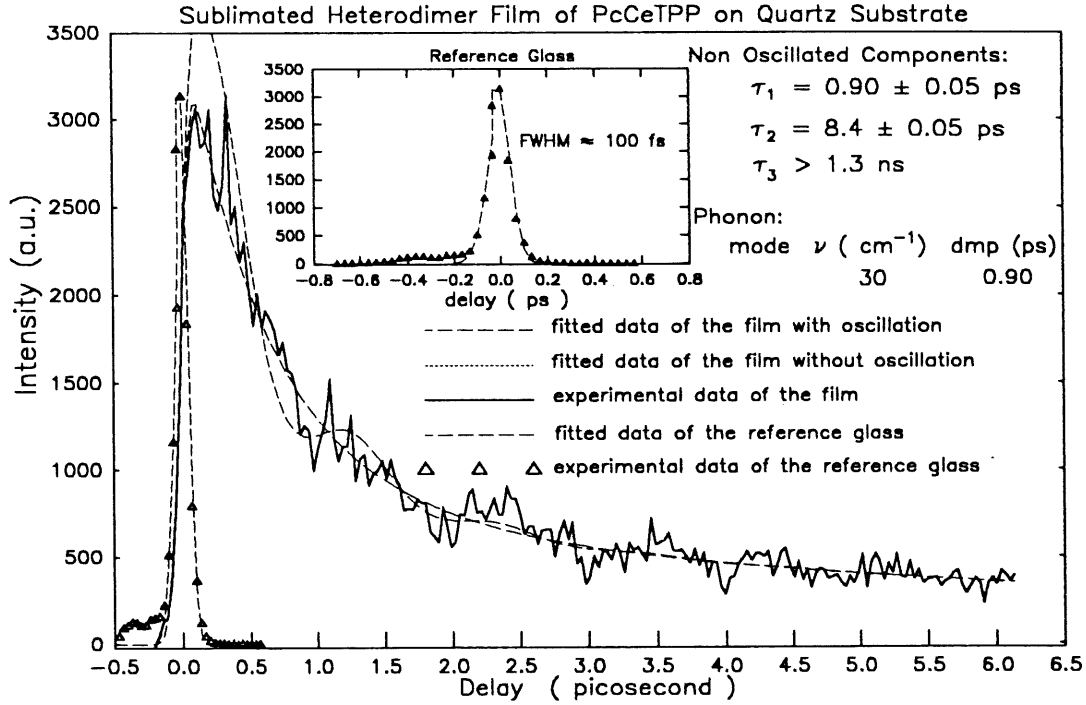

Figure 4.1.2.7.2. Oscillating Part of TRFWM Signal at Phase-Matching Direction as a Function of Pump-to-Probe Delay Time Fitted with a Single Phonon Mode of ν = 30 cm^{-1}, τ_{damp} = 0.90 ps.

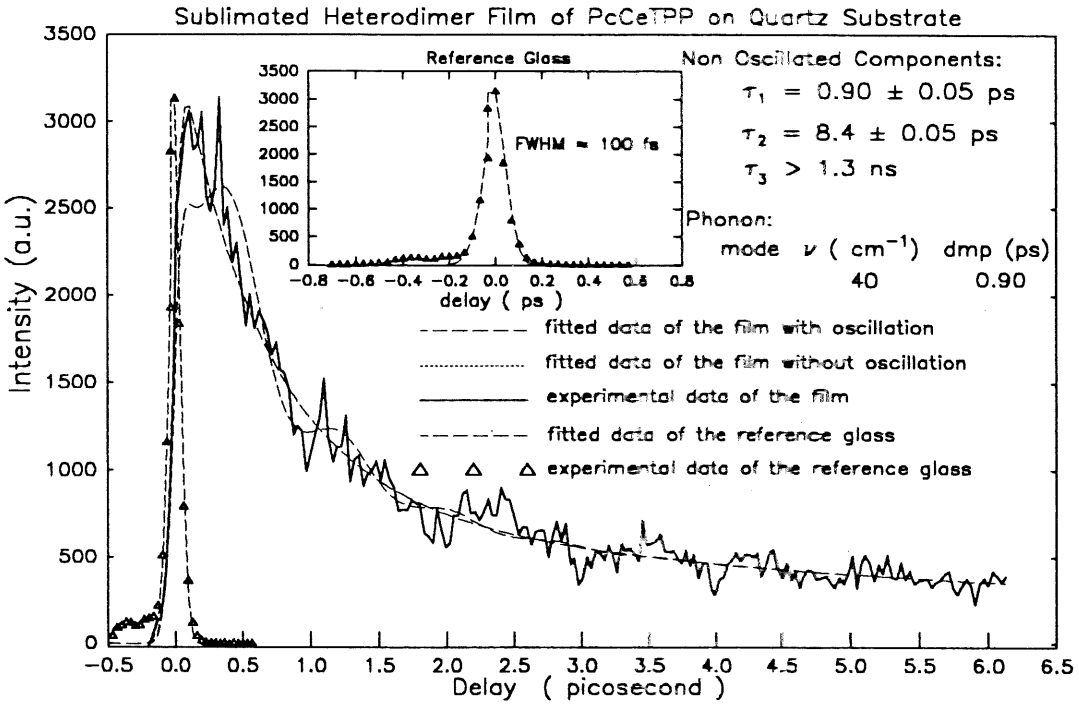

Figure 4.1.2.7.3. Oscillating Part of TRFWM Signal at Phase-Matching Direction as a Function of Pump-to-Probe Delay Time Fitted with a Single Phonon Mode of ν = 40 cm^{-1}, τ_{damp} = 0.90 ps.

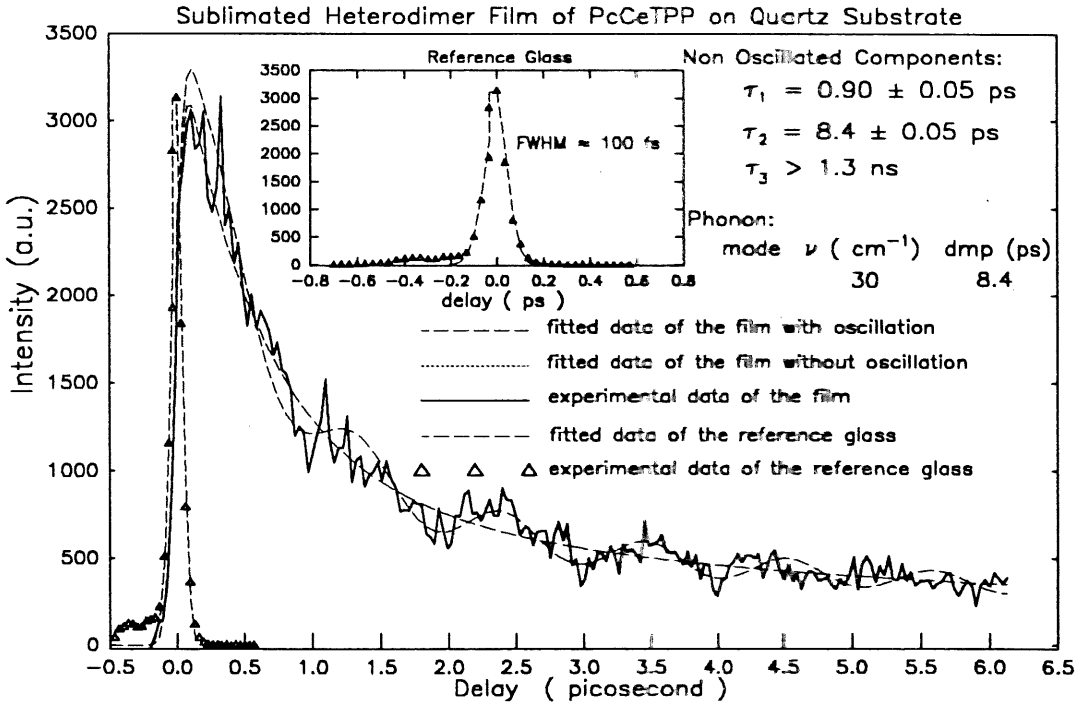

Figure 4.1.2.7.4. Oscillating Part of TRFWM Signal at Phase-Matching Direction as a Function of Pump-to-Probe Delay Time Fitted with a Single Phonon Mode of ν = 30 cm^{-1}, τ_{damp} = 8.4 ps.

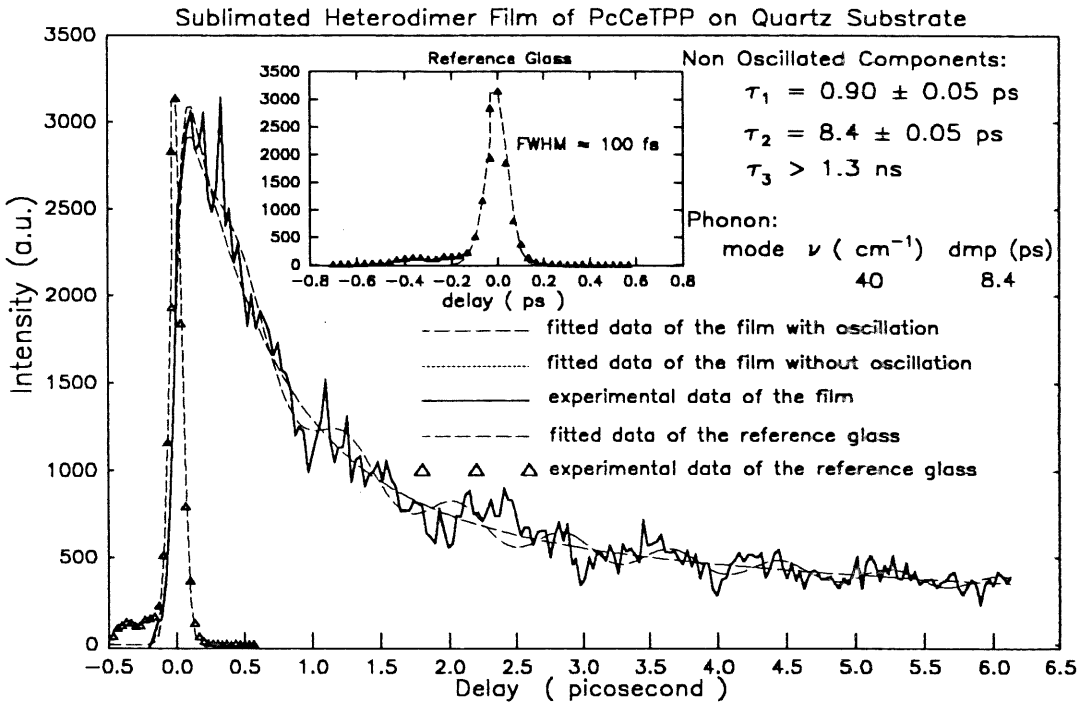

Figure 4.1.2.7.5. Oscillating Part of TRFWM Signal at Phase-Matching Direction as a Function of Pump-to-Probe Delay Time Fitted with a Single Phonon Mode of ν = 40 cm^{-1}, τ_{damp} = 8.4 ps.

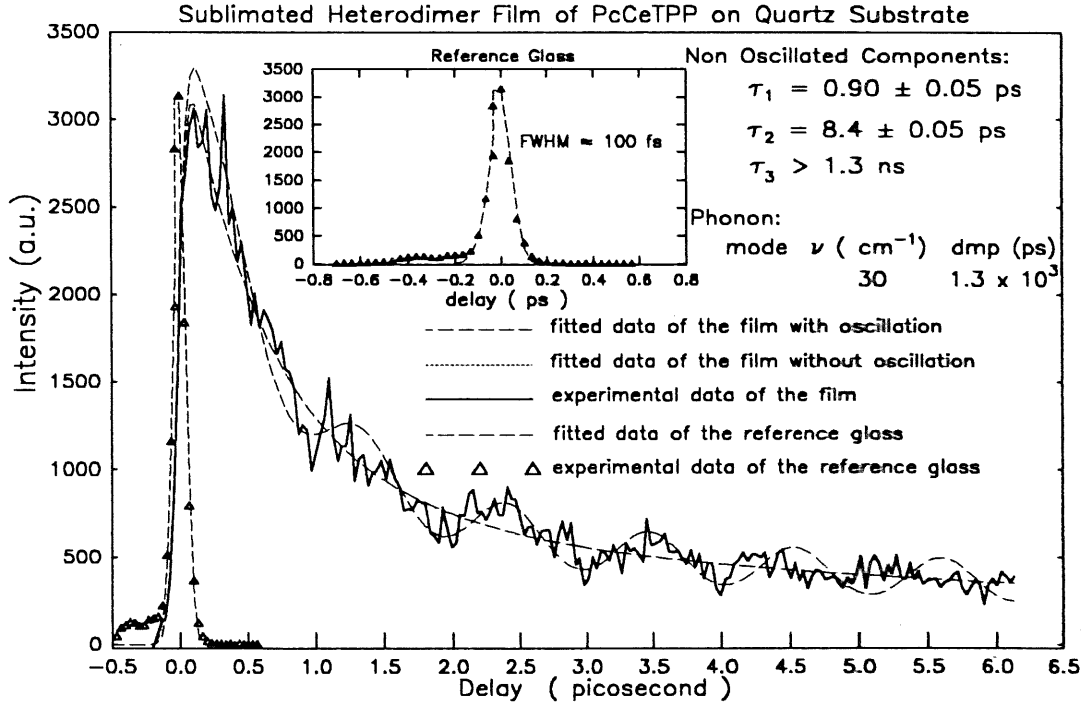

Figure 4.1.2.7.6. Oscillating Part of TRFWM Signal at Phase-Matching Direction as a Function of Pump-to-Probe Delay Time Fitted with a Single Phonon Mode of ν = 30 cm^{-1}, τ_{damp} = 1.3 ns.

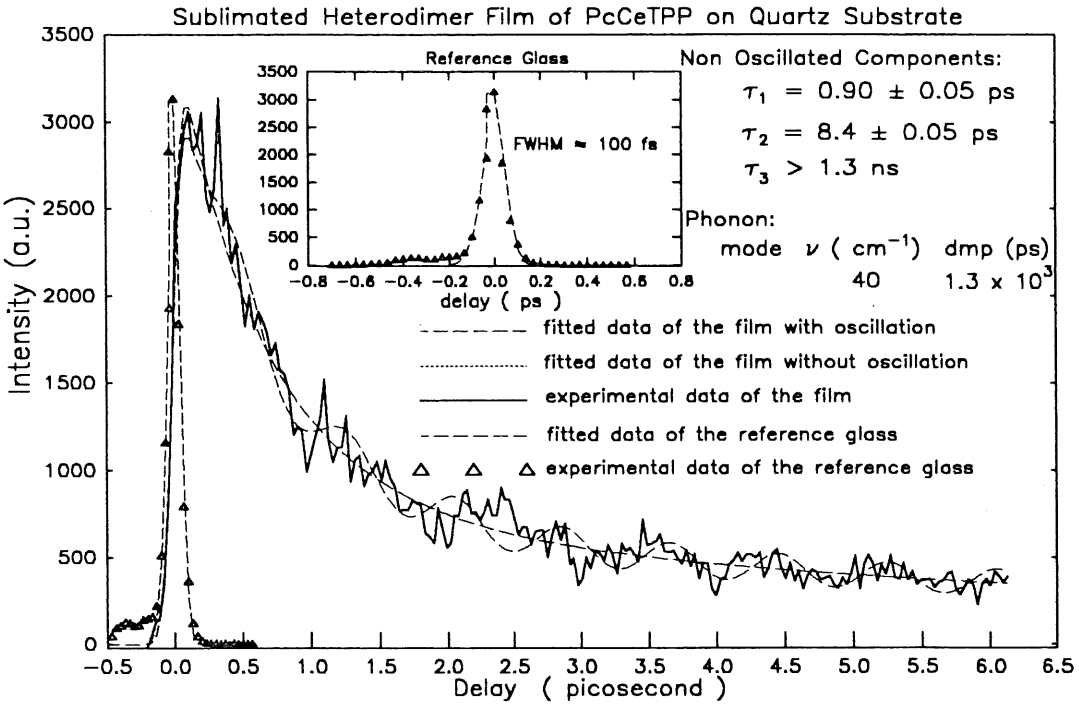

Figure 4.1.2.7.7. Oscillating Part of TRFWM Signal at Phase-Matching Direction as a Function of Pump-to-Probe Delay Time Fitted with a Single Phonon Mode of ν = 40 cm^{-1}, τ_{damp} = 1.3 ns.

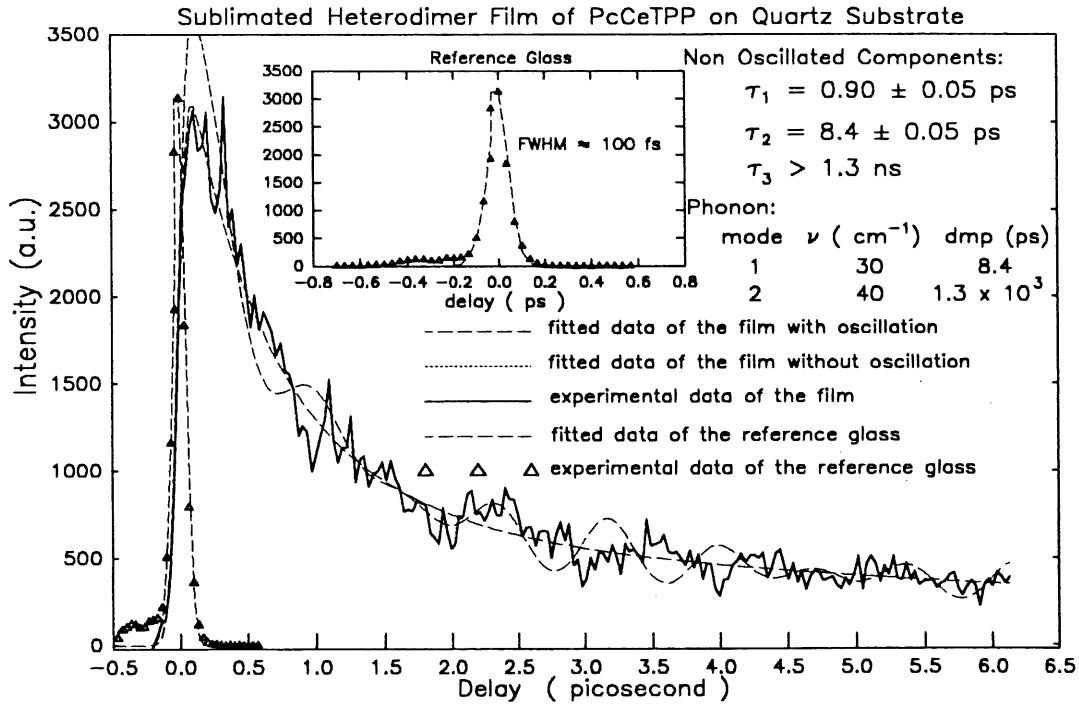

Figure 4.1.2.7.8. Oscillating Part of TRFWM Signal at Phase-Matching Direction as a Function of Pump-to-Probe Delay Time Fitted with a Summation of Two Independent Phonon Modes.

Then we suppose that the oscillating components, originate from the coupling of the excited states. During the fitting of the oscillating data, the parameters of the non-oscillating components are chosen to be fixed. Using (4.1.2.7.1.), for the independent phonon mode choosing $\upsilon_1 = 30\ cm^{-1}$, $\upsilon_2 = 40\ cm^{-1}$ (seen from Fig.4.1.2.7.1.), $\tau_1 = 0.90$ ps, $\tau_2 = 8.4$ ps, $\tau_3 = 1.3$ ns (three fitted components for non-oscillating data, the reason for such choosing will be explained later), the different combinations of these modes give rise to the results shown in Fig. 4.1.2.7.2. for (υ_1, τ_1), Fig. 4.1.2.7.3. for (υ_2, τ_1), Fig. 4.1.2.7.4. for (υ_1, τ_2), Fig. 4.1.2.7.5. for (υ_2, τ_2), Fig.4.1.2.7.6. for (υ_1, τ_3), and Fig. 4.1.2.7.7. for (υ_2, τ_3). From these figures we can see that, for the combination (υ_1, τ_1) or (υ_2, τ_1) only one or two cycles of the experimental data can be fitted. For the combination (υ_1, τ_2) or (υ_2, τ_2), just three cycles of the experimental curve can be fitted, for the combination (υ_1, τ_3) or (υ_2, τ_3), not more than three cycles of the right side of the experimental curve can be fitted. Therefore, it is clear that just one phonon mode is not enough for the fitting of the experimental data.

For the superposition of the two independent phonon modes, the response of a molecular system can be written as:

$$R(t) = \chi^{(3)}_{ijkl,a}\, e^{-t/\tau}\, \frac{\sin(\omega_a t + \varphi_a)}{\omega_a} + \chi^{(3)}_{ijkl,b}\, e^{-t/\tau}\, \frac{\sin(\omega_b t + \varphi_b)}{\omega_b}, \qquad (4.1.2.7.2.)$$

nevertheless, the result of the fitting is proved still unsatisfying. For example, for the combination of $(\upsilon_1, \tau_2) + (\upsilon_2, \tau_2)$, the fitted curve is shown in Fig. 4.1.2.7.8, is even worse than those fitted with a single phonon mode. Obviously, neither a single mode nor any combination of independent modes is an appropriate model for the fitting of the experimental data.

However, the facts that there exist microscopically ordered domains in the sublimated film of the heterodimer $Pc^{2-}Ce^{IV}TPP^{2-}$ (see Fig. 4.1.2.8.1., section 4.1.2.8.) and that during the de-excitation, there is an intramolecular charge transfer between phthalocyanine and central cerium ion in $Pc^{2-}Ce^{IV}TPP^{2-}$ and an intermolecular energy transfer between the neighbouring molecules, which will change the configuration of the system (as discussed in section 4.1.2.3. and section 4.1.2.4.),

impel us to consider the possibility of existing of correlated vibration modes. The previous observation of phonon modulation in TRFWM data on conducting polymer [212] and on ferroelectrics [194, 213, 214] suggests that dipolar excitations are prone to such effects. This shows that the CT state is definitely involved. This is not surprising as there should be considerable distortion of the molecule in the CT state and thus strong electron-phonon coupling. In fact, as show in Fig. 4.1.2.7.9. [210] (where

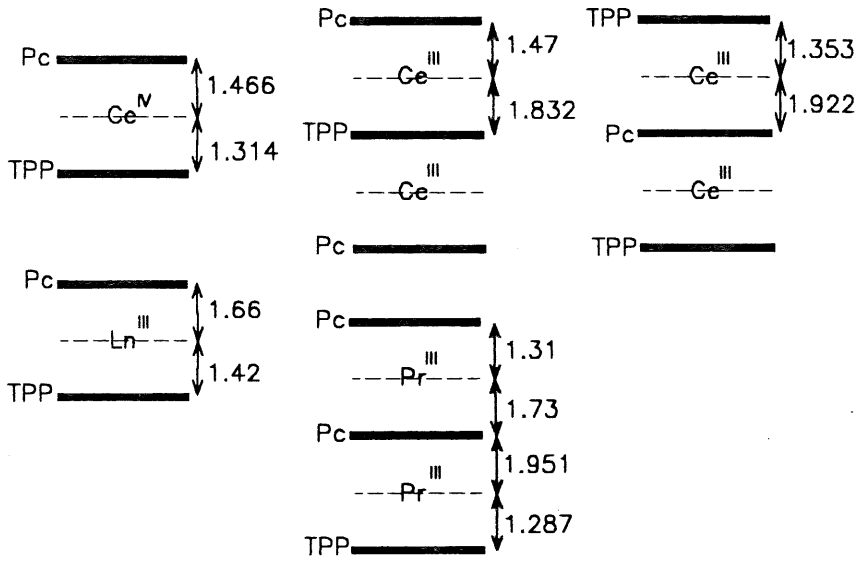

Figure 4.1.2.7.9. Schematic Presentation of Biplan and Triplan Mixturers of Ce^{IV} and Ln^{III} (Lanthanides) with Interplanar Distances In Å.

"Ln" denoting lanthanide), Fig 4.1.2.2.1. (b) and Eq. (4.1.2.2.1.), the S_1 state, the triplet state T_1 and the low-lying state LS have the configuration $Pc^{2-}Ce^{IV}TPP^{2-}$ with a ring-to-ring (or interplane) distance of about 2.78 Å while the CT state has the configuration $Pc^{\bullet-}Ce^{III}TPP^{2-}$ and the interplane distance in this configuration is increased to 3.08 Å . Therefore it is quite reasonable to think that the molecule of a configuration $Pc^{\bullet-}Ce^{III}TPP^{2-}$with bigger interplane distance could have lower vibration frequency and that of a configuration $Pc^{2-}Ce^{IV}TPP^{2-}$ with smaller interplane distance could have higher frequency. During the de-excitation, when the intramolecular electron transfer happens, the molecule will take one of these two configurations, and the total population density should be conserved. Moreover, of the many TRFWM experiments that we have performed on various organic thin film samples, it is only on this one compound that has a CT state that we have observed such modulation, reproducibly.

We thus believe that the phonon modulation is tied to the CT state. Since the excited singlet S_1 state is only a short lived state and the fitting of the oscillation attributed to this state has proved to be unsatisfied, the other possible state involving the oscillation could be the low-lying state LS. The major difference between the cases in polymer conductor [212] and in ferroelectric [213, 214] and our case is that in the former cases the electronic transition does not cause a change in the phonon mode, nevertheless in our case the electronic transition can change molecular configuration and give rise to a change in vibration mode even in a fixed temperature, which in the former cases can happen only when temperature has been changed. Therefore, in our case here, the phonon modes are no longer independent but related to the electronic transition and correlated to each other. This correlated-phonon mode-shifting phenomena in a sublimated thin film is, to the best of our knowledge, a brand-new observation that has never been reported on any atomic or molecular system.

Based on the above discussion, we now propose two reasonable models which fit the experimental data successfully. These tacitly assume that sizable molecular vibrations are triggered by the pump pulses through a Franck-Condon effect ($S_0 \rightarrow S_1$). To fit the two shifting vibration modes, instead of independent phonon modes, a ***correlated phonon mode model*** should be used. They also both shun any important direct contribution to the modulation from the S_1 population as its characteristic decay time is not evident in Fig. 4.1.2.7.1. or in the preliminary fits discussed above. The first model assumes that it is mostly if not exclusively the CT state that contributes to the modulation (short period) while the long period oscillations are associated with the S_1 population. Even though the S_1 vibrations need not directly be seen, their effect is transferred to the CT oscillations through the phase: the phase of the CT oscillations is inherited from the one of the S_1 oscillator at the time of its decay into the CT species. This effectively stretches the modulation period below roughly 2 ps. One gets the following:

$$R_{phonon}(t) = \chi_{n2}^{(3)} \int_0^t dt' \frac{P_1(t')}{T_1^{(CT)}} \sin\left[\omega_{n2}(t-t') + (\omega_{n1}t' + \varphi_{n1})\right] e^{-(t-t')/\tau_2} \qquad (4.1.2.7.3.)$$

where, $\chi_{n2}^{(3)}$ is the phonon third-order nonlinear susceptibility contribution of the charge transfer state, ω_{n1} and ω_{n2} are the frequencies of phonon mode 1 and mode 2,

φ_{n1} is a phase constant. Note that in this modelling one has $P_2(t) = \int_0^t dt' P_1(t') e^{-(t-t')/\tau_2} / T_1^{(CT)}$. The fits can also endure some amount of direct phonon contribution from P_1 of the form $\chi_{n1}^3 \sin(\omega_{n1} t + \varphi_{n1}) P_1(t)$. This model is simple but requires that the $Pc^{2-}Ce^{IV}TPP^{2-}$ configuration, with the shorter interplane distance, have the longer twisting period. The second model assigns the longer period to the CT state vibrations and the shorter period to the slowly rising third component, the LS state:

$$R_{\text{correl.phon.}}(t) = \chi_{n1}^{(3)} \int_0^t \frac{P_1(t')}{T_{12}} dt' \frac{\sin[\omega_{n1}(t-t') + \varphi_{n1}]}{\omega_{n1}} e^{-(t-t')/\tau_{n1}} + \\ + \chi_{n2}^{(3)} \int_0^t \frac{P_2(t')}{T_{23}} dt' \frac{\sin[\omega_{n2}(t-t') + \varphi_{n2}]}{\omega_{n2}} e^{-(t-t')/\tau_{n2}}, \qquad (4.1.2.7.4.)$$

where, $\chi_{n1}^{(3)}$ and $\chi_{n2}^{(3)}$ are the third-order nonlinear susceptibilities contributed by phonon mode 1 and mode 2, P_1 and P_2 are the populations of the excited singlet state S_1 and charge transfer state CT, $T_{12} = T_1^{(CT)}$ and $T_{23} = T_1^{(D2)}$ are the relaxation times of the system from the excited singlet state S_1 to charge transfer state CT and from charge transfer state CT to low lying state LS, ω_{n1}, ω_{n2}, τ_{n1}, τ_{n2} and φ_{n1}, φ_{n2} are the frequencies, damping times and phase constants of the phonon mode 1 and mode 2. The two integrations reflect the observation that phonon mode 1 shifts to phonon mode 2 but the total population keeps in constant, which is just what ***correlated phonon modes*** mean. Note that $P_2(t') / T_1^{(D2)}$ is the CT $\rightarrow$ LS transfer rate. This model presumes that the LS state contributes significantly to the modulation. This raises questions about the nature of this state. If it is the CT state that is solely responsible for the modulation, then the LS state has to involve metastable (deformed ?) CT molecules having a shorter phonon period, at grain boundaries for instance. If not, the long-lived LS state has a $Pc^{2-}Ce^{IV}TPP^{2-}$ configuration and has a strong modulating effect.

Both models have their shortcomings. But what clearly stands out is that the two phonon modes have to be correlated and gradually shift from one mode to the other.

During the fitting, the two frequencies are taken as $\nu_1^0 = 30$ cm^{-1} and $\nu_2^0 = 40$ cm^{-1} at the beginning, and the two damping times as $\tau_1^{pn} = \tau_2 = 8.4$ ps and $\tau_2^{pn} = \tau_3 = 1.3$ ns. ν_1^0 and ν_2^0 are roughly estimated from the experimental curve in Fig. 1.4.3.5.1. . The reason that the damping times are taken as the de-excitation time, is that the changing of the molecular configuration between $Pc^{\bullet}Ce^{III}TPP^{2-}$ and $Pc^{2-}Ce^{IV}TPP^{2-}$ happens during the de-excitation. Since $\tau_1 = 0.90$ ps can not be used even to fit partially the experimental curve by using single phonon mode, as shown in Fig. 4.1.2.7.2. and Fig. 4.1.2.7.3., the choice of the damping times should be made between the two de-excitation times, $\tau_2 = 8.4$ ps, and $\tau_3 = 1.3$ ns. Because $\tau_2 = 8.4$ ps is attributed to the charge transfer state with a configuration $Pc^{\bullet}Ce^{III}TPP^{2-}$ which may have a lower vibration frequency and $\tau_3 = 1.3$ ns is attributed to the charge transfer state with a configuration $Pc^{2-}Ce^{IV}TPP^{2-}$ which may have a higher vibration frequency (see section 4.1.2.9. for the details of the attribution), consequently, the possible combination of the two correlated phonon modes should be ($\nu_1^0 = 30$ cm^{-1} , $\tau_1^{pn} = \tau_2 = 8.4$ ps) and ($\nu_2^0 = 40$ cm^{-1}, $\tau_2^{pn} = \tau_3 = 1.3$ ns).

Using the second two correlated phonon mode model, formulated in (4.1.2.7.4.), fitting the experimental data leads to a thorough confirmation of such prediction: best fitted two correlated phonon modes with the frequencies and damping constants 32 cm^{-1} / 8.5 ps and 41 cm^{-1} / 1.3 ns were obtained. The fitted curve appears as a long dashed line in Fig. 4.1.2.7.1. . According to their damping times, frequencies and related molecular configurations, the first mode is attributed to the charge transfer state CT configuration, and the second mode to a low lying state LS configuration. The correlated phonon mode presentation is completely consistent with the picture of charge and energy transfer, discussed in section 4.1.2.3. and section 4.1.2.4. . This phenomenon can not be just a coincidence, because we have observed reproducibly the same behaviour using the same compound samples sublimated at different times by different apparatus, in the TRFWM experiments at different times. This phenomenon in a sublimated thin film, to our best knowledge, is ***the first time to be observed, studied and reported***. One of the characteristics of intermolecular or intramolecular

electron transfer in the lanthanide heterodimer or heterotrimer systems is that these processes are always accompanied with a changing in molecular configurations, which may cause a vibration mode changes in such kind of systems. Therefore, ***the correlated phonon mode shifting phenomena is only observable in a system relaxing with a changing in molecular configuration***.

One thing we should point out here is that the existence of two vibration modes 30 cm^{-1} and 40 cm^{-1} can be verified in principle by Raman spectroscopic techniques if the symmetry of the modes allows to do that. But, these vibration modes originate from the transient states created by the ultrashort laser pulse. Therefore, even if a high resolution Raman sytem is available, the light source of the system will not be suitable for such detection, because normal light source can not "create" a transient state in a molecular system. To solve this problem, we need a combination of different techniques.

4.1.2.8. Identification of Diffusion Contribution to the Degrating Process in the Sublimated Film of Heterodimer $P^{2-}Ce^{IV}TPP^{2-}$

It is known that there are resonant energy transfers between excited molecules and other excited or non-excited molecules in organic crystalline samples which are initiated by intermolecular interactions [211]. These are equivalent to an exchange of identity between two molecules in different excited states and thus to an effective motion of excitations. This mechanism leads to the migration of the molecular dipoles associated with the CT state and of other excitations from one place to the other, as discussed in section 4.1.2.3 and section 4.1.2.4. in the sublimated film of the heterodimer $Pc^{2-}Ce^{IV}TPP^{2-}$. The diffusion caused by such migrations may give rise to observable effects.

However, this migration is not detectable by all experimental techniques. In the situation at hand, the transient absorption and the four-wave mixing experiments behave quite differently. As we have already pointed out in section 1.1.5.3. , in the

TA experiment, since the sample is homogeneously illuminated and excited, the probe light is totally insensitive to any motion of the excitations as the sample retains its homogeneity. Nevertheless, in the FWM experiment the two pump beams create a sinusoidal-like excited modulation. This spatial excited modulation results in a population grating. If the excited species move, for example a half grating spacing, the grating will be washed out and no diffracted signal will be detected. In fact, in some case, even before moving a half grating spacing, the "washing out" has already happened, the excited species have lost their coherence somewhere and resulted in the lost of the grating. In this way, diffusion will lead to degrating and to a smaller effective relaxation rate.

In TRFWM experiment, optical pumping of an excited state leads to the formation of a transient grating. The decay of the TRFWM signal is due to the decay of the grating and is related to the relaxation of the excited states to the ground. There are many mechanisms that can cause degrating, for example intersystem relaxation (energy transfer between excited states), long-rang electron transfer processes, such as photorefractive effects, rotational and translational diffusion, librational motion, etc.. In the sublimated film of the heterodimer $Pc^{2-}Ce^{IV}TPP^{2-}$, if charge transfer and excitation migration can make a contribution to the degrating process, then, the related temporal form of the ultrafast nonlinear optical response $T_1^{(TG_j)}$ in the TRFWM/TRTG experiments should be:

$$T_1^{(TGj)} = \left(\frac{1}{T_1^{(TAj)}} + \frac{1}{T_1^{(Dj)}}\right)^{-1}, \quad j = 1, 2 \qquad (4.1.2.8.1.)$$

where j = 1, 2 denoting two different components.

Therefore, in addition to the longitudinal relaxation time $T_1^{(TAj)}$, j = 1, 2 detectable by transient absorption experiment, in time-resolved non-degenerate four-wave mixing experiment, charge transfer and excitation migration contribution to the degrating processes related to the de-excitation of the excited states, would give rise to a diffusion decay times $T_1^{(Dj)}$, j = 1, 2. in respect to grating decaying time $T_1^{(TGj)}$, j = 1, 2 [60]:

$$T_1^{(Dj)} = \left(\frac{1}{T_1^{(TGj)}} - \frac{1}{T_1^{(TA_j)}}\right)^{-1} = \frac{\Lambda^2}{4\pi^2 D_j}, \quad j = 1, 2 \qquad (4.1.2.8.2.)$$

where D_j, j = 1, 2 are the diffusion coefficients, Λ is a space period.

By (4.1.2.8.2.), the diffusion decay times can be calculated, consequently giving the results in the forth line of Table 4.1.2.9.1. . If the diffusion really contributes to the degrating process, then the diffusion coefficients should be in a right order of magnitude.

The diffusion coefficients D_j, j = 1, 2 can be estimated as:

$$D_j = \frac{\Lambda^2}{4\pi^2 T_1^{(Dj)}}, \quad j = 1, 2 \qquad (4.1.2.8.3.)$$

where Λ, in general case is interpreted as the grating spacing, which is given by:

$$\Lambda = \frac{\lambda_{pump}}{2 n_{sample} \sin\frac{\theta}{2}} \qquad (4.1.2.8.4.)$$

in which θ is the angle between the two pump beams and n_{sample} is the index of refraction of the sample.

From the geometry of our TRFWM experiment, by (4.1.2.8.4.) Λ is estimated to be 11 μm, from which the calculated diffusion coefficients D_1, D_2 would be much too large. However, it is clearly seen in Fig. 4.1.2.8.1. [207] that the typical size of a microdomain is about 0.2 μm. This is much smaller than the grating period. Presumably, the diffusing species would get trapped or quenched at the grain boundaries. Therefore, it is the averaged size of the microscopic crystalline domains that should be used for Λ instead of the calculated grating spacing period. Using this value, which is shown in the fourth entry of Table 4.1.2.9.1., in (4.1.2.8.3.) leads to the estimated diffusion coefficients, $D_1 = 2.8$ cm²/s and $D_2 = 0.74$ cm²/s. These are listed in the fifth entry of Table 4.1.2.9.1. . Compared to typical values of diffusion coefficients [215 - 226], $D_{CT} = 10$ cm²/s for the charge transfer process and $D_{ET} = 2$ cm²/s for the energy transfer process, the values we have obtained are quite reasonable.

This gives credibility to our hypothesis concerning the role of diffusion mechanisms in the degrating process.

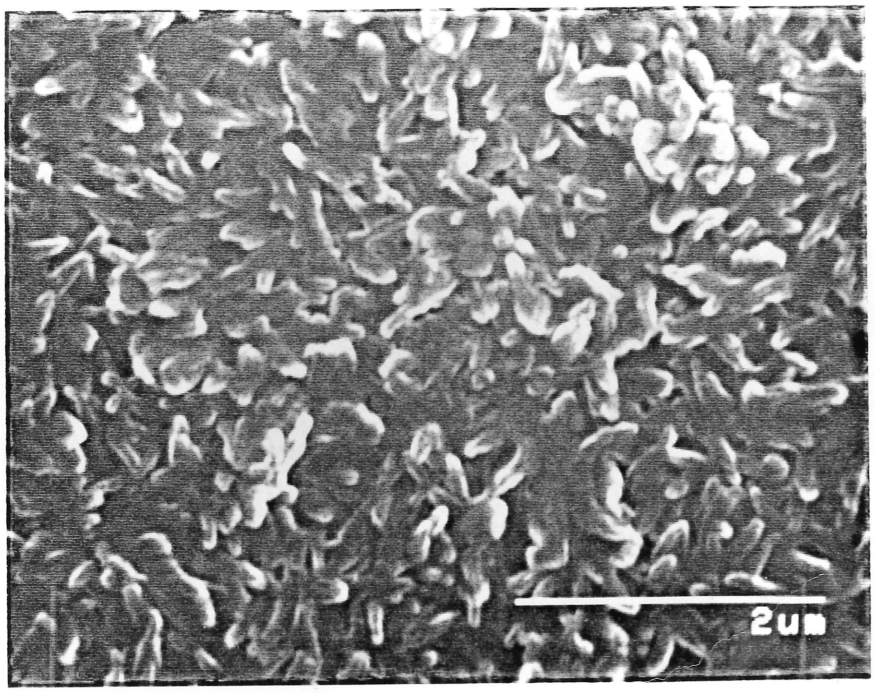

Figure 4.1.2.8.1. Electron Microscope Image of the Microstructure of the Sublimated Film of the Heterodimer $Pc^{2-}Ce^{IV}TPP^{2-}$.

4.1.2.9. Attribution of Different Components of the Time-Resolved Four-Wave Mixing Experimental Data.

To attribute the experimental data to different relaxation mechanisms and paths, comparing with the data from transient absorption for the sublimated film of the heterodimer $Pc^{2-}Ce^{IV}TPP^{2-}$ and identifying different de-excitation mechanisms are essential.

According to the previous analyses, the three time components observed in the TRFWM experiment on the sublimated film of the heterodimer $Pc^{2-}Ce^{IV}TPP^{2-}$,

Table 4.1.2.9.1.

Attribution of the Different Components from the Experiments of Transient Absorption (TA) and Time-Resolved Four-Wave Mixing (TRFWM) / Transient Grating (TG) for the Sublimated Film of the Heterodimer PcCeTPP

Components	1	2	3
Data from transient absorption experiment, $T_1^{(TA)}$[210]	$T_1^{(TA1)} = 1.2$ ps	$T_1^{(TA)} = 22$ ps	$T_1^{(TA3)} = 130$ ps
Data from TRFWM or transient grating (TG) experiment, $T_1^{(TG)}$	$T_1^{(TG1)} = 0.9$ ps	$T_1^{(TG2)} = 8.4$ ps	$T_1^{(TG3)} > 1.3$ ns
Diffusion time $\tau_d = T_1^{(D)} = (1/T_1^{(TG)} - 1/T_1^{(TA)})^{-1}$	$T_1^{(D1)} = 3.6$ ps	$T_1^{(D2)} = 14$ ps	
Averaged microscopic period Λ of the sublimated film	0.2 μm	0.2 μm	
Diffusion coefficient $D = (\Lambda^2/4\pi^2)/\tau_d$	2.8 cm²/s	0.74 cm²/s	

$T_1^{(TG1)}$, $T_1^{(TG2)}$ and $T_1^{(TG3)}$, and their various subcomponents can now be given a proper assignment. We summarize these findings (see Fig. 4.1.2.2.1. (b)). In the TRFWM experiment, the 620 nm pump pulses generate a singlet excited state S_1 with a population $P_1(t)$. This population has a total natural relaxation time $T_1^{(TA1)} = 1.2$ ps which is composed of the relaxation time $T_1^{(CT)}$ into a CT state with a population $P_2(t)$ and of $T_1^{(ISC)}$, assumed to be much smaller than $T_1^{(CT)}$, into a triplet excited state T_1. Because of the existence of singlet excitation migration and a diffusion time $T_1^{(D1)}$ to a low-lying state (LS) with long decay time, the net decay time $T_1^{(TG1)}$ is shorter, as shown by (4.1.2.7.1.), in Table 4.1.2.9.1. and in Fig. 4.1.2.2.1. (b). This component thus contains some undefined element of $T_1^{(ISC)}$ from the singlet excited state S_1 to the triplet excited state T_1, therefore the element of $T_1^{(TA3)} = 130$ ps from

the triplet excited state T_1 to the ground state S_0, and the element of diffusion $T_1^{(D3)}$ from the triplet excited state T_1 to the low lying excited state LS, but the experimental data from the transient experiment do not allow to make any such kind of confirmation of the attribution. The population $P_2(t)$ then relaxes with $T_1^{(TA2)}$ back to the ground state S_0 and, through the CT migration process having diffusion time $T_1^{(D2)}$ to the LS state, with a net decay time $T_1^{(TG2)}$. The longest component $T_1^{(TG3)}$, which is longer than the limit of the TRFWM detecting system of 1.3 ns, is related to the decay of the low lying excited state to the ground state. This long time response is, we believe, the signature of a photorefractive effect occurring during the de-excitation of the grating and, from the discussion on the diffusion mechanisms, involves the grain boundaries (LS state).

4.1.3. Summary

In this section we have demonstrated the time-resolved four-wave mixing studies on a sublimated film of the cerium porphyrin phthalocyanine sandwich mixed heterodimer, $Pc^{2-}Ce^{IV}TPP^{2-}$. To the best of our knowledge, this is ***the first TRFWM study on a sublimated film***. Excited by an ultrashort laser pulse of about 100 fs FWHM at 620 nm, three relaxation components with time constants of $\approx$ 0.90 ps, $\approx$ 8.4 ps, $\geq$ 1.3 ns, and two vibration modes with frequencies and damping times 32 cm^{-1} / 8.4 ps, 41 cm^{-1} / $\geq$ 1.3 ps were observed.

The existence of charge transfer in the heterodimer causes a change in the configuration of the molecule which gives rise to a novel phenomenon of two correlated phonon modes that shift from one to the other. ***This is the first time that a mode frequency shifting phenomenon is observed and reported on a thin film.*** Because the intermolecular or intramolecular electron transfer in the lanthanide heterodimer or heterotrimer systems is always accompanied with a variation of the molecular configurations, this may cause a vibration mode change in such kind of systems. Thereby, the correlated phonon mode shifting phenomena may only be

observable in a system relaxing with a molecular configuration changing, such as lanthanide heterodimer or heterotrimer systems.

The diffusion effects caused by the intramolecular electron transfer and excitation migration have been proved having an important contribution to the degrating process, giving rise to shorter response times in the TRFWM compared with the corresponding processes in transient absorption. They can not be ignored in the analysis of the decay process of a transient grating. Compared with the transient absorption data on the same sample, the relaxation processes were found to be due to the combination of relaxation, intermolecular charge transfer, molecular dipole migration and excitonic migration. The diffusion coefficients were estimated, taking the microscopic structure of the sublimated heterodimer film into consideration, to be 2.8 cm^2/s and 0.74 cm^2/s respectively. These values are consistent with the typical value of the coefficients for the charge and the excitation transfer processes. ***The diffusion contribution to the degrating process is identified for the first time.***

Due to the stacked formation of the heterodimer which favours the delocalization of the conjugated π-electrons, the third-order nonlinear optical susceptibilities have been greatly increased, compared with those of the free phthalocyanine, the mono-metallophthalocyanines, and bis- porphyrin phthalocyanines. The migration processes have effectively shortened the transient grating response time in the heterodimer and caused a relatively large third-order nonlinear optical susceptibility $\chi^{(3)}$, measured as 7.8×10^{-10} esu taking that of fused quartz as reference. The detailed calculation of the value of the $\chi^{(3)}$ will be given in section 4.5. .

Coupling of the charge transfer states and excitation migration by the excitonic coupling between the neighbouring molecules in the sublimated film of the heterodimer $Pc^{2-}Ce^{IV}TPP^{2-}$, are two crucial mechanisms that make intramolecular charge transfer and intermolecular energy transfer feasible, which are normally forbidden in organic crystals or compounds under normal conditions. The migration of charge and excitation finally leads to a long time response which is considered to be related to ***the photorefractive effect observed for the first time in an organic multimer thin film***. This will be discussed in section 4.6. .

4.2. Sublimated Film of Cerium Porphyrin Phthalocyanine Symmetric Trimer

$TPP^{2-}Ce^{III}Pc^{2-}Ce^{III}TPP^{2-}$

4.2.1. Experimental Aspects

The cerium-porphyrin-Phthalocyanine trimer, $TPP^{2-}Ce^{III}Pc^{2-}Ce^{III}TPP^{2-}$ was synthesised by the procedures given elsewhere [227, 228]. The compound was sublimated by vacuum evaporation under a pressure $2 \sim 5 \times 10^{-5}$ torr and a temperature about 450 °C, in the laboratory of Prof. Lê Dao, at *l'NRS-Energie/Matériaux de Varennes, Montréal, Québec, Canada* [209].

The ground state absorption spectrum of the sublimated film was recorded by a HITACHI U-2000 spectrometer. The sample was investigated using a time-resolved four-wave mixing system. The whole system is the same as reported in ref. [211, 212]. The system setup, the experimental procedures are the same as discribed in section 4.1.1.

4.2.2. Results and Discussion

The molecular structure of porphyrin, TPP, phthalocyanine, and the cerium-porphyrin-phthalocyanine trimer, $TPP^{2-}Ce^{III}Pc^{2-}Ce^{III}TPP^{2-}$ are depicted in Fig. 4.2.2.1. TPP, i.e., 5, 10, 15, 20 tetraphenylporphyrin, is formed by replacing C in the positions 5, 10, 15, 20 on the general porphyrin structure by group C_6H_5, and Pc, i.e., phthalocyanine, in position 5, 10, 15, 20 by N, and in 2/3, 7/8, 12/13, 17/18 sides by C_6H_6 (benzene cycle). Because of a strong ring to ring coulombic interaction, a face to face stacked sandwich formation occurs in the trimer.

Fig. 4.2.2.2. gives the ground state absorption spectrum from the UV, to the near-infrared of the trimer $TPP^{2-}Ce^{III}Pc^{2-}Ce^{III}TPP^{2-}$. The spectrum can be interpreted as

two entities of $(TPP^{2-}Ce^{III}\ Pc^{2-})^{-}$, which share the central phthalocyanine that interacts strongly with the two macrocycles [213]. Consequently, the Soret band and Q band of the central chromophore, phthalocyanine, are less intense than those components in heterodimer $TPP^{2-}Ce^{IV}\ Pc^{2-}$, and red shifted.

The TRFWM experimental data of the sublimated film of the trimer $TPP^{2-}Ce^{III}\ Pc^{2-}Ce^{III}\ TPP^{2-}$, are illustrated with different time scales in Fig. 4.2.2.3. ~ Fig. 4.2.2.6. and symbolized by the downward triangles. The fit of the experimental data was done using a three-excited-state population model This model is described in ref. [210], discussed in section 2.7., and given in Appendix I. This yields the full lines in Fig. 4.2.2.3. ~ Fig. 4.2.2.6.

Three measured relaxation components, $T_1^{(TG1)} = 0.37$ ps, $T_1^{(TG2)} = 15.3$ ps and $T_1^{(TG3)} > 1.3$ ns, are given in the third line of Table 4.2.2.1. A schematic representation of the different relaxatin paths for both TA and TRFWM is given in Figure 4.2.2.7. In the experiments, after the excitation $h\nu = hc/\lambda|_{\lambda = 620\ nm}$, the system is in an excited state (π,π^*) which can couple with the unpaired electrons from the Ce^{III}. Resulting from the unpaired electron on each of the two Ce^{III}, the excited states of the trimer can be either triplets (^3T) or quintuplets (^5Q), and the ground state of the trimer is found to be a triplet T_0. In the transient absorption experiment [214], the excitation from the ground state T_0 with the pump pulses at 620 nm populates a first excited state with a population of $P_1(t)$ in an excited triplet state ^3T. This population relaxes with a longitudinal relaxation time $\tau_1 = T_1^{(TA1)} = 0.7$ ps towards a second excited state, a quintuplet ^5Q having a population of $P_2(t)$. Then the excited quintuplet ^5Q population relaxes with a longitudinal relaxation time $\tau_2 = T_1^{(TA2)} = 37$ ps towards the ground state T_0 , as depicted in Fig. 4.2.2.7. (a). This gives rise to the values in the second line of Table 4.2.2.1., and is summarized in the following:

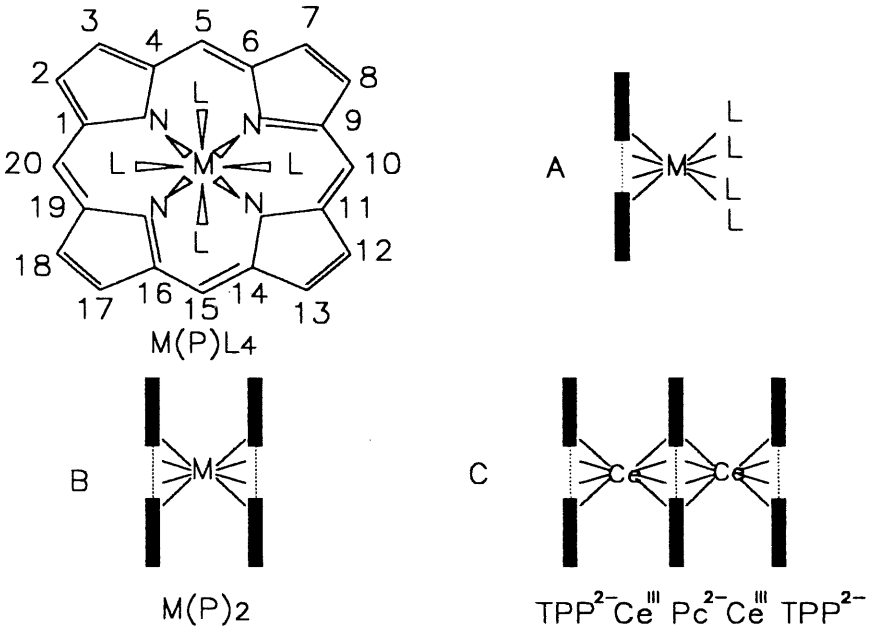

Figure.4.2.2.1. Molecular Structure of Octacoordinated Metal Monotetrapyrroles and Configurations with A: Monotetrapyrroles, B: Bistetrapyrroles $M(P)_2$ and C: Tristetrapyrroles, Symmetric Trimer $Pc(CeTPP)_2$, M=Lanthanide Ion.

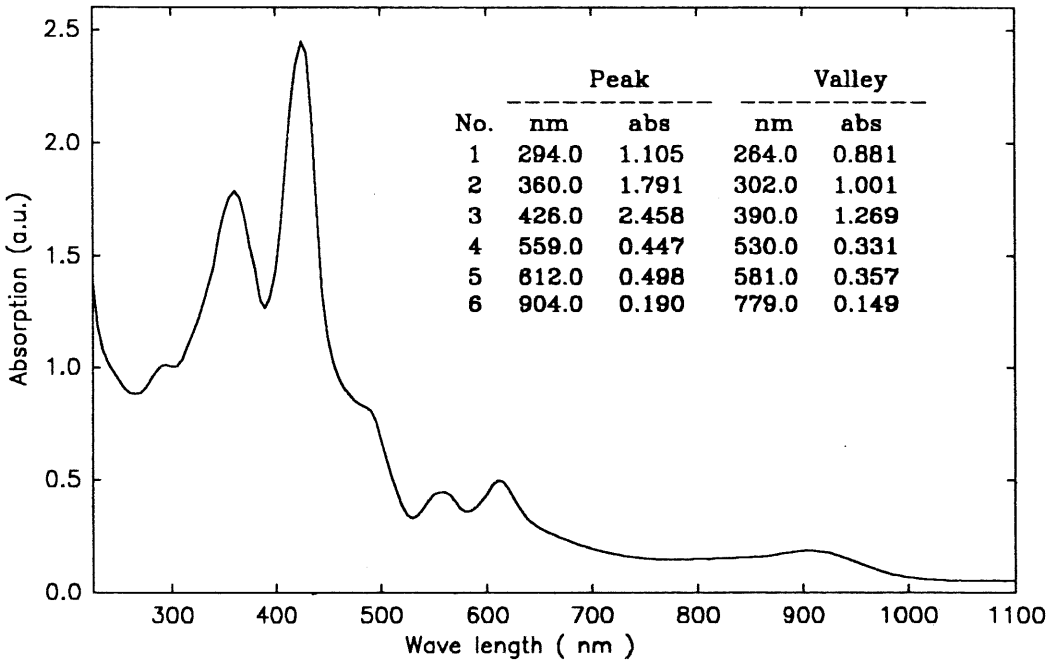

Figure 4.2.2.2. Ground State Absorption Spectrum of the Sublimated Film of the Timer $TPP^{2-}Ce^{III}Pc^{2-}Ce^{III}TPP^{2-}$ on a Quartz Substrate.

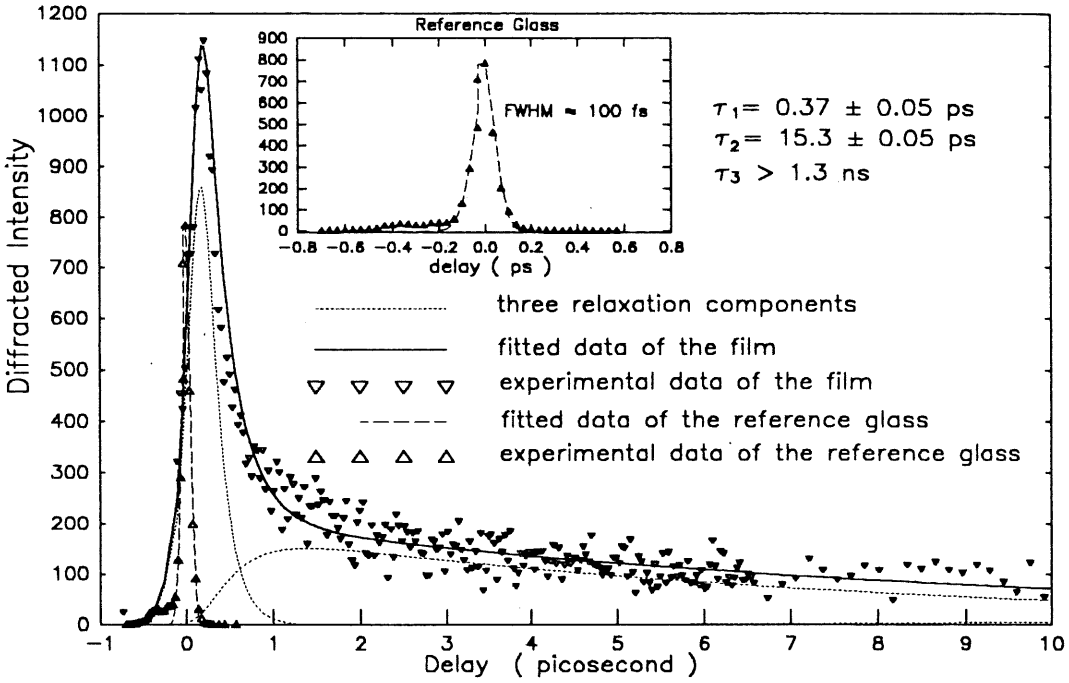

Figure 4.2.2.3. Diffracted TRFWM Signal as a Function of Probe-to-Pump Delay Time for the Sublimated Symmetric Trimer $Pc(CeTPP)_2$ on a Quartz Substrate with a Time Scale up to 10 ps.

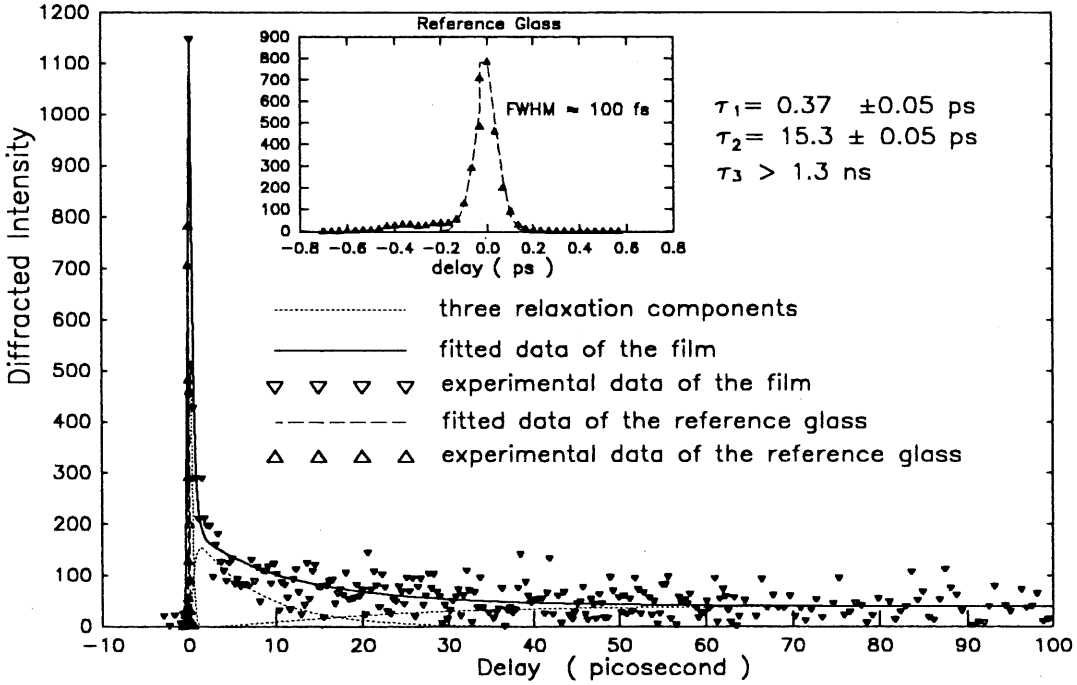

Figure 4.2.2.4. Diffracted TRFWM Signal as a Function of Probe-to-Pump Delay Time for the Sublimated Film of Symmetric Trimer $TPP^{2-}Ce^{III}Pc^{2-}Ce^{III}TPP^{2-}$ on a Quartz Substrate with a Time Scale up to 100 ps.

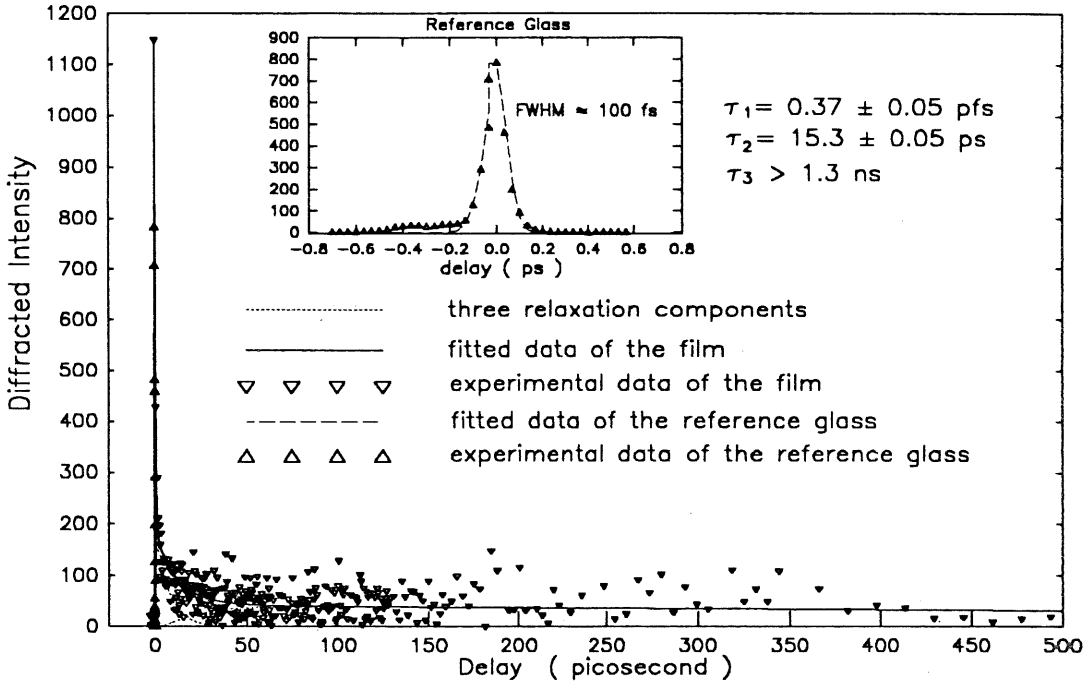

Figure 4.2.2.5. Diffracted TRFWM Signal as a Function of Probe-to-Pump Delay Time for the Sublimated Film of Symmetric Trimer $TPP^{2-}Ce^{III}Pc^{2-}Ce^{III}TPP^{2-}$ on a Quartz Substrate with a Time Scale up to 500 ps.

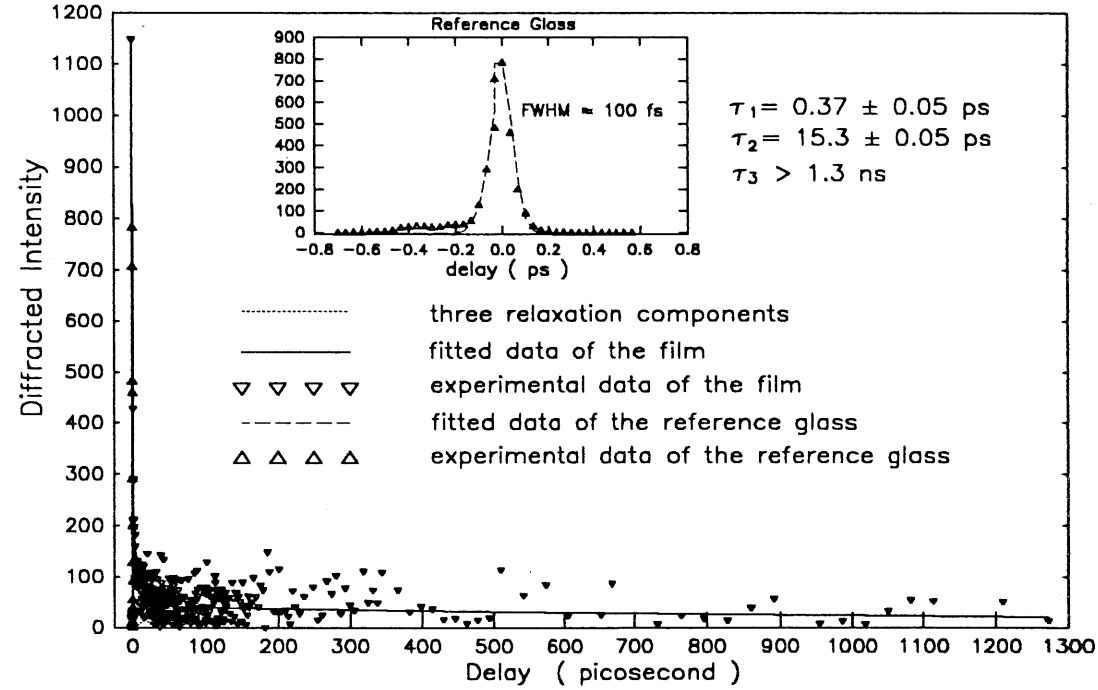

Figure 4.2.2.6 Diffracted TRFWM Signal as a Function of Probe-to-Pump Delay Time for the Sublimated Film of Symmetric Trimer $TPP^{2-}Ce^{III}Pc^{2-}Ce^{III}TPP^{2-}$ on a Quartz Substrate with a Time Scale up to 1.3 ns.

$$
\begin{aligned}
&{}^{T_0}\left[TPP^{2-}Ce^{III}Pc^{2-}Ce^{III}TPP^{2-}\right] \xrightarrow{h\upsilon} {}^{3T}\left[TPP^{2-}Ce^{III}Pc^{2-}Ce^{III}TPP^{2-}\right]^{*},\\
&{}^{3T}\left[TPP^{2-}Ce^{III}Pc^{2-}Ce^{III}TPP^{2-}\right]^{*} \xrightarrow{\tau_1} {}^{5Q}\left[TPP^{2-}Ce^{III}Pc^{2-}Ce^{III}TPP^{2-}\right]^{*}, \quad (4.2.2.1.)\\
&{}^{5Q}\left[TPP^{2-}Ce^{III}Pc^{2-}Ce^{III}TPP^{2-}\right]^{*} \xrightarrow{\tau_2} {}^{T_0}\left[TPP^{2-}Ce^{III}Pc^{2-}Ce^{III}TPP^{2-}\right].
\end{aligned}
$$

At first glance, as shown in Table 4.2.2.1., the differences between the results from the transient absorption experiment and those from the time-resolved four-wave mixing, seem incompatible. Nevertheless, as we have discussed in [229, 230] for the heterodimer and for the symmetrical dimer and trimer in [231], in the symmetric trimer $TPP^{2-}Ce^{III}Pc^{2-}Ce^{III}TPP^{2-}$ there exists energy transfer processes. Taking this point into consideration, the fact that the first and the second components in the third line of Table 4.2.2.1. are shorter than those in the second line of the table, is just an indication of existence of excitation migration in this trimer. In addition to the TA relaxation paths with decaying rate $T_1^{(TAj)}$, $j=1, 2$ the excitation migration through excitonic coupling between neighbouring molecules contributes to the de-population processes of the excited states and gives rise to diffusion decay times $T_1^{(Dj)}$, $j=1, 2$ in (4.1.2.8.2.), yielding a total grating decaying time $T_1^{(TGj)}$, $j=1, 2$ in (4.1.2.8.1.). From (4.1.2.8.1.) and (4.1.2.8.2.), the diffusion decay times can be calculated, consequently giving the results in the fourth line of Table 4.2.2.1. . The diffusion coefficients $D_j(\Lambda)$, $j=1, 2$ can be estimated by using Equation (4.1.2.8.3.).

From the electronic scanning microscope image of the sublimated film of the trimer $TPP^{2-}Ce^{III}Pc^{2-}Ce^{III}TPP^{2-}$, as shown in Fig. 4.2.2.8., it can be seen that the averaged size of the microscopic crystalline domain is about 0.3 μm. This defines the value of Λ used in (4.1.2.8.3.) and shown in the fifth line of Table 4.2.2.1. . The resulting diffusion coefficients are given in the sixth line of Table 4.2.2.1.: D_1 = 30 cm²/s and D_2 = 0.87 cm²/s. These values are quite typical for the diffusion coefficients [215 - 226].

Table 4.2.2.1.

Attribution of the Different Components from the Experiments of Transient Absorption (TA) and Time-Resolved Four-Wave Mixing (TRFWM) / Transient Grating (TG) of the Sublimated Trimer Film $Pc(CeTPP)_2$.

Components	1	2	3
Data from transient absorption experiment, $T_1^{(TA)}$ [210]	$T_1^{(TA1)} = 0.7$ ps	$T_1^{(TA2)} = 37$ ps	
Data from TRFWM or transient grating (TG) experiment, $T_1^{(TG)}$	$T_1^{(TG1)} = 0.37$ ps	$T_1^{(TG2)} = 15.3$ ps	$T_1^{(TG3)} > 1.3$ ns
Diffusion time $\tau_d = T_1^{(D)} = (1/T_1^{(TG)} - 1/T_1^{(TA)})^{-1}$	$T_1^{(D1)} = 0.77$ ps	$T_1^{(D2)} = 26.2$ ps	
Averaged microscopic period Λ of the sublimated film	0.3 μm	0.3 μm	
Diffusion coefficient $D = (\Lambda^2/4\pi^2)/\tau_d$	30 cm^2/s	0.87 cm^2/s	

According to the above analysis, the three observed components in the TRFWM experiment, $T_1^{(TG1)}$, $T_1^{(TG2)}$ and $T_1^{(TG3)}$ can be attributed as follows, as shown in Fig.4.2.2.7. .

The two 620 nm pump pulses generate a triplet excited state ^3T with a population $P_1(t)$. This population has two degrating channels, one with $\tau_1 = T_1^{(TA1)} = 0.7$ ps relaxes into a quintuplet state ^5Q with a population $P_2(t)$, the other, related to excitation migration, with $T_1^{(D1)} = 0.77$ ps relaxes towards a low lying state (LS) with a population $P_3(t)$. The population $P_2(t)$ in ^5Q state furthermore has two degrating paths, one with $\tau_2 = T_1^{(TA2)} = 37$ ps relaxes towards the ground state T_0, the other with $T_1^{(D2)} = 26.2$ ps relaxes towards the low lying state LS. Obviously, the degrating in the second path is a little faster than the first one.

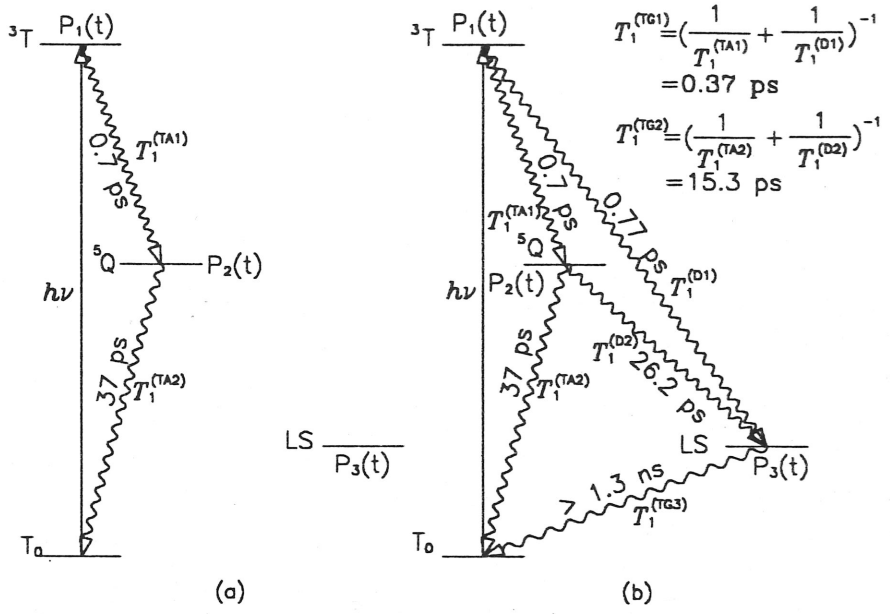

Figure 4.2.2.7. Schematic Presentation of the Relaxation Paths of the Sublimated Film of the Trimer $TPP^{2-}Ce^{III}Pc^{2-}Ce^{III}TPP^{2-}$ in the Experiment of (a): Transient Absorption, (b): Time-Resolved Four-Wave Mixing.

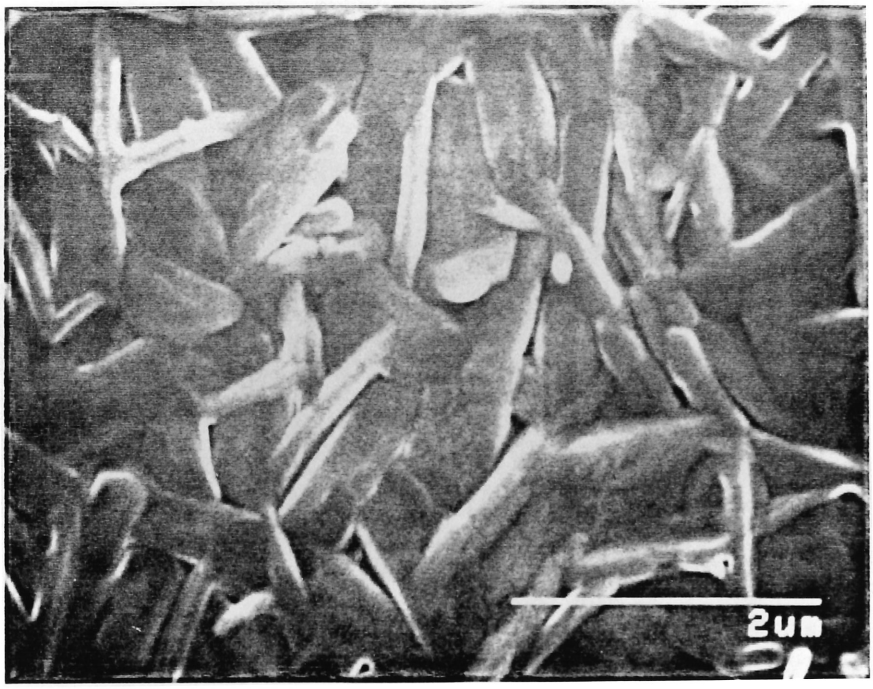

Figure 4.2.2.8. Electron Microscope Image of the Microstructure of the Sublimated Film of the Symmetric Trimer $TPP^{2-}Ce^{III}Pc^{2-}Ce^{III}TPP^{2-}$.

Finally, the low-lying state LS, populated by ^5Q state, relaxes towards the ground state T_0 through excitation migration by means of excitonic coupling between neighbouring molecules as discussed in section 4.1.2.3. ~ 4.1.2.5., with a very long time of $T_1^{(TG3)} > 1.3$ ns. This is directly related to the photorefractive effect in the sublimated film that will be discussed detailed in section 4.6. .

4.2.4. Summary

We have demonstrated that (TRFWM) is a very useful and very sensitive technique with which one can detect various $\chi^{(3)}$ processes, especially, those that can not be measured by TA experiment. The third-order nonlinear optical properties of sublimated films of the cerium-porphyrin-phthalocyanine trimer, $TPP^{2-}Ce^{III}Pc^{2-}Ce^{III}TPP^{2-}$, have been measured by four-wave mixing using 620 nm pump pulses and a 650 nm probe pulse. The dynamics of the diffracted signal shows that the trimer system possesses a subpicosecond response of 0.37 ps, an intermediate response of 15.3 ps and a very long response > 1.3 ns.

Compared to the data from the transient absorption experiment on the same compound, it is found that the response times detected by time-resolved four-wave mixing are shorter than those by transient absorption. This is due to the existence of excitation migration. Taking the microscopic structure of the sublimated trimer film into consideration, the diffusion coefficients of the first two components have been deduced to be 30 cm^2/s and 0.87 cm^2/s respectively, values compatible with diffusion coefficients for energy transfer processes.

Taking the $\chi^{(3)}$ value of fused quartz as reference, the third-order nonlinear optical susceptibility of the trimer is found to be 3.4×10^{-10} esu. This shows that this trimer is among those compounds having the largest $\chi^{(3)}$ values in the family of metallo porphyrins and/or phthalocyanines. The detailed calculation procedure of $\chi^{(3)}$ will be discussed in section 4.5. .

When grating spacing period is bigger than the averaged size of the microscopic crystalline domain of the sublimated film, the latter, instead of the former, should be used to make a correct estimation of the diffusion coefficient. There still exists long-time response in the experimental data of the symmetric trimer $TPP^{2-}Ce^{III}\,Pc^{2-}Ce^{III}\,TPP^{2-}$ as we have observed in the heterodimer $Pc^{2-}Ce^{IV}TPP^{2-}$. This indicates that the migration of the excited species is the origin of the photorefractive effect observed in these systems. This effect will be discussed in section 4.6. .

4.3 Langmuir-Blodgett Film of mixed Dimer of $CoPC_{22}^{4+}$ / H_2PcTS^{4-}

4.3.1. Experimental Aspects

4.3.1.1. Preparation of Langmuir-Blodgett Films

The mixed dimer compound was synthesized and prepared by the group of Dr. T. H. Tran-Thi. A multilayer LB film was made in *CEA, Centre d'Études Atomiques, Saclay, France* on a 37.00 cm by 95.60 cm custom built Langmuir-Blodgett trough system. The trough and moveable barrier were made from Teflon. The mixed dimer was solved in 86 % $CHCl_3$ (chloroform) and 14 % DMSO (C_2H_6SO, dimethylsulfoxide) at the concentration about 6.6×10^{-5} M. The subphase was pure water at room temperature purified through a Millipor MilliQ System. After spreading the prepared solution on the subphase, waiting for about 20 minutes to allow chloroform to evaporate and the film to equilibrate, the monolayer was subsequently compressed slowly up to the desired surface pressure. Force area isotherms were established under the same conditions. Then the monolayer was allowed to stabilize under constant surface pressure until the surface area remained constant in time. Typically, this stabilization process takes about 30 minutes to 1 hour.

The monolayer was deposited onto an optical quality glass slide which was thoroughly cleaned. We first sonicated with 5 ~ 10 % detergent in water, then rinsed with MilliQ water completely following by sonicating with 2 g / 100 ml KOH in 50 % : 50 % (V:V) water/ethanol for about 30 minutes, then rinsing by MilliQ water many times and sonicating in MilliQ water 5 ~ 10 minutes, and finally, sonicated again in ethanol for about 30 minutes to get rid of the extra water on the substrate. Having finished the above procedure, the substrate had been made hydrophilic. This would be sufficient for the deposition of certain types of LB film. To make the substrate hydrophobic, further treatments need to be done. After the above procedure, we sonicated the treated substrate in chloroform for about 5 ~ 10 minutes, then changed the chloroform and repeated the same step. Next, we treated the substrate with $CH_3(CH_2)_{17}SiCl_3$ (octadecyltri-chlorsilane) 1 ml in 200 ml chloroform sonicating for about 30 minutes. Finally, we rinsed the substrate in chloroform and sonicated about 5

~10 minutes 3 times. The treated substrate was stored in ethanol in a closed bottle. The substrate used for depositing layers were never older than one days.

The surface pressure was measured by a spring-coil column balance linked on its tip with a small slide of filter paper which was partially dipped onto the surface to feel the surface pressure. The balance was carefully calibrated under the condition of clean water surface.

The LB film was transferred onto the substrate by the repeated vertical dipping of the substrate into and lifting-off the surface until 300 layers formed. This was done at the constant surface pressure of 20 mN/cm and a steady deposition rate of 0.4 mm/min. According to our experience, to get high quality samples, it is preferable to build a sample continuously using the same monolayer until finished. Otherwise, the sample would give us very large extra diffused light when measured by the TRFWM. This would be a serious problem for a four-wave mixing detection system as it would prove impossible to extract the signal from the noise background.

4.3.1.2. FWM Measurement on Langmuir-Blodgett Films

The dynamics of the third-order nonlinear susceptibility $\chi^{(3)}$ of the LB film of the mixed dimer $CoPC_{22}^{4+}$ / H_2PcTS^{4-} was measured by the non-degenerate four-wave mixing using two 620 nm pulses as pump and one 650 nm pulse as probe. The experiment set-up, similar to that given in [208], has been described in details in Chapter 3. The experimental procedure and conditions are the same as in the cases of the heterodimer $Pc^{2-}Ce^{IV}TPP^{2-}$ and the symmetric trimer $TPP^{2-}Ce^{III}Pc^{2-}Ce^{III}TPP^{2-}$. The only difference is that for LB film has higher level of diffusion light, it is much more difficult to extract the TRFWM signals. In order to extract TRFWM signals from the intense background noise, a special technique called ***transparent shutter,*** described in Chapter 3 section 3.5., has been used in the data acquisition.

4.3.2. Results and Discussion

The structure of mixed dimer $CoPC_{22}^{4+}$ / H_2PcTS^{4-} is shown in Fig. 4.3.2.1. Due to strong ring to ring interaction, the two macrocycles keep a face to face position which favours the charge transfer and energy transfer processes between the two moieties. The long hydrophobic tails have been attached to the porphyrin side to make the LB deposition possible. Fig. 4.3.2.2. is the UV and the visible ground state absorption spectrum of the LB film of $CoPC_{22}^{4+}$ / H_2PcTS^{4-}, and Fig. 4..3.2.3., Fig. 4.3.2.4. are the ground state absorption spectra of the unsubstituted monomers, $CoPC_{22}^{4+}$,$4Br^{4-}$, and H_2PcTS^{4-},Na^{4+}. It can be seen that the coulombic attraction and the π-π interaction of the two conjugated macrocycles, porphyrin and phthalocyanine, have caused a drastic change in the absorption spectra from the unsubstituted monomers to the mixed dimer. In the mixed dimer, the porphyrin Soret band and the phthalocyanine Q band are severely flattened and red shifted compared with the corresponding monomer salt absorption bands. A strong new band appears around 436.5 nm caused by a very strong interaction between the two macrocycles.

The mixed dimer of $CoPC_{22}^{4+}$ / H_2PcTS^{4-} was measured by four-wave mixing pumped at 620 nm and probed at 650 nm. These fall in the strong absorbing region of the dimer and thus give rise to a resonant dynamic third-order nonlinear susceptibility $\chi^{(3)}$ that contains abundant information about the dimer system. The observed diffraction signals as a function of probe delay time in respect to the two synchronized pump pulses, are given Fig. 4.3.2.5. ~ Fig. 4.3.2.8. with different time scales from -1 ~ 10 ps, -5 ~ 100 ps, -10 ~ 500 ps and -25 ps ~ 1.3 ns respectively. The fitting was similar to that of given in reference [229, 231, 232]. But for the best fitting, especially for the longest response component of the case here, a four excited state population model had to be used. The detailed formulas are given in Appendix I, Eq. (A16.) ~ Eq. (A17.).

A standardized fitting procedure has been used in the fitting experimental results, which minimizes the squared function between the model and the experimental data with the following temporal form:

$$S(\tau_d) = \int dt \left[\left(\int d\tau \sum_{i=1}^{4} \chi_i^{(3)} P_i(\tau) \right) I_{pump}(t-\tau) \right]^2 I_{probe}(t-\tau_d). \qquad (4.3.2.1.)$$

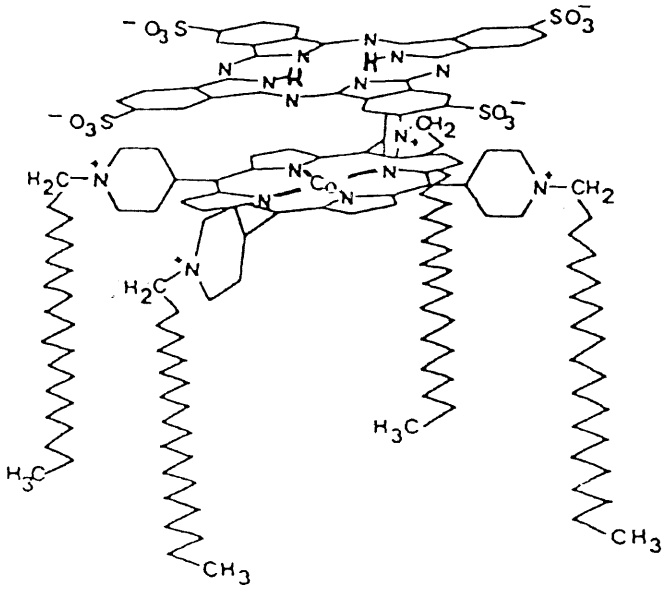

Figure 4.3.2.1 Molecular Structure of the Cobalt Porphyrin Phthalocyanine Mixed Dimer $CoPC_{22}^{4+}/H_2PcTS^{4-}$

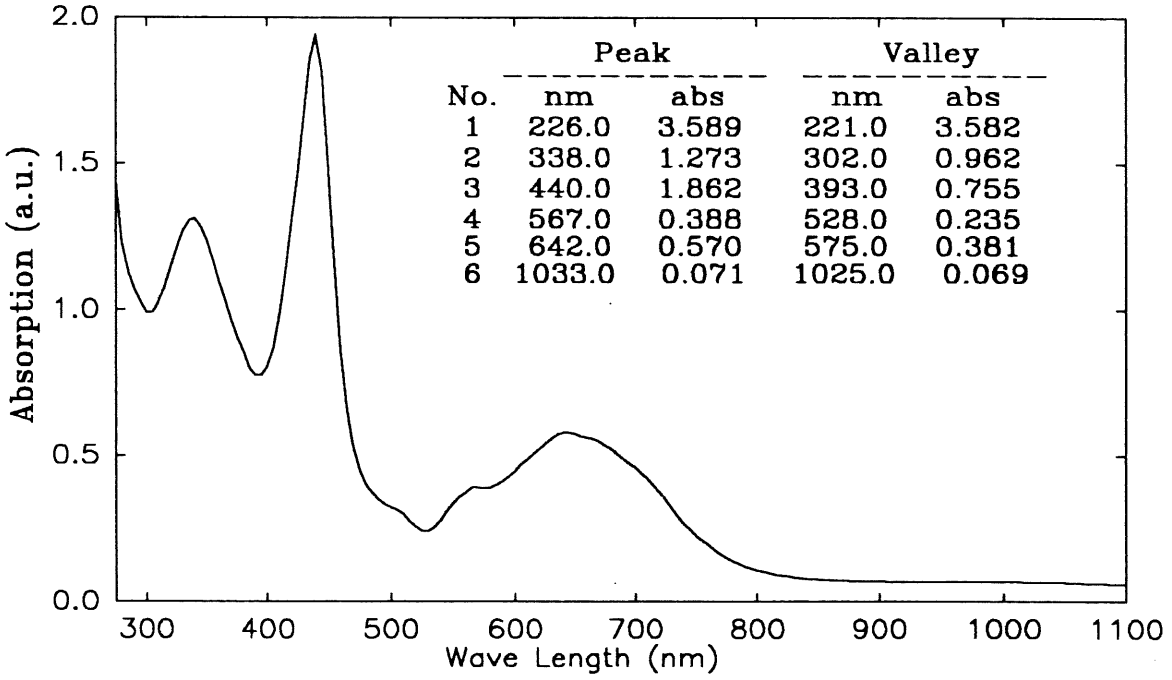

No.	Peak nm	Peak abs	Valley nm	Valley abs
1	226.0	3.589	221.0	3.582
2	338.0	1.273	302.0	0.962
3	440.0	1.862	393.0	0.755
4	567.0	0.388	528.0	0.235
5	642.0	0.570	575.0	0.381
6	1033.0	0.071	1025.0	0.069

Figure 4.3.2.2. Ground State Absorption Spectrum of the Langmuir-Blodgett Film of the Mixed Dimer $CoPC_{22}^{4+}/H_2PcTS^{4-}$ on a Glass Substrate.

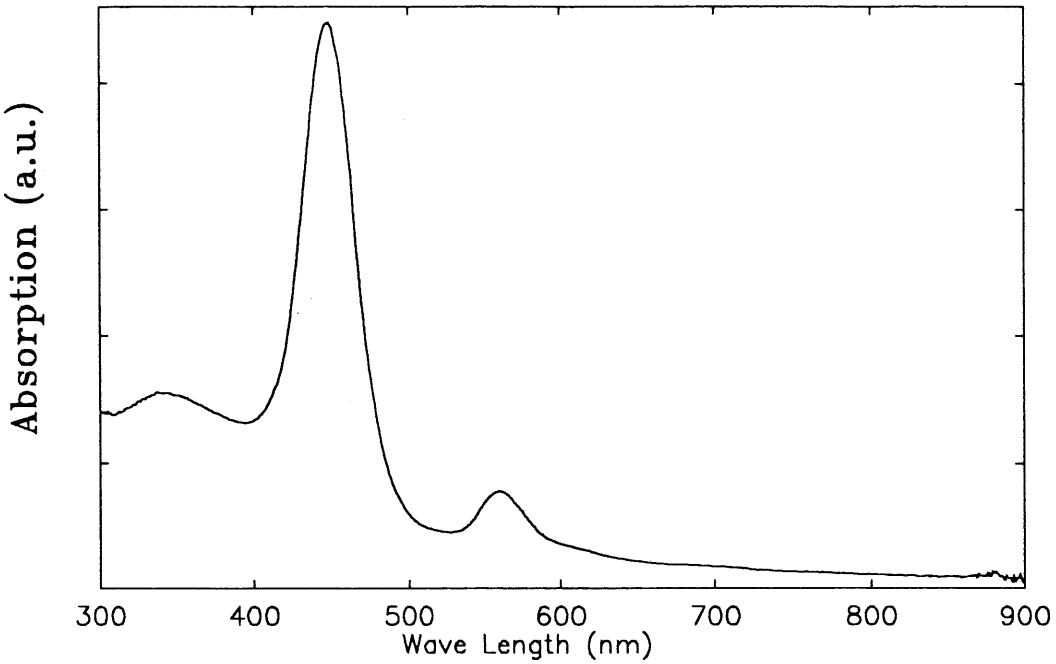

Figure 4.3.2.3. Ground State Absorption Spectrum of the Monomer $CoPC_{22}^{4+}$, $4Br^-$ in a Solution of DMSO/$CHCl_3$.

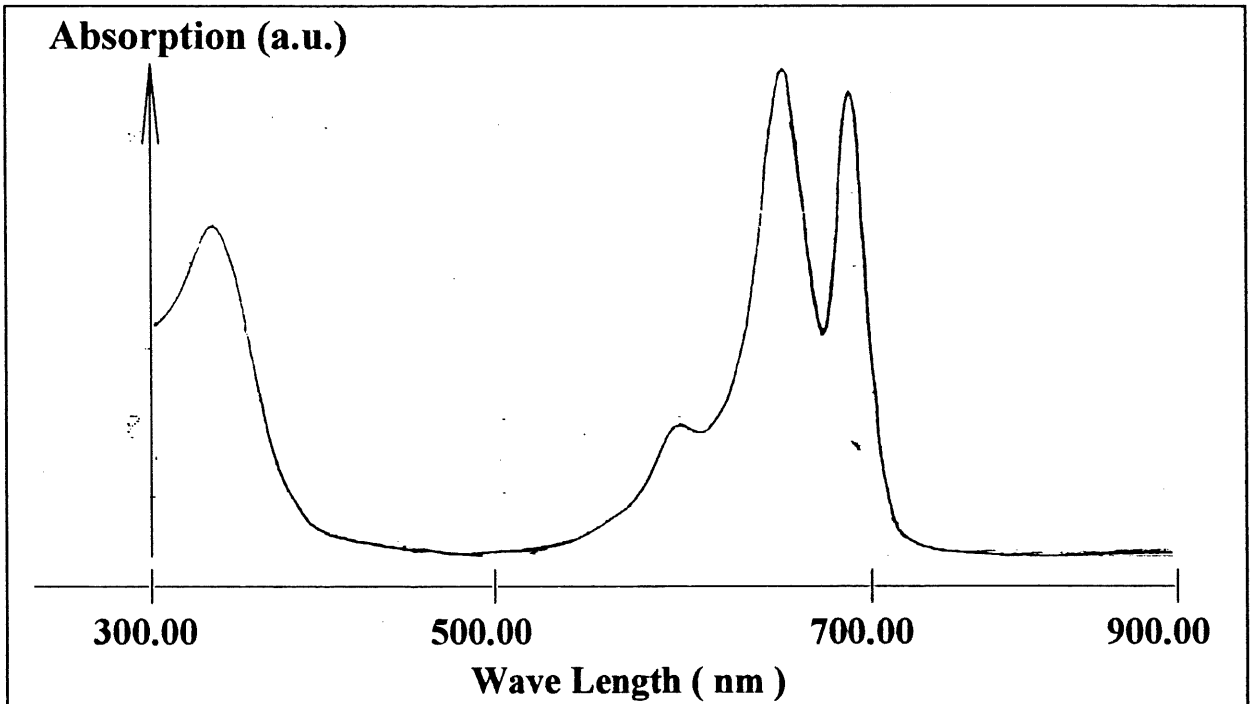

Fig.4.3.2.4. Ground State Absorption Spectrum of the Unsubstituted Monomer H_2PcTS^{4-},$4Na^+$.

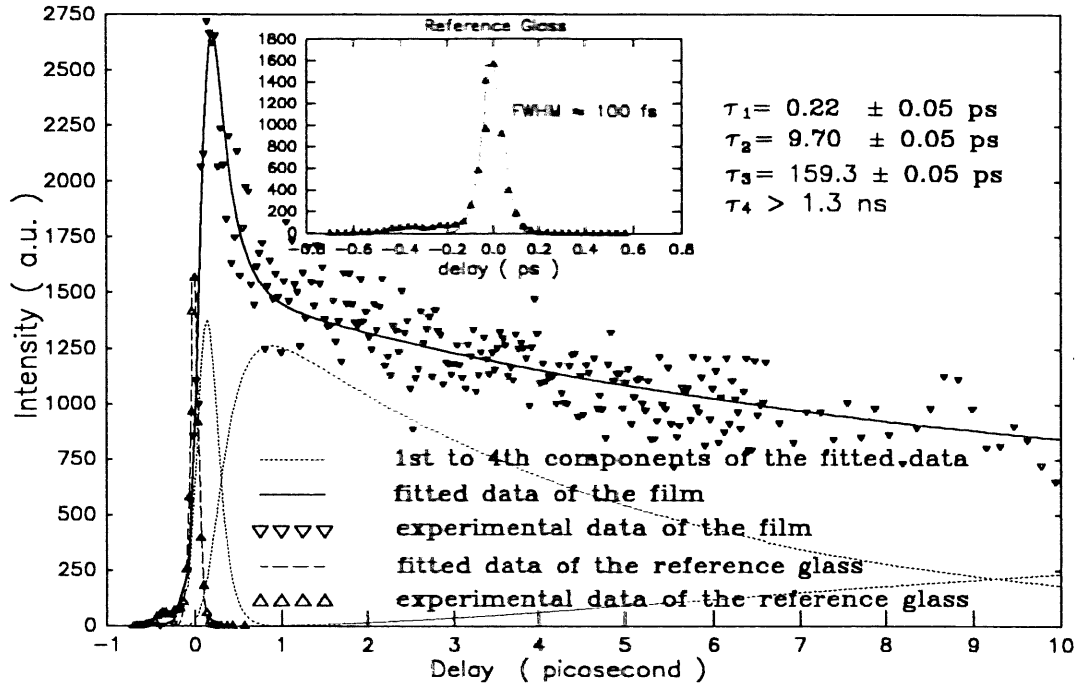

Figure 4.3.2.5. Four-Wave Mixing Signal as a Function of Probe-to-Pump Delay Time for the Langmuir-Blodgett Film of the Mixed Dimer $CoPC_{22}^{4+}/H_2PcTS^{4-}$ on a Glass Substrate, with a Time Scale up to 10 ps.

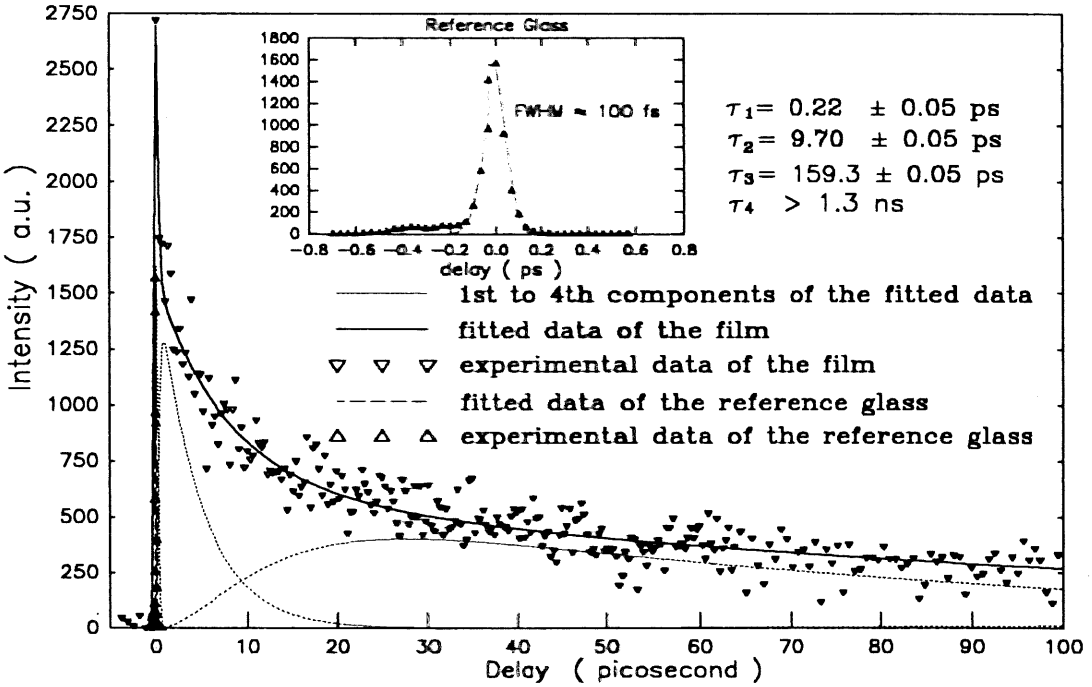

Figure 4.3.2.6. Four-Wave Mixing Signal as a Function of Probe-to-Pump Delay Time for the Langmuir-Blodgett Film of the Mixed Dimer $CoPC_{22}^{4+}/H_2PcTS^{4-}$ on a Glass Substrate with a Time Scale up to 100 ps.

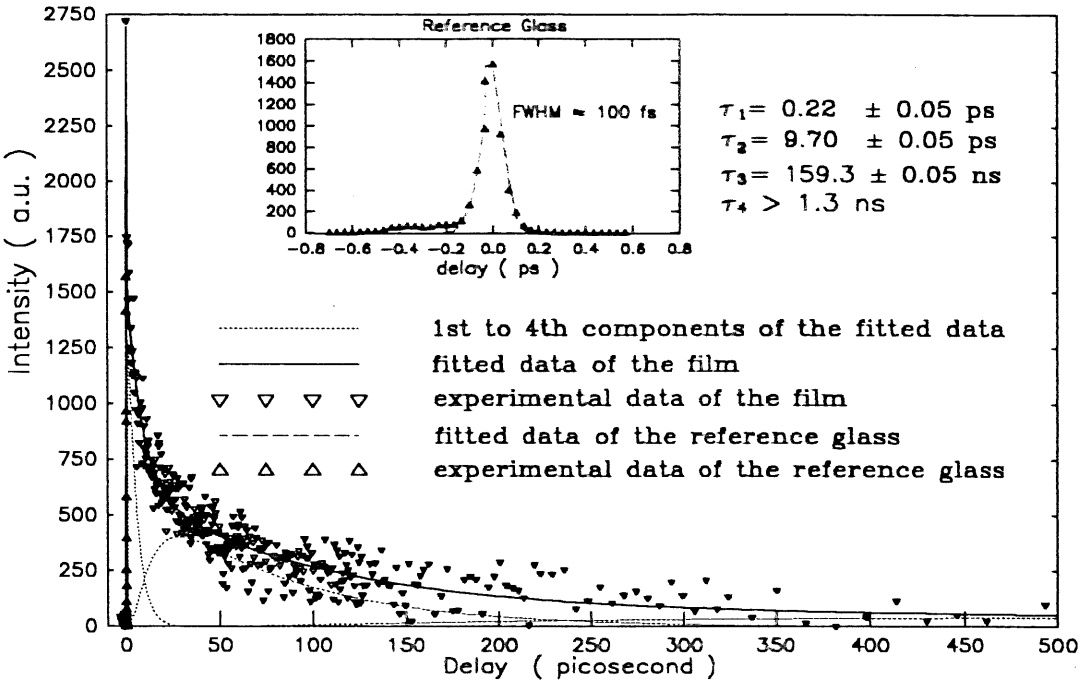

Figure 4.3.2.7. Four-Wave Mixing Signal as a Function of Probe-to-Pump Delay Time for the Langmuir-Blodgett Film of the Mixed Dimer $CoPC_{22}^{4+}/H_2PcTS^{4-}$ on a Glass Substrate with a Time Scale up to 500 ps.

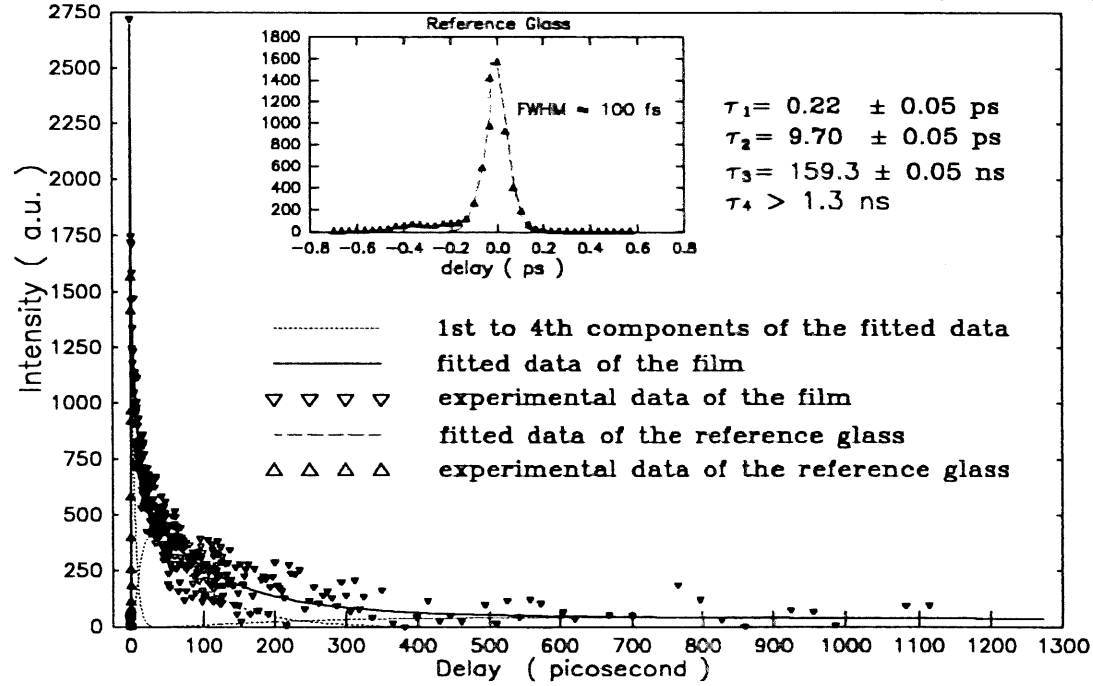

Figure 4.3.2.8. Four-Wave Mixing Signal as a Function of Probe-to-Pump Delay Time for the Langmuir-Blodgett Film of the Mixed Dimer $CoPC_{22}^{4+}/H_2PcTS^{4-}$ on a Glass Substrate with a Time Scale up to 1.3 ns.

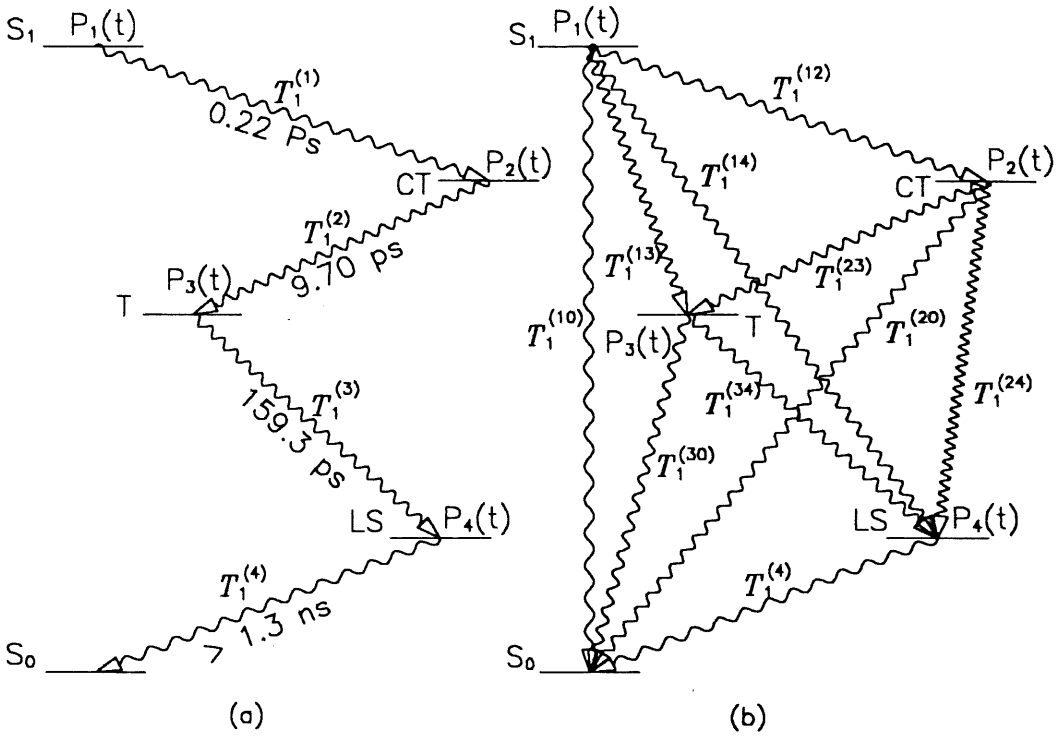

Figure 4.3.2.9. Four Excited State Populations in LB Film of the Mixed Dimer $CoPC_{22}^{4+}/H_2PcTS^{4-}$ (a):Simplest & (b):the Most Complicated Cases.

The fitted theoretical responses correspond to the full lines in Fig. 4.3.2.5. ~ Fig. 4.3.2.8. with different time scales.

Fig. 4.3.2.9. (a) gives schematically the mechanism associated with the model. The mixed dimer of porphyrin-phthalocyanine $CoPC_{22}^{4+}$ / H_2PcTS^{4-} has four temporal components. In the simplest case, the absorption of 620 nm pump pulses generates a first excited state with a population P_1 (t). The population P_1 (t) relaxes with a longitudinal relaxation time $T_1^{(1)} = 0.22$ ps towards a charge transfer state CT with a population P_2 (t). Then the second population relaxes in time $T_1^{(2)} = 9.70$ ps, which results in the intermediate response of the $\chi^{(3)}$, towards a triplet state T with a population P_3 (t). In turn, the population on the triplet state T, P_3 (t), relaxes with a time constant $T_1^{(3)} = 159.3$ ps, which is associated with the long-time response of $\chi^{(3)}$, towards a low lying state LS. Finally, the system relaxes from the low lying state LS towards the ground state with $T_1^{(4)} > 1.3$ ns. Because of the existence of excitation migration as well as charge transfer processes, as commonly seen in the lanthanide

porphyrin phthalocyanine dimer [229], there might exist other channels of relaxation and the resulting mechanisms could be more complicated. This is illustrated in Fig. 4.3.2.9. (b). Nevertheless, the experimental data did not allow to confirm which scheme or relaxation paths are predominant.

Compared with transient absorption experimental results on the same family of compounds, $\left[ZnP(N^{+}C_{22}H_{45})\right]^{4+}/(CuPcTS)^{4-}$[205], $\left[ZnP(N^{+}C_{22}H_{45})\right]^{4+}/(AlClPcTS)^{4-}$ [206], $[Zn(TMPP)]^{4+}/[M(TSPc]^{4-}$, M = Cu, AlCl [227], and especially with the TRFWM experimental results on $\left[ZnP(N^{+}C_{22})\right]^{4+}/(H_2PcTS)^{4-}$ [228] which give three relaxation components τ_1 = 400 fs, τ_2 = 48 ps, τ_3 = 479 ps, our results τ_1 = 0.22 ps, τ_2 = 9.70 ps, τ_3 = 158.3 ps, $\tau_4 \geq 1.3$ ns, have the same order of magnitude of the data for the same family of the compounds, except the longest component relating to the photorefractive effect. Generally speaking [205, 206, 233 - 235], for this family of compounds, there are three observed relaxation components. The first one with several hundred femstoseconds is attributed to the charge-transfer reaction. The second one with several ten picoseconds is attributed to a delayed charge-separation and reorganization of a certain population of the dimers prior to charge separation. The third varying between several ten picoseconds and several hundred picoseconds is attributed to the charge recombination process. In TRFWM experiments, more complicated degrating mechanisms could be involved. For example the diffusion leads to a very long time response associated with the existence of a photorefractive effect. Since there are no comparable transient experimental data on Langmuir-Blodgett films of the mixed dimer $CoPC_{22}^{4+}$ / H_2PcTS^{4-}, the exact attribution of the different components in the TRFWM experimental data is impossible. Nevertheless, from the above analysis, it is clear that the attributions of the TRFWM experimental data the sample to the corresponding paths and mechanisms are quite reasonable.

4.3.3. Summary

We have performed a TRFWM study on the dynamics of third-order nonlinear optical processes in a Langmuir-Blodgett film of the mixed dimer $CoPC_{22}^{4+}$ / H_2PcTS^{4-} using 100 fs FWHM 620 nm pump pulses and a 650 nm probe pulse.

The TRFWM experimental data shows that the Langmuir Blodgett film of the electrostatic mixed dimer obtained by pairing porphyrin and phthalocyanine moieties bearing oppositely charge substituents, $CoPC_{22}^{4+}$ / H_2PcTS^{4-}, has a very short response time compared to the experimental data on the same family of compounds. It also contains a very long time response of about 1.3 ns, which is believed to be related photorefractive effect in this material (see section 4.6.).

This LB film has a relatively large third-order nonlinear optical susceptibility $\chi^{(3)}$compared with those of natural phthalocyanine, mono-metallophthalocyanines and bis-metallo-phthalocyanines (see section 4.5.). It is thus proved that time resolved four-wave mixing is a sensitive and useful tool with which to probe the nonlinear optical processes in LB films.

The absolute value of the third-order nonlinear optical susceptibility of the film is estimated as 8.3×10^{-11} esu taking that of the fused quartz as reference. Its determination will be explained in section 4.6. .

4.4. Neodymium Porphyrin Phthalothyanine Symmetric Dimer $NdPc_2$ and Trimer $(NdPc)_2TPP$

4.4.1. Experimental Aspects

The bis- and tris- neodymium-porphyrin-phthalocyanine, $Pc^{2-}Nd^{III}Pc^{-}$ and $Pc^{2-}Nd^{III}TPP^{2-}Nd^{III}Pc^{2-}$ were synthesized at *CEA*, the *Centre d'Études Atomiques de Saclay, France*, by the group of Dr. T. H. Tran-Thi [141]. The thin films were sublimated using a procedure similar to the ones in ref. [229, 230]. The evaporation was performed at a pressure of 2.5×10^{-6} torr and a temperature starting from 243 °C ~ 360 °C in 5 minutes to 490 °C for $NdPc_2$,.and a presure of 1.1×10^{-5} torr and a temperature of 460 °C ~ 468 °C for $NdPc_2TPP$, in the laboratory of Prof. Lê Dao at *l'NRS-Energie/Materiaux de Varennes, Montréal, Québec, Canada.*

The ground state absorption spectra of the sublimated film of the dimer $Pc^{2-}Nd^{III}Pc^{-}$ and the sublimated film of the trimer $Pc^{2-}Nd^{III}TPP^{2-}Nd^{III}Pc^{2-}$, deposited on quartz substrates, were recorded on HITACHI U-2000 spectrometer.

The dynamics of the third-order nonlinear optical susceptibilities $\chi^{(3)}$ of the samples were measured by a time resolved non-degenerate four-wave mixing system same as in ref. [122, 229, 230]. The experimental procedure and conditions are the same as metioned in the references. The calculation of the third-order nonlinear susceptibility will be given in section 4.5.

4.4.2. Results and Discussion

The molecular structure of porphyrin, TPP, phthalocyanine, the neodymium phthalocyanine dimer $Pc^{2-}Nd^{III}Pc^{\bullet}$ and the neodymium porphyrin-phthalocyanine trimer $Pc^{2-}Nd^{III}TPP^{2-}Nd^{III}Pc^{2-}$, is given in Fig. 4.4.2.0. Because of a strong ring to ring coulombic interaction, a face to face stacked sandwich formation is produced in

the dimer and the trimer. This favours energy and charge transfer processes. In Fig.4.4.2.0. TPP, i.e., 5, 10, 15, 20 tetraphenylporphyrin is formed by replacing C in the position 5, 10, 15, 20 in the general porphyrin by group C_6H_5, and Pc, i.e., phthalocyanine, in position 5, 10, 15, 20 by N and in 2/3, 7/8, 12/13, 17/18 sides by C_6H_6 (benzene cycle). As we have discussed in section 1.2.3., the electron structure of the trimer is $Pc^{2-}Nd^{3+}TPP^{2-}Nd^{3+}Pc^{2-}$, where the six electrons are shared between the phthalocyanine rings at the two sides and porphyrin at the center.

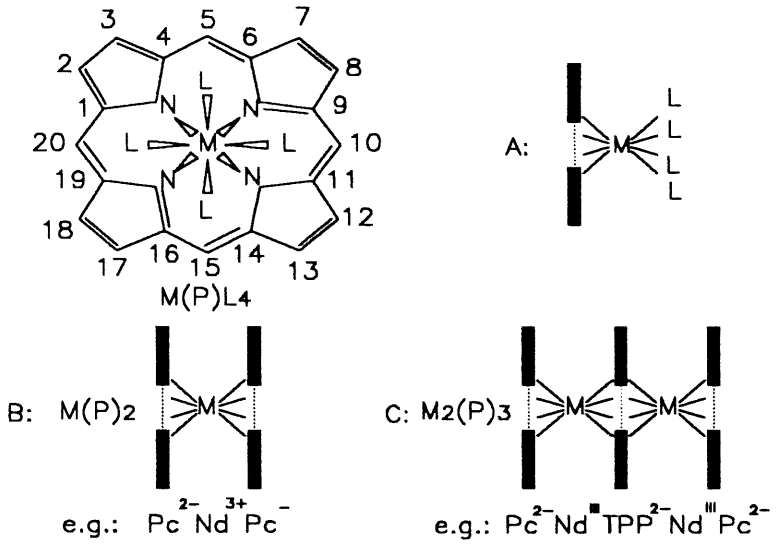

Figure 4.4.2.0. Molecular Structures of Octacoordinated Metal Mono–tetrapyrroles and Configurations with A: Monotetrapyrroles, B: Bis–tetrapyrroles $M(P)_2$ and C: Tristetrapyrroles $M_2(P)_3$, M = Lanthanide Metal Ion to Form the Dimer: $NdPc_2$ and the Trimer: $(NdPc)_2TPP$, etc.

Fig. 4.4.2.1. gives the ground state absorption spectrum from the UV to the near-infrared of the sublimated film of the dimer $Pc^{2-}Nd^{III}Pc^{\bullet}$. The bands in the spectrum can be assigned by analogy to the spectrum of $LuPc_2$ [158, 236]. The intense bands in the visible and UV are the Q and Soret band characteristic of the phthalocyanine rings. The intense band near 664 nm is the analogue of Q band of the monomer. The weaker near-infrared absorption band around 1034 nm is due to the low lying intervalence charge transfer transition, a characteristic of mixed valence compounds, in contrary to the bis-metallophthalocyanine anions, which have the electronic structure $Pc^{2-}M^{3+}Pc^{2-}$ having no intervalence transition and for which the spectrum shows a broad near-IR absorption.

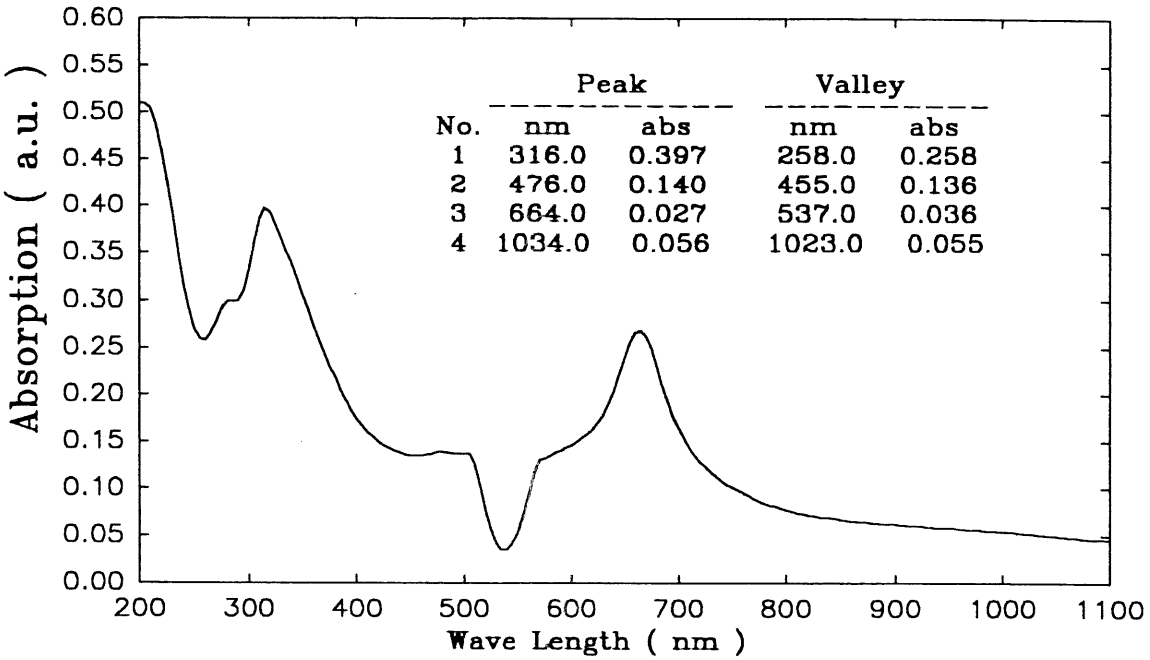

Figure 4.4.2.1. Ground State Absorption Spectrum of the Sublimated Film of the Dimer $NdPc$ on a Quartz Substrate.

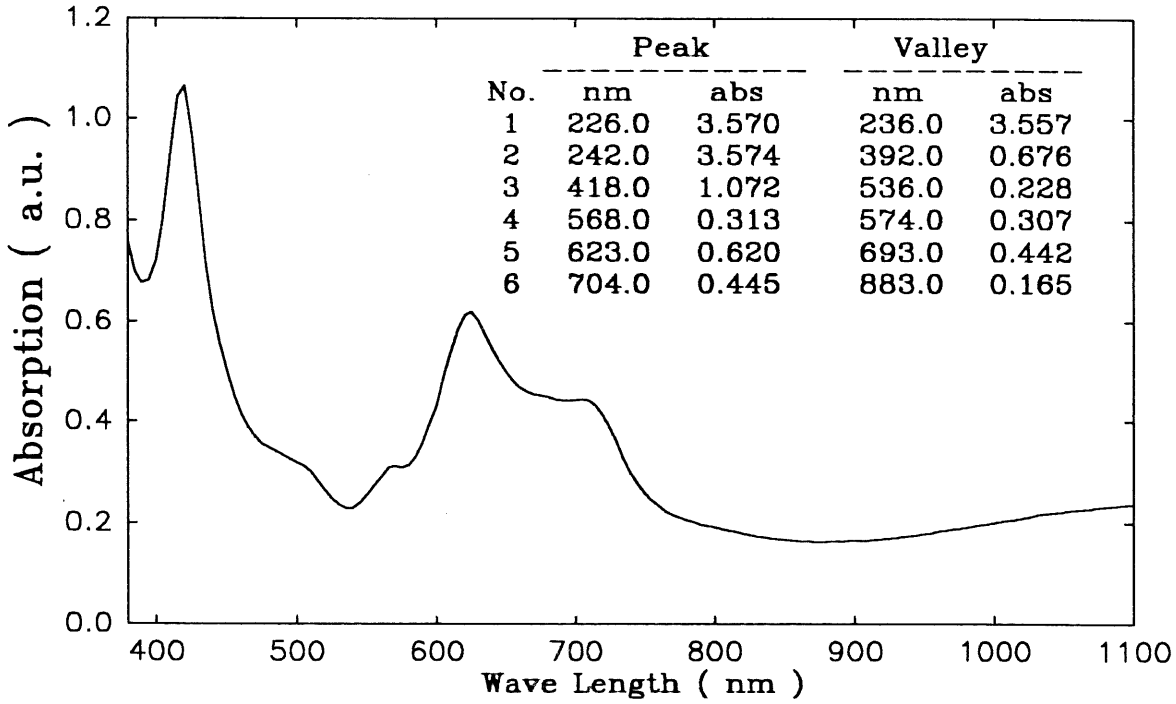

Figure 4.4.2.2. Ground State Absorption Spectrum of the Sublimated Film of the Trimer Nd_2Pc_2TPP on a Quartz Substrate.

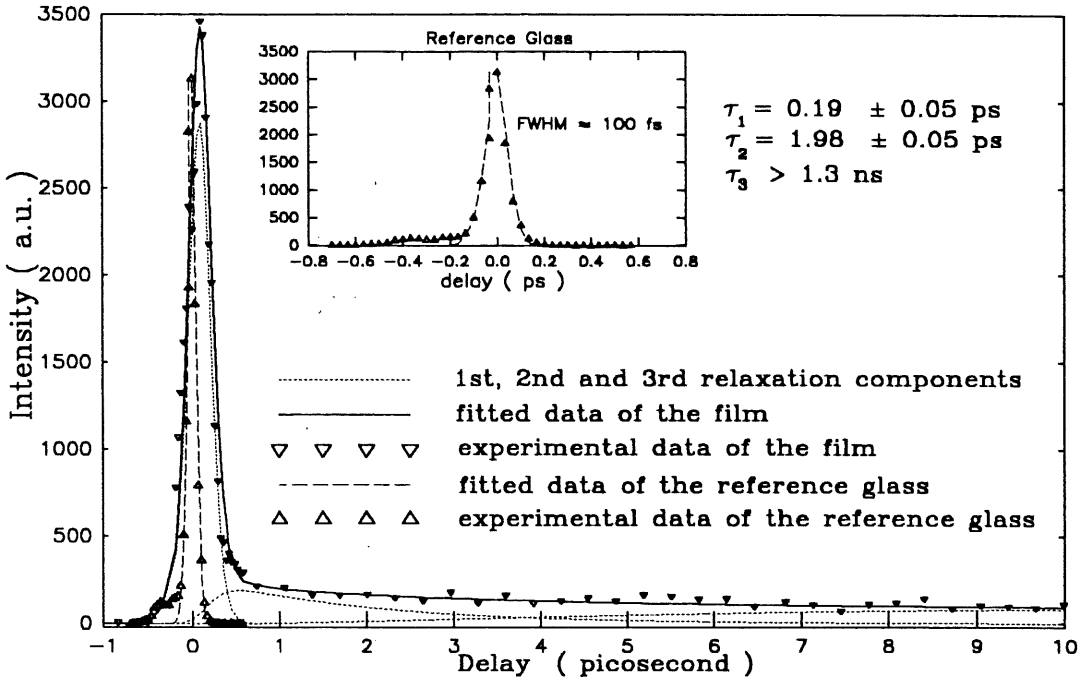

Figure 4.4.2.3. Time-Resolved Non-Degenerate Four-Wave Mixing Signal as a Function of the Probe-to-Pump Delay Time for the Sublimated Film of the Dimer $NdPc_2$ on a Quartz Substrate with a Time Scale up to 10 ps.

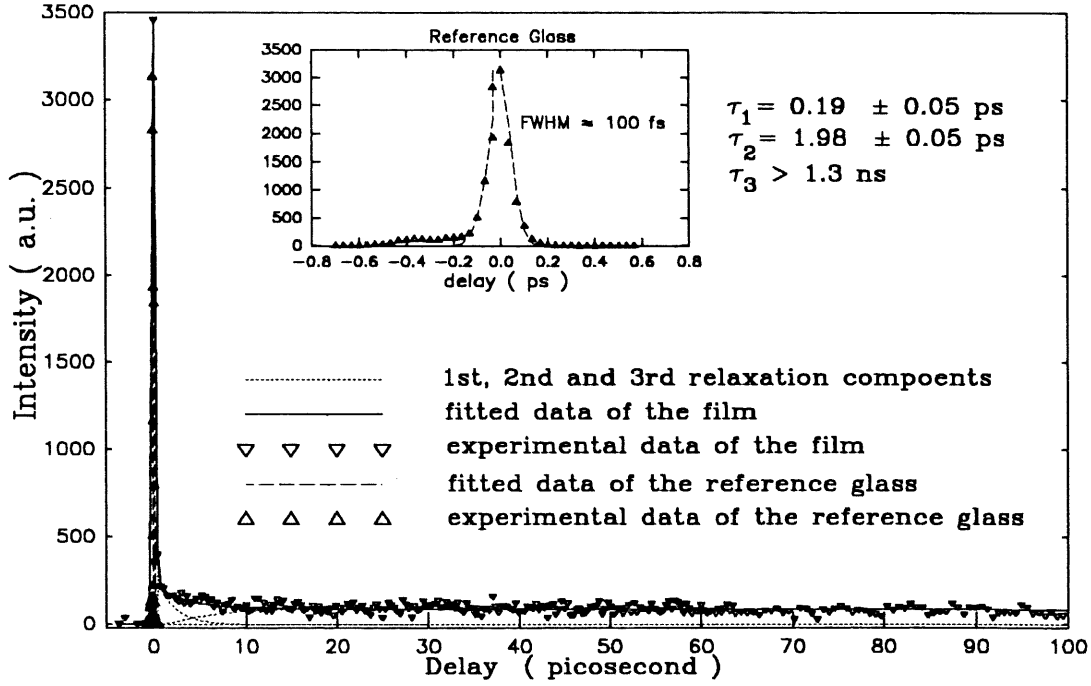

Figure 4.4.2.4 Time-Resolved Non-Degenerate Four-Wave Mixing Signal as a Function of Probe-to-Pump Delay Time for the Sublimated Film of the Dimer $NdPc_2$ on a Quartz Substrate with a Time Scale up to 100 ps.

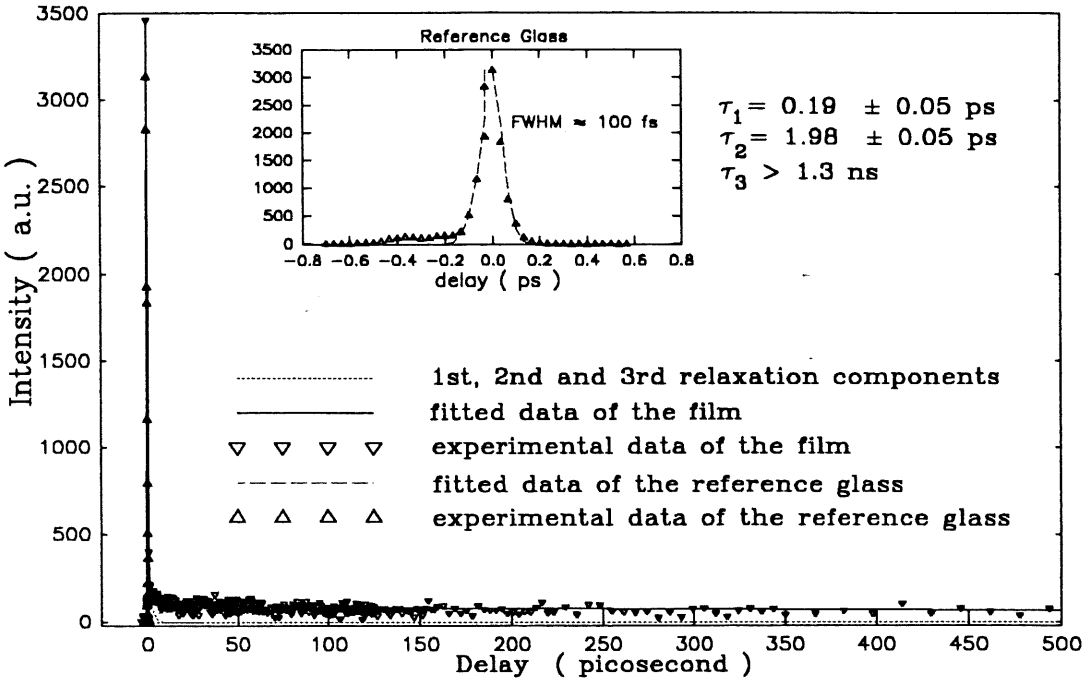

Figure 4.4.2.5 Time-Resolved Non-Degenerate Four-Wave Mixing Signal as a Function of Probe-to-Pump Delay Time for the Sublimated Film of the Dimer $NdPc_2$ on a Quartz Substrate with a Time Scale up to 500 ps.

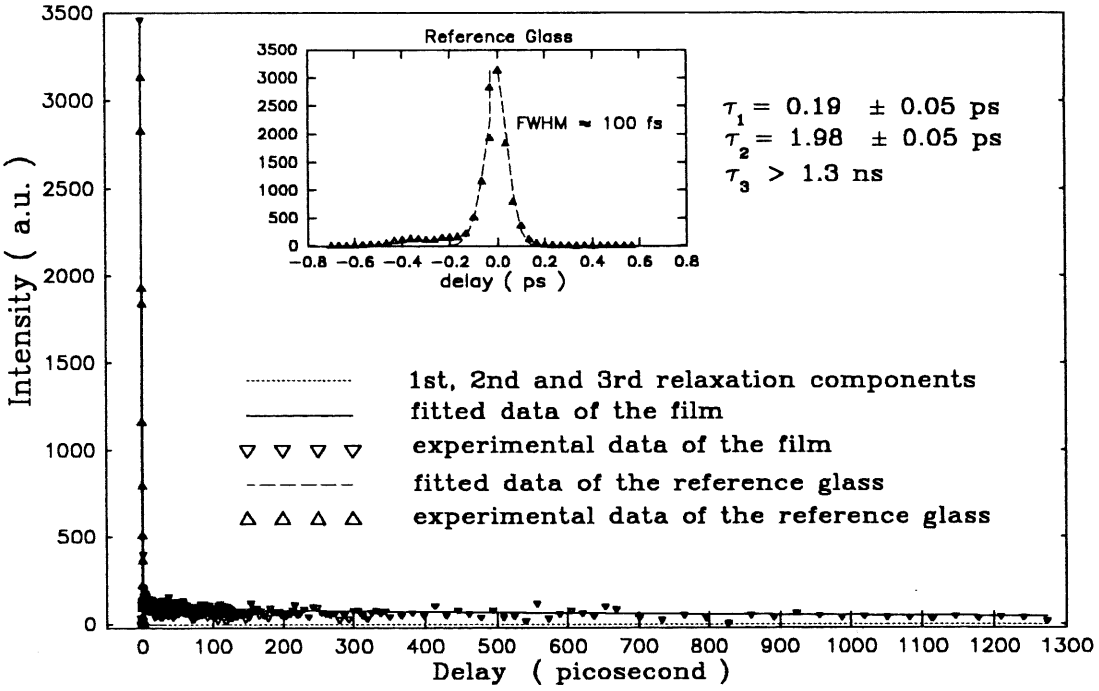

Figure 4.4.2.6. Time-Resolved Non-Degenerate Four-Wave Mixing Signal as a Function of Probe-to-Pump Delay Time for the Sublimated Film of the Dimer $NdPc_2$ on a Quartz Substrate, with a Time Scale up to 1.3 ns.

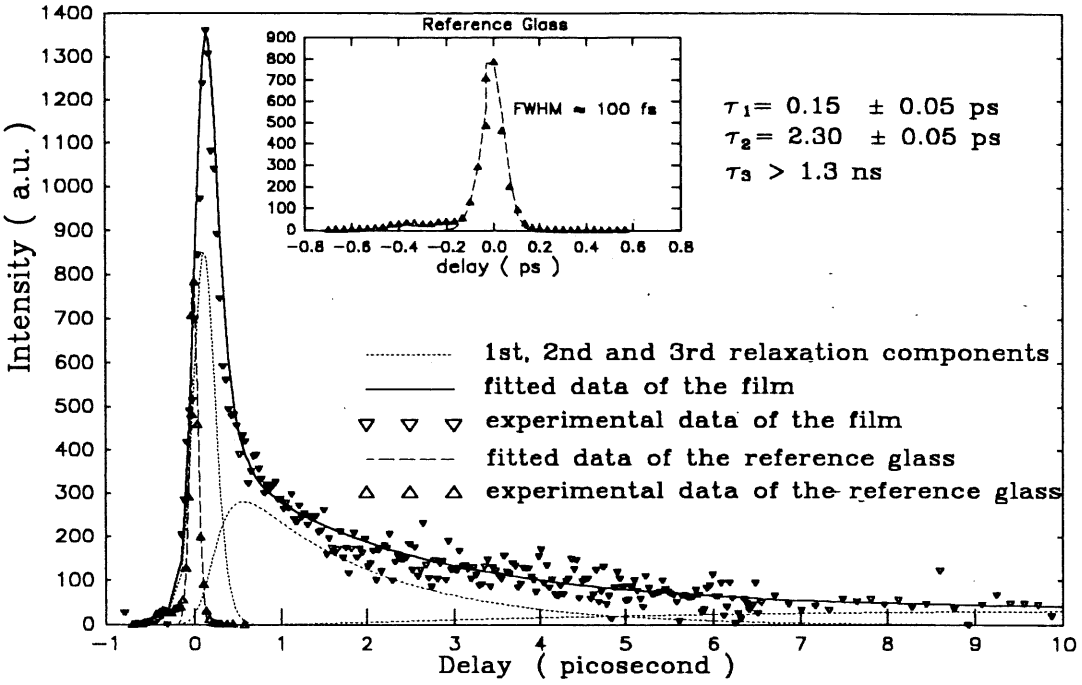

Figure 4.4.2.7 Time-Resolved Non-Degenerate Four-Wave Mixing Signal as a Function of Probe-to-Pump Delay Time for the Sublimated Film of the Trimer (NdPc)2TPP on a Quartz Substrate, with a Time Scale up to 10 ps.

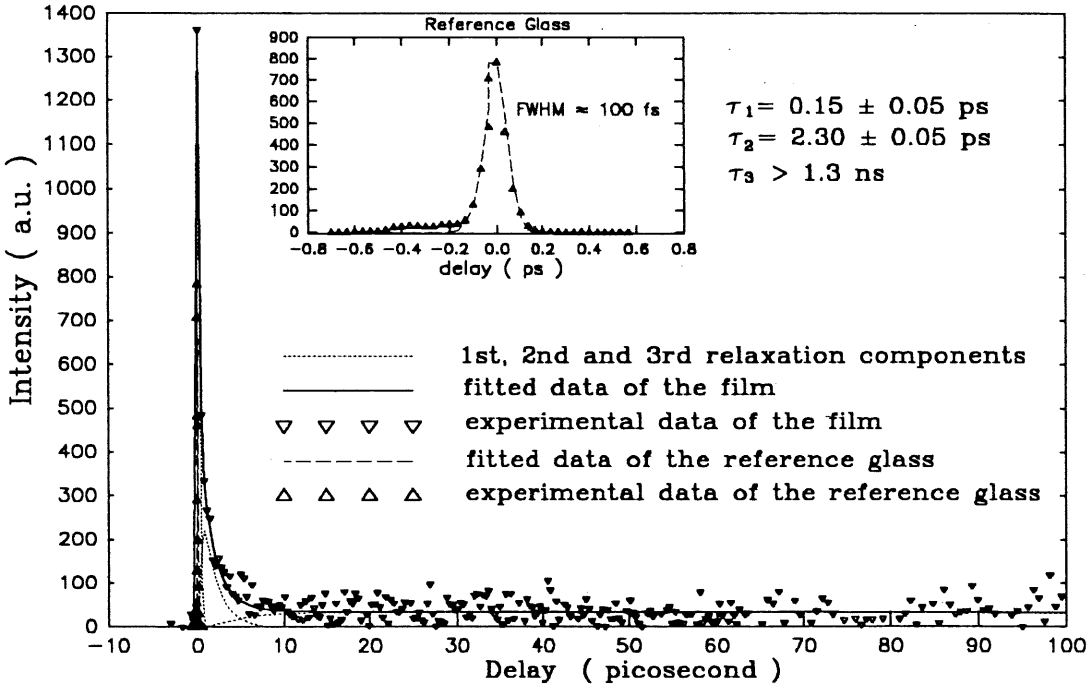

Figure 4.4.2.8 Time-Resolved Non-Degenerate Four-Wave Mixing Signal as a Function of Probe-to-Pump Delay Time for the Sublimated Film of the Trimer $(NdPc)_2TPP$ on a Quartz Substrate, with a Time Scale up to 100 ps.

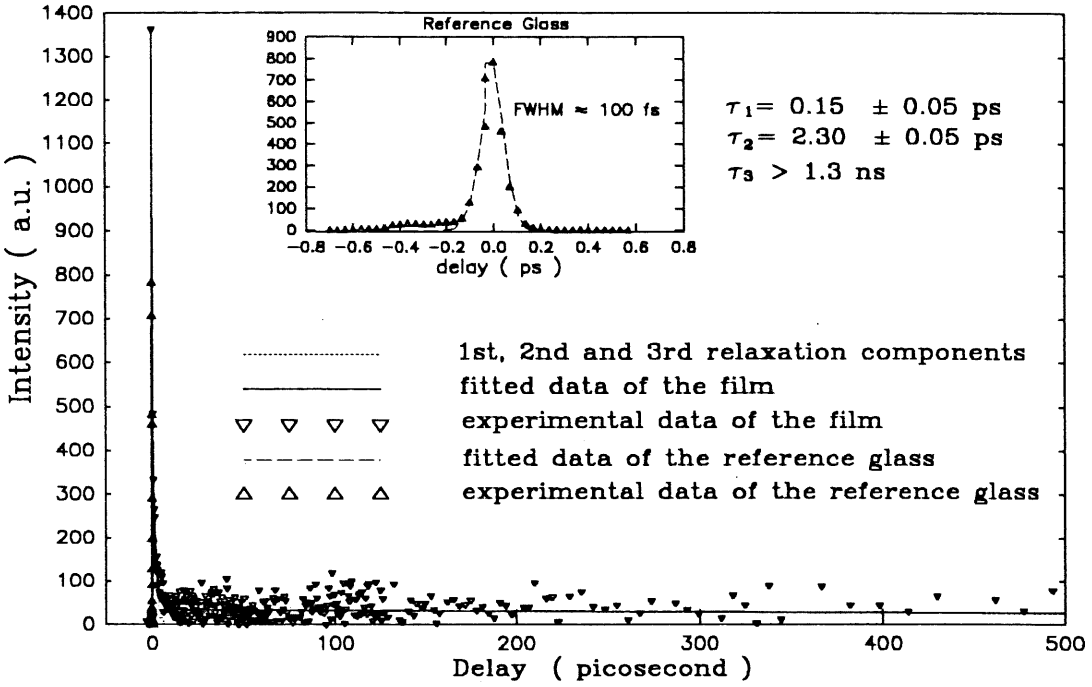

Figure 4.4.2.9 Time-Resolved Non-Degenerate Four-Wave Mixing Signal as a Function of Probe-to-Pump Delay Time for the Sublimated Film of the Trimer $(NdPc)_2TPP$ on a Quartz Substrate, with a Time Scale up to 500 ps.

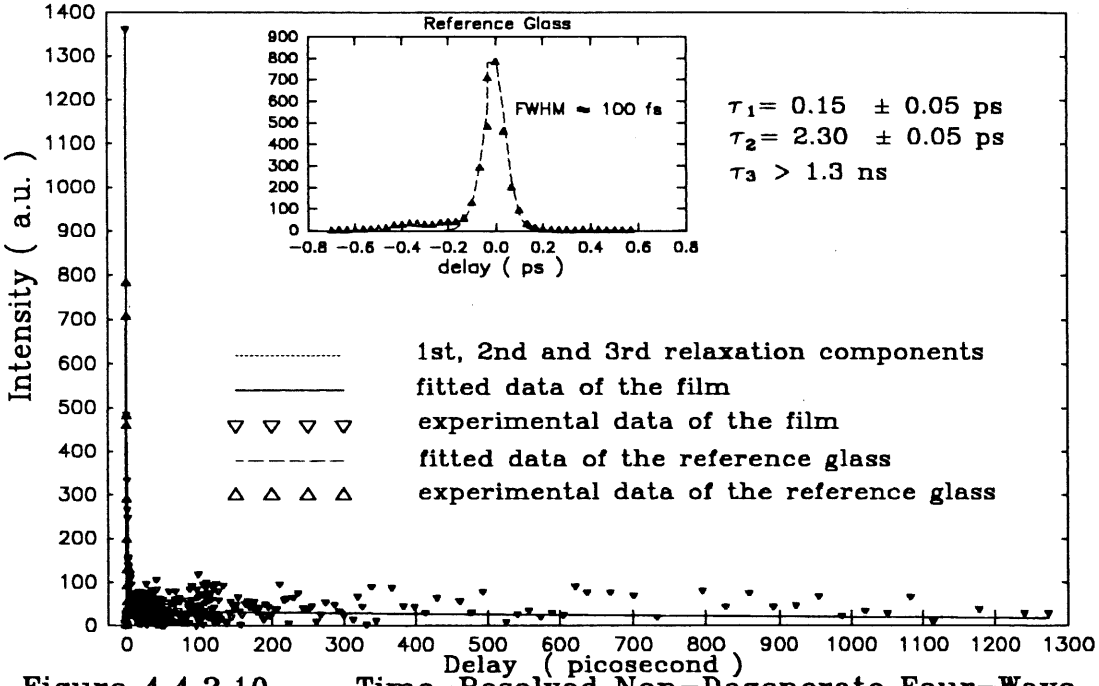

Figure 4.4.2.10. Time-Resolved Non-Degenerate Four-Wave Mixing Signal as a Function of Probe-to-Pump Delay Time for the Sublimated Film of the Trimer $(NdPc)_2TPP$ on a Quartz Substrate with a Time Scale up to 1.3 ns.

Fig. 4.4.2.2, shows the ground state absorption spectrum from the UV to the near-infrared of the trimer $Pc^{2-}Nd^{III}TPP^{2-}Nd^{III}Pc^{2-}$. The spectrum, similar to that of the trimer $TPP^{2-}Ce^{III}Pc^{2-}Ce^{III}TPP^{2-}$, can be interpreted as coming from two entities of $Pc^{2-}Nd^{III}$, which share the central porphyrin that interacts strongly with the two macrocycles [237]. Consequently, the Soret band and Q band of the central chromophore, porphyrin, are less intense than those components in the heterodimer $Pc^{2-}Nd^{III}TPP^{-}$, and shifted to the red side.

Three components, $T_1^{(TG1)} = 0.19$ ps, $T_1^{(TG2)} = 1.98$ ps and $T_1^{(TG3)} > 1.3$ ns for the dimer $Pc^{2-}Nd^{III}Pc^{\bullet}$, and those components $T_1^{(TG1)} = 0.15$ ps, $T_1^{(TG2)} = 2.30$ ps and $T_1^{(TG3)} > 1.3$ ns for the trimer $Pc^{2-}Nd^{III}TPP^{2-}Nd^{III}Pc^{2-}$, have been deduced from the fits of the TRNDFWM experimental data, which gives the third line of Table 4.4.2.1. for the dimer $Pc^{2-}Nd^{III}Pc^{\bullet}$ and that of Table 4.4.2.2. for the trimer $Pc^{2-}Nd^{III}TPP^{2-}Nd^{III}Pc^{2-}$. In order to attribute the experimental data to different relaxation mechanisms and paths, a comparison between the TRNDFWM results and the data from transient absorption for the dimer and the trimer is essential. Because these data are presently not available, we have used the data of compounds in the same family of bis- lanthanide phthalocyanine and tris- lanthanide porphyrin phthalocyanine. From reference [229], we take the data of the dimer $Pc^{2-}Pr^{III}Pc^{\bullet}$ as the reference for the dimer $Pc^{2-}Nd^{III}Pc^{-}$, giving rise to the second line of Table 4.4.2.1., and take the data of the trimer $TPP^{2-}Pr^{III}Pc^{2-}Pr^{III}TPP^{2-}$ as the reference for the trimer $Pc^{2-}Nd^{III}TPP^{2-}Nd^{III}Pc^{2-}$, giving rise to the second line of Table 4.4.2.2. .

A lanthanide bisphthalocyanine with a metal ion M^{III}, e.g., Nd^{III} that has an electron configuration $4f^3$, is paramagnetic and one of the cycles is a radical. The singlet excited states (π, π^*) and triplet excited states (π, π^*) of the biplane are coupled with single the electron from the cycle, resulting in a ground state that is a doublet $^2S_0$ while the excited states are doublets ^2S and quadruplets ^4Q. In transient absorption experiments, the excitation from the ground state $^2S_0$ with the pump pulses of 620 nm

generates a first excited state with a population $P_1(t)$ in an excited doublet ^2S. This population relaxes with a longitudinal relaxation time $\tau_1 = T_1^{(TA1)}$ towards a second excited state of quadruplet ^4Q with a population $P_2(t)$, then the excited quadruplet ^4Q relaxes with a longitudinal relaxation time $\tau_2 = T_1^{(TA2)}$towards the ground state $^2S_0$. This is depicted in Fig. 4.4.2.11. (a), and shown in the following scheme:

$$
\begin{aligned}
&{}^2S_0\left[Pc^{2-}Nd^{III}Pc^{-}\right] \xrightarrow{h\upsilon} {}^2S\left[Pc^{2-}Nd^{III}Pc^{-}\right]^*,\\
&{}^2S\left[Pc^{2-}Nd^{III}Pc^{-}\right]^* \xrightarrow{\tau_1} {}^4Q\left[Pc^{2-}Nd^{III}Pc^{-}\right]^*,\\
&{}^4Q\left[Pc^{2-}Nd^{III}Pc^{-}\right]^* \xrightarrow{\tau_2} {}^2S_0\left[Pc^{2-}Nd^{III}Pc^{-}\right].
\end{aligned}
\qquad (4.4.2.1)
$$

For the trimer $Pc^{2-}Nd^{III}TPP^{2-}Nd^{III}Pc^{2-}$, a symmetric tris- porphyrin phthalocyanine, intersystem conversion will be the predominant relaxation mechanism. Taking the results of the symmetric lanthanide tris- phthalocyanine porphyrin as reference [210], a schematic presentation is given in Fig. 4.4.2.12. In the experiments, after the excitation $h\upsilon = hc/\lambda|_{\lambda = 620\ nm}$, the system is put into an excited state (π, π^*) which can couple with the unpaired electrons in the system resulting in excited states being either triplets (^3T) or quintuplets (^5Q). With the same principle, the ground state of the trimer is found to be a triplet T_0. In transient absorption experiment, the excitation from the ground state T_0 with the pump pulse of 620 nm, generates a first excited state with a population $P_1(t)$ in an excited triplet ^3T. This population relaxes with a longitudinal relaxation time $\tau_1 = T_1^{(TA1)}$ towards an excited state of quintuplet ^5Q with a population $P_2(t)$, then the excited quintuplet ^5Q relaxes with a longitudinal relaxation time $\tau_2 = T_1^{(TA2)}$ towards the ground state T_0. This is depicted in Fig. 4.4.2.12. (a), and shown in the following scheme:

Table 4.4.2.1.

Attribution of the Different Components from Time-Resolved Non-Degenerated Four-Wave Mixing (TRFWM) / Transient Grating (TG) Experiment for the Sublimated Film of the Dimer $Pc^{2-}Nd^{III}Pc^{\bullet}$.

Components	1	2	3
Reference data from transient absorption experiment, $T_1^{(TA)}$ [a] of the dimer in the same family	$T_1^{(TA1)} = 1.1$ ps	$T_1^{(TA1)} = 67$ ps	
Data from TRNDFWM or transient grating (TG) experiment, $T_1^{(TG)}$	$T_1^{(TG1)} = 0.19$ ps	$T_1^{(TG2)} = 1.98$ ps	$T_1^{(TG3)}$ >1.3ns
Estimated Diffusion time $\tau_d = T_1^{(D)} = (1/T_1^{(TG)} - 1/T_1^{(TA)})^{-1}$	$T_1^{(D1)} = 0.23$ ps	$T_1^{(D2)} = 2.04$ ps	
Estimated averaged microscopic period Λ of the sublimated film [b]	0.1 μm	0.1 μm	
Diffusion coefficient $D = (\Lambda^2/4\pi^2)/\tau_d$	11 cm^2/s	1.2 cm^2/s	

[a]: ref. [210], p86, $Pc^{2-}\,Pr^{III}\,Pc^{\bullet}$.;

[b]: estimated by the heterodimer $Pc^{2-}\,Ce^{IV}\,TPP^{2-}$.

Table 4.4.2.2.

Attribution of the Different Components from Time-Resolved Non-Degenerated Four-Wave Mixing (TRFWM) /Transient Grating (TG) Experiment for the Sublimated Film of the Trimer $Pc^{2-}Nd^{III}TPP^{2-}Nd^{III}Pc^{2-}$

Components	1	2	3
Reference data from transient absorption experiment, $T_1^{(TA)}$ [c] of the trimer in the same family	$T_1^{(TA1)} = 0.7$ ps	$T_1^{(TA2)} = 78.5$ ps	
Data from TRNDFWM or transient grating (TG) experiment, $T_1^{(TG1)}$	$T_1^{(TG1)} = 0.15$ ps	$T_1^{(TG2)} = 2.30$ ps	$T_1^{(TG3)}$ > 1.3 ns
Estimated Diffusion time $\tau_d = T_1^{(D)} = (1/T_1^{(TG)} - 1/T_1^{(TA)})^{-1}$	$T_1^{(D1)} = 0.19$ ps	$T_1^{(D2)} = 2.40$ ps	
Estimated averaged microscopic period Λ of the sublimated film [d]	0.1 μm	0.1 μm	
Diffusion coefficient $D = (\Lambda^2/4\pi^2)/\tau_d$	13 cm^2/s	1.1 cm^2/s	

[c]: ref. [210], p.86, $TPP^{2-}\,Pr^{III}\,Pc^{2-}\,Pr^{III}\,TPP^{2-}$;

[d]: estimated by the trimer $TPP^{2-}\,Ce^{III}\,Pc^{2-}\,Ce^{III}\,TPP^{2-}$.

$$
\begin{aligned}
&{}^{T_0}\left[Pc^{2-}Nd^{III}TPP^{2-}Nd^{III}Pc^{2-}\right] \xrightarrow{h\upsilon} {}^{3T}\left[Pc^{2-}Nd^{III}TPP^{2-}Nd^{III}Pc^{2-}\right]^{*},\\
&{}^{3T}\left[Pc^{2-}Nd^{III}TPP^{2-}Nd^{III}Pc^{2-}\right]^{*} \xrightarrow{\tau_1} {}^{5Q}\left[Pc^{2-}Nd^{III}TPP^{2-}Nd^{III}Pc^{2-}\right]^{*}, \qquad (4.4.2.2.)\\
&{}^{5Q}\left[Pc^{2-}Nd^{III}TPP^{2-}Nd^{III}Pc^{2-}\right]^{*} \xrightarrow{\tau_2} {}^{T_0}\left[Pc^{2-}Nd^{III}TPP^{2-}Nd^{III}Pc^{2-}\right].
\end{aligned}
$$

In a TRNDFWM experiment, optical pumping of an excited state leads to the formation of an transient grating. The decay of the TRNDFWM signal is due to the decay of the grating and is related to the relaxation of the excited states to the ground state. There are many mechanisms that can cause degrating, for example, intersystem relaxation (energy transfer between excited states), long-range electron transfer processes, such as photorefractive effects, rotational and translational diffusion, liberational motion, etc. In symmetric bis- phthalocyanine and tris-phthalocyanine-porphyrin the predominant process, rather than being electron transfer, is excitation migration which causes an ultrafast nonlinear optical response and gives a temporal response time $T_1^{(TGj)}$ as given in (4.1.2.8.1.). In addition to the longitudinal relaxation time $T_1^{(TAj)}$, $j = 1, 2$ detectable by transient absorption experiment, in time-resolved non-degenerate four-wave mixing experiment, the excitation migration through the excitonic coupling between the neighbouring molecules contributes likewise to the depopulation processes of the excited states, which gives rise to diffusion decay times $T_1^{(Dj)}$, $j = 1, 2$ as given in (4.1.2.8.2.), in respect to grating decaying time $T_1^{(TGj)}$, $j = 1, 2$. By (4.1.2.8.6.), the diffusion decay times can be calculated, consequently giving the results in the fourth line of Table 4.4.2.1. for the dimer and Table 4.4.2.2. for the trimer. The diffusion coefficients D_j, j = 1, 2 can be estimated by (4.1.2.8.3.).

By the given geometry in our TRFWM experiment, the space period of the grating, Λ can be estimated to be 11.28 μm, with which the obtained diffusion coefficients D_1, D_2 would be unreasonably large. The exact data of the microcrystal domains of the dimer $Pc^{2-}Pr^{III}Pc^{\bullet}$ and of the trimer $TPP^{2-}Pr^{III}Pc^{2-}Pr^{III}TPP^{2-}$ are not available

presently, however we can estimate them by the given data of heterodimer $Pc^{2-}Ce^{IV}TPP^{2-}$ [122] and the trimer $TPP^{2-}Ce^{III}Pc^{2-}Ce^{III}TPP^{2-}$ [229]. Suppose the diffusion coefficients of the dimer $Pc^{2-}Nd^{III}Pc^{\bullet}$ and the trimer $Pc^{2-}Nd^{III}TPP^{2-}Nd^{III}Pc^{2-}$ are of the same order of magnitude of those of the heterodimer $Pc^{2-}Ce^{IV}TPP^{2-}$ and $TPP^{2-}Ce^{III}Pc^{2-}Ce^{III}TPP^{2-}$, then the size of the mirocrystal domain of the dimer $Pc^{2-}Pr^{III}Pc^{\bullet}$ can be estimated as **0.05 μm / 0.077 μm** by 2.8 cm²/s / 0.74 cm²/s of the heterodimer $Pc^{2-}Ce^{IV}TPP^{2-}$, and that of the trimer $TPP^{2-}Pr^{III}Pc^{2-}Pr^{III}TPP^{2-}$ as **0.14 μm / 0.09 μm** by 30 cm²/s / 0.87 cm²/s of the trimer $TPP^{2-}Ce^{III}Pc^{2-}Ce^{III}TPP^{2-}$. For the reason of simplification and unification, the two values are just taken as **0.1 μm**. Since this estimated averaged size of about 0.1 μm, is smaller than that of the grating period, therefore, it is the averaged size of the microscopic crystalline domains that should be used instead of the calculated grating spacing period. This estimated averaged value is put in the fifth line of the Table 4.4.2.1. for the dimer and Table .4.4.2.2. for the trimer, and into (4.1.2.8.3.) yielding the estimated diffusion coefficients given in the sixth line of the Tables: D_1 = 11 cm²/s and D_2 = 1.2 cm²/s, for the dimer $Pc^{2-}Nd^{III}Pc^{\bullet}$, and D_1 = 13 cm²/s and D_2 = 1.1 cm²/s, for the trimer $Pc^{2-}Nd^{III}TPP^{2-}Nd^{III}Pc^{2-}$. These values are quite reasonable because they are of the same order of magnitude as typical values of the diffusion coefficient: $D_{\text{Charge Transfer}}$ = 10 cm²/s and $D_{\text{Energy Transfer}}$ = 2.0 cm²/s [215 - 226].

On the basis of the above analysis, the three observed components in our TRFWM experiment, $T_1^{(TG1)}$, $T_1^{(TG2)}$ and $T_1^{(TG3)}$, for the dimer and the trimer can be attributed as shown in the schematic presentations in Fig. 4.4.2.11. (b) and in Fig. 4.4.2.12. (b).

In the TRNDFWM experiments, two 620 nm pump pulses generate an excited state with a population $P_1(t)$ (doublet ^2S for the dimer $Pc^{2-}Nd^{III}Pc^{\bullet}$, and triplet ^3T for the trimer $Pc^{2-}Nd^{III}TPP^{2-}Nd^{III}Pc^{2-}$). This population, with $\tau_1 = T_1^{(TA1)}$ (≈ 1.1 ps for the dimer, ≈ 0.7 ps for the trimer, estimated by ref. [210]) relaxes into the next excited state with a population $P_2(t)$ (quadruplet ^4Q for the dimer, and quintuplet

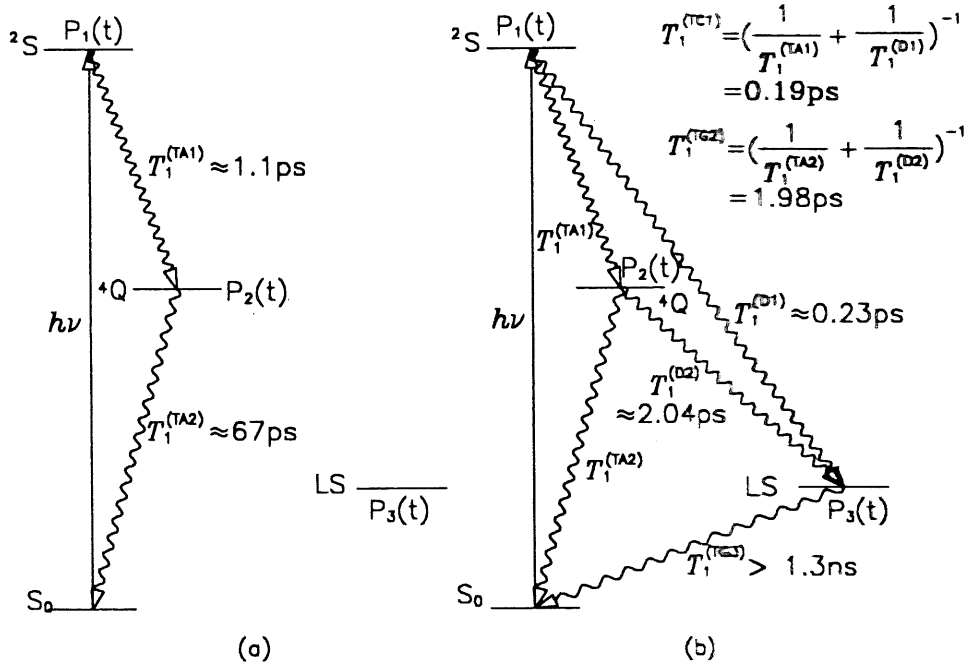

Figure 4.4.2.11. Schematic Presentation of the Relaxation Paths of the Sublimated Film of the Dimer $NdPc_2$ in the Experiment of (a): Transient Absorption and (b): Time-Resolved Four-Wave Mixing.

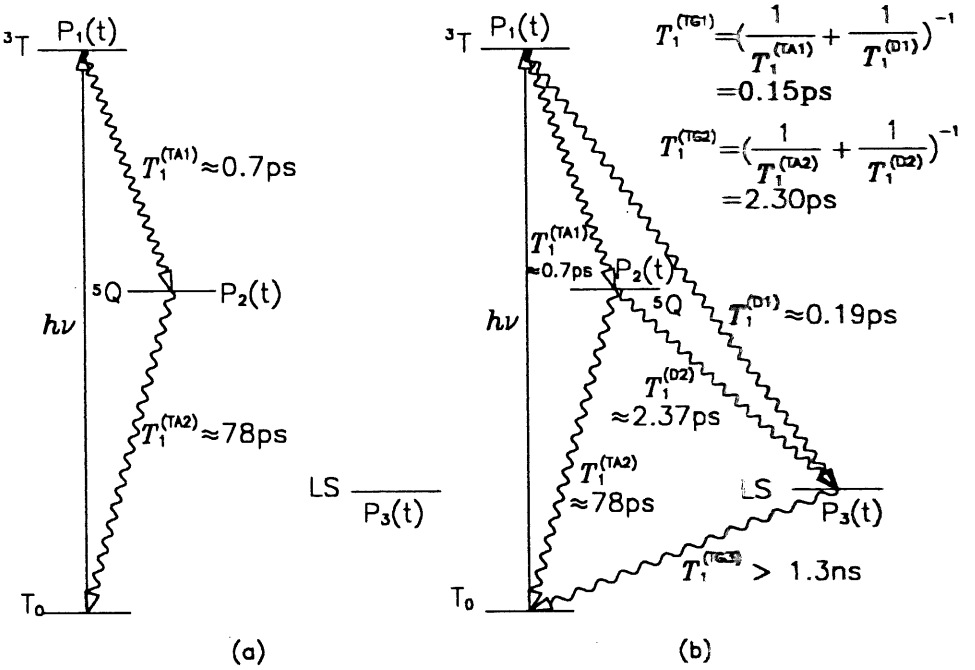

Figure 4.4.2.12. Schematic Presentation of the Relaxation Paths of the Sublimated Film of the Trimer $(NdPc)_2TPP$ in the Experiment of (a): Transient Absorption (TA), (b):Time-Resolved Four-Wave Mixing.

^5Q for the trimer), then with $\tau_2 = T_1^{(TA2)}$(≈ 67 ps for the dimer, ≈ 78 ps for the trimer, estimated by ref. [210]) relaxes towards the ground state (S_0 for the dimer, and T_0 for the trimer). Because of the existence of excitation migration, the first two transient grating decaying times $T_1^{(TG1)}$ and $T_1^{(TG2)}$ are much shorter than the longitudinal life times of the excited states, as shown by (4.1.2.8.1.), in Table 4.4.2.1., in Table 4.4.2.2., in Fig.4.4.2.11. (b), and in Fig. 4.4.2.12. (b). The diffusion times $T_1^{(D1)}$ and $T_1^{(D2)}$ are related to the excitation migration by excitonic coupling between neighbouring molecules. The longest components, $T_1^{(TG3)}$ in the dimer and in the trimer, are related to the system returning from the low lying excited states (LS) to the ground states. They take longer times than the limit of the TRNDFWM detecting system, i.e., 1.3 ns. These long times responses originate from the same effect — *photorefractivity* — as the other three samples discussed in section 4.1 ~ 4.3. . This will be treated thoroughly in section 4.6. .

4.4.3. Summary

We have presented time-resolved non-degenerate four-wave mixing (TRNDFWM) measurements on the third order nonlinear optical properties of sublimated films of the neodymium phthalocyanine dimer $Pc^{2-}Nd^{III}Pc^{\bullet-}$ and the neodymium porphyrin phthalocyanine trimer, $Pc^{2-}Nd^{III}TPP^{2-}Nd^{III}Pc^{2-}$.

The dynamics of the diffracted signal show that the dimer system possesses a fast subpicosecond relaxation time of 0.19 ps, an intermediate relaxation time of 1.98 ps and a very long relaxation time of > 1.3 ns, while the trimer system possesses those of 0.15 ps, 2.30 ps and > 1.3 ns. The longest response times are supposed to be related to photorefractive effect which will be discussed in detail in section 4.6. .

The existence of the excitation migration has, however, effectively shortened the response times. In the case of symmetric dimer $Pc^{2-}Nd^{III}Pc^{\bullet-}$ and the trimer,

$Pc^{2-}Nd^{III}TPP^{2-}Nd^{III}Pc^{2-}$, excitation migration is one of the predominant degrating processes. Comparing with the data from transient absorption experiments on the samples of the same family of lanthanide bis- and tris-phthalocyanine-porphyrins, it is found that the relaxation times detected by time-resolved non-degenerate four-wave mixing are shorter than those by transient absorption due to the existence of excitation migration. TRNDFWM is a very effective and very sensitive technique for detecting various $\chi^{(3)}$ processes, especially, for those processes that cannot be detected by transient absorption experiments.

When the grating spacing is bigger than the averaged size of the microscopic crystalline domain of the sublimated film, the latter, instead of the former, should be used to make a correct estimation of the diffusion coefficient. Taking the microscopic structure and diffusion coefficients of the sublimated film of the dimer $Pc^{2-}Ce^{IV}TPP^{2-}$ and the trimer $TPP^{2-}Ce^{III}Pc^{2-}Ce^{III}TPP^{2-}$ that we have investigated in previous sections, as references to estimate the averaged sizes of the microscopic crystal domains of the dimer and the trimer, the diffusion coefficients of the first two components have been estimated to be 12 cm^2/s and 1.2 cm^2/s for the dimer, and 13 cm^2/s and 1.1 cm^2/s for the trimer, which are compatible to typical values of the diffusion coefficient for energy transfer processes.

Owing to the stacked formation of the dimer and the trimer which favours the delocalization of the conjugated π-electrons, we will show in the next section that the third-order optical nonlinear susceptibilities have been greatly increased as compared to those of the free phthalocyanine and the mono-metallophthalocyanines. The results show that the third-order nonlinear optical susceptibility $\chi^{(3)}$, measured to be 15×10^{-10} esu for the dimer and 8.8×10^{-10} esu for the trimer. Details about the $\chi^{(3)}$ calculation will be given in section 4.5. .

4.5. Determination of the Absolute Values of the Third-Order Nonlinear Optical Susceptibilities $\chi^{(3)}$

In this section, we will calculate and calibrate the absolute values of the third-order nonlinear optical susceptibility $\chi^{(3)}$ for the sublimated thin films of the dimer $Pc^{2-}Nd^{III}Pc^{\bullet}$, the heterodimer $Pc^{2-}Ce^{IV}TPP^{2-}$, the trimer $TPP^{2-}Ce^{III}Pc^{2-}Ce^{III}TPP^{2-}$, $Pc^{2-}Nd^{III}TPP^{2-}Nd^{III}Pc^{2-}$, and the Langmuir-Blodgett films of mixed dimer $CoPC_{22}{}^{4+}$ / H_2PcTS^{4-}, by comparing the TRFWM data of these thin films with that of reference silica glass under the same experimental conditions, using an analysis appropriate for thin absorbing materials [238, 239].

4.5.1. The Expression of the Third-Order Nonlinear Optical Susceptibility $\chi^{(3)}$

If the spatial arrangement of the four-wave mixing beams is as shown in Fig. 3.4.1.1., which gives the wave vector diagram shown in Fig. 3.4.1.2., then the pump lights, the probe light and the diffracted signal light can be expressed as:

$$E_j(\omega_j) = E_{0j} e^{i(\tilde{k}_j \cdot r - \omega_j t)}, \quad j = 1,2: pump, \quad j = 3: probe, \quad j = 4: signal; \tag{4.5.1.1.}$$

where,

$$\tilde{k}_j = k_j - k_0 \kappa_j = k_j - i\frac{1}{2}\alpha_j , \tag{4.5.1.2.}$$

$$\tilde{k}_4 = \tilde{k}_1 - \tilde{k}_2 + \tilde{k}_3 , \tag{4.5.1.3.}$$

$$\omega_4 = \omega_1 - \omega_2 + \omega_3 , \tag{4.5.1.4.}$$

and

$$\boldsymbol{P}^{(4)}(\omega_4) = \chi^{(3)}(\omega_4 = \omega_1 - \omega_2 + \omega_3) : \boldsymbol{E}(\omega_1)\boldsymbol{E}^{*}(\omega_2)\boldsymbol{E}(\omega_3) \qquad (4.5.1.5.)$$

Putting (4.5.1.5.) into the coupled wave equation (2.3.15.), with the approximation of SVA, (Chapter 2, section 2.3. ~ 2.4.), one get [188]:

$$\frac{\partial \boldsymbol{E}_4}{\partial z} \pm \frac{\omega^2}{c^2} n_4 \boldsymbol{E}_4 = \pm i \frac{\omega^2}{2 k \varepsilon_0 c^2} \mathbf{P}^{NL}(z,t)\, e^{-i(kz \mp \omega t)}, \qquad (4.5.1.6.)$$

where, (+, +, –) is for forward propagating wave, (–, –, +) for backward propagating wave. Under the approximation of IPW, CPI, and with the boundary condition:

$$\boldsymbol{E}_4(0) = 0, \qquad (4.5.1.7.)$$

by coupled wave approach, we can get the solution for the forward propagating wave as:

$$\boldsymbol{E}_{4i} = \frac{2\pi\omega_4^2}{(\Delta \boldsymbol{k} \cdot \boldsymbol{e}_z) k_4 c} \chi^{(3)}_{ijkl}(\omega_4) : \boldsymbol{E}_{1j} \boldsymbol{E}^{*}_{2k}\, \boldsymbol{E}_{3l} (1 - e^{-i\Delta \boldsymbol{k} \cdot \boldsymbol{z}}) e^{-\frac{1}{2}\alpha_{4i} z}. \qquad (4.5.1.8.)$$

In our case here,

$$|\alpha_1| = |\alpha_2|, \quad |\alpha_3| = |\alpha_4|, \qquad (4.5.1.9.)$$

and under phase-matching,

$$\Delta \boldsymbol{k} = \boldsymbol{k}_1 - \boldsymbol{k}_2 + \boldsymbol{k}_3 - \boldsymbol{k}_4 = 0, \qquad (4.5.1.10.)$$

$$-i\Delta \tilde{\boldsymbol{k}} \cdot \boldsymbol{z} = -i(\Delta \boldsymbol{k} - i\frac{1}{2}\Delta \alpha) \cdot \boldsymbol{z} = -\frac{1}{2} z(\alpha_{1j\,z} - \alpha_{2k\,z} + \alpha_{3l\,z} + \alpha_{4i\,z}) = -\alpha z, \qquad (4.5.1.11.)$$

using the relation

$$k = \frac{\omega}{c} n, \qquad (4.5.1.12.)$$

finally, (4.5.1.8.) becomes:

$$E_{4i} = \frac{2\pi k_4}{i\alpha n^2}\chi^{(3)}_{ijkl}(\omega_4):E_{1j}E^*_{2k}\,E_{3l}(1-e^{-\alpha z})e^{-\frac{1}{2}\alpha z}. \qquad (4.5.1.13.)$$

If the signal travelling distances in a reference and a sample are l_{ref} and l respectively, by comparing the FWM signals of the sample with that of the reference under the same experimental conditions, we get:

$$\chi^{(3)}_s(\omega_4) = \chi^{(3)}_{ref}(\omega_4)\left(\frac{I_4}{I_{4ref}}\right)^{\frac{1}{2}}\frac{e^{-\alpha_{ref}l_{ref}/2}(1-e^{-\alpha_{ref}l_{ref}})}{e^{-\alpha l/2}(1-e^{-\alpha l})}\frac{\alpha n^2}{\alpha_{ref}n^2_{ref}}. \qquad (4.5.1.14.)$$

If the reference is nearly lossless, therefore,

$$\frac{(1-e^{-\alpha_{ref}l_{ref}})}{\alpha_{ref}l_{ref}} \approx 1, \qquad (4.5.1.15.)$$

and

$$e^{-\alpha_{ref}l/2} \approx 1, \qquad (4.5.1.16.)$$

in this case, we have:

$$\chi^{(3)} = \chi^{(3)}_{ref}\left(\frac{I_4}{I_{4ref}}\right)^{\frac{1}{2}}\left(\frac{n}{n_{ref}}\right)^2\left(\frac{l_{ref}}{l}\right)\left(\frac{\alpha l}{e^{-\alpha l/2}(1-e^{-\alpha l})}\right). \qquad (4.5.1.17)$$

4.5.2. The Calculation of the Absolute Values of the Third-Order Nonlinear Optical Susceptibility $\chi^{(3)}$ of the Samples

To get the absolute values of the third-order nonlinear optical susceptibility $\chi^{(3)}$ of the samples, one needs to use the $\chi^{(3)}$ value of a given material whose $\chi^{(3)}$ is already

known as reference. Commonly used reference materials are CS_2 and fused quartz. Because using CS_2 one needs to calibrate the FWM contribution from its container (often a quartz cell), which would cause extra problems in some cases, we chose fused quartz as a reference material, which at 620 mn and 650 nm is lossless.

In the FWM experiment, the pump power often needs to be adjusted to a suitable level under the damage threshold of the samples, by changing the optical density of the attenuators in the light path. Thereby, the actual formula used to calculate $\chi^{(3)}$ values of the samples should be:

$$\chi^{(3)} = \chi^{(3)}_{ref}\left(\frac{I_4 / I_0^3}{I_{4ref}/I_{0ref}^3}\right)^{\frac{1}{2}}\left(\frac{n}{n_{ref}}\right)^2\left(\frac{l_{ref}}{l}\right)\left(\frac{\alpha l}{e^{-\alpha l/2}(1-e^{-\alpha l})}\right). \qquad (4.5.2.1.)$$

In (4.5.2.1.), $\chi^{(3)}_{ref} = \chi^{(3)}_{quartz} = 2.8 \times 10^{-14}$ esu [240], is the reference value of the third-order nonlinear susceptibility $\chi^{(3)}$ for quartz. l_{ref} is the thickness of the silica glass slide. $n_{ref} = n_{quartz} = 1.457399$ [241], is the refractive index of the reference quartz. l is the sample thickness which was measured by a TENCOR profilometor, model Alpha-Step 200. In a small angle FWM geometry, the interaction distance l_c of the beams is generally big enough to make $l_c > l_{ref}$ and $l_c > l$. If not, l and l_{ref} should be replaced by l_c. The measured values of the thickness of the samples are given in the sixth line of Table 4.5.2.1. . n is the refractive index of the sample which was measured by an *Applied Material* ellipsometer model II. The experimental data on the refractive index of the samples are listed in the fifth line of Table 4.5.2.1. . α is the absorption coefficient of the sample at the laser wavelength of 650 nm in cm^{-1} , which was measured by routine transmission-absorption measurement procedures. The α data of the samples are expressed in terms of optical density OD and have been written into the fourth line of the Table 4.5.1.1. . I_4, I_{4ref} are the intensities of the TRFM signals of the sample and the reference under the same experimental conditions, which appear in the eleventh and the ninth lines of Table 4.5.1.1. . I_0, I_{0ref} are the signals proportional to the source laser intensities used during the experiment. The subscript *ref* refers to the reference material which is fused quartz. The reference was assumed

to have no absorption at the pump and probe wave length 620 nm, 650 nm. Under our given TRFWM geometry and focusing of the pump and probe pulses, the beam overlapping distance is longer than the thickness of the reference silica glass and those of the samples. This has been tested by recording the TRFWM signal while moving the reference quartz slide along the symmetric axis of the four beams. Since the thicknesses of the films are much smaller than the overlapping distance, the measured actual thicknesses of the films in the sixth line of Table 4.5.1.1. are used to make the calculation. The obtained peak values of the third-order nonlinear optical susceptibilities of the samples, are listed in the sixteenth line of Table 4.5.1.1.: $\chi^{(3)}_{PcCeTPP} = 7.8 \times 10^{-10}$ esu, $\chi^{(3)}_{TPP^{2-}Ce^{III}Pc^{2-}Ce^{III}TPP^{2-}} = 3.4 \times 10^{-10}$ esu, $\chi^{(3)}_{NdPc_2} = 15 \times 10^{-10}$ esu, $\chi^{(3)}_{(NdPc)_2TPP} = 8.9 \times 10^{-10}$ esu, and $\chi^{(3)}_{CoPC_{22}{}^{4+}/H_2PcTS^{4-}} = 8.3 \times 10^{-11}$ esu. These values of $\chi^{(3)}_{xxxx}(-\omega_{signal}, \omega_{pump1}, -\omega_{pump2}, \omega_{probe})$, compared with those values of natural phthalocyanine, mono-metallophthalocyanines, and bis-metallophthalocyanines [242 - 248], listed in Table 4.5.2.2. is among those with the largest $\chi^{(3)}$. This is presumably because of the stacked sandwich formation which extensively increases the delocalization of the π-conjugated electrons and thus increases the $\chi^{(3)}$ response. On the other hand, the excitation migration and charge transfer cause much shorter response times than those without contribution of these processes. In Langmuir-Blodgett films, orderly molecular assemblies may also give an orientational contribution to the $\chi^{(3)}$ value. Since the 620 nm pumps fall in the strong absorption band of these samples, the resonance enhancement effect will also effectively increase the $\chi^{(3)}$ response of these samples.

Table 4.5.2.1.

Peak Values of the Third-Order Nonlinear Optical Susceptibilities $\chi^{(3)}$.

Name of the Sample:	PcCeTPP	$Pc(CeTPP)_2$	$NdPc_2$	$TPP(NdPC)_2$	$CoPC_{22}^{4+}$/ H_2PcTS^{4-}
I_0	2.048	2.252	2.099	2.252	2.203
I	0.2100	0.8040	1.255	0.4990	0.4930
$\Delta OD = \ln(\frac{I_0}{I})$	2.278	1.030	0.5143	1.507	1.497
n_{sample} [a]	1.807	1.838	1.762	1.754	1.680
l_{sample} (Å) [b]	2395	1325	305	1325	11690
$n_{substrate}$ [c]	1.445702	1.45702	1.45702	1.45702	1.51507
Substrate	quartz	quartz	quartz	quartz	glass
I_{ref}	12780	12780	12780	4319	10540
OD_{ref}	0.70	0.70	0.70	0.70	0.70
I_{sample}	2418	1149	3462	1362	2721
OD_{sample}	0.70	0.70	0.70	0.70	0.70
n_{ref}	1.45670	1.45670	1.45670	1.45670	1.45670
l_{ref}	1.25 mm	1.25 mm	1.25 mm	1.25 mm	1.25 mm
$\chi^{(3)}_{ref}$ ($\times 10^{-14}$ esu)	2.8	2.8	2.8	2.8	2.8
$\chi^{(3)}_{sample}$ ($\times 10^{-10}$ esu) [d]	7.8	3.4	15	8.8	0.83

[a]: Measured by Ellipsometer II, *Applied Material Inc.*
[b]: Measured by TENCOR profilometor, model Alpha-Step 200
[c]: from Melles Griot, *Optics Guide 5*, ISSN 1051-4384, 1990.
[d]: Calculated by (4.5.2.1.)

Table 4.5.2.2.

Third-Order Nonlinear Optical Susceptibility $\chi^{(3)}$ of Some Metallophthalocyanines

Compound [a]	Experimental Technique	$(-\omega_4, \omega_1, \omega_2, \omega_3)$	$\chi^{(3)}(-\omega_4, \omega_1, \omega_2, \omega_3)$ ($\times 10^{-12}$ esu)	Reference
H_2PcCP4	DFMW	$(-\omega, \omega, \omega, -\omega)$	4.0	[242]
PbPcCP4	DFMW	$(-\omega, \omega, \omega, -\omega)$	20.0	[242]
PtPcCP4	DFMW	$(-\omega, \omega, \omega, -\omega)$	200.0	[242]
RSiPc	DFMW	$(-\omega, \omega, \omega, -\omega)$	1800.0	[242]
PtPc	DFMW	$(-\omega, \omega, \omega, -\omega)$	200.0	[242]
$Sc(Pc)_2$	DFMW	$(-\omega, \omega, \omega, -\omega)$	1700	[242]
ClGaPc	THG	$(-3\omega, \omega, \omega, \omega)$	25.0	[242]
FAlPc	THG	$(-3\omega, \omega, \omega, \omega)$	50.0	[242]
CuPc	THG	$(-3\omega, \omega, \omega, \omega)$	4.0	[242]
ClInPc	THG	$(-3\omega, \omega, \omega, \omega)$	130.0	[242]
VOPc	THG	$(-3\omega, \omega, \omega, \omega)$	18.5	[242]
TiOPc	THG	$(-3\omega, \omega, \omega, \omega)$	27.0	[242]
CoPc	THG	$(-3\omega, \omega, \omega, \omega)$	0.76	[242]
NiPc	THG	$(-3\omega, \omega, \omega, \omega)$	0.80	[242]
$CuPc(C_4H_9S)_4$	THG	$(-3\omega, \omega, \omega, \omega)$	3.7	[242]
$CuPc(C_{10}H_{21}S)_4$	THG	$(-3\omega, \omega, \omega, \omega)$	26.0	[242]
$VOPc(C_6H_{13}S)_4$	THG	$(-3\omega, \omega, \omega, \omega)$	9.8	[242]
VOPc	THG	$(-3\omega, \omega, \omega, \omega)$ $\lambda = 1.907$ μm	93	[243]
SnPc	THG	$(-3\omega, \omega, \omega, \omega)$ $\lambda = 1.907$ μm	40	[243]
CoPc	THG	$(-3\omega, \omega, \omega, \omega)$ $\lambda = 1.907$ μm	7.5	[243]
H_2Pc	THG	$(-3\omega, \omega, \omega, \omega)$ $\lambda = 1.907$ μm	3.0	[243]
NiPc	THG	$(-3\omega, \omega, \omega, \omega)$ $\lambda = 1.907$ μm	2.3	[243]

TBVOPc	THG	$(-3\omega, \omega, \omega, \omega)$ $\lambda = 1.907$ μm	6.0	[243]
TBH_2Pc	THG	$(-3\omega, \omega, \omega, \omega)$ $\lambda = 1.907$ μm	1.9	[243]
TBNiPc	THG	$(-3\omega, \omega, \omega, \omega)$ $\lambda = 1.907$ μm	2.0	[243]
FAlPc	THG	$(-3\omega, \omega, \omega, \omega)$ 1064 (355) nm	50	[244]
ClAlPc	THG	$(-3\omega, \omega, \omega, \omega)$ 1064 (355) nm	25	[244]
VOPc	THG	$(-3\omega, \omega, \omega, \omega)$ 1907 (636) nm	190	[245]
VO(t-BuPc)	THG	$(-3\omega, \omega, \omega, \omega)$ 1907 (636) nm	7.5	[245]
H_2Pc	THG	$(-3\omega, \omega, \omega, \omega)$ 1907 (636) nm	6	[245]
H_2(t-BuPc)	THG	$(-3\omega, \omega, \omega, \omega)$ 1907 (636) nm	3	[245]
Pc-R′	THG	$(-3\omega, \omega, \omega, \omega)$ 1064 (355) nm	1-3	[246]
CuPc	THG	$(-3\omega, \omega, \omega, \omega)$ 1064 (355) nm 1907 (636) nm	7.5 3.4	[247] [248]
Si-nPc	THG	$(-3\omega, \omega, \omega, \omega)$ 1907 (636) nm 1543 (514) nm	$\gamma = 3 \times 10^{-33}$[b] $\gamma = 5 \times 10^{-35}$[b]	[248] [248]

[a]: CP4 = Tetrakis(cumylphenoxy),
R = $(OSiMe(Ph)OH)_2$,
VO = alkoxy derivatives of vanadyl,
R′ = Polysiloxane,
nPc = naphthalocyanine

[b]: *second hyperpolarizability*, defined in Chapter2, (2.1.9).

4.6. Photorefractive Effect

Of the many nonlinear optical effects that TRFWM is sensitive to, photorefractivity, is one of the most interesting ones. As described in section 1.3.2., the photorefractive effect is a light-induced change in the index of refraction of a crystalline material. The standard model goes as follows. It normally takes place in four steps: first strong pump fields generate a large number of charge carriers, then these carriers are transported, afterwards trapped, and finally, by the Pockels effect, the refractive index is modulated. Though referred to as "optical damage" when the effect was first discovered, it was soon realized that refractive index gratings written and stored in such crystals could be used for a wide range of optical applications. Photorefractive crystals can be used to make up simple phase conjugators with applications in distortion correction, laser power combining, remote sensing, and tracking systems. These materials may also play an important role in various optical computing and signal processing devices such as reconfigurable optical interconnectors, associative memories, and passive limiters for sensor protection.

The most widely studied photorefractive materials can be divided into four classes, as listed in Table 1.3.2.1., : ferroelectric oxides and tungsten bronze-type crystals, oxides of the sillenite family, semi-insulating compound semiconductors, and organics. For the organics, there are two categories are known: doped organic crystals [180], for example pyridinium ylide [180], and doped organic polymers, for examples bisA-DPDA (bisphenol-*A*-diglycidylether 4-nitro-1, 2-phenylenediamine) [181] , PVK-TNF (poly *N*-vinylcarbazole 2, 4, 7, -trinitro-9-fluorennone) [182] and PMMA:DTNBI:C_{60} (poly-methylmethacrylate: 1, 2, -dimethyl-2, 2-tetramethylene-5-nitrobenzimidazoline: fullerene) [183]. ***Up to date, photorefractive effect in organic multimer (dimer, heterodimer, trimer, or heterotrimer, etc.) films have never been observed and reported.***

In our TRNDFWM investigation on organo-metallic systems, we have observed **long-time responses** up to 1.3 ns, ***in all the five lanthanide porphyrin phthalocyanine multimer thin film samples*** (Figure 4.1.2.1.4. for $Pc^{2-}Ce^{IV}TPP^{2-}$, Figure 4.2.2.6. for $TPP^{2-}Ce^{III}Pc^{2-}Ce^{III}TPP^{2-}$, Figure 4.3.2.8. for $CoPC_{22}^{4+}$ / H_2PcTS^{4-}, 4.4.2.6. for $Pc^{2-}Nd^{III}Pc^{\bullet}$, and 4.4.2.10. for $Pc^{2-}Nd^{III}TPP^{2-}Nd^{III}Pc^{2-}$). Because we have

introduced a special noise reduction technique, called ***Transparent Shuttle*** (Figure 3.4.0.1., and section 3.5.), to get the signal S free from the background noise B by substracting B from the collected light A (equation (3.5.1.), even these long-time response signals are not very strong, but they are clear enough to be distinguished from the background. **What we got are definitely real signals.** Since even the compounds that we got the long-time responses, are different molecular systems (dimer (DM) for $Pc^{2-}Nd^{III}Pc^{\bullet}$, heterodimer (HDM) for $Pc^{2-}Ce^{IV}TPP^{2-}$, trimer (TM) for $TPP^{2-}Ce^{III}Pc^{2-}Ce^{III}TPP^{2-}$ and for $Pc^{2-}Nd^{III}TPP^{2-}Nd^{III}Pc^{2-}$, mixed dimer (MDM) for $CoPC_{22}{}^{4+}$ / H_2PcTS^{4-}), and are made into different thin films (sublimated films for the first four of the above five, Langmuir-Blodgett film of the last of the above five), they possess the same long-time responses. Therefore, there should be something in common which gives rise to the same phenomenon. We find what in common for these molecular systems are that there exist microscopically ordered domains, there exist charge and energy migration processes, which we believe to be most probably related to a well know phenomenon, ***photorefractivity***.

The common elements we have found in these DM, HDM, TM, HTM, MDM systems, as we have discussed in section 4.1.3.3., section 4.1.3.4. and section 4.1.3.5., is that, in these systems, there always exist either intramolecular charge transfer or intermolecular energy transfer, or both. These transport cause molecular dipoles or excitonic excitations to migrate from one molecule to the others in the microcrystalline domains. Any free charges, if they are produced, are thus expected to similarly diffuse. If there exist some barriers or "trapping centers", these moving molecular dipoles or excitations will be expected to be held down or trapped there.

In the sublimated films, as discussed in sections 4.1.3.8. and 4.2.3.8. and as shown in Fig. 4.1.3.8.1. and Fig. 4.2.3.8.1., the grain boundaries are natural candidates. These microscopic crystalline domains averaged between 0.2 μm and 0.3 μm, will capture the moving molecular dipoles or excitations and hold them there.

In Langmuir-Blodgett film, though theoretically speaking, the molecules should be arranged more regularly. Nevertheless, according to our experiments, this is not always the case: even in some "high quality" Langmuir Blodgett films, the diffusion light could be so intense that the TRFWM experiment was impossible to carry out.

There are definitely local irregularities in these films. In fact, during the deposition of the Langmuir-Blodgett film, the molecules in the monolayer on the subphase, could be clustered, crystallized, or polymerized. Therefore, in the resulting Langmuir-Blodgett film, there exist some local irregularities is just a natural thing. We have observed such kind of irregularities on the Langmuir-Blodgett film when measuring the sample thickness. Thus, in Langmuir-Blodgett film, moving excited species will be also held down or trapped on the boundary between two homogeneous regions.

Now it is clear that photorefractive effect can happen in the sublimated and Langmuir-Blodgett films of lanthanide porphyrin phthalocyanine dimer/heterodimer and trimer/heterotrimer systems, and, it is really happening there. In these systems, there are large number of electron donors, either porphyrin or phthalocyanine depending on the cases, which will form molecular dipoles and excitonic excitation when excited by laser pump. When studied by TRFWM, two strong pump pulses create a great quantity of excited species. Due to the similarity between the neighbouring molecules, these molecular dipoles or excitations will be quickly and effectively transported, migrated or diffused from one excited molecule to the other by the coupling of the charge transfer states (section 4.1.3.3.), by the spin-orbital coupling (section 4.1.3.4.) and by excitoninc coupling (section 4.1.3.5.) between the neighbouring molecules. The boundary of the microscopic crystalline domains in sublimated films, as shown in Fig. 4.1.3.8.1., and Fig. 4.2.3.8., and the boundary between two homogeneous regions in Langmuir-Blodgett film, which play the roles as "trapping center" in semiconductor and other crystalline material, will trap and hold down the moving charges or excitations. These trapping and holding down will eventually created new internal space charge fields, which alter the local refractive index of the material by the Pockels effect, and give us a long time response, as shown in Fig. 4.1.3.1.4, Fig. 4.2.3.6., Fig. 4.3.3.8., Fig. 4.4.3.6., and Fig. 4.4.3.10. . If the above mechanism is correct (and it appears established for the materials known to the date), then, we have actually observed ***the first photorefractive effect in an organic multimer thin film.***

The photo-production of free carriers is unfortunately hypothetical. We have no direct evidence of such production other than the existence of the photorefractive

effect. We are sure, however, that excitons are produced and also a CT state in the HDM system. The size of the photorefractive effect is at least four times larger in the HDM than in any other system. This suggests that the CT dipole may play a novel role in photorefractivity. Are dipole layers generated at grain boundaries consistent with the phonon modulation models and could they generate internal electrical fields? Do the dipoles transfer their energy at the grain boundaries and generate metastable excited states or even free carriers in the bulk? Or perhaps the CT state favours the creation of bulk free charge carriers? These questions have not been answered yet.

A thorough investigation on the photorefractive effect of the lanthanide dimer/heterodimer and symmetric trimer thin film needs complete identification of ionizing centers and charge species involved, knowing relative importance of electrons and holes, detailed structure of the microscopic crystalline domains, and the establishment of an appropriate theoretical model, especially for the organic crystals and thin films.

Photorefractive effect is caused by free electrons which are released from donors by the incident light. The observation of this effect needs some spatial modulation of the light intensity. Periodic grating-like excitation, for example, four-wave mixing scheme, is particularly well suitable for experimental observation of the photorefractive effect and is convenient for its theoretical descriptions.

The movement of the photoexcited free charge carriers can be affected by three different mechanisms: *diffusion*, *drift* (when existing an external electrical field) and the *photovoltaic effect*. In common cases, the free charge carriers are moving in the lattice field of the crystal of the material. This kind of moving is generally forbidden in organics even in crystals under normal conditions, and that is why organic photorefractive materials are rarely seen. However, except mechanism of the free charge carriers moving in lattice field, in lanthanide porphyrin phthalocyanine dimer/heterodimer trimer/ heterotrimer systems, there exist the other two equivalent mechanisms: molecular dipole migration by charge transfer state coupling, by spin-orbital coupling and excitonic excitation migration by excitonic coupling, between the

neighbouring molecules. These are probably ***one of the most efficient ways to create photorefractive effect in organic materials***.

To make organic photorefractive materials, people just followed the same thinking as making semiconductors: doping, which gives rise to doped organic crystals and doped organic polymers. Nevertheless, the growth of doped organic crystals is a very difficult process because during the crystallization most dopants are expelled. Polymers on the other hand, though relatively easier to be doped, but they need to be doped with charge-generating and transporting agents [249, 250] to make them photoconducting or with poling guest or attached nonlinear chromophores to make them electrooptic [251, 252]. This will cause some extra problem as controlling the ratio between the base, the charge-generating agents and the transporting agents, etc. Contrary to these, lanthanide porphyrin phthalocyanine multimers (dimers, heterodimers, trimers, heterotrimers, etc.) offer another simpler and entirely new approach to photorefractivity: they integrate donor, acceptor and charge transporting mechanism into one unity. The multimers themselves are donors and acceptors, thus need no further doping. The molecular dipole and excitation migration by intersystem couplings between the molecules of lanthanide porphyrin phthalocyanine dimer/heterodimer trimer/heterotrimer have opened new approaches to the photorefractive effects. Furthermore, the common deficiencies in the photorefractive materials presently available, for examples, low sensitivity, inappropriate dimension, etc., can be overcome by the molecular engineering. In this sense, lanthanide porphyrin phthalocyanine dimer/heterodimer trimer/heterotrimer systems could be ***one of the most promising new family of organic materials for the investigations and applications of photorefractive effect.***

In order to fully evaluate this new family of organic photorefractive materials for photorefractive applications, the following aspects need be considered for further studies:

1. photorefractive sensitivity,
2. dynamic range (maximum refractive index change),
3. phase shift between refractive index and light intensity distribution,
4. photorefractive recording and erasure time,
5. spatial frequency dependence,

6. electric field dependence,
7. laser wavelength for inducing refractive index change,
8. resolution,
9. signal-to-noise ratio, and
10. room temperature operation.

We have found photorefractivity in these materials. Contrary to other photorefractive materials, ***lanthanide porphyrin phthalocyanine multimers*** (dimers, heterodimers, trimers, heterotrimers, etc.) ***offer a simpler and entirely new approach to photorefractivity***: they integrate donor, acceptor and charge or molecular dipole transporting mechanism into one unity. They also provide natural trapping centers: the grain boundaries. The multimers themselves are donors and acceptors and there is thus no need for doping. They may provide the free charge carriers usually associated with the photorefractive effect. However, the molecular dipole and excitation migration by intersystem couplings between the molecules of lanthanide porphyrin phthalocyanine dimer/heterodimer trimer/heterotrimer opens new channels to the photorefractive effect. It is hoped that the common deficiencies in the photorefractive materials presently available, for examples, low sensitivity, inappropriate dimension, etc., can be overcome by molecular engineering. In this sense, lanthanide porphyrin phthalocyanine dimer/heterodimer trimer/heterotrimer systems could be a most promising new family of organic materials for the investigations and applications of the photorefractive effect, though there is still a long way to go to make this new family of photorefractive materials viable to the photorefractive applications.

Chapter 5.

Conclusion

We have presented the results of time-resolved four-wave mixing (TRFWM) studies on sublimated and Langmuir-Blodgett thin films of the lanthanide porphyrin phthalocyanine dimer/heterodimer and the symmetric trimer systems. ***This is the first non-degenerate time-resolved four-wave mixing study on sublimated films.***

It has been shown that TRFWM is one of the most sensitive, most useful and most powerful techniques for probing the dynamics of the third-order nonlinear optical processes in materials, especially, those not detectable by transient absorption and other ultrashort time-resolved spectroscopic techniques.

The diffusion processes play an important role in the degrating and can not be neglected when considering the mechanisms related to nonlinear optical processes. In the lanthanide porphyrin phthalocyanine dimer/heterodimer and trimer/heterotrimer systems, there exist intramolecular charge transfer and intermolecular energy transfer processes which cause molecular dipole and excitonic excitation migrating from one place to the other. This diffusion finally gives rise to observable experimental effects, for example shorter de-grating time.

The diffusion contribution to degrating processes is identified and investigated for the first time. This was achieved by comparing the TRFWM results with those from the transient absorption experiments on the same samples and making an estimation of the diffusion coefficients. The calculated diffusion coefficients are compatible with the typical values of the diffusion coefficient for dipole transfer and for energy transfer processes. This confirms the role of diffusion in the degrating process.

Due to the stacked sandwich formation of the dimer/heterodimer trimer/ heterotrimer, which favours the delocalization of the conjugated π-electrons, the third-order nonlinear optical susceptibilities in these systems have been greatly increased

compared with those of the free phthalocyanine and the metallo-phthalocyanines/porphyrins.

The phenomenon of two correlated-phonon mode-shifting has been observed for the first time. It is related to the charge transfer process in the heterodimer. One of the characteristics of intramolecular electron transfer in the lanthanide heterodimer or heterotrimer systems is that these processes are always accompanied with a change in molecular configuration. This causes a vibration mode change. We conclude that, ***the correlated-phonon mode-shifting phenomenon may only be observable in a system relaxing with changes in the molecular configuration.***

The knowledge of the detailed structure of the microscopic crystalline domains in sublimated films and the arrangement of the molecules in Langmuir-Blodgett films is crucial for the attribution of the third-order nonlinear optical processes to the different physical mechanisms. When the grating spacing period is bigger than the averaged size of the microscopic crystalline domains of a sublimated film, the latter, instead of the former, should be used to make a correct estimation of the diffusion coefficient.

The photorefractive effect is one of the most important nonlinear optical phenomena, which exists in ferroelectrics, sillenites, compound semiconductors and doped organics. The lanthanide porphyrin phthalocyanine dimer/heterodimer and trimer/heterotrimer systems have both electron donors and acceptors. In these systems, there always exist either intramolecular charge transfer or intermolecular energy transfer. These intramolecular and intermolecular transport processes cause molecular dipoles or excitonic excitations to migrate quickly and effectively from one molecule to the others. The boundary of the microscopic crystalline domains in the sublimated films and the local irregularities in Langmuir-Blodgett film play an important role as "trapping center" (as in semiconductors and other photorefractive crystals), at which the moving molecular dipoles or excitations will be held down or trapped. This may eventually create new internal space charge fields, which alter the local refractive index of the material by the Pockels effect, and gave a long time response in all these lanthanide porphyrin phthalocyanine dimer/heterodimer and trimer/heterotrimer systems. ***We have observed the first photorefractive effect in an organic multimer thin film.***

Aside from the motion of free carriers in conventional photorefractive materials, there exist the other two equivalent mechanisms in sublimated and Langmuir-Blodgett thin films of lanthanide porphyrin phthalocyanine dimer/heterodimer and symmetric trimer systems. The molecular dipole migration by charge transfer state coupling or by spin-orbital coupling and excitonic excitation migration by excitonic coupling between the neighbouring molecules, are possibly ***one of the most efficient ways to build up photorefractive effect in organic materials***. This photorefractive effect can be enhanced and optimized by molecular engineering, which at the same time can overcome the deficiencies in the existing non-organic photorefractive materials. Therefore, lanthanide porphyrin phthalocyanine dimer/heterodimer trimer/heterotrimer systems ***offer an entirely new approach to photorefractivity*** and they could be ***a promising new family of organic materials for the investigation and the application of the photorefractive effect.***

From the above, we can see that, in lanthanide porphyrin phthalocyanine dimer/heterodimer and trimer/heterotrimer systems, three seemingly non-related phenomena, ***diffusion contribution to degrating process, correlated-phonon mode shifting*** and ***photorefractive effect,*** have a common origin: intramolecular charge transfer (ICT), molecular dipole migration (MDM) and excitonic excitation migration (EEM) processes occur in theses systems.

From this work, it is clear that metallo porphyrin phthalocyanine dimer/heterodimer and trimer/heterotrimer are very versatile and have very great potential as nonlinear optical materials. The nonlinear optical research on these materials is just at its beginning. An improved understanding of the relationship between the molecular structure and the microscopic nonlinearities, is essential for the development of new molecular systems for nonlinear optics. A systematic investigation covering a diversity of species and sequentially built structures will help to establish comprehensive nonlinear optical theoretical models and computational methods to predict structural requirements necessary for large optical nonlinearities.

Appendix I

Transient Response of Population Relaxation

In order to extract the information from time-resolved four wave mixing experimental data, we need to make a theoretical calculation to fit the data and consequently decide the relate parameters. During this process, as we have developed in Chapter 2, section 2.7., needs to use transient response of the population relaxation of a system with a certain energy levels and relaxation paths. In the fitting, we need a four-level system solution to treat the problem of three relaxation components, and a five-level system solution to deal with the problem of four relaxation components.

Suppose we have a ten-level system, where, $E_1 > E_2 > E_3 > E_4 > E_0$, and E_1 to E_4 are the excited states and E_0 is the ground state. We are going to give the transient response for the system excited to the highest level and relaxing from one level to the others.

The differential equations for the system can be written as

$$\frac{dP_1}{dt} = -\frac{P_1}{T_1}, \quad \frac{1}{T_1} = \frac{1}{T_{10}} + \sum_{i=2}^{4}\frac{1}{T_{1i}} = \frac{1}{T_1}(g_{10} + \sum_{i=2}^{4} g_{1i}), \quad (g_{10} + \sum_{i=2}^{4} g_{1i}) = 1; \qquad (A1.)$$

$$\frac{dP_2}{dt} = -\frac{P_2}{T_2} + g_{12}\frac{P_1}{T_1} = -\frac{P_2}{T_2} + \frac{P_1}{T_{12}}, \quad \frac{1}{T_2} = \frac{1}{T_{20}} + \sum_{i=3}^{4}\frac{1}{T_{2i}} = \frac{1}{T_2}(g_{20} + \sum_{i=3}^{4} g_{2i}); \quad (A2.)$$

$$\frac{dP_3}{dt} = -\frac{P_3}{T_3} + g_{13}\frac{P_1}{T_1} + g_{23}\frac{P_2}{T_2} = -\frac{P_3}{T_3} + \frac{P_1}{T_{13}} + \frac{P_2}{T_{23}},$$
$$\frac{1}{T_3} = \frac{1}{T_{30}} + \frac{1}{T_{34}} = \frac{1}{T_3}(g_{30} + g_{34}), \quad (g_{30} + g_{34}) = 1; \qquad (A3.)$$

$$\frac{dP_4}{dt} = -\frac{P_4}{T_4} + g_{14}\frac{P_1}{T_1} + g_{24}\frac{P_2}{T_2} + g_{34}\frac{P_3}{T_3} = -\frac{P_4}{T_4} + \frac{P_1}{T_{14}} + \frac{P_2}{T_{24}} + \frac{P_3}{T_{34}},$$
$$\frac{1}{T_4} = \frac{1}{T_{40}} = \frac{1}{T_4} g_{40}, \quad g_{40} = 1; \qquad \text{(A4.)}$$

where P_i and T_i are the population and the relaxation time of the ith level respectively, T_{ij} is the relaxation time of the system from the ith level to the jth level, and $g_{ij} = \frac{T_{ij}}{T_{i0}}$, $j = 0, i+1, \cdots, 4$, is the statistical weight related to the ith level and the jth level, which could take the values between 0 and 1 depending on the specific cases.

Solving the equations under the initial conditions as

$$P_1(0) = 1, P_n(0) = 0, \quad n = 2, 3, 4; \qquad \text{(A5.)}$$

we can get the following population evolution equations:

$$P_n(t) = \sum_{i=1}^{n} A_{ni}\, e^{-t/T_i}, \quad n = 1, 2, 3, 4; \qquad \text{(A6.)}$$

i.e.

$$\left.\begin{aligned} P_1(t) &= A_{11}\, e^{-t/T_1}, \\ P_2(t) &= A_{21}\, e^{-t/T_1} + A_{22}\, e^{-t/T_2}, \\ P_3(t) &= A_{31}\, e^{-t/T_1} + A_{32}\, e^{-t/T_2} + A_{33}\, e^{-t/T_3}, \\ P_4(t) &= A_{41}\, e^{-t/T_1} + A_{42}\, e^{-t/T_2} + A_{43}\, e^{-t/T_3} + A_{44}\, e^{-t/T_4}, \end{aligned}\right\} \qquad \text{(A7.)}$$

where the parameter A_{ij} are:

$$A_{11} = 1,\ A_{21} = \frac{g_{12}}{T_1} A_{11} \frac{T_1 T_2}{T_1 - T_2},\ A_{22} = -A_{21},\ A_{31} = (\frac{g_{13}}{T_1} A_{11} + \frac{g_{23}}{T_2} A_{21}) \frac{T_1 T_3}{T_1 - T_3},$$

$$A_{32} = \frac{g_{23}}{T_2} A_{22} \frac{T_2 T_3}{T_2 - T_3},\quad A_{33} = -(A_{31} + A_{32}),$$

$$A_{41} = (\frac{g_{14}}{T_1} A_{11} + \frac{g_{24}}{T_2} A_{21} + \frac{g_{34}}{T_3} A_{31}) \frac{T_1 T_4}{T_1 - T_4},$$

$$A_{42} = (\frac{g_{24}}{T_2} A_{22} + \frac{g_{34}}{T_3} A_{32}) \frac{T_2 T_4}{T_2 - T_4},$$

$$A_{43} = \frac{g_{34}}{T_3} A_{33} \frac{T_3 T_4}{T_3 - T_4},\quad A_{44} = -(A_{41} + A_{42} + A_{43}),$$

(A8.)

Therefore, the transient response to the relaxation of the system can be expressed as:

$$R(t) = \sum_{i=1}^{4} \chi_i^{(3)} P_i(t) = \sum_{i=1}^{4} \sum_{j=1}^{i} \chi_i^{(3)} A_{ij}\, e^{-t/T_j}, \qquad \text{(A9.)}$$

i.e.

$$R(t) = \chi_1^{(3)} A_{11}\, e^{-t/T_1} + \chi^2 (A_{21}\, e^{-t/T_1} + A_{22}\, e^{-t/T_2}) + \chi_3^{(3)} (A_{31}\, e^{-t/T_1} + A_{32}\, e^{-t/T_2} + A_{33}\, e^{-t/T_3}) +$$
$$+ \chi_4^{(3)} (A_{41}\, e^{-t/T_1} + A_{42}\, e^{-t/T_2} + A_{43}\, e^{-t/T_3} + A_{44}\, e^{-t/T_4}),$$

(A10).

$$R(t) = (\chi_1^{(3)} A_{11} + \chi_2^{(3)} A_{21} + \chi_3^{(3)} A_{31} + \chi_4^{(3)} A_{41})\, e^{-t/T_1} + (\chi_2^{(3)} A_{22} + \chi_3^{(3)} A_{32} + \chi_4^{(3)} A_{42})\, e^{-t/T_2} +$$
$$+ (\chi_3^{(3)} A_{33} + \chi_4^{(3)} A_{43})\, e^{-t/T_3} + (\chi_4^{(3)} A_{44})\, e^{-t/T_4}.$$

(A11.)

This *five-level system* or *four excited state population model* have been used in section 4.3.3. .

For the transient response of a four-level or three excited state system, the population relaxation formula similar to (A9) – (A10) are:

$$R(t) = \sum_{i=1}^{3} \chi_i^{(3)} P_i(t) = \sum_{i=1}^{3} \sum_{j=1}^{i} \chi_i^{(3)} A_{ij} e^{-t/T_j}, \qquad (A12.)$$

and

$$R(t) = \chi_1^{(3)} A_{11} e^{-t/T_1} + \chi_2^{(3)} (A_{21} e^{-t/T_1} + A_{22} e^{-t/T_2}) + \chi_3^{(3)} (A_{31} e^{-t/T_1} + A_{32} e^{-t/T_2} + A_{33} e^{-t/T_3})$$
$$= (\chi_1^{(3)} A_{11} + \chi_2^{(3)} A_{21} + \chi_3^{(3)} A_{31}) e^{-t/T_1} + (\chi_2^{(3)} A_{22} + \chi_3^{(3)} A_{32}) e^{-t/T_2} + (\chi_3^{(3)} A_{33}) e^{-t/T_3} \qquad (A13.)$$

where,

$$A_{11} = 1, \quad A_{21} = \frac{g_{12}}{T_1} A_{11} \frac{T_1 T_2}{T_1 - T_2} = \frac{g_{12}}{T_1} \frac{T_1 T_2}{T_1 - T_2}, \quad A_{22} = -A_{21} = -\frac{g_{12}}{T_1} \frac{T_1 T_2}{T_1 - T_2},$$
$$A_{31} = (\frac{g_{13}}{T_1} A_{11} + \frac{g_{23}}{T_2} A_{21}) \frac{T_1 T_3}{T_1 - T_3} = (\frac{g_{13}}{T_1} - \frac{g_{12}}{T_1} \frac{g_{23}}{T_2} \frac{T_1 T_2}{T_1 - T_2}) \frac{T_1 T_3}{T_1 - T_3},$$
$$A_{32} = \frac{g_{23}}{T_2} A_{22} \frac{T_2 T_3}{T_2 - T_3} = -\frac{g_{12}}{T_1} \frac{g_{23}}{T_2} \frac{T_1 T_2}{T_1 - T_2} \frac{T_2 T_3}{T_2 - T_3},$$
$$A_{33} = -(A_{31} + A_{32}) = -(\frac{g_{13}}{T_1} - \frac{g_{12}}{T_1} \frac{g_{23}}{T_2} \frac{T_1 T_2}{T_1 - T_2}) \frac{T_1 T_3}{T_1 - T_3} + \frac{g_{12}}{T_1} \frac{g_{23}}{T_2} \frac{T_1 T_2}{T_1 - T_2} \frac{T_2 T_3}{T_2 - T_3}. \qquad (A14.)$$

Substituting these into (A8.) one gets the final analytical expression, used in the fitting of experimental data in section 4.1, 4.2. and 4.4., as:

$$R(t) = \left[\chi_1^{(3)} + \chi_2^{(3)} \frac{g_{12}}{T_1} \frac{T_1 T_2}{T_1 - T_2} + \chi_3^{(3)} (\frac{g_{13}}{T_1} - \frac{g_{12}}{T_1} \frac{g_{23}}{T_2} \frac{T_1 T_2}{T_1 - T_2}) \frac{T_1 T_3}{T_1 - T_3}\right] e^{-t/T_1} +$$
$$+ \left[-\chi_2^{(3)} \frac{g_{12}}{T_1} \frac{T_1 T_2}{T_1 - T_2} - \chi_3^{(3)} \frac{g_{12}}{T_1} \frac{g_{23}}{T_2} \frac{T_1 T_2}{T_1 - T_2} \frac{T_2 T_3}{T_2 - T_3}\right] e^{-t/T_2} +$$
$$+ \chi_3^{(3)} \left[-(\frac{g_{13}}{T_1} - \frac{g_{12}}{T_1} \frac{g_{23}}{T_2} \frac{T_1 T_2}{T_1 - T_2}) \frac{T_1 T_3}{T_1 - T_3} + \frac{g_{12}}{T_1} \frac{g_{23}}{T_2} \frac{T_1 T_2}{T_1 - T_2} \frac{T_2 T_3}{T_2 - T_3}\right] e^{-t/T_3}. \qquad (A15.)$$

Appendix II. Transient Response of Four-Wave Mixing in aMedium, a Quantum Mechanical View

In Appendix 2, we will examine how $\mathbf{P}^{(3)}(z,t)$ can be obtained using the density matrix description.

In quantum mechanics, a system's state is governed by the Schrödinger equation

$$i\hbar\frac{\partial|\varphi(t)>}{\partial t} = \hat{H}|\varphi(t)>, \qquad (A2.1.)$$

where $\hat{H}$ is the Hamiltonian, $|\varphi(t)>$ is a state of the system. The Hamiltonian $\hat{H}$ includes the unperturbed Hamiltonian $\hat{H}_0$, and the interaction Hamiltonian $\hat{H}_1$:

$$\hat{H} = \hat{H}_0 + \hat{H}_1 . \qquad (A2.2.)$$

The solution of equation (A2.1.) is

$$|\varphi(t)>= \hat{U}(t,t_1)|\varphi(t_1)>, \qquad (A2.3.)$$

where $\hat{U}(t,t_1)$ is the time-development operator.

In order to calculate the expectation value of a physical quantity $\hat{Q}$, a projection operator $\hat{P}(\psi)$ has to be introduced:

$$\hat{P}(\psi) =|\psi(t)><\psi(t)|, \qquad (A2.4.)$$

where $|\psi(t)>$ is an element of a complete orthonormal set of eigenvectors of $\hat{H}(t)$.

Putting the projection operator into the Schrödinger equation, one can get the equation of motion for the projection operator $\hat{P}(\psi)$

$$i\hbar\frac{\partial\hat{P}(\psi)}{\partial t} =\left[\hat{H}, \hat{P}(\psi)\right]. \qquad (A2.5.)$$

The expectation value of the observable $\hat{Q}$ in the states $\psi_1, \psi_2, \cdots\cdots, \psi_n$, can be expressed as the trace of the projection operator

$$\left\langle \hat{Q} \right\rangle_j = tr\left\{ \hat{P}(\psi_j)\hat{Q} \right\}, \qquad (A2.6.)$$

and the probable value of the operator $\hat{Q}$ when the system is in a mixture of the states $\psi_1, \psi_2, \cdots\cdots, \psi_n$, is given by:

$$\left\langle \hat{Q} \right\rangle = \sum_j P_j tr\left\{ \hat{P}(\psi_j)\hat{Q} \right\} = \sum_j tr\left\{ P_j \hat{P}(\psi_j)\hat{Q} \right\}. \qquad (A2.7.)$$

By defining

$$\hat{\rho} = \sum_j P_j \hat{P}(\psi_j), \qquad (A2.8.)$$

(A2.7.) can be written as:

$$\left\langle \hat{Q} \right\rangle = tr\left\{ \hat{\rho}\hat{Q} \right\}. \qquad (A2.9.)$$

Equation (A2.8.) defines *the density operator* of the system. P_j is the probability of finding the system in the state ψ_j at time $t = -\infty$, when $\hat{H}_1 = 0$.

The probability P_j is independent of time, and thus:

$$i\hbar \frac{\partial \hat{\rho}}{\partial t} = i\hbar \sum_j P_j \frac{\partial \hat{P}(\psi_j)}{\partial t}. \qquad (A2.9.)$$

Using the equation of motion of the projection operator (A2.5.), the equation (A2.10.) becomes:

$$i\hbar \frac{\partial \hat{\rho}}{\partial t} = \sum_j P_j \left[\hat{H}, \hat{P}(\psi_j) \right] = \left[\hat{H}, \sum_j P_j \hat{P}(\psi_j) \right] = \left[\hat{H}, \hat{\rho} \right]. \qquad (A2.11.)$$

This is the Liouville equation for the density operator $\hat{\rho}$.

Putting the Hamiltonian of the system $\hat{H} = \hat{H}_0 + \hat{H}_1$ into (A2.11.), one can get

$$i\hbar \frac{\partial \hat{\rho}}{\partial t} = \left[\hat{H}_0 + \hat{H}_1, \hat{\rho} \right] = \left[\hat{H}_0, \hat{\rho} \right] + \left[\hat{H}_1, \hat{\rho} \right], \qquad (A2.12.)$$

where $\hat{\rho}$ can be expanded as a series:

$$\hat{\rho}(t) = \hat{\rho}^{(0)} + \hat{\rho}^{(1)} + \hat{\rho}^{(2)} + \hat{\rho}^{(3)} + \cdots\cdots \hat{\rho}^{(j)} + \cdots\cdots = \sum_{m=0} \hat{\rho}^{(m)}. \qquad (A2.13.)$$

Therefore, we have:

$$i\hbar \frac{\partial}{\partial t} \sum_{j=0} \hat{\rho}^{(j)}(t) = \left[\hat{H}_0, \sum_{j=0} \hat{\rho}^{(j)}(t) \right] + \left[\hat{H}_1, \sum_{j=0} \hat{\rho}^{(j)}(t) \right]. \qquad (A2.14.)$$

By comparing the same orders of the powers in both sides of (A2.14.), we can get the differential equations satisfied by the different orders of the perturbation series as:

$$\begin{aligned}
i\hbar \frac{\partial \hat{\rho}^{(0)}(t)}{\partial t} &= \left[\hat{H}_0, \hat{\rho}^{(0)}(t) \right], \\
i\hbar \frac{\partial \hat{\rho}^{(1)}(t)}{\partial t} &= \left[\hat{H}_0, \hat{\rho}^{(1)}(t) \right] + \left[\hat{H}_1, \hat{\rho}^{(0)}(t) \right], \\
i\hbar \frac{\partial \hat{\rho}^{(2)}(t)}{\partial t} &= \left[\hat{H}_0, \hat{\rho}^{(2)}(t) \right] + \left[\hat{H}_1, \hat{\rho}^{(1)}(t) \right], \\
i\hbar \frac{\partial \hat{\rho}^{(3)}(t)}{\partial t} &= \left[\hat{H}_0, \hat{\rho}^{(3)}(t) \right] + \left[\hat{H}_1, \hat{\rho}^{(2)}(t) \right], \\
&\vdots \qquad\qquad \vdots \qquad\qquad \vdots \\
i\hbar \frac{\partial \hat{\rho}^{(j)}(t)}{\partial t} &= \left[\hat{H}_0, \hat{\rho}^{(j)}(t) \right] + \left[\hat{H}_1, \hat{\rho}^{(j-1)}(t) \right], \\
&\vdots \qquad\qquad \vdots \qquad\qquad \vdots
\end{aligned} \qquad (A2.15.)$$

Using the time evolution unitary operator $\hat{U}_0(t) \equiv \hat{U}(t, t_1 = -\infty)$, multiplying (A2.15.) from the left by $\hat{U}_0^{\dagger}(t) = \hat{U}_0(-t)$ and from the right by $\hat{U}_0(t)$, and making use of the relation $\hat{U}_0^{\dagger}(t)\hat{U}_0(t) = \hat{U}_0(-t)\hat{U}_0(t) = 1$, one can get the *j*th-order density operator as:

$$\hat{\rho}^{(j)}(t)=\frac{\hat{U}_0(t)}{(i\hbar)^j}\int_{-\infty}^{t}dt_1\int_{-\infty}^{t_1}dt_2\int_{-\infty}^{t_2}dt_3\cdots\int_{-\infty}^{t_{j-1}}dt_j\times$$
$$\times\left[\hat{H}_1'(t_1),\left[\hat{H}_1'(t_2),\left[\hat{H}_1'(t_3),\left[\cdots\left[\hat{H}_1'(t_j),\hat{\rho}^{(0)}(t_j)\right]\cdots\right]\right]\right]\right]\hat{U}_0^{+}(t), \qquad (A2.16.)$$

where

$$\hat{H}_1'(t_m)=\hat{U}_0^{+}(t_m)\hat{H}_1(0)\hat{U}_0(t_m),\quad m=1,2,3,\cdots,j\,. \qquad (A2.17.)$$

For j = 3, one has

$$\hat{\rho}^{(3)}(t)=\frac{\hat{U}_0(t)}{(i\hbar)^3}\int_{-\infty}^{t}dt_1\int_{-\infty}^{t_1}dt_2\int_{-\infty}^{t_2}dt_3\left[\hat{H}_1'(t_1),\left[\hat{H}_1'(t_2),\left[\hat{H}_1'(t_3),\hat{\rho}^{(0)}(t_3)\right]\right]\right]\hat{U}_0^{+}(t) \qquad (A2.18.)$$

Once the expressions of the density operator are available through a quantum mechanical calculation, the *j*th-order nonlinear optical polarization $\boldsymbol{P}^{(j)}$ can be deduced as follows.

The external field exerted on a medium introduces a polarization which we write as

$$\mathbf{P}(t)=\mathbf{P}^{(1)}(t)+\mathbf{P}^{(2)}(t)+\mathbf{P}^{(3)}(t)+\cdots\cdots+\mathbf{P}^{(j)}(t)+\cdots\cdots. \qquad (A2.19.)$$

If the volume of the medium V is small enough, and for a total electric dipole momentum of the system $\boldsymbol{D}$, then the different orders of the polarization can be expressed as

$$\mathbf{P}^{(1)}(t)=\frac{1}{V}tr\{\hat{\rho}^{(1)}(t)\boldsymbol{D}\},\ \mathbf{P}^{(2)}(t)=\frac{1}{V}tr\{\hat{\rho}^{(2)}(t)\boldsymbol{D}\},$$
$$\mathbf{P}^{(3)}(t)=\frac{1}{V}tr\{\hat{\rho}^{(3)}(t)\boldsymbol{D}\},\cdots\cdots,\ \mathbf{P}^{(j)}(t)=\frac{1}{V}tr\{\hat{\rho}^{(j)}(t)\boldsymbol{D}\},\quad\cdots\cdots. \qquad (A2.20.)$$

In the general case, the term *nonlinear polarization* means

$$\mathbf{P}^{(j)}(t)=\mathbf{P}^{NL(j)}(t),\quad j\geq 2. \qquad (A2.21.)$$

$\boldsymbol{P}^{(j)}(t)$ can be expressed in another form using subscripts μ, α_1, α_2, ... , α_j, etc. to denote one of the components of the cartesian coordinates x, y, z:

$$P_{\mu}^{(j)}(t) = \varepsilon_0 \int_{-\infty}^{+\infty} d\omega_1 \int_{-\infty}^{+\infty} d\omega_2 \int_{-\infty}^{+\infty} d\omega_3 \cdots \int_{-\infty}^{+\infty} d\omega_n \chi^{(j)}_{\mu\alpha_1\alpha_2\cdots\alpha_j}(\omega_1, \omega_2, \cdots\cdots, \omega_j) \times$$
$$\times E_{\alpha_1}(\omega_1) E_{\alpha_2}(\omega_2) \cdots E_{\alpha_j}(\omega_j) e^{-i\sum_{m=1}^{j}\omega_m t}. \qquad (A2.22.)$$

Fourier transforming (2.8.1.22.) while using (2.8.1.18.) and $\hat{H}_1(t) = -\boldsymbol{R}(t)\cdot\mathbf{E}(t)$, one gets for j = 3

$$\chi^{(3)}_{\mu\alpha\beta\gamma}(\omega_1, \omega_2, \omega_3) =$$
$$= \frac{1}{\varepsilon_0 V}\frac{\hat{S}}{6}\int_{-\infty}^{+\infty} dt_1 \int_{-\infty}^{+\infty} dt_2 \int_{-\infty}^{+\infty} dt_3 \, tr\left\{\hat{\rho}_0\left[\left[\left[\hat{D}_\mu, \hat{D}_\alpha(t_1)\right], \hat{D}_\beta(t_2)\right], \hat{D}_\gamma(t_3)\right]\right\} \times \qquad (A2.23.)$$
$$\times e^{-i(\omega_1 t_1 + \omega_2 t_2 + \omega_3 t_3)},$$

where $\hat{S}$ is a symmetric operator [33, 213 - 216].

We have now obtained the expression for the third-order nonlinear optical polarizability $\chi^{(3)}$, with which the third-order nonlinear polarization can be expressed as

$$\mathbf{P}^{NL(3)} = \vdots\vdots\chi^{(3)} : \boldsymbol{EEE}. \qquad (A2.24.)$$

This is the source term in third-order coupled wave equation, from which the problem of the third-order nonlinear optical wave propagation in a medium can be solved.

References

1. S. R. Marder in *Inorganic Materials*, D. W. Bruce and D. O. Hare eds., Wiley Chichester, **1992**, p136.
2. J. C. Calabrese, L. -T. Cheng, J. C. Green, S. R. Marder, W. Tam, *J. Am. Chem. Soc.*, 113 (**1991**) 7227.
3. C. C. Frazier, M. A. Harvey, M. P. Cockerham, H. M. Hand, E. A. Chauchard, C. H. Lee, *J. Phys. Chem.*, 90 (**1986**) 5703.
4. G. L. Geofrey, M. S. Wrighton, *Organometallic Photochemistry*, Academic Press, New York, **1979**.
5. B. J. Coe, C. J. Jones, J. A. McCleverty, Dj. Bloor, P. V. Kolinsky, R. J. Jones, *J. Chem. Commun.*, (**1979**) 1485.
6. S. K. Kurtz, T. T. Perry, *J. Appl. Phys.*, 39 (**1968**) 3798.
7. J. P. Dougherty, S. K. Kurtz, *J. Appl. Crystallogr.*, 9 (**1976**) 145.
8. J. M. Halbout, S. Blit, C. L. Tang, *IEEE J. Quantum Electron.*, QE-17 (**1981**) 513.
9. M. J. Rosker, C. L. Tang, *IEEE J. Quantum Electron.*, QE-20 (**1984**) 334.
10. K. D. Singer, A. F. Garito, *J. Chem. Phys.*, 75 (**1981**) 3572.
11. J. L. Oudar, H. Le Person, *Opt. Commun.*, 15 (**1975**) 258.
12. B. F. Levine, C. G. Bethea, *Appl. Phys. Lett.*, 24 (**1974**) 445.
13. L. -T. Cheng, W. Tam, S. R. Marder, A. E. Stiegman, G. Rikken, C. W. Spargler, *J. Phys. Chem.*, 95 (**1991**) 10643.
14. K. Clays, A. Persoons, *Rev. Sci. Instrum.*, 63 (**1992**) 3285.
15. K. Clays, A. Persoons, *Phys. Rev. Lett.*, 66 (**1991**) 2980.
16. J. W. Perry, ACS Symp. Ser., 71 (**1991**) 455.
17. F. Kajzar, J. Mesier, *Phys. Rev. A*, 32 (**1985**) 2352.
18. J. L. Oudar, *J. Chem. Phys.*, 67 (**1977**) 446.

19. J. L. Oudar, D. S. Chemla, *J. Chem. Phys.*, 66 (**1977**) 2664.

20. L. -T. Cheng, W. Tam, S. H. Stevenson, G. R. Meredith, G. Rikken, S. R. Marder, *J. Phys. Chem.*, 95 (**1991**) 10631.

21. R. W. Hellwarth, *Prog. Quantum Electron.*, 5 (**1977**) 1.

22. M. D. Levenson, *IEEE J. Quantum Electron.*, QE-0 (**1974**) 110.

23. N. J. Long, *Angew. Chem. Int. Ed. Engl.*, 34 (**1995**) 21.

24. Q. F. Zhou, H. J. Tian, S. Y. Shen, H. J. Xu, *Photographic Sci. Photochem.*, 10 (**1992**) 144.

25. T. H. Tran-Tri, S. Palacin, B. Clergeot, *Chem. Phys. Lett.*, 157 (**1989**) 92.

26. T. Fournier, T. H. Tran-Thi, N. Herlet, C. Sanchez, *Chem. Phys. Lett.*, 208 (**1993**) 101.

27. T. H. Tran-Thi, D. Markovisi, R. Even and J. Simon, *Chem. Phys. Lett.*, 139 (**1987**) 207.

28. S. Gaspard, C. Giannotti, P. Maillard, C. Scheeffer, T. H. Tran-Thi, *J. Chem. Soc. Chem. Commun.*, (**1986**) 1239.

29. T. H. Tran-Thi, C. Thiec, S. Gaspard, *J. Phys. Chem.*, 93 (**1989**) 1226.

30. J. X. Lin, Q. Yu, Q. F. Zhou, H. J. Xu, *J. Chem. Soc. Chem. Commun.*, (**1990**) 260.

31. L. Li, S. Y. Shen, Q. Yu, Q. F. Zhou, H. J. Xu, *J. Chem. Soc. Chemmun.*, (**1991**) 619.

32. H. J. Tian, Q. F. Zhou, S. Y. Shen, H. J. Xu, *The 6th Nation. Lum Symposium of China, Hefei, Anhui, China, Oct.* **1992**.

33. I. E. Hargrove, R. L. Fork, M. A. Pollack, *Appl. Phys. Lett.*, 5 (**1964**) 4.

34. S. E. Harris, R. Targ, *Appl. Phys. Lett.*, 5 (**1964**) 205.

35. H. Mocker and R. Collins, *Appl. Phys. Lett.*, 7 (**1965**) 270.

36. A. J. De Maria, D. AA. Stestser, H. Heyman, *Appl. Phys. Lett.*, 8 (**1966**) 22.

37. W. Zinth, W. Kaiser in *Ultrashort Laser Pulses and Applications*, Topics in Applied Physics Vol. 60, W. Kaiser Ed., Springer-Verlag, Berlin, **1988**.

38. R. L. Fork, B. I. Greene, C. V. Shank, *Appl. Phys. Lett.*. 38 (**1981**) 671.

39. R. L. Fork, O. E. Martinez, J. P. Gordon, *Appl. Phys. lett.*, 9 (**1984**) 150.

40. J. A. Valdmanis, R. L. Fork and J. P. Gordon, *Opt. Lett.* 10 (**1985**) 131.

41. E. B. Treacy, *J. Quantum Electron*, QE-5 (**1969**) 454.

42. L. F. Mollenauer, R. H. Stolen and J. P. Gordon, *Phys. Rev. Lett.*, 45 (**1980**) 1095.

43. L. F. Mollenauer, R. H. Stolen and J. P. Gordon, *Opt. Lett.*, 8 (**1983**) 289.

44. L. F. Mollenauer, R. H. Stolen and J. P. Gordon, *Opt. Lett.* 9 (**1984**) 13.

45. F. M. Mitschke and L. F. Mollenauer, *IEEE J. QE-22* (**1986**) 2242.

46. C. V. Shank, R. L. Fork, R. Yen, R. H. Stolen & W. J. Tomlinson, *Appl. Phys. Lett.*, **40** (1982) 761.

47. J. G. Fujimoto, A. M. Wwiner and E. P. Ippen, *Appl. Phys. Lett.*, 44 (**1984**) 832.

48. J. M. Halbout and D. Grischkowsky, *Appl. Phys. Lett.*, 45 (**1984**) 1281.

49. W. H. Knox, R. L. Fork, M. C. Downer, R. H. Stolen, C. V. Shank, J. Valdmanis, *Appl. Phys. Lett.*, 46 (**1985**) 1120.

50. R. L. Fork, C. H. Brito Crutz, P. C. Becker and C. V. Shank, *Opt. Lett.*, 12 (**1986**) 483.

51. J. Diels, J. Fontaine, I. McMichael, F. Simoni, *Appl. Opt.*, 24 (**1985**) 1270.

52. G. R. Fleming, *Chemical Application of Ultrafast Spectroscopy*, J. E. Baldwin, J. B. Goodenough, J. Halpern, J. S. Rowlinson Eds., Oxford University Press, New York **1986**

53. R. R. Alfano, L. L. Hope, S. L. Shapiro, *Phys. Rev.*, A6, (**1972**) 433.

54. R. R. Alfano, S. L. Shapiro, *Phys. Rev. Lett.*, 24 (**1970**) 584.

55. A. Penzkofer, A. Laubereau, W. Kaiser, *Phys. Rev. Lett.* 31 (**1973**) 863.

56. A. Penzkofer, A. Seilmeier, W. Kaiser, *Opt. Comm.* **14**(**1975**) 363.

57. D. H. Auston in *Ultrashort Light Pulses – Picosecond Techniques and Applications,* Topics in Applied Physics Vol 18, S. L. Shapiro Ed., Springer-Verlag, Berlin **1977**.

58. W. Zinth, W. Kaiser in *Ultrashort Laser Pulses and Applications*, Topics in Applied Physics Vol. 60, W. Kaiser Ed., Springer-Verlag, Berlin, **1988**, p273.

59. G. R. Fleming, *Chemical Application of Ultrafast Spectroscopy*, J. E. Baldwin, J. B. Goodenough, J. Halpern, J. S. Rowlinson Eds., Oxford University Press, New York **1986**, p79-80.

60. H. J. Eichler, P. Günter, D. W. Pohl, *Laser-Induced Dynamic Gratings,* Spinger -Verlag, Berlin, **1986**.

61. J. P. Woerdman, *Philips Res. Rep. Suppl.*, No.7 (**1971**).

62. A. D. Adler, F. R. Iongo, F. Kampas and J. Kim, *J. Inorg. Nucl. Chem.*, 322 (**1970**) 2443.

63. A. D. Adler, F. R. Iongo, J. D. Finarelli, J. Goldmacher, J. Assour, L. Korsakoff, *J. Org. Chem.*, 32 (**1976**) 476.

64. A. Braun and J. Tcherniac, *J. Ber. Dtsch. Chem. Ges.*, 42 (**1907**) 2709.

65. R. P. Linstead, *J. Chem. Soc.*, (**1934**) 1016.

66. G. Booth, *Chimia.*, 19 (**1965**) 201.

67. O. A. Aktsipetrov, N. N. Akhmediev, E. D. Mishina and V. R. Novak, *JETP Lett.*, 37 (**1983**) 207.

68. J. Zyss, *J. Mol. Electron.*, 1 (**1985**) 25.

69. P. N. Prasad and D. R. Ulrich, *Nonlinear Optical and Electroactive Polymers*, Plenum, New York, **1988**.

70. D. J. Williams, *Angnew. Chem. Int. Ed. Engl.*, 23 (**1984**) 690.

71. D. S. Chemla and J. Zyss, *NLO Porperites of Organic Molecules and Crystals,* Academic Press Inc., New York, **1987**.

72. J. Zyss and I. Ledoux, *Echo Rech*, 127 (**1987**) 19.

73. J. Zyss and J. L. Oudar, *Phys. Rev. A*, 26 (1982) 2076.

74. G. Soula, *Actual. Chim.*, (Nov./Dec.) (1988) 249.

75. A. E. Stiegman, E. Graham, et al., *J. Am. Chem. Soc.* 113 (1991) 7658.

76. P. G. Huggard, W. Blan an D. Schweitzer, *Appl. Phys. Lett.*, 51 (1987) 2183.

77. G. Maloney, H. Byrne, W. M. Dennis, et al., *Chem. Phys.*, 121 (1988) 21.

78. S. R. Marder et al. eds., *Materials for Nonlinear Optics, Chemical Perspectives,* ACS Symp. Series, Vol. 455, The Am. Chem. Soc., Washington, DC., 1992.

79. T. Kurihara, N. Oba, Y. Mori, S. Tomance and T.Kaino, *J. Appl. Phys.* 70 (1991) 17.

80. D. J. Williams ed., *Nolinear Optical Properties of Organic and Polymeric Materials,* ACS Sympos. Series 233, Am. Chem. Soc., Washington, DC., 1983.

81. T. Kobayashi ed., *Nonlinear Optics of Organics and Semiconductors,* Springer Proceedings in Physics 36, Springer-Verlag, Berlin, 1989.

82. R. A. Hann, D. Bloor eds., *Organic Materials for Nonlinear Optics,* Royal Soc. Chem., London, 1989.

83. L. Y. Chiang et al eds., *Advanced Organic Solid State Materials,* Materials Research Society Proceedings, Vol. 173, Pittsbuyrgh, PA, 1990.

84. G. Khanarian ed., *Nonlinear Optical Properities of Organic Materials III* SPIE: Bettingham, WA, Vol. 1337, 1990.

85. J. Messier et al., eds., *Organic Molecules for Nonlinear Optics and Photonics,* NATO Advanced Study Institute Series E, Kluwer Academic, Boston, 1991., Vol. 194.

86. Z. Z. Ho, C. Y. Ju, W. M. Hetherington III, *J. Appl. Phys.*, 62 (1987) 716.

87. T. Wada et al. in, *Nonlinear Optics of Organics and Semiconductors* T. Kobayashi ed., Springer Proceedings in Physics 36, Springer-Verlag, Berlin, 1989, p292.

88. T. Wada et al. in, *Photoresponsive Materials,* Porceedings of Materials Research Society, International Meeting on Advanced Materials, Materials Research Society, Pittsburgh, 12 (**1989**) 75.

89. J. W. Wu et al., *J. Opt. Soc. Am. B,* 6 (**1989**) 707.

90. J. S. Shirk et al., *Appl. Phys. Lett.*, 55 (**1989**) 1287.

91. M. Hosoda et al., *Jpn. J. Appl. Phys.*, 30 (**1991**) L1486.

92. Thu-Hua Tran-Thi, Thierry Fournier, André De Cian, Driss Chabach, Raymond Weiss, Daniel Houde, Claude Pépin, and Lê Dao, *Chem. Phys. Lett.*, 213 (**1993**) 139.

93. P. N. Prasad et al., S*PIE Proc.*, 878 (**1988**) 106.

94. Z. Z. Ho and N. Peyghambarian, *Chem. Phys. Lett.*, 148 (**1988**) 107.

95. D. R. Cooulter et al., *SPIE Proc.*, 1105 (**1989**) 42.

96. M. K. Casslevens et al., *J. Chem. Phys.*, 92 (**1990**) 2016.

97. H. Sasabe et al., *Mol. Cryst. Liq. Cryst.*, 189 (**1990**) 155.

98. N. Q. Wang et al. *Mol. Cryst. Liq. Cryst.*, 189 (**1990**) 39.

99. Po-A. Chollet et al., *SPIE Proc.*, 1273 (**1990**) 87.

100. R. A. Norwood and J.R.Sounik, *Appl. Phys. Lett.*, 60 (**1992**) 295.

101. J. R. Heflin, K. Y. Wong and O. Zamani, *Phys. Rev.*, B38 (**1988**) 1573.

102. G. M. Carter, J. V. Hryniewicz et al., *Appl. Phys. Lett.*, 49 (**1986**) 998.

103. J. W. Buchler and B. Scharbert, *J. Am. Chem. Soc.*, 110 (**1988**) 4272.

104. Y. Lin, K. Shigehara, M. Hra and A. Yamada, *J. Am. Chem. Soc* ., 113 (**1991**) 440.

105. F. H. Moser and A. L. Thomas, *The Phthalocyanines,* CRC Press Inc., Florida, **1983**.

106. Z. Z. Ho, C. Y. Yu and W. M. Hetherington III, *J. Appl. Phys.*, 62 (**1987**) 716.

107. P. N. Prasard, M. K. Casstevents, J. Pfleger and P. Logsdon, *SPIE Proc.*, **878 (1988)** 106.

108. Z. Z. Ho and N. Peyghambarian, *Chem. Phys. Lett.*, 148 **(1988)** 107.

109. J. S. Shirk, J. R. Lindle et al., *Appl. Phys. Lett.*, 55 **(1989)** 1287.

110. J. W. W, J. R. Heflin, R. A. Norwood, K. Y. Wong et. al., *J. Opt. Soc. Am. B*, 6 **(1989)** 707.

111. D. R. Coulter, V. M. Miskowski, J. W. Perry et al., SPIE, *Materials for Optical Switches, Isolators and Limiters,* 1105 **(1989)** 42.

112. M. K. Casstevens, M. Samoc, J. Pfleger and P. N. Prasard, *J. Chem. Phys.*, 92 **(1990)** 2016.

113. H. Sasabe, T. Wada, M. Hosoda et al., *Mol. Cryst. Liq. Cryst.*, 189 **(1990)** 155.

114. N. Q. Wang, Y. M. Cai, J. R. Heflin and A. F. Carito, *Mol. Cryst. Liq. Cryst.*, 189 **(1990)** 39

115. P. A. Chollet, F. Kajzar and J. Le Moigne, *Proc. SPIE Int. Soc. Opt. Eng.*, 1273 **(1990)** 87.

116. J. S. Shirk, J. R. Lindle et al., in *Materials for Nonlinear Optics: Chemical Perspectives,* S. R. Marder, J. E. sohn and G. D. Stucky eds., ACS Symposium Series, 455 **(1991)** 626.

117. C. Bubeck, D. Neher et al., in *Nonlinear Optical Effects in Organic Polymers,* J. Meissier et al. eds., Kluwer, **1989.**

118. D. K. Gerger and C. A. Kelly, *Inorg. Chim. Acta,* 154 **(1988)** 137.

119. S. Gaspard, *C. R. Acad. Sci.*, Paris, 298 **(1984)** 379-382.

120. T. H. Tran-Thi and S. Gaspard, *Chem. Phys. Lett.*, 148 **(1988)** 327.

121. J. F. Lipskier and T. H. Tran-Thi, *Inrog. Chem.*, 32 **(1993)** 722.

122. C. Kirmaier, D. Holten, *Photosynth. Res.*, 103 (**1987**) 225.

123. S. G. Boxer, *Biochem. Biophys. Acta,* 726 (**1983**) 265.

124. J. W. Buchler, H. -G. Kapellman, M. Knoff, K. -L. Lay, S. Z. Pfeifer, *Naturforsch. B: Anorg. Chem., Org. Chem.*, 38B (**1983**) 1339-1345.

125. J. W. Buchler, A. De Cian, M. Fischer, M. Kihn-Botulinski, H. Paulus, R. Weiss, J. Am. Chem. Soc. 108 (**1986**) 3652-3659.

126. J. W. Buchler, K. Elsässer, M. Kihn-Botulinski, B. Scharbert, *Angew. Chem., Int. Ed. Engl.*, 25 (**1986**) 286-287.

127. J. W. Buchler, K. Elsässer, M. Kihn-Botulinski, B. Scharbert, S. Transil, In Porphyrins: *Excited States and Dynamics;* M. Gouterman, P. M. Rentzepis and K. D. Strtaub Eds. *ACS Symposium Series 321*, American Chemical Society:, Woshington, DC, (**1986**) 94-104.

128. J. W. Buchler, B. Scharbert, *J. Am. Chem. Soc.*, 110 (**1988**) 4272-4276.

129. J. W. Buchler, A. De Cian, J. Fischer, P. Hammerschmitt, J. Löffler, B. Scharbert, R. Weiss, *Chem. Ber.*, 122 (**1989**) 2219-2228.

130. J. Löffler, *Doctoral Thesis*, Technische Hochschule Darmstadt. **1989**.

131. R. J. Donohoe, J. K. Duchowski, D. F. Bocian, *J. Am Chem. Soc.*, 110 (**1988**) 6119-6124.

132. J. L. Hoard, *Annals of the New York Academy of Sciences*, 206 (**1973**) 18.

133. W. R. Scheidt, *The Porphyrins* Vol.III, *Phys. Chem. Part A*, Academic Press, New York, (**1978**) 463.

134. J. Buchler, K. Elsässer, M. Kihn-Botulinski, B. Scharbert, *Angew. Chem.*98 (**1986**) 257.

135. J. Buchler, K. Elsässer, M. Kihn-Botulinski, B. Scharbert, S. Tail, *ACS Symp. Ser.*,31 (**1986**) 94.

136. J. W. Buchler, *Comments Inorg. Chem.*, 6 (**1987**) 175.

137. G. S. Girolami, S. N. Milam, K, N, Suslick, *J. Am. Chem. Soc*, 110 (**1988**) 2011.

138. J. Deisenhofer, O. Epp, K. Miki, R. Huber, H. Michel, *J. Mol. Biol.*, 180 (**1984**) 385.

139. J. Deisenhofer, O. Epp, K. Miki, R. Huber, H. Michel, *Nature* 318 (**1985**) 618.

140. J. Deisenhofer, O. Epp, K. Miki, R. Huber, H. Michel, *Nachr. Chem. Tech. Lab.*, 34 (**1986**) 416.

141. A. De Cian, M. Moussavi, J. Fischer and R. Weiss, *Inorg. Chem.* 24 (**1985**) 3162.

142. R. J. Donohue, J. K. Duchowski and D. Bocian, J. Am. Chem. Soc., 110 (**1988**) 6199.

143. P. Turek, P. Retit, J. -J. André, R. Even, B. Boudjema, G. Guillaud, M. Maitrot, *J. Am. Chem. Soc.*, 109 (**1987**) 5119.

144. T. H. Tran-Thi and S. Gaspard, *Chem. Phys. Lett.*, 148 (**1988**) 327.

145. I. S. Kirin, P. N. Moskalev and Y. A. Makashev, *Russsian J. Inorg.Chem.*, 10 (**1965**) 1065.

146. G. C. S. Collins and D. J. Schiffrin, *J. Electroanal. Chem.*, 139 (**1982**) 335.

147. M. M. Nicholson, F. A. Pizzarello, *J. Electrchem. Soc.*, 128 (**1981**) 1740.

148. M. -T. Riou, M. Auregan, C. Clarisse, *J. Eletroanal. Chem.*, 187 (**1985**) 349.

149. J. J. André, K. Holczer, P. Petit, M. -T. Riou, C. Clarisse, R. Even, M. Fourmigué, J. Simon, *Chem. Phys. Letters*, 115 (**1985**) 463.

150. M. Maitrot, G. Guillaud, B. Boudjema, J. J. André, H. Strzelecka, J. Simon, R. Even, *Chem. Phys. Letters*, 133 (**1987**) 59.

151. J. J. André, J. Simon, R. Even, B. Boudjema, G. Guillaud, M. Maitrot, *Synth. Met.*, 18 (**1987**) 683.

152. A. T. Chang and J. C. Marchon, *Inorg. Chim. Acta*, 53 (**1981**) L241.

153. A. De Cian, M. Moussavi, J. Fischer and R. Weiss, *Inorg. Chem.*, 24 (**1985**) 3162.

154. M. B. Robin and P. Day, *Adv. Inorg. Radiochem.*, 10 (**1967**) 247.

155. N. S. Hush, *Prog. Inorg. Chem.*, 8 (**1967**) 391.

156. K. Y. Wong and P. N. Schatz, *Prog. Inorg. Chem.*, 28 (**1981**) 369.

157. D. Markovitsi, T. H. Tran-Thi, R. Even and J. Simon, *Chem. Phys. Lett.*, 37 (**1987**) 107.

158. E. Orti, J. L. Bredas and C. Clarisse, *J. Chem. Phys.*, 92 (**1990**) 1288.

159. H. S. Nalwa, A. Kakuta and A. Mukoh, *Chem. Phys. Lett.*, 203 (**1993**) 109.

160. H. S. Nalwa, A. Kakuta and A. Mukoh, *Phys. Chem.*, 97 (**1993**) 1097.

161. J. S. Shirk, R. G. S. Pong, F. J. Bartoli, and A. W. Snow, *Appl. Phys. Lett.*, 63 (**1993**) 1880.

162. K. Braja et L. Chen et al., *Appl. Phys. Lett.*, 66 (**1995**) 932.

163. D. V. G. L. N. Rao, F. J. Aranda, J. F. Roach and D. E. Remy, *Appl. Phys. Lett.*, 58 (**1991**) 1241.

164. J. S. Shirk, J. R. Lindle et al., *Appl. Phys. Lett.*, 55 (**1989**) 1287.

165. H. S. Nalwa, *Appl. Organoment. Chem.*, 5 (**1991**) 349.

166. B. F. Levine, C. G. Bethea, C. D. Thurmond, R. T. Lynch, J. L. Bernstein, *J. Appl. Phys.*, 50 (**1979**) 2523.

167. G. F. Lipscomb, A. F. Garito, R. Narang, *J. Chem. Phys.* 75 (**1981**) 1509.

168. H. Taube, *Electron Transfer Reactions of Complex Ions in Solution*, New York and London, Accademic Press, **1970**.

169. J. S. Litter, *Essay on Free Radical Chemistry, Special Publication, London Chem. Soc.*, 24 (**1970**) 383.

170. J. S. Litter, *International Review of Science, Organic Chemistry Series one*, 10 (**1973**) 237.

171. R. J. H. Clark, *Chem. Soc. Rev.*, 13 (**1984**) 219

172. D. E. Richardson and H. Taube, *Coord. Chem. Rev.*, 60 (**1984**) 107

173. D. B. Brown, "*Mixed Valence Compounds*", NATO Adv. Study Series D., Reidel Publishing Company, Netherlands, **1980**.

174. A Vogler, in Chapter 5.5 of *Photon Induced Electron Transfer, Part D*, Elsevier Science Publishers B. V. , Netherlands, **1988.**

175. T. J. Meyer, *Pure Applied Chem.*, 58 (**1986**) 1193.

176. R. O. Kan, *Organinc Photochemistry*, McGraw-Hill, New York, **1966**.

177. H. H. Jaffe and M. Orchin, *Theory and Applications of Ultraviolet Spectroscopy*, John Wiley and Sons, New York, **1962**.

178. M. A. Fox, *Advances in Photochemistry*, John Wiley and Sons, New York, 13 (**1986**) 237.

179. L. M. Bernardo, J. C. Lopes, O. D. Soares in *Nonlinear Optical Materials*, H. Kuhn, J. Robillard eds., CRC Press, London, **1992**, p235.

180. A. Gailis, A. D. Durandin, V. Skudra, *Latv. PSR Zinat. Akad. Vestis. Teh. Zinat Ser.*, **1988**, 119, *Chem. Abs.*, 100:1463a.

181. S. Ducharme, J. C. Scott, R. J. Twieg and W. E. Moerner, *Phys. Rev. Lett.*, Vol.66, No.14 (**1991**) 1846.

182. K. Meerholz, B. L. Volodln, Sandalphon, B, Klppelen and N. Peyghambarlan, *Nature*, 371 (**1994**) 497.

183. S. M. Silence, R. J. Twieg, G. C. Bjorklund, and W. E. Moerner, *Phys. Rev. Lett.*, vol.66, No.14 (**1994**) 1846.

184. A. Ashkin, D. D. Boyel, J. M. Dziedzic, R. G. Smith, A. A. Ballman, K. Nassau, *Appl. Phys. Lett.*, 9 (**1966**) 72.

185. J. Feinberg, *Phys. Today*, Oct. (**1986**) 46.

186. G. C. Valley, M. B. Klwin, R. A. Mullen, D. Rytz, B. Wechsler, *Ann. Rev. Mater. Sci.*, 18 (**1988**) 165.

187. P. Günter, H. -J. Huignard, *Photorefractive Materials and Their Application* I and II, *Topic in Applied Physics*, vol.61 & vol.62, Springer-Verlag ,Berlin, **1988**.

188. Y. R. Shen, *The Principles of Nonlinear Optics*, John Wiley & Sons Inc., New York, **1984**.

189. J. D. Jackson, *Classical Electrodynamics*, McGraw - Hill, New York, **1975**, 2nd ed.

190. N. Bloembergen, *Nonlinear Optics*, Bejamin, New York , **1965**

191. J. A. Armstrong, N. Bloembergen, and P. S. Pershan, *Phys. Rev.*,127 (**1962**) 1918.

192. Paras N. Prasad, David J. Williams, *Introduction to Nonlinear Optical Effects in Molecules and Polymers*, John Wiley & Sons, Inc., New York **1991**, p.273.

193. M. Bass, P. A. Franken et al, *Phys. Rev. Lett.*, 8 (**1962**) 18.

194. P. Grenier, Ph. D. Thesis, *Étude de la dynamique de la transition de phase ferroélectrique dans un cristal de* $KTa_{0.93}Nb_{0.7}O_3$ *à l'aide d'une technique de mélange à quatre ondes résolu dans le temps*, Département de Physique, Facultédes Sciences, Université de Sherbrooke, Québec, Canada, **1994**.

195. J. A. Valdamanis and R. L. Fork, *IEEE J. Quntum. Electr.*, 22 (**1986**) 12.

196. R. L. Fork, B. I. Greene, C. V. Shank, *Appl. Phys. Lett.*, 38 (**1981**) 671.

197. R. L. Fork, C. V. Shank, R. Yee, C. A. Hirlimann, *IEEE J. Quantum. Electr.*, 19 (**1983**) 500.

198. D. Kühlke, W. Rudolph, and B. Wilhemi, *IEEE J. Quantum. Electr.*, 19 (**1983**) 526.

199. M. S. Stix, E. P. Ippen, *IEEE J. Quant. Electr.*, 19 (**1983**) 520.

200. O. E. Martinez, R. L. Fork, J. P. Gordon, *J. Opt. Soc. Am.*, B2 (**1985**) 753.

201. J. C. Diels, W. Dietel, J. J. Fontaine, W. Rudolph and B. Wilhelmi, *J. Opt. Soc. Am.*, B2 (**1985**) 680.

202. R. L. Fork, O. E. Martinez, J. P. Gordon, *Opt. Lett.*, 10 (**1985**) 313.

203. J. A. Valdmanis, R. L. Fork, J. P. Gordon, *Opt. Lett.*, 10 (**1985**) 131.

204. E. P. Ippen and C. V. Shank in *Ultrashort Light Pulses --- Picosecond Techniques and Applications,* Topics in Applied Physics Vol 18, S. L. Shapiro Ed., Springer-Verlag, Berlin **1977**, p83-88.

205. T. H. Tran-Thi, J. F. Lipskier, M. Simoes, S. Palacin, *Thin Solid Films*, 210-211 (**1991**) 150.

206. T. H. Than-Thi, J. F. Lipskier, D. Houde, C. Pépin, R. Langlois, S. Palacin, *J. Chem. Soc. Faraday Trans.*, 88 (**1992**) 2529.

207. T. Fournier, *Ph. D. thesis, Etude des Processus de Transfert de Charge dans des Matériau à Base de Porphrines et de Phtalocyanines: de laPhase Liquide à l'État Solide,* Univerité de Paris-sud, U.F.R. Scientifique d'Orsay, ORSAY n° d'ordre: 3423, **1994**.

208. J. Etchepare et al., *Opt. Commun.*, 63 (**1987**) 329.

209. M. Lachkar et al., *New J. Chem.*, 12 (**1988**) 729.

210. Isabelle Salabert, *Ph. D. thesis, Properiétés Physiques et Photophysiques des Biplans et Triplans Mixtes de Porphyrins et de Phthalocyanines, These de École Centrale de Paris,* Number 1995-39, 26 October **1995**.

211. A.S. Davydov, Theory of Molecular Excitons (Plenum, New York, 1971).

212. K. D. Trùòng, P. Grenier, D. Houde and A. D. Bandrauk, Chem. Phys. Lett., 196 (**1992**) 280.

213. P. Grenier, D. Houde, S. Jandl, and L. A. Boatner, Phys. Rev., B 47 (**1993**) 1.

214. P. Grenier, D. Houde, S. Jandl, and L. A. Boatner, Phys. Rev., B 50 (**1994**) 16295.

215. D. H. Auston, C. V. Shank, P. Lefur, *Phys. Rev. Lett.*, 35 (**1976**) 1035.

216. B. Sermage, H. J. Eichler et al., *Appl. Phys. Lett.*, 42 (**1983**) 259.

217. H. J. Eichler, F. Massmann, *J. Appl. Phys.*, 53 (**1982**) 3237.

218. J. P. Woerdman, *Philips Res. Rep. Suppl.*, 7 (**1971**).

219. K. Jarasiunas, J. Vaitkus, *Phys. Stat. Sol.*, A44 (**1977**) 793.

220. S. C. Moss, J. R. Lindle et al., *Appl. Phys. Lett.*, 39 (**1981**) 227.

221. K. Jarasiunas, H. J. Gerritsen, *Appl. Phys. Lett.*, 33 (**1978**) 190.

222. I. Broser, R. Broser, M. Rosenzweig, in *Landolt-Börnstein,* vol. 176, Springer, Berlin, Heidelberg, **1982**, p. 190.

223. V. Butkus, *Sov. Phys. Coll.*, 23 (**1983**) No.6.

224. S. Komuro, Y. Aoyagi et al., *Appl. Phys. Lett.*, 42 (**1983**) 79.

225. T. Miyoshi, YU. Aoyagi et al., *Jap. J. Phys.*, 22 (**1983**) 886.

226. J. Vaitkus, *Sov. Phys. Coll.*, 25 (**1985**) No.4.

227. T. H. Tran-Thi, J. F. Lipskier et al., *Thin Solid Film*, 210-211 (**1992**) 349.

228. T. H. Tran-Thi, J. F. Lipskier, D. Houde et al., *J. Chem. Soc Faraday Trans.*, 88 (**1992**) 2549.

229. Ligang Pan, Laurent G. Caron, Daniel Houde et al., *Time-resolved Four-wav Mixing Study on the Sublimated Film of Cerium Porphyrin Phthalocyanine Heterodimer System*, **1995**, Submitted to *Phys. Rev. B* for publication.

230. Ligang Pan, Laurent. G. Caron, Daniel Houde et al., *Dynamics of Third-order Nonlinear Optical Processes in Langmuir-Blodgett Film of Mixed Dimer of* $CoPC_{22}^{4+}/H_2PcTS^{4-}$ *by Femtosecond Time-Resolved Four-wave Mixing*, **1995**, Submitted to *Solid Thin Film* for publication.

231. Ligang Pan, Laurent. G. Caron, Daniel Houde et al., *Third-Order Nonlinear Optical Susceptibility of Neodymium Porphyrin-Phthalothyanine Symmetric Dimer* $NdPc_2$*and Trimer* $(NdPc)_2TPP$ *by Time-Resolved Non-Degenerate Four-Wave Mixing,* **1995**, Submitted to *Solid Thin Film* for publication.

232. Ligang Pan, Laurent G. Caron, Daniel Houde et al., *Time-resolved Third-order Nonlinear Optical Susceptibility of Sublimated Film of Cerium Porphyrin Phthalocyanine Symmetric Trimer System* by Four-Wave Mixing, **1995**, Submitted to *Solid Thin Film* for publication.

233. T. H. Tran-Thi, T. A. Mattioli, D. Chabach, A. De Cian, R. Weiss, *J. Phys. Chem.* 98 (**1994**) 8279.

234. T. H. Tran-Thi, J. F. Lipskier, D. Houde, C. Pépin, E. Keszei, J. P. Jay-Gerin, *J. Chem. Soc. Faraday Trans.*, 88 (**1992**) 2129.

235. K. D. Truong, A. D. Bandrauk, T. H. Tran-Thi, P. Grenier, D. Houde, S. Palacin, *Thin Solid Films*, 244 (**1994**) 981.

236. R. Even, J. Sion and P. Markovitsi, *Chem. Phys. Lett.*, 137 (**1987**) 107.

237. T. H. Tran-Thi, T. A. Mattioli, D. Chabach, A. De Cian, R. Weiss, *J. Phys. Chem.*, 98 (**1994**) 8279.

238. D. J. McGraw, A. E. Seigman, G. M. Wallraff and R. D. Miller, *Appl. Phys Lett.*, 54 (**1989**) 1713.

239. R. G. Cars and M. G. Gower, *IEEE J. Quant. Eletr.*, QE18 (**1989**) 1713.

240. G. R. Meredith, B. Buchalter, C. Hanzlik, *J. Chem. Phys.*, 78 (**1983**) 1533.

241. Melles Griot Inc., *Optics Guide 5,* ISSN 1051-4384, p3-5 p3-6, **1990**.

242. H. S. Nalwa, *Appl. Organoment. Chem.*, 5 (**1991**) 394.

243. M. Hosoda, T. Wada, A. Yamada, A. F. Garito, and H. Sasabe, *Mol. Cryst. Liq. Cryst.*, 3 (**1992**) 183 - 191.

244. Z. Z. Ho, C. Y. Yu and W. M. Hetherington III., *J. Appl. Phys.*, 62 (**1987**) 716.

245. H. Sasabe, T. Wada, M. Hosoda, H. Ohkawa, A. Yamada and A. F. Garito, *Mol. Cryst. Liq. Cryst.*, 189 (**1990**) 155.

246. C. Bubeck, D. Neher, A. Kaltbeitzel, G. Duda, T. Arndt, T. Asuer and G. Wegener, in *Nonlinear Optical Effects in Organic Polymers,* J. Messier et al. eds., Kluwer, **1989**.

247. P-A. Chollet, F. Kajzar and J. Le Moigne, *Proc. SPIE Int. Soc. Opt. Eng.*, 1273 (**1990**) 87.

248. N. Q. Wang, Y. M. Cai, J. R. Heflin and A. F. Garito, *Mol. Cryst. Liq Cryst.*, 189 (**1990**) 39.

249. M. Ardon, E. Lell-Döller, and J. W. Weigl, *Mol. Cryst.*, 2 (**1967**) 241.

250. L. B. Schein, A. Rosenberg, and S. L. Rice, *J. Appl. Phys.*, 60 (**1986**) 4287.

251. D. J. Williams, in *Nonlinear Optical Properties of Organic Molecules and Crystals*, edited by D. S. Chemla and J. Zyss, Academic, Orlando, **1987**, p.405-435.

252. G. R. Möhlmann, in *Organic Materials for Nonlinear Optics*, edited by R. A. Hann and D. Bloor, royal Society of Chemistry, London, **1989**, p275.